Arabinda Kumar Rath
Narayan Sahoo *Editors*

Particle Radiotherapy

Emerging Technology for Treatment of Cancer

Springer

Particle Radiotherapy

Arabinda Kumar Rath • Narayan Sahoo
Editors

Particle Radiotherapy

Emerging Technology for Treatment of Cancer

Springer

Editors
Arabinda Kumar Rath
Hemalata Hospitals and Research Center
Bhubaneswar, Odisha, India

Narayan Sahoo
Department of Radiation Physics
University of Texas-
MD Anderson Cancer Center
Houston, TX, USA

ISBN 978-81-322-2621-5 ISBN 978-81-322-2622-2 (eBook)
DOI 10.1007/978-81-322-2622-2

Library of Congress Control Number: 2016930029

Springer New Delhi Heidelberg New York Dordrecht London

Printed on acid-free paper

Springer India Ltd. is part of Springer Science+Business Media (www.springer.com)

Foreword

When Dr. A. K. Rath asked me to write the foreword for this book, *Particle Radiotherapy: Emerging Technology for Treatment of Cancer*, I was surprised because it has been nearly 20 years since I took voluntary retirement from Los Alamos National Laboratory to devote my time fully to provide appropriate radiation treatment for cancer with a hope that it could serve as a model for rural India. Earlier, for more than three decades, I devoted my work in the emerging field of particle radiotherapy during 1961–1995. Dr. Rath assured me that the observations made by me in my review papers nearly 20 years ago are still valid today and they need to be in the foreword of this book. My first interaction with Dr. Rath was nearly 10 years ago when he invited me to make a presentation during AMPICON 2006 held in Bhubaneswar where I spoke on 'Our Spiritual and Professional Heritage: Opportunity and Challenge for Medical Physicists of India in the New Millennium'. I had expressed my hope that the emerging technologies would meet the challenges in this New Millennium.

I understand that this book is intended primarily for those engaged in the application of radiation in the treatment of cancer. The leading article 'Particle Radiotherapy: An Introduction' by the editor Dr. A. K. Rath provides a good introduction on the increasing global interest in this millennium. Various international experts in the field of proton and carbon-ion radiotherapy have provided interesting chapters on the latest developments as well as challenges ahead in implementing the best form of proton and carbon-ion therapy in a robust manner.

I find it interesting to note that both the editors of this interesting book hail from the state of Odisha, one of the historic states of India: Dr. A. K. Rath is a senior medical physicist in India and Dr. Narayan Sahoo is a senior medical physicist working with protons at M.D. Anderson Cancer Center in the United States. Both are familiar with the challenging problems in providing appropriate cancer care for all the needy patients as pointed by a series of interesting articles on global health in the July 1, 2014 issue of the *Red Journal*.

I would briefly present the early historical beginnings of particle radiotherapy and the challenges we need to face in providing appropriate radiation treatment to all the cancer patients, especially those in rural India.

Particle therapy has a very long history, starting with fast neutrons during the mid-1930s. The idea of using protons also predates the introduction of Cobalt-60 which provided immense relief to a very large number of cancer patients globally at affordable cost, relative simplicity and robustness in

treating patients. Unfortunately, cobalt machines are getting replaced prematurely, especially in developing countries including India, due to reasons other than in the best interests of patients that need appropriate treatment at affordable costs.

Dr. Robert Wilson in the year 1946 published the first paper formally proposing protons in an elegant manner. It was a classic paper that needs to be studied by everybody working in this field. I had the pleasure of knowing Dr. Wilson and learned from him directly the timing and circumstances in which his idea of using protons for cancer treatment arose. It is worth noting that he was part of the Manhattan Project in Los Alamos, which was assigned with the task of building nuclear weapons. Dejected by the aftermath of Hiroshima and Nagasaki bombings, he became interested in doing science for the benefit of mankind. He joined the cradle of 'big science', the Radiation Laboratory of Ernest O. Lawrence at Berkeley. Thus one can see the beginnings of proton radiotherapy were also idealistically similar to the beginnings of radiation treatment of cancer by Roentgen, Madam Curie, L.H. Gray and several others.

During the early 1970s, with the declaration of war on cancer by the then United States President Nixon, considerable funding was available and it gave a big boost for clinical use of neutrons, negative pions (pions), and heavy ions. I had the privilege of conducting pre-therapeutic experiments on dosimetry and radiobiology of pions and heavy ions during the 1960s in Berkeley. Thereafter I continued comparative studies over the next two decades at Los Alamos National Laboratory using clinically relevant protons, heavy ions, pions and fast neutrons with the support of the U.S. National Cancer Institute.

The decade of the 1970s witnessed heavy competition for funds from different institutions. The interest in fast neutrons was revived by the clinical reinvestigations of fast neutrons and the eloquent arguments of Dr. Jack Fowler on the efficacy of fast neutrons in dealing with hypoxic cells in the tumor. The radiotherapy community at that time was inclined more towards the importance of reduced oxygen enhancement ratio (OER) achievable with fast neutrons and with the expectation of even more reduced OER with heavy ions and pions.

Although dose localization is an important factor in radiotherapy, proton beams did not get adequate attention during the 1970s in spite of their superior dose localization. Interestingly, Dr. Robert Wilson, the first proponent of protons for radiotherapy, was heading the National Accelerator facility near Chicago at that time and was approached by the radiotherapy community around Chicago to provide them with a neutron beam which is relatively complex to produce compared to protons. Accordingly, neutron beam was provided to them. The number of fast neutron facilities in the world increased rapidly to nearly 20 during 1970s reaching a plateau during the 1980s, while the number of proton therapy facilities remained to be only about five along with a few pion and heavy ion physics facilities that were very complex and expensive. Also, there was considerable interest among accelerator engineers in designing pion and heavy ion facilities dedicated to medical purposes although the clinical evidence was lacking. Some of us in the field even at that

time advocated the importance of clinical studies of protons by building medically dedicated facilities while research continued with pions and heavy ions using physics facilities.

I had the privilege of doing comparative studies of particles using therapeutically relevant beams for the first time and they revealed that the oxygen enhancement ration (OER) of heavy ions and pions were much higher than the expected low OERs on the basis of studies from low energy heavy ions. The U.S. National Cancer Institute with a select group of scientists called in a special meeting at Massachusetts General Hospital, Boston, around 1977 to discuss my new results since they were considering several proposals for funding to build medically dedicated accelerators at that time. Naturally, my findings were not palatable for some people planning to build medically dedicated pion and heavy ion facilities. Fortunately for me several other investigators repeated these measurements and obtained similar results. I had the privilege of participating in various international cooperative meetings in the field of particle therapy. In some of these meetings, whenever appropriate, based on my research findings, I stressed the importance of using protons clinically by building medically dedicated proton therapy facilities during the 1970s, at a time protons were not so popular compared to esoteric pions and heavy ions.

After 80 years of research, fast neutrons finally proved to be the treatment of choice for advanced salivary gland tumors through randomized trials in several countries. Two cyclotrons for neutron therapy were specially built with the funding from the US National Cancer Institute: one in M.D. Anderson Cancer Center, Houston, and another in the University of California, Los Angeles, so that these two special facilities can serve most of the patients with advanced salivary gland tumor since it is relatively a rare tumor. Ironically, both these cyclotrons were shut down due to lack of referrals from other medical centers, indicating that there are several other human factors besides scientific knowledge in taking proper care of cancer patients. Neutron therapy discontinued globally.

Another interesting experience came from the use of pions for radiotherapy. In spite of its interesting and unique star formation near the end of their tracks, pions were not found to be superior to the conventional radiotherapy by the group in Vancouver, Canada. The pion therapy programs in Los Alamos, USA, and Villigen, Switzerland, also discontinued. Even the famous scientists including Fermi thought that pions are ideal for cancer treatment. This clearly indicates that the potential advantage on the basis of physics and radiobiology alone is not sufficient proof for clinical improvement, which is much more complex. In some ways, this negative result is a blessing since we do not need such expensive machinery for cancer care. Among heavy ions, only carbon ions are being used rather than heavier ions such as neon that was used earlier in Berkeley during the 1980s probably because of the propensity of late effects to normal tissues.

Thus, in the particle therapy race among the particles, neutrons, protons pions and heavy ions, protons, in spite of the very low start in early 1970s, is the only main survivor. However, caution is required because of the unusual multiplication of proton therapy machines globally including in developing

countries in this New Millennium. Dr. Mazal and his associates in their chapter 'Physical Rationale for Proton Therapy and Elements to Build a Clinical Center', in this book, made an interesting comment: there are about ten companies that are bidding to build proton machines for cancer centers, much more in number than for Linacs with a caution for long term prospects for servicing due to potential danger for the survival of some of these competing companies.

The future course of proton radiotherapy needs thoughtful and collective guidance by the organizations such as PTCOG, which was technically very effective. Randomized trials comparing proton therapy are in progress with the best form of conventional radiotherapy, which is becoming increasingly formidable.

It is natural for developing countries to try to be in the forefront in emerging fields. Radiation therapy continues to be one of the main forms of cancer treatment and hence it is important to provide this much needed treatment to all the needy patients in a cost effective manner while continuing to participate and contribute to the modern developments to improve the human condition. It is ironic that I stress now on the importance of providing appropriate radiotherapy for all the needy patients after having spent most of my research career in the field of using particle therapy.

I hope that India with its increasing burden of cancer patients, growing strength of entrepreneurs and rich cultural heritage of caring for the sick and old will come up with solutions for cancer treatment worthy of emulation by developing nations of the world.

I would like to conclude with the following quotation:

> "The men who are cursed with the gift of the literal mind are the unfortunate ones who are always busy with their nets and neglect the fishing". Rabindranath Tagore

M.R. Raju, D.Sc.
International Cancer Center, Mahatma Gandhi Memorial
Medical Trust, Pedaamiram, AP, India

Fellow, Los Alamos National Laboratory, Los Alamos, NM, USA

Preface

The success of clinical radiotherapy is judged by the extent of complication free tumor control it can provide. In the current practice of radiotherapy, very precise methods of image-guided intensity-modulated beam delivery can be used to deliver highly conformal radiotherapy to the target. However, normal tissue tolerance remains the main limiting factor in delivering sufficient dose to the target to maximize the tumor control probability (TCP). Developments in radiotherapy are driven by the desire to find suitable modalities and techniques to reduce dose to the normal tissue leading to lower normal tissue complication probability (NTCP) that would allow delivery of higher dose to the target to improve the therapeutic gain. Therapeutic beams of particles like C-12 ion and proton (referred as particles in this preface and in other chapters of this book) are attractive options to achieve this goal because of their ability to reduce the dose to the critical organs and normal tissue due to their finite range in the tissue-like media. The availability of discrete scanning C-12 and proton beam delivery technology has also made intensity-modulated particle beam therapy possible. There is a growing interest in clinical practice to utilize these modalities to improve the efficacy of the radiation therapy. Although the dose distribution of particle beam in water medium is precisely known, many aspects of physical and biological effective dose distribution inside the patient remain uncertain. The particle beam dose distribution is more sensitive to small intra-fraction and inter-fraction changes in the patient anatomy, setup errors, and internal organ motion. There are ongoing efforts to design treatment plans to mitigate some of the physical and biological uncertainties in the treatment planning process. Further improvements in the efficacy of the particle beam therapy will depend on our ability to reduce these uncertainties through the knowledge gained from past clinical experience and future research endeavors. Keeping this in mind, a daylong symposium was organized in November 2013 in Kolkata, India, to hear the views of leading experts on the current state of the art and future developments of the delivery system, dosimetry, treatment planning, and radiation biology for particle therapy. The idea to publish a book based on the material presented at the symposium and with some additional chapters was conceived to share the

knowledge and wisdom of these experts with the wider community interested in radiation oncology. This book starts with a foreword by Dr. M. Raju who made many groundbreaking contributions to the early development of particle therapy. Dr. Rath, one of us, provides as essay in Chap. 1 on the historical developments and his views on the future directions of particle therapy using his vast knowledge gained both from attending many national and international conferences on this subject and from close interaction with many experts in the field. Dr. Mohan, who has made many seminal contributions to the field of radiation oncology physics and proton therapy, and his co-authors share their expert views on the future developments to improve the efficacy particle therapy in Chap. 2. IBA is the world's leading vendor of the proton therapy delivery system. The current state of the art and future developments in the beam production system are described by Dr. Emma Pearson et al. from IBA Medical Accelerator Solutions: R&D Department in Chap. 3. Japan is a leader in the use of the C-ion therapy. In Chap. 4, Dr. Koji Noda, the Director of the Accelerator and Medical Physics Department of the National Institute of Radiological Sciences in Chiba, Japan, describes his experience in the development of C-ion therapy technologies in Japan. Dr. Mazal is the Head of Medical Physics of Institut Curie, Paris, France, including the Proton Therapy Center in Orsay (CPO). He and his colleagues from France share their expert knowledge on the physics, biology, technology and clinical indications for proton therapy, and logistics to build a clinical proton therapy facility in Chap. 5. In Chap. 6, Dr. Sahoo, one of us, and his co-authors provide a review of the radiation dosimetry in proton therapy. Dr. Marco Schwarz, a leading expert on the clinical proton therapy, and his colleagues from Trento, Italy, describe their perspective of the current and future clinical use of the proton pencil beam scanning technology in Chap. 7. Dr. Kooy is a well-known expert on the clinical use of proton therapy and is involved in the development of new generation of proton therapy treatment planning system. Chap. 8 provides his insights about the treatment planning for protons. Dr. Jäkel is the Medical Physics Director of the Heavy Ion Therapy facility in Heidelberg, Germany, and is a well-known expert on the heavy ion therapy physics. His perspectives of radiation therapy with protons and heavy ions are given in Chap. 9. Robust optimization of treatment plans is considered to be essential to mitigate range, set up, and internal organ motion related uncertainties in particle therapy. Dr. Liu, an expert on robust optimization, describes the current practice and future developments in robust optimization and robustness quantification methodology for proton therapy planning in Chap. 10. One of the attractive features of particle therapy is their higher radiobiological effectiveness (RBE) on cell kill compared to photons used in external beam radiotherapy due to higher linear energy transfer during the energy deposition process. However, the uncertainties in the RBE values of particle beams are large and more work is needed to find their clinically relevant values. Dr. Matsufuji is a leading expert on modeling and analyzing

the biological and clinical effectiveness of the carbon ion therapy. He shares his insights on the modeling of biological effective dose for carbon ion therapy in Chap. 11. Most of the new proton therapy facilities are equipped with pencil beam scanning because of its ability to deliver more conformal dose to the target compared to the passively scattered proton beam. In Chap. 12, Dr. Lomax, a well-known expert on proton pencil beam scanning technology, describes the methodology for planning and mitigating the range and motion related uncertainties in this popular proton therapy modality. In summary, this book covers important aspects of physics and radiobiology, delivery system, facility design, treatment planning, and future directions for particle therapy. It is our sincere hope that readers will find this book as a useful resource for their professional endeavors related to particle therapy.

We express our sincere appreciation of the efforts of all the authors in writing their chapters. We are also thankful to many people at Springer who were involved in the publication of this book. We are happy that this book is published, and is in the hands of interested readers who are aspiring to gain some knowledge or information from the collective insights of the authors of different chapters.

Arabinda Kumar Rath
Hemalata Hospitals and Research Center, Bhubaneswar, Odisha, India

Narayan Sahoo
Department of Radiation Physics,
University of Texas M.D. Anderson Cancer Center,
Houston, TX, USA

Contents

1 Particle Radiotherapy: An Introduction 1
Arabinda Kumar Rath

2 Particle Therapy in the Third Millennium: Current Status and Future Outlook 7
Radhe Mohan, Uwe Titt, and Fada Guan

3 Development of Cyclotrons for Proton and Particle Therapy 21
Emma Pearson, Willem Kleeven, Vincent Nuttens, Simon Zaremba, Jarno Van de Walle, Eric Forton, Robin Choo, and Yves Jongen

4 Development of C-Ion Radiotherapy Technologies in Japan 37
Koji Noda

5 Physical Rationale for Proton Therapy and Elements to Build a Clinical Center 59
A. Mazal, N. Fournier-Bidoz, F. Goudjil, S. Delacroix, C. Nauraye, L. DeMarzi, C. Mabit, I. Pasquié, M. Robilliard, A. Patriarca, C. Wessels, C. Alapetite, S. Helfre, H. Mammar, S. Bolle, V. Calugarou, L. Feuvret, J.L. Habrand, L. Desjardins, R. Dendale, and A. Fourquet

6 Radiation Dosimetry of Proton Beams 77
Narayan Sahoo, Gabriel O. Sawakuchi, Michael T. Gillin, and Xiaorong R. Zhu

7 Clinical Pencil Beam Scanning: Present and Future Practices 95
Marco Schwarz, Carlo Algranati, Lamberto Widesott, Paolo Farace, Stefano Lorentini, Roberto Righetto, Daniele Ravanelli, and Francesco Fracchiolla

8 Treatment Planning for Protons: An Essay 111
Hanne Kooy

9 Radiation Therapy with Protons and Heavy Ions 127
Oliver Jäkel

10 Robustness Quantification and Worst-Case Robust Optimization in Intensity-Modulated Proton Therapy 139
Wei Liu

11 Modeling of Biological Effect of Charged Particles for C-Ion RT 157
Naruhiro Matsufuji

12 SFUD, IMPT, and Plan Robustness 169
Antony Lomax

Particle Radiotherapy: An Introduction

1

Arabinda Kumar Rath

There were 14.1 million new cancer cases, 8.2 million cancer deaths, and 32.6 million people living with cancer (within 5 year of diagnosis) in 2012 worldwide [1]. From 1954 through December 2014, a total of 137,179 patients across the world have been treated with all forms of particle therapy since it was first started in Berkeley in 1954 [2]. Presently particle radiotherapy treatment constitutes about 1 % of the total number of patients receiving radiotherapy worldwide. In the recent past, there is a significant interest by all stakeholders in this decades old technology and the chance that it will emerge as a technology of choice as a prime modality of cancer treatment is very high. The book is an attempt to have a closer look on what are the physical and biological factors that make particles the choice of radiotherapy and the clinical evidence that are slowly pouring in from the exponentially growing number of particle therapy centers worldwide treating cancer patients.

A.K. Rath, PhD
Hemalata Hospitals and Research Center,
Bhubaneswar 751023, Odisha, India
e-mail: akrath@hemalatahospitals.com

1.1 History of Development

Treatment of cancer using ionizing radiation was started soon after the discovery of X-rays by Roentgen in 1895. The first such successful treatment of cancer with cure has been reported to have been achieved as early as July 4, 1899, in Stockholm [3]. Photons or X-ray therapy that dominated radiotherapy for the first half of the last century can be broadly classified into three phases as superficial therapy (10–150 KV), deep (or orthovoltage) therapy (200–300 KV), and megavoltage (or super voltage) therapy (above 1 MV). High-energy X-rays (photons) especially with the Linear Accelerator technology has led to the success of radiotherapy as one of the primary modality of cancer treatment in the last three decades. Ernest Rutherford first coined the term "proton" and reported its existence 1919. The first reported literature of particle acceleration dates back to 1936 when Lawrence developed the first cyclotron in Berkeley, and later he built a 37 in. cyclotron by the year 1939 for which he was awarded the Noble Prize the same year. Robert Wilson wrote a classic paper in 1946 that suggested the potential use of particle beams for treatment of cancer. Using the 184 in. cyclotron developed in Berkeley, the first proton therapy treatment was delivered in 1954 and was used for patient treatment till its decommissioning in 1987. Similar efforts were made in Uppsala Sweden, and patient treatment with 185 MeV

A.K. Rath, N. Sahoo (eds.), *Particle Radiotherapy: Emerging Technology for Treatment of Cancer*,
DOI 10.1007/978-81-322-2622-2_1

proton beam was undertaken from 1957 to 1968. The Harvard Cyclotron was used for patient treatment from 1959. Particle therapy started in Russia in 1967, in Japan in 1979, and in South Africa in 1993. The first hospital based proton therapy facility was built in Loma Linda University in the USA in 1990 and has been treating patients since then.

1.2 Physical Basis of Particle Therapy

Therapeutic use of protons was first suggested by Robert R Wilson in 1946 [4]. The depth dose curves of protons are completely different from those of photons (X-rays) because these charged particles have very little scattering when penetrating the matter and give the highest dose near the end of their range which is known as the "Bragg peak" after which there is drastic fall of dose within a short distance (Fig. 1.1). Much before the clinical success of today's megavoltage X-rays (photons) in precision radiotherapy, it was pointed out as early as in 1974 that on the basis of the physical factors such as higher LET (Fig. 1.2), the particles of choice for radiotherapy are protons or helium ions [5]. At Harvard a comparison of the dose distribution of protons to Co-60 gamma rays and 22-MeV photons from a betatron was done [6]. They found out that the dose to normal tissues outside the treatment volume is about 70 % of the tumor dose when Co-60 gamma rays are used. This normal tissue dose is reduced to about 40 % when 22-MeV X-rays are used, and this is reduced further to about 22 % when protons are used. In addition, the dose with protons can be made more uniform throughout the treatment volume including the edges. Thus, using multiport proton irradiation, the dose given to all of normal tissues can be reduced even more than that achieved with 22-MeV X-rays. They had shown that the use of high-energy protons or other heavy-charged particles makes possible substantially improved control of the geometric distribution of therapeutic radiations over that obtainable with super-voltage X-rays or electrons and suggests the possibility of better clinical control of some types of malignant lesions with reduced complication rates. Sufficient clinical experience with protons has already been obtained to show that their effects are not markedly different from those of high-voltage X-rays if equal radiation doses are compared. In a review [7] of the physical, technical, radiological, and clinical status of proton therapy, it was reported that protons produce effects similar to those of X-rays, but dose distribution and range make protons more flexible and useful therapeutically. The ability to confine the major fraction of proton absorbed dose to a designated volume allows the decrease of dose to normal tissue or the increase of dose to the cancer. Improved dose distribution is quantified by determining the ratio of normal

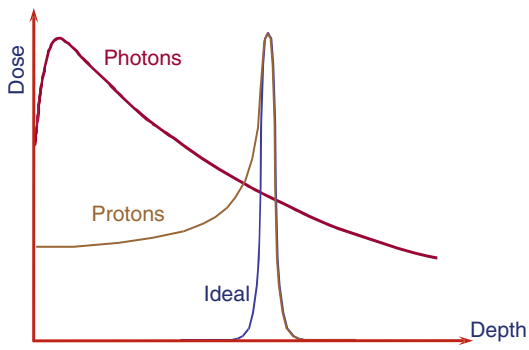

Fig. 1.1 Depth dose characteristics of Photons Versus Protons showing the "bargg peak" in protons which is much closer to the ideal beam in external beam radiotherapy.

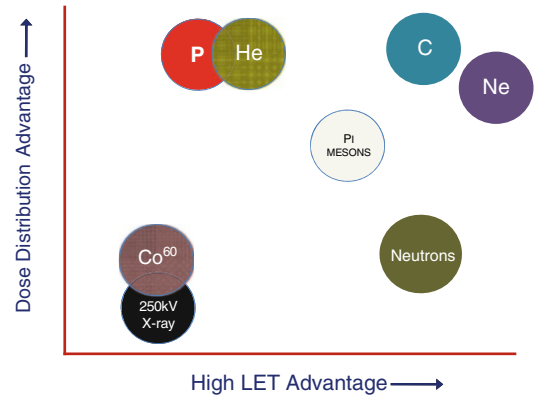

Fig. 1.2 Dr Raju's idea demonstrating the relative advantage of particles proposed in 1974 representing the relative merits of high Linear Energy Transfer (High LET) particles

tissue dose for X-rays to that for protons in different treatment plans. Normal tissue integral dose from X-rays therapy is generally 2–5 times as high as that anticipated from proton therapy.

1.3 Facilities and Patients Statistics

Exact up-to-date statistics are available from PTCOG for each of the treating facilities all over the world. The numbers for each type of particle treated so far in the world are as follows. Patients treated with He are 2054 (1957–1992), with pions are 1100 (1974–1994), with C-ions are 15,736 (1994 to present), with other ions are 433 (1975–1992), and with protons are 118,195 (1954 to present) which makes the grand total as 137,179 as of the end of 2014. Of the total of about 137,000 patients treated with particle therapy worldwide from 1954 to 2014, 15,400 were treated in 2014 alone making it more than 10 % being treated only in last 1 year. In 2014, about 10 % of patients were pediatric and another 10 % were treated for ocular melanomas. Forty-eight particle therapy facilities were in clinical operation at the end of 2014. Of the total cases treated worldwide with particles, 86 % are treated with protons and 14 % are treated with carbon ions and with other particles. Five new particle therapy centers started patient treatments in 2014. This again is more than 10 % increase in facilities in 1 year. Further as on date, more than 30 more new particle therapy centers are under construction that will add about 80 treatment rooms in the near future. They are spread out all over the world with half of these are in the USA and one-third are in Asia. In 2015 about 15 centers were expected to start commissioning, and about half of them were planning to start treating patients before the end of 2015.

These figures are impressive and growth story of particle radiotherapy is truly exponential. Now there is a school of thought that as the ancillary technology for particle therapy is maturing now these data will further get strengthened and as the integrations become better we will have more success stories following in the near future. But there is another school of thought that we are having only incremental benefits which are very small and do not justify the kind of cost that a particle therapy facility requires. Though the growth story is impressive, will particle therapy be a viable alternative to photons if not replace it completely is a question that is still to be answered. The physics of particle radiotherapy has been a promising one since the beginning, but in an era of cost consciousness, the debate is should the limited resources of healthcare be spent on a technology which is expensive and may be the most expensive in medical sciences ever. Several of the authors in this book have pointed out as part of their discussions by quoting several studies of theirs as well as others that there are promises and pitfalls in particle radiotherapy. The real challenge today is to make this theoretically superior technology accessible and affordable to millions of cancer patients worldwide.

1.4 Physical Advantages Versus Clinical Realities

High LET radiation from particles as a more effective alternative to photons for routine clinical treatment of resistant tumors has not yet been addressed to the satisfaction of the medical fraternity. The reason for this is that though the physics of particles and their dose deposition capabilities are well understood, delivering them safely to the desired target area in a patient, the dose response and complications thereof are not fully understood. A considerable progress though has been made in understanding the radiobiology of the different particles that includes proton, carbon ions, helium ions, pi mesons, and neutrons initially proposed as choice of particles for radiotherapy [8]. High-energy X-rays (photons) have reached a point of saturation in radiotherapy; it is evident that they cannot further be improved only on the basis of dose distribution advantages. It is only with protons and particles (light and heavy ions) that we will be able to get further dose distribution advantages. Increasing radiation dose to tumor increases tumor control probability leading to higher cure rates in cancer. This was well

recognized almost half a century ago that there is no "tumoricidal threshold dose," and the higher the dose, the higher is the probability of radiation-induced cell killing [9]. Recent data from dose escalation studies with protons [10] in a randomized controlled trial shows superior long-term cancer control for men with localized prostate cancer receiving high-dose versus conventional-dose radiation. This was achieved without an increase in grade ≥3 late urinary or rectal morbidity. Similarly treatments with carbon ion have already shown significant improvements in local control as well as improved survival rates as has been reported by the working Group for Lung Cancer in Japan with carbon ion radiotherapy for stage I non-small cell lung cancer study [11] more than a decade ago.

Is the field of particle therapy a "trap" for physicists and engineers who want to solve everything in a hurry as was put in a candid way by Dr MR Raju [12] almost two decades ago after working in the field for three decades. Let us ask the fundamental question "has radiotherapy helped cancer control?" The answer is a big and emphatic "yes." It was recognized in early parts of the last century that radiation possesses very high tumoricidal effect. That has propelled a century of research in radiation therapy to localize and deliver the radiation precisely to the tumor or cancer cells called as targets. All forms of radiotherapy have always focused on this fundamental concept. As the energy of photons increased from the kilo voltage level to megavoltage level, it was realized that higher photon energy per se will not be making therapy more effective. After reaching optimum energy level, research was focused on target definition and ability to contain the radiation to the boundaries of these targets. Simultaneous developments in imaging and computational power helped bridge the gap better, and the era of conformal radiotherapy was born. The last two decades since the mid-1990s, which is the era of IMRT and IGRT, have witnessed quantum leaps in radiotherapy with photons. Higher number of fractions which were used to reduce complication is no more the norm, and hypofractionation with unconventional fractions ranging from single to five or seven has now become the norm for delivering radiation with stereotactic body radiotherapy (SBRT). It is now realized that photons have limitations and can no more be tailored to achieve further dose escalation by the current methods of delivery.

Recent reports suggest that disregarding relative biological effectiveness (RBE) variations might lead to suboptimal proton plans giving lower effect in the tumor and higher effect in normal tissues than expected [13]. As per the current assumption of RBE = 1.1, higher doses to the tumor and lower doses to the normal tissues were obtained for the proton plans compared to the photon plans. In contrast, when accounting for RBE variations, the comparison showed lower doses to the tumor and hot spots in organs at risk in the proton plans. These hot spots resulted in higher estimated NTCPs in the proton plans compared to the photon plans. For cases where the target is situated close to structures sensitive to hot spot doses, this trend may lead to bias in favor of proton plans in treatment plan comparisons. This has called for re-discussion on the role of variable relative biological effectiveness (RBE) in particle therapy, and it is now becoming more and more evident that for various end points of clinical relevance the biological response is differentially modulated by particles as compared by photons [14]. Thus, the presumptions like RBE of 1.1 for protons for the whole radiation field can no longer be used to predict response. In fact it is proposed by several pioneers in the field that biological modeling rather than physical dose modeling is going to be the way of treatment planning in the near future of radiotherapy.

1.5 The Cost Factor

The success of the last two decades of photon therapy has however not been translated directly into the success of particle therapy primarily due to some of the important factors like technology of particle therapy which is too expensive at present. Even among particles, there is a

significant difference in cost between the proton therapy and carbon ion therapy. The particle accelerators are basically high-end physics research equipment and not a routine hospital equipment. Cyclotrons that were traditionally physics research installed in university and academic setups have now been downsized, but still the infrastructure costs are in several orders higher than the photon therapy facilities. The order of cost and complexity difference between the linear accelerator technology with photon delivery and those for protons are in a scale 10–20 times higher and those for carbon ions are in a scale of 100 times higher, making it difficult for becoming a routine hospital equipment. The proton therapy done primarily with cyclotrons is now custom made for therapy facilities helping cost reduction. But this has been done in the last decade and a lot more is yet to be done to reduce cost. The total number of all particle therapy centers has not yet reached 50 where as there are thousands of photon accelerators that are available in the field since the last two decades. The synchrotrons and synchrocyclotrons used for production of carbon ions are very expensive even today and are beyond the reach of hospitals. The complexity also demands higher number of qualified manpower, and it is just not possible to bridge this gap in a short period of time. The cost component being too expensive to build and too expensive to maintain still haunts the field of particle radiotherapy today.

1.6 Consolidation Phase and Future Outlook

But the good news is that proton therapy has gained attention as a primary modality of radiation therapy in countries like the USA. Academic centers like university hospitals as well as community hospitals have built or are in the process of building proton therapy centers primarily to achieve competitive advantages. Clinical outcome data that had come from the proton therapy center in the last decade were from older technologies like passive scattering proton therapy (PSPT). But the newer facilities are having better capabilities of delivery with modern technology of particle generation and are likely to be superseded by intensity-modulated proton therapy (IMPT). Initial data though smaller in number show improvement in dose distribution by IMPT [15] as compared to the best conventional photon radiotherapy that has been reported. Such physical data are likely to result in longer-term success clinically in proving particle therapy superior to photon therapy of the present day. With more and more centers coming up with IMPT facilities, there will be opportunity to justify the adoption of proton therapy in more number of clinical indications than those that are currently used in routine practice of particle therapy. Recently PTCOG have initiated multi institutional trials for different clinical sites that helps bringing parity in delivery techniques as well uniformity in clinical parameters that in turn will help better reporting of larger series of data which will help to accept the technology. The early adopters of protons in the USA were primarily focusing on prostate cancer treatment, but today the clinical investigations are spread over various sites and indications like oropharynx, macular degeneration, pediatrics, early lung cancer, primary liver cancer, early breast cancer, as well as locally advanced lung cancer.

The fact remains that clinical data as on date are too small and have not been able to justify the wide spread acceptance of protons and particle therapy worldwide. The refinements in technology and integration with better imaging, planning, and delivery techniques are taking place at a fast pace, and it is only in this decade there has been an exponential increase in clinical facilities as well as patient numbers with protons and particle therapy facilities worldwide. The century of research in radiation and decades of patient treatment with particles have helped the development of particle therapy as an important clinical modality for treatment of cancer for the present and future. Sparse clinical data due to few facility and prohibitively expensive technology however still continues to be a challenge for making particle therapy a common tool for cancer care. The last two decades' significant growth in facilities and

patient number is an indication that this technology is in the right track and the future of particle therapy is definitely promising. Research in particle therapy is now at a feverish pitch, and if the present outcomes are any indication, it may not be long before this "hype" of particle radiotherapy could turn into "hope" for cancer patients worldwide.

References

1. Ferlay J, Soerjomataram I, Ervik M, Dikshit R, Eser S, Mathers C, Rebelo M, Parkin DM, Forman D, Bray, F. GLOBOCAN 2012 v1.0, cancer incidence and mortality worldwide: IARC CancerBase No. 11 [Internet]. Lyon: International Agency for Research on Cancer; 2013. From: http://globocan.iarc.fr.
2. Jermann M. Particle therapy statistics in 2014. Int J Particle Ther. 2015;2(1):50–4.
3. Mould RF. A century of X-rays and radioactivity in medicine: with emphasis on photographic records of the early years. 1993, IOP Publication, London, UK.
4. Wilson RR. Radiological use of fast protons. Radiology. 1946;47:487–91.
5. Raju MR. Pions and heavy ions in radiotherapy. Presented at the Xlth international cancer congress, Florence; 20–26 Oct 1974. Excerpta medica international congress series, vol 353. Surgery, radiotherapy and chemotherapy of cancer, vol 5. pp. 161–7.
6. Koehler AM, Preston WM. Protons in radiation therapy. Radiology. 1972;104:191–5.
7. Archambeau J, Bennett GW, Levine GS, Cowen R, Akanuma A. Proton radiation therapy. Radiology. 1974;110:445–57.
8. Raju MR. Heavy Particle Radiotherapy. Academic Press; 1980.
9. Suit H, Wette R. Radiation dose fractionation and tumor control probability. Radiat Res. 1966;29: 267–81.
10. Zietman AL, Bae K, Slater JD, Shipley WU, Efstathiou JA, et al. Randomized trial comparing conventional-dose with high-dose conformal radiation therapy in early-stage adenocarcinoma of the prostate: long-term results from Proton Radiation Oncology Group/American College of Radiology 95–09. J Clin Oncol. 2010;28(7):1106–11.
11. Miyamato T, Yamamoto N, Nishimura H, et al. Carbon ion radiotherapy for stage I non-small cell lung cancer. Radiother Oncol. 2003;66:127–40.
12. Raju MR. Particle radiotherapy: historical developments and current status. Radiat Res. 1996;145(4):391–407.
13. Wedenberg M, Toma-Dasu I. Disregarding RBE variation in treatment plan comparison may lead to bias in favor of proton plans. Med Phys. 2014;41:091706.
14. Tommasino T, Durante M. Proton radiobiology. Cancers. 2015;7:353–81.
15. van de Water TA, Lomax AJ, Bijl HP, de Jong ME, Schilstra C, et al. Potential benefits of scanned intensity-modulated proton therapy versus advanced photon therapy with regard to sparing of the salivary glands in oropharyngeal cancer. Int J Radiat Oncol Biol Phys. 2011;79(4):1216–24.

2 Particle Therapy in the Third Millennium: Current Status and Future Outlook

Radhe Mohan, Uwe Titt, and Fada Guan

2.1 Introduction

Robert Wilson's recognition of the therapeutic potential of the physical characteristics of protons formed the foundation of particle therapy. He proposed the use of charged particles for the radiotherapy of cancers in 1946 [1]. Although the clinical promise of particle therapy was considered undisputable, there were only intermittent developments and limited adoption of this modality until the end of the twentieth century, presumably because of the high cost of establishing and operating clinical particle therapy facilities. Most of the particle treatments during that period were carried out at facilities designed for physics experiments. Notable among these facilities were Lawrence Berkeley National Lab (LBNL) (1955–1992, protons); MGH-Harvard Cyclotron (1961–2001, protons); LBNL (1975–1992, heavy ions); HIMAC, NIRS, Japan (1994–, Carbon ions); Paul Scherrer Institute (PSI), Switzerland (1996–, protons); and GSI, Germany (1997–, Carbon ions). Of these, PSI is the only facility that has employed scanning beams and intensity-modulated proton therapy (IMPT) from the inception. Loma Linda University was the first to establish a hospital-based proton therapy facility in 1990, followed by NCC, Japan, in 1998.

Since 2001, there has been a rapid growth in the number of clinical particle therapy facilities, and the rate of growth is increasing. Prominent among the new facilities are the MGH, University of Florida (Jacksonville) and MD Anderson Cancer Center (MDACC) proton therapy centers and the heavy ion facilities at the University of Heidelberg, Germany, and at CNAO, Pavia, Italy. This is by no means a complete list, and many more are in development or are planned. Based on PTCOG (http://www.ptcog.ch/) estimates, the number of patients treated with particles worldwide as of March 2013 was approximately 115,000. This includes about 100,000 treated with protons, 11,000 with carbon, 2,000 with helium, and 2,000 with other ions.

The original rationale for particle therapy was based on the physical characteristics of particles. It was assumed that, biologically, protons and photons are nearly the same. For heavier ions, increased biological effectiveness is considered another advantage. Based on the original work of Goitein et al. during the late 1970s and early 1980s, which introduced clinical 3D conformal radiotherapy (3DCRT), online image guidance utilizing orthogonal kV X-rays, etc., the potential of proton therapy surpassed the best that could be achieved with the photon therapy then available. Since then, the state of the art of photon therapy has evolved rapidly with the development of

R. Mohan, PhD (✉) • U. Titt, PhD • F. Guan, PhD
Department of Radiation Physics, MD Anderson Cancer Center, Houston, TX, USA
e-mail: rmohan@mdanderson.org

A.K. Rath, N. Sahoo (eds.), *Particle Radiotherapy: Emerging Technology for Treatment of Cancer*,
DOI 10.1007/978-81-322-2622-2_2

3DCRT, multi-leaf collimators, IMRT, on-board and in-room volumetric image guidance, and much more. However, the state of the art of particle therapy has not kept pace (with the exception of scanning beams and IMPT at PSI), presumably due to the very high cost of particle therapy facilities and the small number of investigators involved in addressing particle therapy issues. Because of this, photon therapy may have become competitive or even leap-frogged over particle therapy. Conceivably, as a result, the clinical evidence demonstrating the superiority of particle therapy over photon therapy has been limited and unconvincing. Thus, as new particle therapy centers proliferate, particularly in the United States, concerns are being expressed, and questions are being raised about the benefits vs. cost of particle therapy.

Fortunately, even though the cost of particle therapy remains high and of major concern, with the establishment of particle therapy centers at some major cancer centers (e.g., MDACC), there has been a major increase in research activity in the last decade or so. This is leading to a greater understanding of the reasons underlying the limitations of particle therapy as practiced currently and to the development of novel methods and strategies to overcome these limitations and to reduce the cost of particle therapy (Fig.2.1, Mohan, unpublished).

The following sections describe the rationale for particle therapy, the current state of the art, and its limitations and summarize ongoing and planned research to advance it. While most of the discussion is on protons, issues related to carbon therapy and the potential of other light ions are also addressed.

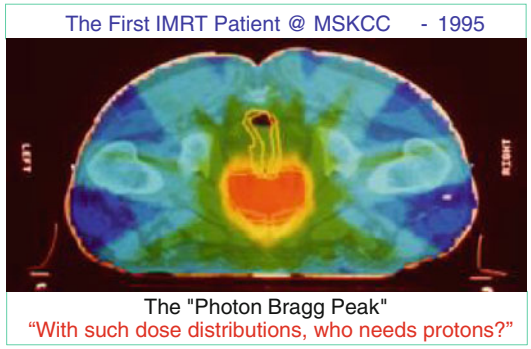

Fig. 2.1 Rapid advancements in photon therapy in the 1980s and 1990s made photon therapy competitive with particle therapy. Comparable progress is needed in particle therapy to realize its highest potential

2.2 Rationale for Charged Particle Therapy

As charged particles traverse a medium (e.g., a patient or a water phantom), they scatter and lose energy continuously. The rate of energy loss per unit distance traveled, called "linear energy transfer," or LET, increases as particles slow down until their energy is fully depleted and they come to a sudden stop. The shape of the resulting depth dose curve, called the Bragg curve, is illustrated in Fig. 2.2. A lower dose is deposited at points at the entrance and in the plateau region, i.e., in the region before the steep rise in dose, and most of the dose is deposited in a region around the Bragg peak. Because of the statistical nature of the scattering and energy loss processes, there is straggling of the range of the particles, and, therefore, the steepness of the distal fall-off of dose is somewhat moderated, the magnitude of which depends on the initial energy. The depth of maximum penetration also depends on the initial particle energy. This type of dose deposition pattern does not lend itself to treating finite-size, arbitrarily shaped tumors. Therefore, the incident beam is spread out longitudinally and laterally, using scatterers and range modulators, and shaped, using apertures and compensators, to produce a volume of high dose that conforms to the shape of the target. Alternatively, pencil beams (beamlets) of a sequence of energies and varying intensities are scanned to produce a pattern of conformal dose distribution that optimally balances tumor dose against normal tissue sparing. These two modes of treatment planning and delivery are called passively scattered particle therapy (PSPT) and intensity-modulated particle therapy (IMPT).

In contrast, photons deposit the largest amount of dose near the entrance and continue to deposit significant dose beyond the target (Fig. 2.2). In

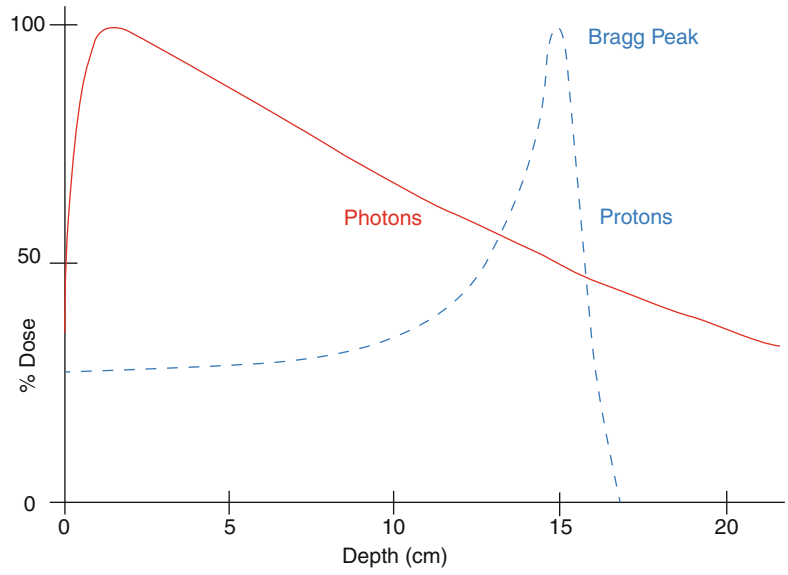

Fig. 2.2 Typical depth dose characteristics of protons and photons in water

short, the rationale for particle therapy is that it deposits low dose proximal to the tumor target and virtually no dose beyond the target. Heavier ions have similar characteristics except that their interactions with the media may result in a low-dose fragmentation tail of lower atomic number particles distal to the end of the range of the primary particles.

The physical characteristics of particles can be used to produce dose distributions that appear to be exquisitely superior compared to those possible with photons. Examples of medulloblastoma, nasopharynx and base of skull [1] are shown in Fig. 2.3. The potential of particle therapy over photons and the potential of carbon ions over both protons and photons are, in principle, evident based on physical dose distributions.

In addition to their physical characteristics, the biological effectiveness of particles must also be considered. For protons, the relative biological effectiveness (RBE), based on the average of multiple experiments, has been assumed to have a constant value of 1.1 for all cancers and normal tissues. This is an approximation that could have unforeseen consequences, and more accurate determination of RBE and its proper incorporation into proton treatment plan design and evaluation may lead to further enhancement of the effectiveness of protons. For heavier ions, LET is considerably higher than that of protons, produces more complex DNA double-strand breaks, and, therefore, leads to much higher RBE. Furthermore, it can no longer be approximated by a constant value. Heavier ions also have a lower oxygen-enhancement ratio (OER). Both the higher RBE and the lower OER, especially in and around the Bragg peak, can be a considerable advantage in tumor cell killing, particularly for resistant tumor cells. This is the primary rationale for using heavier ions for cancer treatments.

Figure 2.4 shows LET and dose as a function of depth for three different particles, and Fig. 2.5 shows RBE-weighted depth doses for protons and carbon and RBE and OER as a function of LET for alpha particles. Note that even for protons the RBE varies.

2.3 Current Status

Although particle therapy has been used for many decades, the number of patients treated with it is considerably smaller than with photons. Because of the recent dramatic increase in the number of facilities and the associated high cost, questions have been raised about the efficacy, cost effectiveness, and the motivation of establishing such facilities. The following are some examples.

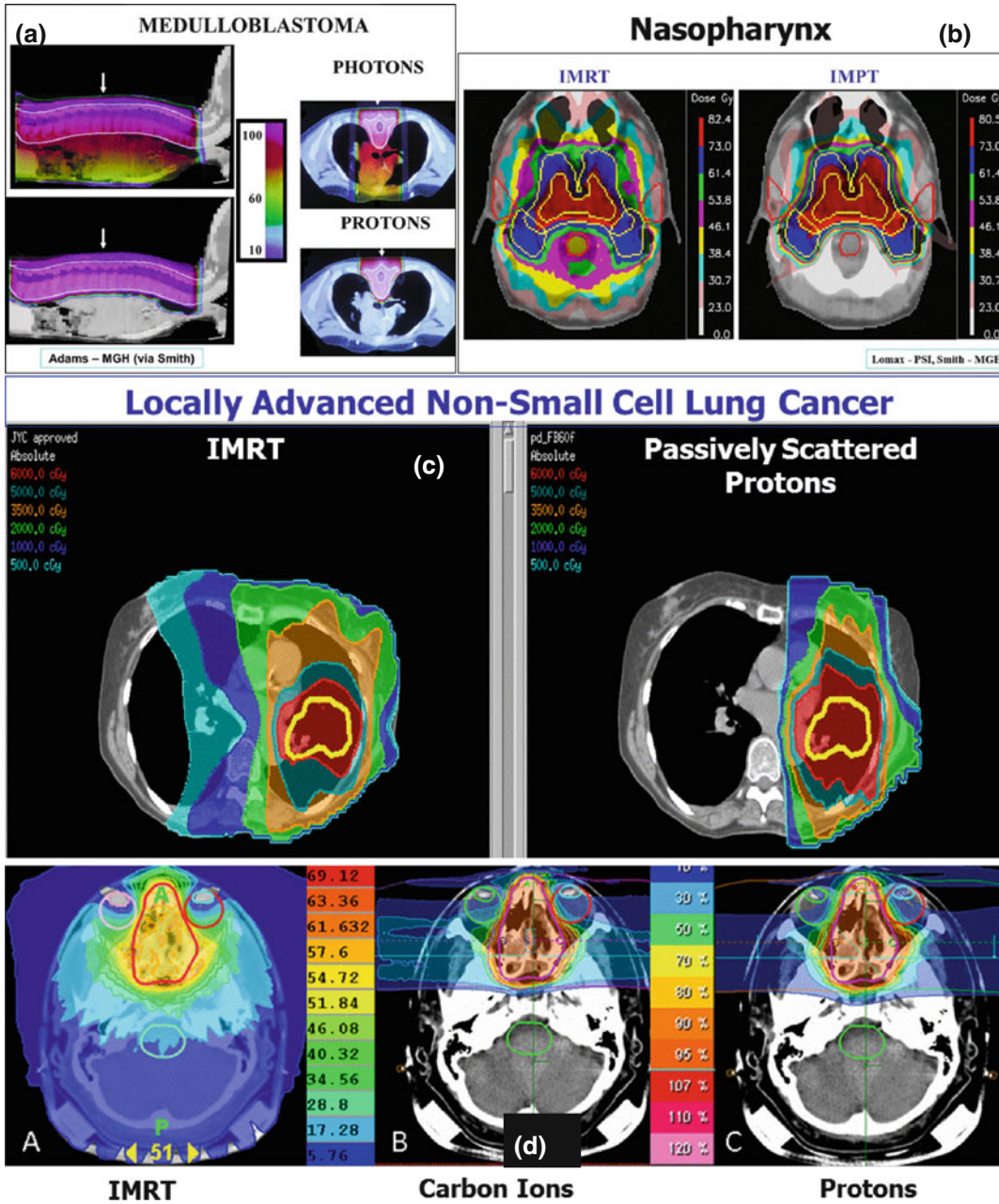

Fig. 2.3 (**a**) Passively scattered proton therapy vs. 3D conformal therapy of medulloblastoma (courtesy of MGH). (**b**) IMRT vs. IMPT of nasopharynx (courtesy of Tony Lomax, PSI). (**c**) IMRT vs. PSPT of locally advanced NSCLC from Chang et al. [2]. (**d**) IMRT vs. protons vs. carbon ions for base of skull [1]

Brada et al. performed a systematic review and analysis of published clinical results of proton therapy in 2007 and "found no convincing evidence that protons [implicitly, particles in general] are superior to photons [5]." Five years later, De Ruysscher et al. updated the findings of Brada et al. and confirmed that Brada's conclusions still stand and that "except for rare indications such as childhood cancer, the gain from introducing proton therapies into clinical practice remains controversial [6]."

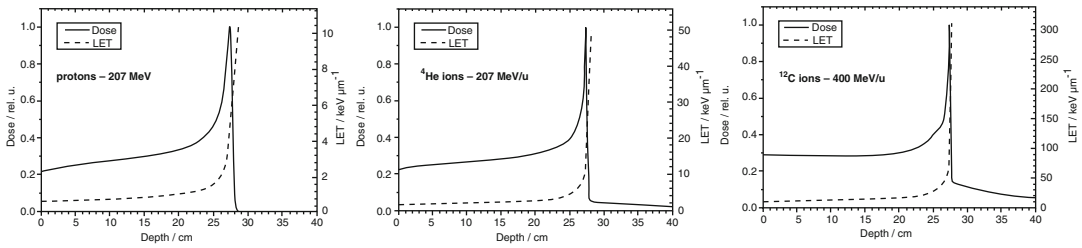

Fig. 2.4 Depth-dose and depth-LET curves for 20 cm radius fields of protons, ^{4}He and ^{12}C, all with a range of ~28 cm (Guan—unpublished)

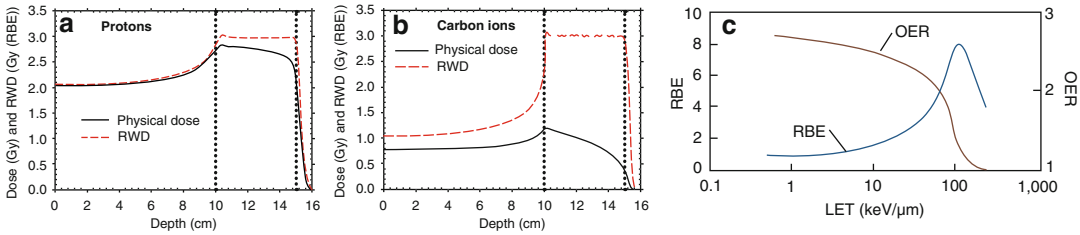

Fig. 2.5 (**a**, **b**) Physical doses for proton and carbon ion SOBP required to yield a constant RBE-weighted dose (RWD) of 3 Gy (RBE) are shown. Each SOBP consists of pristine Bragg peaks with fluences optimized to yield a constant RWD [3]. (**c**) RBE and OER as functions of LET for T1 kidney cells irradiated with alpha particles and deuterons [4]

Similarly, ASTRO's Emerging Technology Committee published an evidence-based review of proton beam therapy and found that there was no evidence to date to recommend proton beam therapy for the lung, head and neck, GI, and non-CNS pediatric malignancies [7]. In some cases (hepatocellular carcinoma and prostate), protons have been found to be effective but not superior, and in other cases (e.g., CNS), there is insufficient data to draw conclusions. However, there is evidence of the benefit with protons for ocular melanomas and chordomas.

Recently, there have been reports of additional positive experiences based on small studies. For instance, Chang et al.'s phase 2 study of high-dose proton therapy with concurrent chemotherapy for unresectable stage III non-small cell lung cancer, which involved 44 patients, reported an impressive median survival of 29 months, grade 3 pneumonitis of 3 %, and grade 5 esophagitis of 12 % [8]. Another example, from a presentation by Frank at the ASTRO 2013 Annual Meeting, reported a considerably reduced incidence and duration of the use of feeding tube for IMPT compared to IMRT for oropharyngeal cancers.

However, until recently, there have been no randomized trials and no high-level systematic large-scale studies directly comparing protons and photons. Thus, the overall evidence can at best be considered low level and mixed. Weak evidence is not just limited to protons but is also true for carbon ion therapy. Debus of DKFZ during his presentation at the PTCOG 52 meeting in 2013 concluded that, while there are clinical data from prospective phase I/II and phase II trials that support the hypothesis that there is a role of carbon ions in oncology, evidence of clear superiority is lacking.

There is also a lively debate about the socio-economic aspects of proton therapy. For instance, at the 2007 ASTRO Annual Meeting, Tim Williams, then president of ASTRO, wondered about the reasons (motives) for establishing proton therapy centers. His list included belief in clinical efficacy, program differentiator, revenue generation, institutional prestige, and defensive maneuver. Unfortunately, motives are not always altruistic. Even the belief in clinical efficacy is, in general, based on the dose distribution characteristics of protons and on treatment planning studies rather than on clinical data.

An obvious question is "Why has the clear advantage of particles on paper not translated into clinical practice?" There may be multiple factors including immature technology or limited experience up to now; the greater vulnerability of particles to uncertainties such as interfractional changes, intra-fractional motion, and setup variability; the accuracy of computed dose distributions; uncertainty in relative biological effectiveness (RBE), etc. Some of the limitations of particle therapy and concerns about them have been apparent for several decades. For instance, Goitein et al., realizing the vulnerability of protons to uncertainties, suggested various means for accounting for them [9–12]. Even in the face of such uncertainties, the gap between protons and photons at that time was large enough that protons could safely be assumed to be superior. However, with the major advances in photon therapy over the years, that is no longer the case. Furthermore, due to the availability of advanced and sophisticated imaging and treatment planning tools, research is revealing the consequences of the impact of uncertainties on particle therapy. The following subsections give some illustrative examples.

2.3.1 Interfractional Variations

Figure 2.6 illustrates the greater vulnerability of proton dose distributions to interfractional anatomic variations compared to IMRT. After 2 weeks of radiotherapy, the tumor volume has cavitated considerably. For IMRT, the application of the original beam and intensity configuration to the CT image 2 weeks later produces virtually the same dose distributions. For protons, however, the loss of tumor tissue allows protons to penetrate much further. Accommodation of such dose perturbations requires frequent repeat CT imaging, evaluation of anatomy changes on dose distribution, and adaptive replanning, if indicated.

2.3.2 Respiratory Motion

Figure 2.7 is an example of the impact of the respiratory motion of the tumor on proton dose distributions. The proton dose distributions shown on the left were designed using an average of a free-breathing CT. The green, orange, and red structures are the motion-incorporated internal target (ITV), clinical target (CTV), and gross target (GTV) volumes. The prescribed dose is indicated by the yellow isodose line and assumed to correspond to the dose expected to be delivered. The right panel shows that the dose distribution in the maximum inhale phase is quite different from the one used to make the treatment decision.

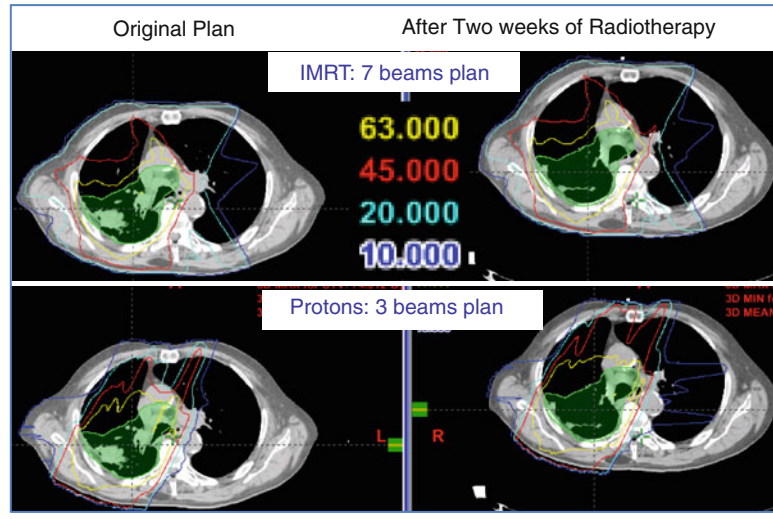

Fig. 2.6 Illustration of the greater impact of tumor shrinkage over the course of treatments on proton dose distributions than on IMRT dose distributions

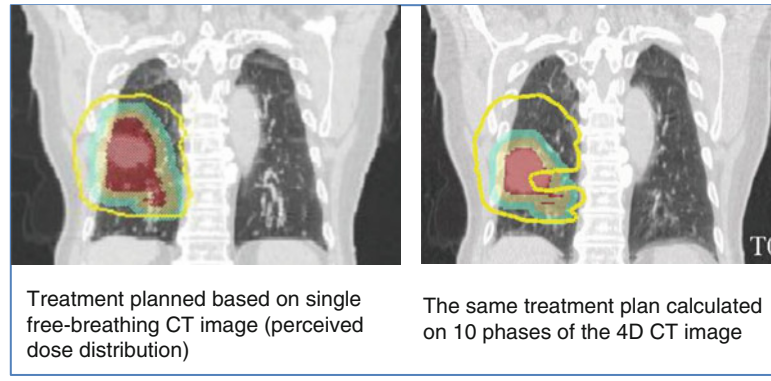

Fig. 2.7 The impact of respiratory motion of the lung tumor on the proton dose distribution. It should be pointed out that it is not just the motion of the tumor that needs to be considered but the motion of any portion of the anatomy in the path of the protons

2.3.3 Relative Biological Effectiveness

There are important gaps in our knowledge of the biological effectiveness of particles, including protons. While the following discussion is focused on protons, uncertainties in relative biological effectiveness (RBE) of any of the particles would have unwanted consequences.

There is evidence that the (RBE) of protons is a complex function of numerous factors including depth of penetration (implicitly on LET), dose per fraction, total dose, cell type, oxygenation, biological end point, etc. [13–16]. Yet, in current practice, RBE is simplistically assumed to be 1.1 in all situations [17, 18]. This assumption may lead to an increased risk of injury to surrounding normal tissues where RBE may be higher than 1.1 or to recurrences in tumors where RBE may be less than 1.1. Moreover, the opportunity to explicitly take advantage of the higher RBE to achieve greater killing of tumor cells is not realized.

The claim is often made that there is no clinical evidence to suggest that the assumption of RBE of 1.1 has caused any harm. To date majority of clinical proton treatments have employed PSPT [19]. This, along with statistical uncertainties from the limited clinical data, has likely obscured the importance of RBE variability.

Another rationale sometimes given in support of the continued use of proton RBE of 1.1 is that the high RBE is confined to a very narrow region from just before the Bragg peak to the end of distal fall-off. Because of the very rapid fall-off of dose, the increased RBE is, therefore, biologically inconsequential. However, the distal edge is often degraded by the passage of beams through tissues, especially through complex heterogeneities, and may extend over a significant volume.

Furthermore, IMPT dose distributions contributed by individual beams are highly heterogeneous. This means that the biologically effective dose delivered may be substantially different from the dose based on RBE of 1.1. On the other hand, the inherent flexibility of IMPT offers the opportunity to capitalize on variable RBE through the incorporation of such information into the treatment optimization process. Higher LET protons have a higher biologically effectiveness for the same dose deposited. Thus, for the same dose deposited, one can use a smaller number of the high LET protons or a larger number of lower LET protons. This concept can be used to confine high RBE portions of beamlets into the target volume and away from critical normal structures, producing more effective treatments.

2.4 Current Research and Future Outlook

Even though the clinical evidence in favor of particle therapy is limited so far, in principle, it has significant potential. Current research is directed toward understanding the limiting physical and biological factors, some of which were mentioned in the previous section. It is hoped that the translation of the knowledge thus gained will allow particle therapy to achieve its true poten-

tial. Examples of this research include minimizing uncertainties through the development of more accurate dose calculation algorithms, in-room volumetric imaging for image-guided particle therapy, adaptive replanning to account for interfractional anatomic changes, improved understanding of the impact of various uncertainties on dose distributions and outcomes, improved understanding of RBE through in vitro and in vivo experiments and through correlation of treatment responses with accurate estimates of biologically effective dose distributions, etc. Other research includes the incorporation of residual uncertainties in the evaluation of the robustness of particle therapy dose distributions and the use of robust optimization techniques to render the dose distributions resilient to uncertainties. Furthermore, randomized and other high-level clinical trials comparing particle therapy with photon therapy to generate convincing evidence and to produce important informative data are being designed and undertaken. The following subsections give a small number of examples of the ongoing research.

2.4.1 Robustness Evaluation and Robust Optimization

To estimate the robustness of a particle therapy dose distribution, it must be evaluated under various uncertainty scenarios to choose the one that represents the most likely outcome. For instance, one can randomly sample a large number of uncertainty scenarios from the possible values of setup and particle range and compute dose distribution for each scenario. The scenario that allows for the required coverage of the target and sparing of normal tissues with a high probability (e.g., 2σ) should be chosen for making treatment decisions.

Because of the impracticality of the computation of a very large number of uncertainty scenarios, alternate approaches have been suggested. In one such approach, nine uncertainty scenarios of position variation (±dx, ±dy, ±dz) and range (±dr) plus the nominal scenario are chosen such that there is a high probability (e.g., 2σ) of the CTV and the organs at risk (OAR) are within the uncertainty bounds. Bands of DVHs of the nine dose distributions (see Fig. 2.8) qualitatively convey the relative robustness of dose distributions. The widths of the bands may be used as a quantitative measure of uncertainty, and the DVHs corresponding to the overall "worst-case" scenario (representing the balance among coverage of the target and sparing of normal tissues with 2σ probability) may be used as the basis for treatment decisions. Without loss of generality, the position uncertainty parameters may be assumed to be the same as the CTV-to-PTV and OAR-to-ORV margins used in photon therapy. Then, the worst-case approach of evaluation of dose distributions is an analog of PTV- and ORV-based planning and evaluation of photon dose distributions, except that the former also accounts for range uncertainties and the perturbation of dose distributions within the CTV and OAR volumes.

Research-related robustness evaluation so far has been limited mainly to position and range uncertainties and mostly to qualitative evaluation. There is a need for further research to define robustness quantitatively and to estimate the required thresholds of robustness. There is also a need to include inter- and intra-fractional and RBE uncertainties in robustness evaluation.

In addition to evaluating robustness, it is also important to make particle therapy more resilient in the face of uncertainties. There are multiple ways of achieving this. Robustness improvement strategies for PSPT include increasing the number of beams, avoiding beam directions through complex heterogeneities, smearing of compensators to account for misalignment of structures of different densities, and enlarging margins. However, enlarging margins any more than those customarily used in photon therapy is not desirable.

For IMPT, a suitable strategy currently being investigated and implemented clinically is robust optimization. Several approaches have been proposed in which IMPT dose distributions are optimized taking into consideration multiple uncertainty scenarios so that the resulting dose distribution seen on a treatment plan reflects a high degree of confidence (again 2σ). In one such

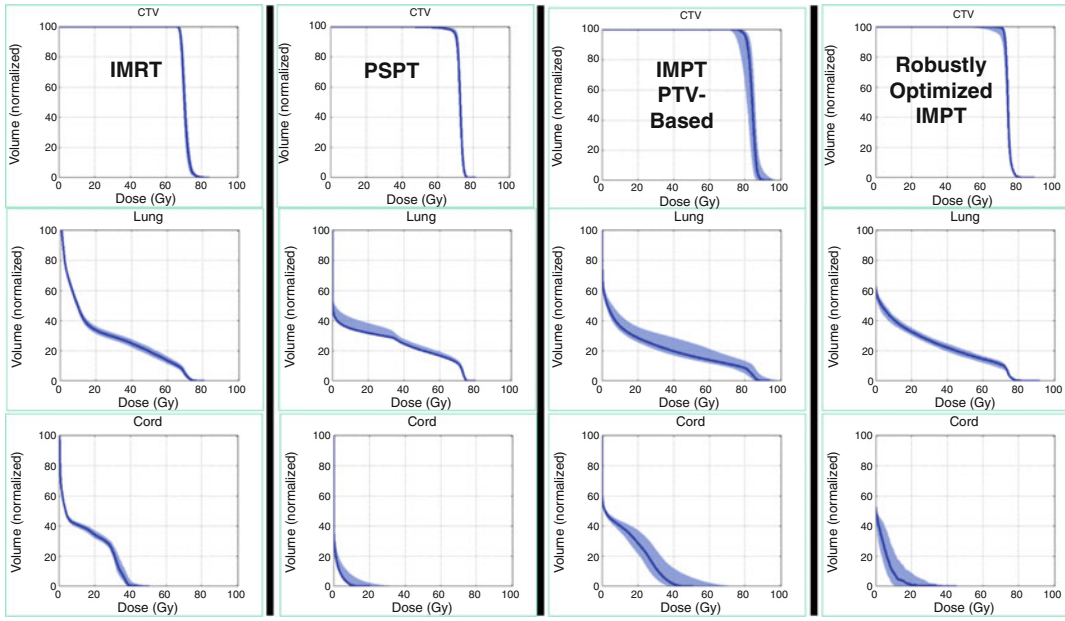

Fig. 2.8 Intercomparison of IMRT, PSPT, and IMPT dose distributions. IMPT dose distributions were optimized in two different ways: the traditional approach of using CTV-to-PTV margins (third column) and using robust optimization. Bands of DVHs for CTV, normal lung, and spinal cord under nine different uncertainty scenarios are shown. As expected, IMRT dose distribution is the most robust followed by PSPT. PTV margin-based optimized IMPT is the least robust, but with robust optimization, robustness improves significantly

approach [20–24], the worst dose in each voxel among the nine scenarios is selected for the computation of the objective function in each iteration. For the CTV, the worst dose is the minimum, and for normal tissues, the worst dose is the maximum of the nine scenarios. Figure 2.8 compares the robustness and optimality of dose distributions of an NSCLC patient obtained with IMRT, PSPT, and PTV-based IMPT optimization and IMPT robust optimization.

As for the case for robustness evaluation, robust optimization has not incorporated inter- and intra-fractional variations so far. However, there are indications that only incorporating positioning and range uncertainties in robust optimization makes dose distributions resilient to those uncertainties that are not included. This is presumably because of the fact that robust optimization reduces dose gradients within individual fields as well as in the composite dose distributions. However, there is need for further research to develop strategies to incorporate all uncertainties, including those in RBE, into robust optimization.

2.4.2 Accurate Determination of RBE

The latest clinical results are beginning to indicate that the RBE of protons may deviate significantly from 1.1. It may be of the order of 1.0 at the entrance and higher than 1.3 at the Bragg peak and points beyond. The correlation of clinical response and pre- to post-treatment changes in tissue biomarkers, CT, MR, and PET images with accurate estimates of the dose distributions actually received by the patients is hypothesized to lead to improved quantitation of RBE. In addition, in vitro and in vivo experiments are being undertaken to accurately map the RBE as a function of the various parameters mentioned above. Figure 2.9 shows results of a high-throughput experiment to determine RBE as a function of

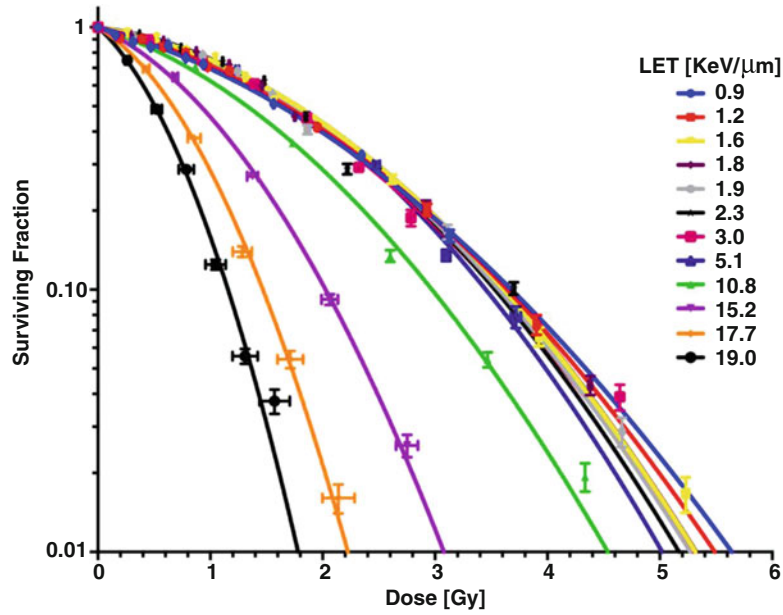

Fig. 2.9 Results obtained with the irradiation of H460 non-small cell lung cancer cells in 96-well plates with a scanning proton beam of 79.7 MeV having passed through an especially deigned device to slow the protons down to different energies to increase their LET. The plate was divided into 12 columns of 8 wells each, with each column receiving a different combination of dose and LET. The results indicate significant dependence of cell survival on LET and therefore on RBE. They suggest that continued use of RBE of 1.1 is inappropriate [25]

dose per fraction and LET for H460 non-small cell lung cancer cells [25].

2.4.3 Determination of Optimum Ions

With the exception of limited studies with multiple ion species at Lawrence Berkley National Lab, most particle radiotherapy has employed protons and carbon ions. The number of facilities and the number of patients treated with the latter are very small compared to the former. In the current state of the art, only protons and carbon ions are considered seriously.

Protons scatter laterally to a significant degree and, therefore, have a sizable penumbra and are difficult to shape to conform to the target and to avoid adjacent critical normal tissues. Their biological effectiveness is not significantly different from that of photons. Carbon ions, being considerably heavier, scatter very little and have a sharp penumbra and are, therefore, suitable for producing a high degree of conformation. They have a much higher RBE (in the range of 1.4–3.5), which is an advantage for tumor control but may be a disadvantage for normal tissues, especially with regard to late effects. Furthermore, while in contrast with protons, the RBE of carbon ions is accepted as variable, it has a high degree of uncertainty. Carbon ions have a lower oxygen-enhancement ratio, which, combined with high RBE, makes them very attractive for treating highly radio-resistant tumors. On the other hand, treatment with carbon ions leads to significant contribution from nuclear fragments to dose distal to the target. These fragments, which are substantially lighter than the carbon ions, can travel large distances further than the range of the primary particles. Additionally, carbon ions produce a large halo of secondary particles that could have ramifications with regard to radiation-induced carcinogenesis. Similar concerns exist with ions heavier than carbon as well. The point is that neither protons nor carbon ions may be optimum for radiotherapy and that there is need to evaluate other ions. Kemp et al., for instance, have indicated that helium, lithium, and oxygen ions remain potentially of clinical interest, but that lithium ions may have a significant advantage over all other ions [26]. Work being done at MDACC shows that helium ions may also have advantages over protons and carbon ions. Figure 2.10 shows some sample results. Radiotherapy with helium ions should also be less costly compared with heavier ions.

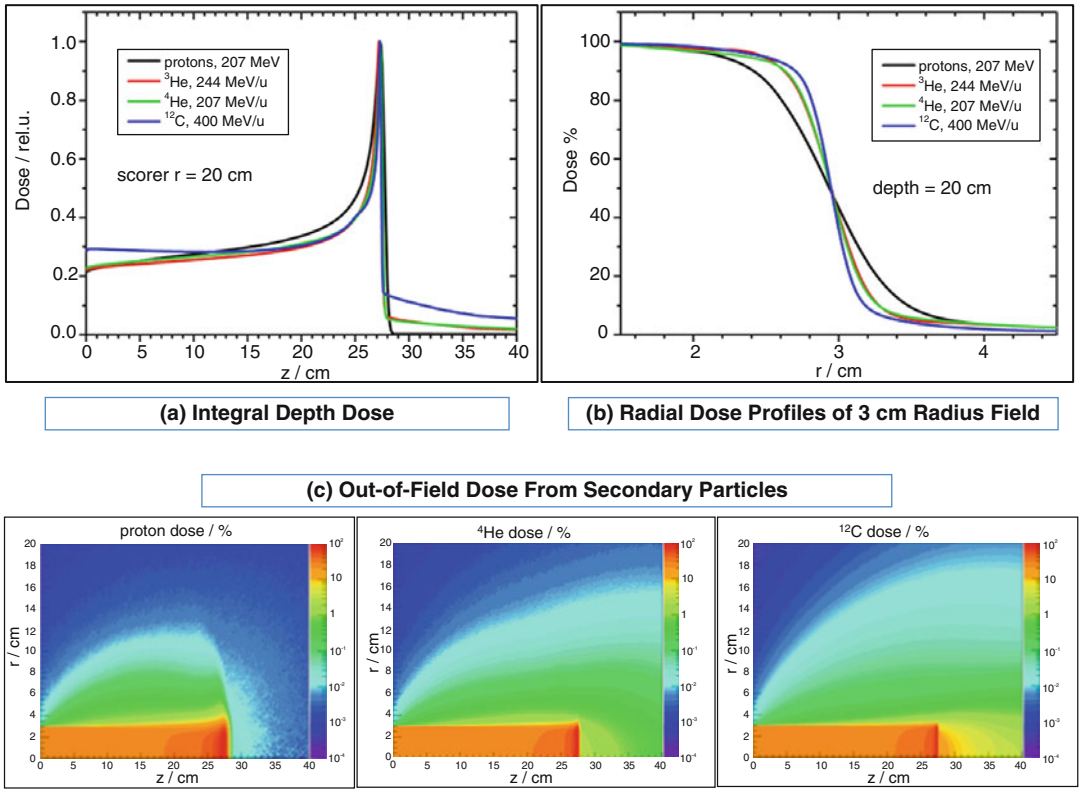

Fig. 2.10 Comparison of dose distribution characteristics of scanned monoenergetic beams of range ~28 cm each of ^{3}He, ^{4}He, protons, and ^{12}C ions. (**a**) Carbon ions have a fragmentation tail, which can add up to a significant distal dose when a sequence of energies is used to irradiate a finite-sized volume. Panel (**b**) shows that protons have a large penumbra and carbon ions have the smallest penumbra but that the sharpening of penumbra from ^{3}He to ^{12}C is very small. Panel (**c**) shows the increase in lateral and distal low-dose halo for heavier ions. (Titt and Guan—unpublished)

2.5 Summary

While particle therapy has been used for over 60 years, its high cost has been a major factor in preventing its widespread utilization in spite of its apparent high potential. Although some of limitations of particle therapy, including its vulnerability to uncertainties, were recognized early on, recent large-scale implementation and the new imaging modalities are revealing significant weaknesses of the present state of the art and their possible role in the absence of convincing evidence demonstrating the superiority of particle therapy. Considerable research is going on; much more is needed. This is likely to occur as the number of scientists and clinicians participating in particle therapy research and clinical practice increases. The future prospects for particle therapy are promising. However, it is urgent that we conduct high-quality research and translate the knowledge thus gained into clinical trials and routine practice to produce convincing evidence of its true potential. Otherwise, it will be difficult to obtain adequate funding to establish particle therapy facilities and to justify the high cost of particle therapy. Thus, the benefits of this promising modality will not be realized.

References

1. Kosaki K, Ecker S, Habermehl D, Rieken S, Jakel O, Herfarth K, Debus J, Combs SE. Comparison of intensity modulated radiotherapy (IMRT) with intensity modulated particle therapy (IMPT) using fixed

beams or an ion gantry for the treatment of patients with skull base meningiomas. Radiat Oncol. 2012;7:44. http://www.ncbi.nlm.nih.gov/pubmed/22439607.
2. Chang JY, Zhang X, Wang X, Kang Y, Riley B, Bilton S, Mohan R, Komaki R, Cox JD. Significant reduction of normal tissue dose by proton radiotherapy compared with three-dimensional conformal or intensity-modulated radiation therapy in stage i or stage iii non-small-cell lung cancer. Int J Radiat Oncol Biol Phys. 2006;65:1087–96. http://www.ncbi.nlm.nih.gov/pubmed/16682145.
3. Frese MC, Yu VK, Stewart RD, Carlson DJ. A mechanism-based approach to predict the relative biological effectiveness of protons and carbon ions in radiation therapy. Int J Radiat Oncol Biol Phys. 2012;83:442–50. http://www.ncbi.nlm.nih.gov/pubmed/22099045.
4. Barendsen GW, Koot CJ, Van Kersen GR, Bewley DK, Field SB, Parnell CJ. The effect of oxygen on impairment of the proliferative capacity of human cells in culture by ionizing radiations of different let. Int J Radiat Biol Relat Stud Phys Chem Med. 1966;10:317–27. http://www.ncbi.nlm.nih.gov/pubmed/5297012.
5. Brada M, Pijls-Johannesma M, De Ruysscher D. Proton therapy in clinical practice: current clinical evidence. J Clin Oncol. 2007;25:965–70. http://www.ncbi.nlm.nih.gov/entrez/query.fcgi?cmd=Retrieve&db=PubMed&dopt=Citation&list_uids=17350945.
6. De Ruysscher D, Mark Lodge M, Jones B, Brada M, Munro A, Jefferson T, Pijls-Johannesma M. Charged particles in radiotherapy: a 5-year update of a systematic review. Radiother Oncol. 2012;103:5–7. http://www.ncbi.nlm.nih.gov/pubmed/22326572.
7. Allen AM, Pawlicki T, Dong L, Fourkal E, Buyyounouski M, Cengel K, Plastaras J, Bucci MK, Yock TI, Bonilla L, Price R, Harris EE, Konski AA. An evidence based review of proton beam therapy: the report of astro's emerging technology committee. Radiother Oncol. 2012;103:8–11. http://www.ncbi.nlm.nih.gov/pubmed/22405807.
8. Chang JY, Komaki R, Lu C, Wen HY, Allen PK, Tsao A, Gillin M, Mohan R, Cox JD. Phase 2 study of high-dose proton therapy with concurrent chemotherapy for unresectable stage iii nonsmall cell lung cancer. Cancer. 2011;117:4707–13. http://www.ncbi.nlm.nih.gov/pubmed/21437893.
9. Goitein M. Calculation of the uncertainty in the dose delivered during radiation therapy. Med Phys. 1985;12:608–12. http://www.ncbi.nlm.nih.gov/entrez/query.fcgi?cmd=Retrieve&db=PubMed&dopt=Citation&list_uids=4046996.
10. Urie M, Goitein M, Holley WR, Chen GT. Degradation of the bragg peak due to inhomogeneities. Phys Med Biol. 1986;31:1–15. http://www.ncbi.nlm.nih.gov/entrez/query.fcgi?cmd=Retrieve&db=PubMed&dopt=Citation&list_uids=3952143.
11. Urie MM, Goitein M, Doppke K, Kutcher JG, LoSasso T, Mohan R, Munzenrider JE, Sontag M, Wong JW. The role of uncertainty analysis in treatment planning. Int J Radiat Oncol Biol Phys. 1991;21:91–107. http://www.ncbi.nlm.nih.gov/entrez/query.fcgi?cmd=Retrieve&db=PubMed&dopt=Citation&list_uids=1903372.
12. Urie M, Goitein M, Wagner M. Compensating for heterogeneities in proton radiation therapy. Phys Med Biol. 1984;29:553–66. http://www.ncbi.nlm.nih.gov/entrez/query.fcgi?cmd=Retrieve&db=PubMed&dopt=Citation&list_uids=6330772.
13. Britten RA, Nazaryan V, Davis LK, Klein SB, Nichiporov D, Mendonca MS, Wolanski M, Nie X, George J, Keppel C. Variations in the rbe for cell killing along the depth-dose profile of a modulated proton therapy beam. Radiat Res. 2013;179:21–8. http://www.ncbi.nlm.nih.gov/pubmed/23148508.
14. Robertson JB, Williams JR, Schmidt RA, Little JB, Flynn DF, Suit HD. Radiobiological studies of a high-energy modulated proton beam utilizing cultured mammalian cells. Cancer. 1975;35:1664–77. http://www.ncbi.nlm.nih.gov/pubmed/807318.
15. Girdhani S, Sachs R, Hlatky L. Biological effects of proton radiation: what we know and don't know. Radiat Res. 2013;179:257–72. http://www.ncbi.nlm.nih.gov/pubmed/23373900.
16. Paganetti H, Niemierko A, Ancukiewicz M, Gerweck LE, Goitein M, Loeffler JS, Suit HD. Relative biological effectiveness (rbe) values for proton beam therapy. Int J Radiat Oncol Biol Phys. 2002;53:407–21. http://www.ncbi.nlm.nih.gov/entrez/query.fcgi?cmd=Retrieve&db=PubMed&dopt=Citation&list_uids=12023146.
17. ICRU-78-Report-Committee. ICRU report 78, prescribing, recording, and reporting proton-beam therapy. J ICRU. 2007;7:1–210.
18. Delaney T, Kooy H. Proton and charged particle radiotherapy. Philadelphia: Lippincott Williams & Wilkins; 2008.
19. Flanz J, Smith A. Technology for proton therapy. Cancer J. 2009;15:292–7. http://www.ncbi.nlm.nih.gov/pubmed/19672145.
20. Cao W, Lim GJ, Lee A, Li Y, Liu W, Ronald Zhu X, Zhang X. Uncertainty incorporated beam angle optimization for IMPT treatment planning. Med Phys. 2012;39:5248–56. http://www.ncbi.nlm.nih.gov/pubmed/22894449
21. Liu W, Frank SJ, Li X, Li Y, Park PC, Dong L, Ronald Zhu X, Mohan R. Effectiveness of robust optimization in intensity-modulated proton therapy planning for head and neck cancers. Med Phys. 2013;40:051711. http://www.ncbi.nlm.nih.gov/pubmed/23635259.
22. Liu W, Frank SJ, Li X, Li Y, Zhu RX, Mohan R. Ptv-based IMPT optimization incorporating planning risk volumes vs robust optimization. Med Phys. 2013;40:021709. http://www.ncbi.nlm.nih.gov/pubmed/23387732.

23. Liu W, Li Y, Li X, Cao W, Zhang X. Influence of robust optimization in intensity-modulated proton therapy with different dose delivery techniques. Med Phys. 2012;39:3089–101. http://www.ncbi.nlm.nih.gov/pubmed/22755694.
24. Liu W, Zhang X, Li Y, Mohan R. Robust optimization of intensity modulated proton therapy. Med Phys. 2012;39:1079–91. http://www.ncbi.nlm.nih.gov/pubmed/22320818.
25. Guan F, Bronk L, Titt U, Lin SH, Mirkovic D, Kerr MD, Zhu XR, Dinh J, Sobieski M, Stephan C, Peeler CR, Taleei R, Mohan R, Grosshans DR. Spatial mapping of the biologic effectiveness of scanned particle beams: towards biologically optimized particle therapy. Sci Rep 5. 2015;9850:1–10. http://www.ncbi.nlm.nih.gov/pubmed/25984967.
26. Kempe J, Gudowska I, Brahme A. Depth absorbed dose and let distributions of therapeutic 1h, 4he, 7li, and 12c beams. Med Phys. 2007;34:183–92. http://www.ncbi.nlm.nih.gov/entrez/query.fcgi?cmd=Retrieve&db=PubMed&dopt=Citation&list_uids=17278503.

Development of Cyclotrons for Proton and Particle Therapy

3

Emma Pearson, Willem Kleeven, Vincent Nuttens, Simon Zaremba, Jarno Van de Walle, Eric Forton, Robin Choo, and Yves Jongen

All particle therapy systems are modular systems built with smaller subsystems. The various modules are (1) the beam production system, (2) the beam transport system, and (3) the beam delivery system as shown in Fig. 3.1.

The beam production system is the "engine" of the particle therapy system. It is responsible for the acceleration of particles to energies capable of reaching the depths required for radiation therapy. Commonly used beam production systems include cyclotrons and synchrotrons, whereas newer designs such as linear accelerators or dielectric wall accelerators have also been proposed, but are currently still not used in any particle therapy systems.

In this chapter, we first introduce the basic properties of accelerators and cyclotrons to the reader. It is important to understand the difference between the two main families of cyclotrons: the isochronous cyclotron and the synchrocyclotron. In the second section, we examine how cyclotrons started to be used for medical applications: because they were easily available and they still constitute the best compromise for particle therapy purposes. The third section is devoted to currently available cyclotrons for particle therapy. The last section discusses future trends.

E. Pearson (✉) • W. Kleeven • V. Nuttens
S. Zaremba • J. Van de Walle • E. Forton
R. Choo • Y. Jongen
Medical Accelerator Solutions: R&D Department, IBA, Louvain-la-Neuve, Belgium
e-mail: Emma.Pearson@iba-group.com

3.1 Accelerator Basics

Accelerators use static or oscillating radio frequency (RF) electric fields to accelerate electrically charged particles like protons, electrons, etc. The kinetic energies obtained from electrostatic accelerators are too low for proton therapy applications. Oscillating RF electric fields overcome this limitation.

In a linear accelerator (linac), the radio frequency accelerating electrodes are placed along a straight line (Fig. 3.2).

For proton beams to be used for radiation therapy purposes, there is a need to accelerate protons up to 230 MeV. This will allow for the proton beam to reach a depth of 32 g/cm^2. To achieve this energy, a relatively long linear accelerator with many accelerating RF cavities is needed. This will take a large footprint and uses significant electric wall plug power. In addition, the linear accelerator technology is considered as rather expensive compared to other solutions.

To reduce the size of the accelerator, one could imagine "winding" it into itself, using magnetic fields to bend the particle trajectories. In 1932, E.O. Lawrence [1] realized that a particle moving in a constant magnetic field moves on a circular trajectory at a frequency that is independent of its energy: the same particle, in the same magnetic field but with two different energies simply, has two circular trajectories with different radii but the same orbital frequency!

A.K. Rath, N. Sahoo (eds.), *Particle Radiotherapy: Emerging Technology for Treatment of Cancer*,
DOI 10.1007/978-81-322-2622-2_3

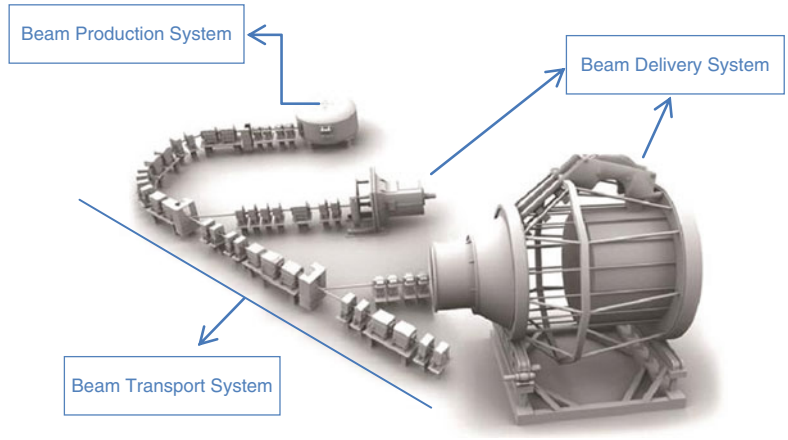

Fig. 3.1 Basic modular design of particle therapy systems

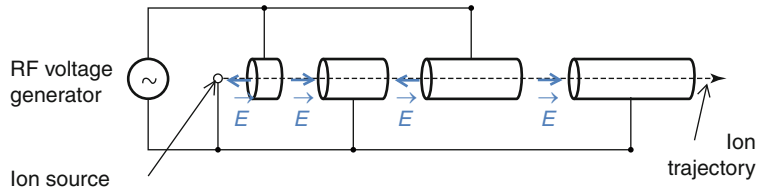

Fig. 3.2 Simple illustration of the linear accelerator (Wideroe structure)

The revolution frequency, called the cyclotron frequency, is proportional to the charge q and the magnetic field, B, and inversely proportional to the particle mass, m:

$$f = \frac{qB}{2\pi m} \tag{3.1}$$

(for a proton in a 1 T magnetic field, $f \sim 15$ MHz).

Based on this idea, the multiple cavities used in the linac can be merged into a single cavity. The required RF-frequencies are relatively low (as compared to a linac), and therefore the electric fields can be created continuously, and this new accelerator, named the *cyclotron*, provides a continuous wave (CW) beam.

The cyclotron accelerating structures (electrodes) are called "dees" because of their letter "D"-like shape in the early days. The dees act as a Faraday cage that screens the electric fields inside and confines them only to the accelerating gaps between the two dees. The ion is accelerated each time it crosses this gap. As a result of the acceleration, the curvature radius of the particle will increase, and its trajectory will be spiral shaped (Fig. 3.3). This is the key point to understanding the beauty of the isochronous cyclotron: it results in a compact accelerator using a single magnet and a single accelerating cavity operating at a constant frequency.

However, when the speed of the particle increases, the relativistic effects on the particle are no longer negligible (for protons: 1 % at 10 MeV, 11 % at 100 MeV, and 25 % at 230 MeV), and the mass increase of the particle decreases the value of its revolution frequency, and the particle goes out of phase (desynchronized) with respect to the RF system.

In the beginning of the cyclotron era, relativistic effects were not taken into account, and the problem of accelerated particles going out of synchronism had limited the final kinetic energies that could be achieved. Historically, the first solution proposed to obtain higher energies was to keep the rotationally symmetric magnetic field as before and to reduce the frequency of the RF system during the acceleration in order to compensate the mass increase. This idea was proposed in 1945 independently by Veksler [2] and by McMillan [3]. A new category of accelerator was born: the *synchrocyclotron* or the frequency modulated (FM) cyclotron (Fig. 3.3). The synchrocyclotron solution helped to overpass the

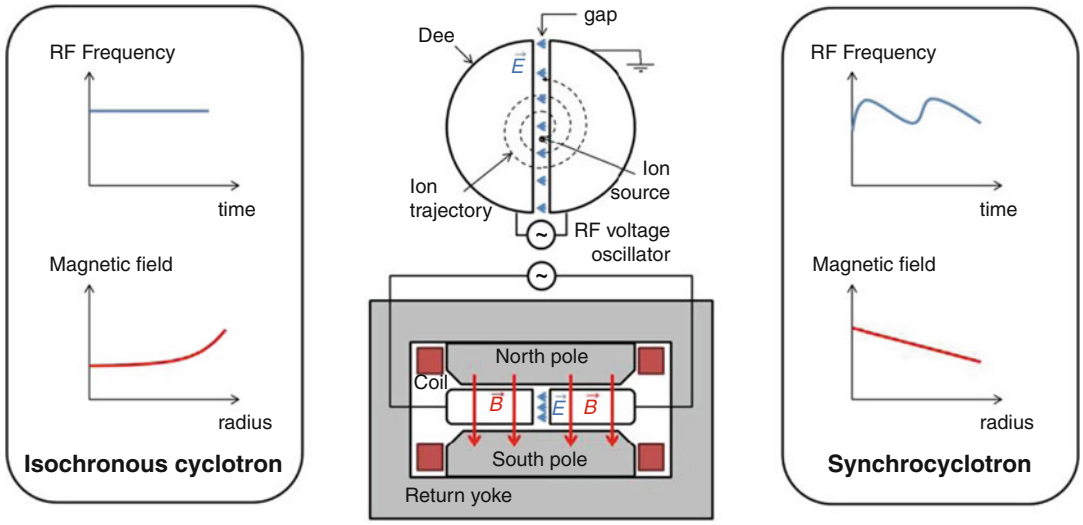

Fig. 3.3 Simple illustration of the isochronous cyclotron and synchrocyclotron

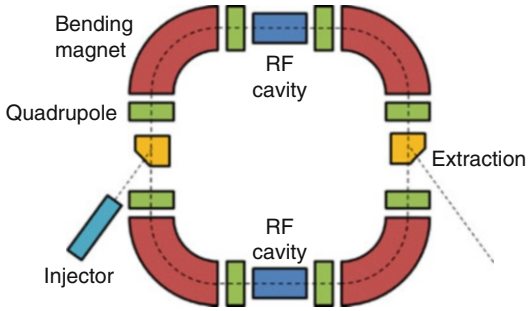

Fig. 3.4 Simple illustration of the synchrotron

previous kinetic energy limit of accelerated particles.

Besides the cyclotron and the synchrocyclotron, the *synchrotron* is the third type of circular accelerator used in particle therapy. This accelerator was invented simultaneously with the synchrocyclotron also by Veksler [2] and by McMillan [3]. In this case, the orbit trajectory is kept constant during acceleration, and the beam travels in a quasi-circular ring of bending magnets (Fig. 3.4). During the acceleration, the revolution frequency increases, and therefore a simultaneous increase of the magnetic field is needed as may be deduced from Eq. (3.1). Hence, both the bending magnetic field and the frequency of the RF system need to be pulsed.

Both cyclotrons and synchrocyclotrons can accelerate the beam starting from the (internal) ion source (very low kinetic energy) to the final kinetic energy in one single stage. For synchrotrons, this is not possible. A first pre-accelerator (also called an injector) is needed to speed up the particle to typically 1–7 MeV and then inject the beam into the synchrotron.

The typical synchrotron consists of a number of discrete dipole magnets and focusing quadrupoles, whereas cyclotrons or synchrocyclotrons usually have just one magnet. Therefore, the footprint of a synchrotron-based proton therapy facility is often larger than for a cyclotron facility. Nevertheless, Hitachi, a supplier of synchrotron-based proton therapy systems, is developing a very compact synchrotron [4] of 5.1 m diameter compared to 7.8 m in the previous design.

Besides the required condition of synchronism (or longitudinal stability) between the particle and the RF fields, the requirement of vertical focusing and stability is also crucial for the three types of circular accelerators that were discussed. Different methods of vertical focusing are possible: weak focusing, sector focusing, and strong focusing.

The method of weak focusing is used in a synchrocyclotron: it relies on the slow decrease of

the rotationally symmetric magnetic field with increasing radius. In isochronous cyclotrons, the average magnetic field has to increase with radius to compensate for the relativistic mass increase. A rotationally symmetric field therefore would not provide any focusing.

Thomas [5] proposed a solution in 1938 (thus already 7 years before the invention of the synchrocyclotron and the synchrotron) consisting of a periodic magnetic structure of hills (also called poles) and valleys, as illustrated in Fig. 3.5. It deforms the orbit to a noncircular shape and creates vertical magnetic forces that push the particles back to the median plane at each entrance into and exit from a hill sector. The solution could not be applied immediately due to the increased complexity of the magnetic structure. That is the reason why synchrocyclotrons were widely used at the birth of proton therapy.

Only about 20 years later, due to the availability of improved computational techniques, the Thomas concept allowed for the realization of the new family of isochronous cyclotrons. The first operation of such an azimuthally varying field (AVF) cyclotron was achieved in 1958 in Delft, Netherlands, by F.A. Heyn and Khoe Kong Tat [6].

For the development of the synchrotron, an important milestone was the discovery of the strong focusing (or alternating focusing) principle by Christofilos in 1950 [7] and by Courant, Livingston, and Snyder in 1952 [8]. Soon after that the same principle could be implemented in cyclotrons. This was done by replacing the radial (Thomas) sectors by spiral-shaped sectors. In the first step, this led to yet another type of circular accelerator called the FFAG (Fixed-Frequency Alternating Gradient) accelerator proposed by Kerst and Symon in 1954 [9]. One of the first spiral-sector isochronous cyclotrons was realized at Harwell [10].

An important difference between the three types of circular accelerators is the time structure of the beam. In all three cases, the micro-structure is determined by the RF-frequency. For an isochronous cyclotron, the RF-frequency is constant and therefore the macro-structure of the beam is CW (continuous wave). In the synchrocyclotron the beam is pulsed at a rate that is determined by the variable capacitor which modulates the RF-frequency as needed for the acceleration. The pulse rate can go up to a few kHz. For the synchrotron, the beam is also pulsed but at a much lower rate. This is due to eddy currents in the magnet iron and also the self-inductance of the magnets which limit their rise time. Repetition rates can go from 0.5 Hz for the slow cycling synchrotrons up to ~30 Hz for the fast cycling ones [11].

For pulsed operations, the beam intensity that can be obtained is generally lower than for continuous wave operations. This is due to the fact that only during a small fraction of the RF pulse can particles be trapped into stable orbits. This has been well explained in the papers of Bohm and Foldy [12, 13]. This intensity limitation was previously an important factor for passive scattering proton therapy systems as there was a need for the beam to pass through multiple scattering materials before reaching the tumor volume. However, this concern has decreased over time as most proton therapy systems are now treating with active scanning methods where the proton beam is directly deposited into the tumor volume via iso-energy slices. Such active scanning methods are also known as pencil beam scanning or spot scanning.

For pencil beam scanning, it is important to have fast and reliable control of the beam intensity

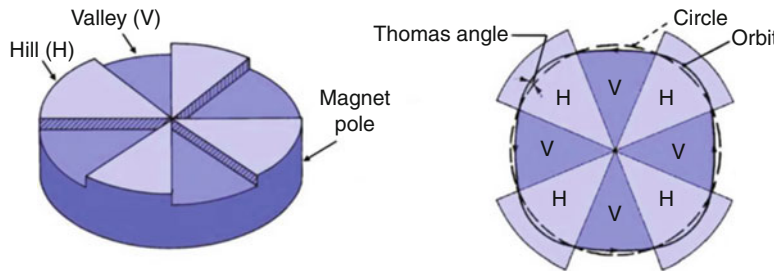

Fig. 3.5 Illustration of sector focusing in a cyclotron

as every spot to be delivered in the tumor volume has a different dose weight. This is relatively easy in the isochronous cyclotron where the current can be controlled directly at the ion source. For the synchrocyclotron, the beam intensity can be adjusted from pulse to pulse by adjusting the ion source or the RF voltage. As the pulse from a synchrocyclotron is of the order of kHz, this is also adequate for pencil beam scanning. For the synchrotron, the intensity adjustment needs to be done during the extraction from the ring within each pulse. As the pulse rate of the synchrotron is of the order of Hz, the rapid adjustment of its beam intensity is considered as more difficult than for cyclotron-based systems.

An advantage of the synchrotron is its variable energy feature. Recent developments show that the energy changes can be done from pulse to pulse within an RF cycle at 30 Hz [11], and the accelerator cycle can be synchronized with the respiratory cycle. Higher energies are easier to reach with the synchrotron making the possibility to go to 330 MeV for proton tomography. Cyclotrons and synchrocyclotrons are usually fixed energy machines and require an external energy degrader and an energy selection system (ESS) to reduce the proton energy from the nominal value (230 or 250 MeV) to lower energies with the minimum at 70 MeV convenient for shallow-seated tumors. The degrader (often made of carbon) produces secondary neutrons and gamma rays that must be shielded by the concrete walls. On the other hand, the energy degrader also provides a strong decoupling of the accelerator and beam transport line which makes control easier and more robust.

In Table 3.1 we summarize the discussion on the main similarities and differences between the three types of circular accelerators used for proton therapy.

3.2 Proton Therapy: From Laboratory to Dedicated Medical Facility

The paper from 1946, written by Dr. Robert R. Wilson [14], contains the first information concerning the radiological uses of fast protons and created the future basis for proton therapy. The article discusses the need for accelerators producing proton beams with kinetic energies above 125 MeV and perhaps reaching as high as 400 MeV. Accelerators producing such high kinetic energies were very rare or still under development during that time. Most of these accelerators were based in research institutions and were cyclotrons and synchrocyclotrons.

Table 3.1 A brief overview of the main differences between the three commonly used circular accelerators for proton therapy

	Isochronous cyclotron	Synchrocyclotron	Synchrotron
Magnetic field	Fixed	Fixed	Varying
RF-frequency	Fixed	Varying	Varying
Orbit size	Outward spiral	Outward spiral	Fixed
Energy	Fixed	Fixed	Adjustable
Operation	Continuous	Pulsed (fast)	Pulsed (slow)
Acceleration stages	Single	Single	Multiple
Ion source	Internal	Internal	External
Vertical focusing	Spiral sector focusing	Weak	Strong
Intensity control	Easier	Average	More difficult
Footprint	Average	Smaller	Larger
Weight	Larger	Smaller	Average
Complexity	Easier	Average	More difficult
Beam intensity	High	Average	Low
Beam output emittance	Symmetrical	Symmetrical	Elliptical
Power consumption	Average	Lowest	Highest
Cost	Average	Lowest	Highest

Stimulated by the ideas of R. R. Wilson, the first experiments on biological tissue started in the early 1950s using the Berkeley 184-inch (4.67 m pole diameter) synchrocyclotron (Fig. 3.6) [15]. The development of this accelerator started in the early 1940s, and the first proton beam was obtained in 1948. The synchrocyclotron patent was filed in 1947 and granted in 1952 by McMillan [16], and the first patient was treated in 1954.

The Gustaf Werner Institute in Uppsala, Sweden, performed physics experiments with high-energy protons during the early 1950s leading to the first therapeutic treatment in 1957 [17].

The Harvard Cyclotron Laboratory (HCL) was mainly focused on nuclear physics research [18]. However, starting from 1961, the synchrocyclotron was also successfully used for the proton therapy of different types of cancer (Fig. 3.7) [19]. The period between 1970 and 1990 was the most successful for HCL, resulting in the creation of a strong scientific team and the development of many technologies related to different aspects of proton therapy.

This explains why synchrocyclotrons were the accelerators of choice in the early days of particle therapy: they were easily available.

In the 1980s, proton therapy became more mature and required its own clinical environment, independent of scientific institutes which were more focused on nuclear physics research. This triggered the design of dedicated centers and allowed exploring accelerator solutions besides synchrocyclotrons.

The first hospital-based proton therapy facility was opened in 1990 at the Loma Linda University Medical Center (LLUMC) in California, USA [20]. Dr J. Slater and his team chose a small synchrotron as the proton accelerator [21]. It was designed and realized by the accelerator team from the Fermi National Accelerator Laboratory (Fermilab). At the time of construction, the Loma Linda team had considered that a synchrotron offered the best combination of precision, reliability, flexibility, and optimum beam characteristics for a medical machine with less residual radiation than other types of accelerator.

The cyclotron was proposed in dedicated facilities in 1990, when Y. Jongen and the Ion Beam Applications (IBA) team in Louvain-la-Neuve, Belgium, proposed the isochronous cyclotron as an accelerator for its commercial proton therapy solution [22]. The development of this solution was done in collaboration with Sumitomo Heavy Industries (SHI), Japan. The first IBA proton therapy facility was installed in Massachusetts General Hospital (MGH), Boston, USA, and patients in the Northeast Proton Therapy Center (NPTC) have been treated since 2001 [23]. SHI installed the first facility in the National Cancer Center in Kashiwa where the first patient was treated in November 1998.

In 2001, ACCEL (now part of Varian Medical Systems) proposed the first commercial

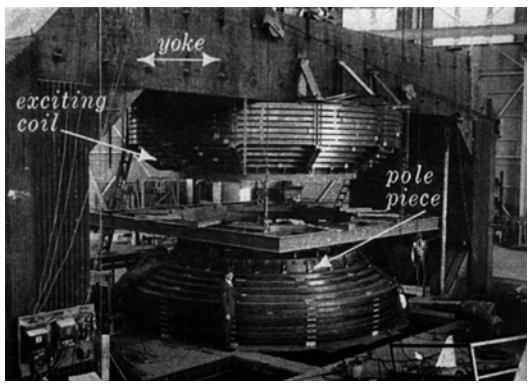

Fig. 3.6 The electromagnet of the 184-inch Berkeley synchrocyclotron, under construction during the period 1940–1942 [15]

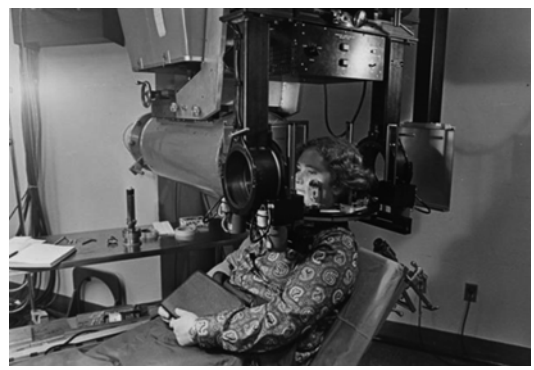

Fig. 3.7 Demonstration of a patient in position for treatment in the early days of the Harvard Cyclotron Laboratory [19]

superconducting isochronous cyclotron for cancer treatment based on a design proposed by Professor H. Blosser and the National Superconducting Cyclotron Laboratory (NSCL), East Lansing, IL, USA, in 1993 [24]. The use of superconducting coils created a higher magnetic field allowing the size and weight of the machine to be reduced.

In the early days of proton therapy, synchrotrons were considered the accelerator of choice for centers planning for proton therapy. Ever since IBA introduced a commercial design for cyclotron-based proton therapy systems, the popularity of using cyclotrons has increased continuously. Cyclotron-based systems are typically more user friendly as there are very few parameters to vary when operating the facility, whereas synchrotron-based systems require a team of experienced operators to operate the facility.

In 2014, 73 % of all operating and planned proton therapy centers in the world use a cyclotron-based system (both cyclotrons and synchrocyclotrons). Figure 3.8 shows the breakdown between cyclotron- and synchrotron-based facilities that are currently in operation or under planning.

This development is now driven by end-users, who quickly started to demand smaller, more cost-effective accelerators and easy to operate proton therapy systems. In addition, beam dynamics considerations favor the synchrocyclotron when a compact system needs to be designed. This led the company Still River Systems (today Mevion Medical Systems Inc.) to start manufacturing a superconducting synchrocyclotron for proton therapy based on a design by Dr. T. Antaya from MIT, Boston, MA, USA [25]. The first Mevion proton therapy system was installed in S. Lee Kling Proton Therapy Center at Barnes-Jewish Hospital in St. Louis, MO, USA, and the first patient was treated in December 2013 [26].

In 2008 Ion Beam Applications (IBA) also started development of a superconducting synchrocyclotron for proton therapy with the support of AIMA Development, Nice, France [27]. The first IBA superconducting synchrocyclotron for the Proteus®ONE

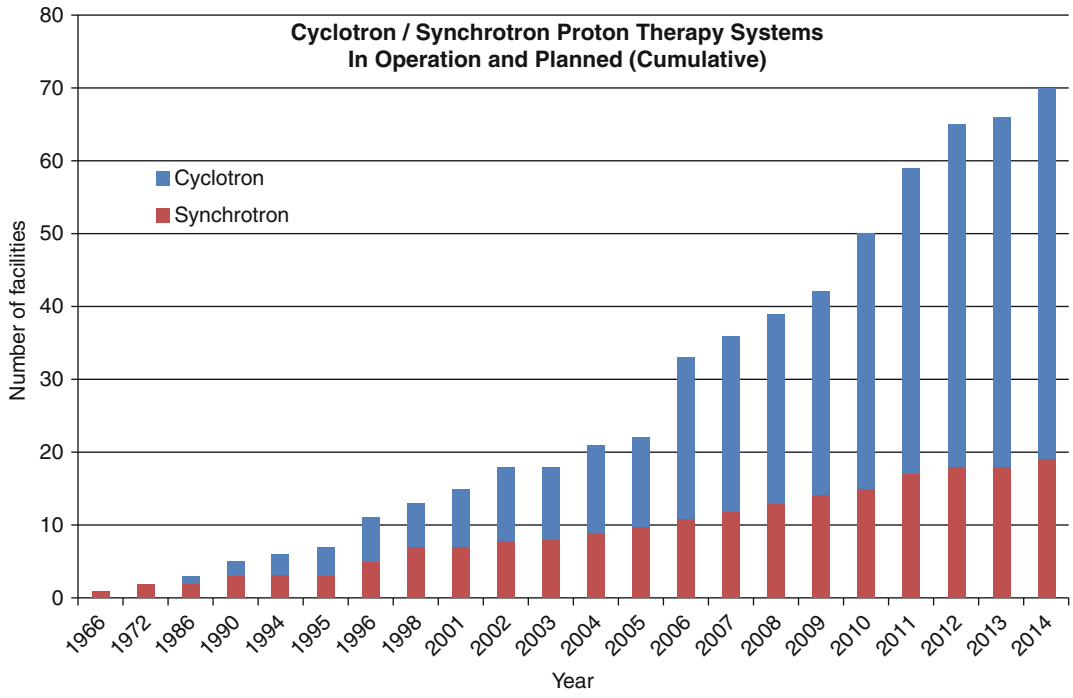

Fig. 3.8 Stacked histogram of the number of cyclotrons and synchrotrons in operation or under planning (for proton-only accelerators above 200 MeV)

compact single-room solution [28] has been installed at the Centre de Protonthérapie Antoine-Lacassagne in Nice, France, since May 2014.

Currently, for heavy ion therapy such as carbon ions, only synchrotron-based facilities are in operation. This is because carbon ions require an acceleration of more than 350 MeV/u in order to reach ranges that are suitable for radiation therapy. For resistive cyclotrons, this would be very challenging to build as the diameter of the cyclotron would be very large and the machine would be heavy. In 2006, IBA introduced the design of a superconducting cyclotron which allows for carbon ions to be accelerated to 400 MeV/u despite having a relatively small diameter of 6.6 m. It remains to be seen if the popularity of using cyclotrons for proton therapy would be mimicked by the heavy ion therapy industry (Fig. 3.9).

3.3 Overview of Commercial Cyclotrons

The development of commercial cyclotrons for use in proton therapy started in the early 1990s. Due to their simplicity, reliability, low cost, and ability to modulate the proton beam current quickly and accurately, they have contributed considerably to the expansion of proton therapy installations worldwide. Currently, four companies are offering cyclotron-based proton therapy installations (isochronous cyclotron or synchro-cyclotron) as the drive accelerator. Table 3.2 summarizes the main parameters and differences between the commercial cyclotrons which are on the market and which are discussed below.

3.3.1 Isochronous Cyclotrons

With the Cyclone®230, the Belgian company Ion Beam Applications (IBA) has the largest installed base of cyclotrons for proton therapy in the world. Twenty-four of these cyclotrons are in operation in 2014.

The Cyclone®230 is a 220 ton isochronous cyclotron with a diameter of 4.34 m and a height of 2.1 m. The peak magnetic field of 2.9 T is obtained with a resistive coil which consumes about 175 kW of electric power. The beam is extracted at a fixed energy of 230 MeV at a radius of about 1.1 m with an electrostatic deflector. The maximum extracted

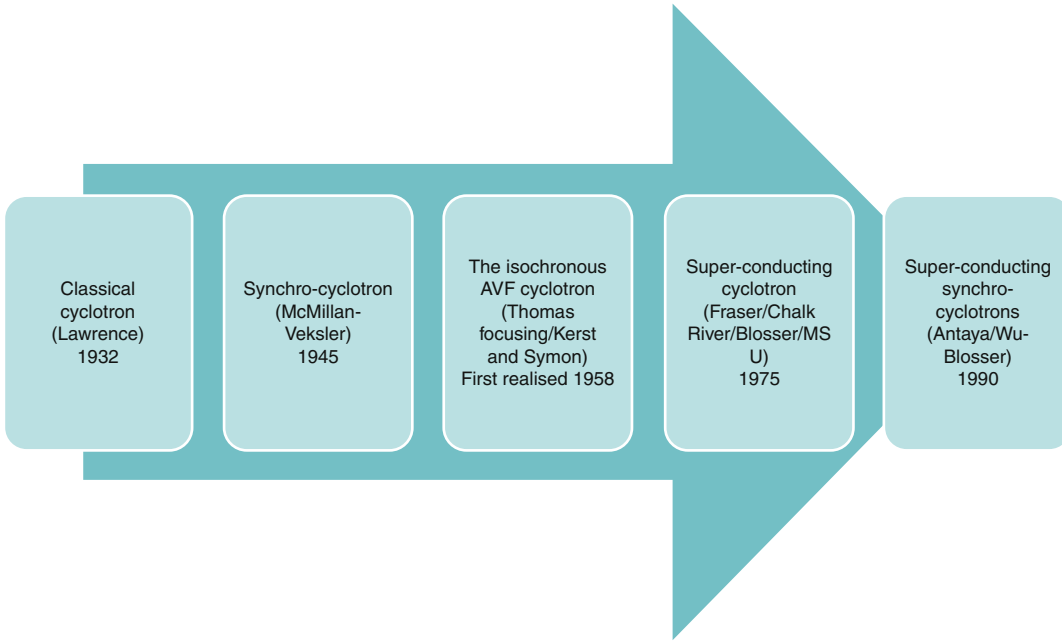

Fig. 3.9 Key milestones in the development of cyclotrons for proton therapy

Table 3.2 Overview of the main properties of the commercial cyclotrons for proton therapy

	Isochronous cyclotrons		Synchrocyclotrons	
	IBA/SHI Cyclone®230	VARIAN ProBeam®	MEVION Monarch S250	IBA S2C2
Weight	220 ton	90 ton	20 ton	50 ton
Diameter	4.34 m	3.1 m	<1.8 m	2.5 m
Height	2.1 m	1.6 m	<1 m	1.56 m
Coil	Resistive	Superconducting NbTi	Superconducting Nb_3Sn	Superconducting NbTi
Extraction energy	230 MeV	250 MeV	250 MeV	230 MeV
Cooling	Water	He-Cooled	Cryogen-free	Cryogen-free
Beam time structure	CW	CW	Pulsed	Pulsed
Peak field	2.9 T	3.8 T	9 T	5.7 T

continuous beam intensity can be as high as 1 μA but is limited to 500 nA for safety reasons. The fixed frequency RF system operates at 106 MHz and consumes about 100 kW. The dee voltage varies between 60 kV in the center and 120 kV at extraction. The vertical stability of the circulating proton beam is obtained by the azimuthally varying field and the spiraled pole edges, a characteristic feature of high-energy isochronous cyclotrons. A view inside the Cyclone®230 is shown in Fig. 3.10. The unique feature of this cyclotron is the elliptical shape of the pole gap which allows to increase the region of isochronous field and which facilitates the extraction.

Sumitomo Heavy Industries (SHI) provides a proton therapy system based on the same isochronous cyclotron, since SHI and IBA collaborated on the design of the cyclotron. Since 2001, the IBA and SHI systems have undergone separate developments. After the first operational proton therapy facility at the National Cancer Center in Kashiwa, Japan, three more proton centers based on the isochronous 230 MeV have been built by SHI for Taiwan, Korea, and Japan [29] (Fig. 3.11).

Varian Medical Systems (VMS) offers a proton therapy solution based on a superconducting isochronous cyclotron. This isochronous cyclotron was originally designed by Professor H. Blosser from the NSCL in the United States, and the first cyclotron was built by the company ACCEL in 2001. The latter was incorporated into Varian Medical Systems in 2007. The first cyclotron of this type was installed at the Paul Scherrer Institute (PSI) in Switzerland in 2005. Even though the magnetic field is induced by superconducting coils, the peak magnetic field of this cyclotron is only 3.8 T, which is low compared to the superconducting synchrocyclotrons, which will be discussed below. The reason for this is found in the fact that the vertical stability of the proton beam, which is obtained by the azimuthally varying field and the spiraled pole edges, is reduced when the average field is increased. Due to this reduced vertical stability with increasing magnetic field, isochronous cyclotrons cannot be reduced much more in size, and the alternative synchrocyclotron has to be (re-)considered if the size of the cyclotron needs to be reduced. Nevertheless, thanks to its superconducting coil, the ACCEL isochronous cyclotron has smaller dimensions than the Cyclone®230: a diameter of 3.1 m, a height of 1.6 m, and a weight of about 90 tons (Fig. 3.12).

The superconducting coil is embedded in a liquid helium bath at 4 K, and the total cooling power in the closed He systems is about 5 W. The beam is extracted at a fixed energy of 250 MeV with an electrostatic deflector, and the maximum extracted continuous beam intensity is about 800 nA. The fixed frequency RF system operates at 72.8 MHz and consumes about 115 kW. The dee voltage varies between 80 and 130 kV [30] over the four dees. Ten proton therapy centers are either currently operational or planned using this superconducting isochronous cyclotron.

Table 3.2 shows the main properties of commercial cyclotrons used for proton therapy.

Fig. 3.10 External (*top image*) and internal (*bottom image*) view of the Cyclone®230 from IBA. The four sectors with spiraled poles and elliptical pole facing together with the two dees are visible

Fig. 3.11 The SHI 230 MeV isochronous cyclotron for proton therapy

Fig. 3.12 The superconducting isochronous cyclotron from Varian Medical Systems

3.3.2 Superconducting Synchrocyclotrons

In 2007, the company Still River Systems (today Mevion Medical Systems Inc.) started the manufacturing of a superconducting synchrocyclotron for proton therapy based on the patent of Dr. T. Antaya from the Massachusetts Institute of Technology (MIT) in Boston (USA). This accelerator has a central magnetic field of 9 T, and this high field is obtained with a Nb_3Sn superconducting coil, cooled by cryocoolers. The unique feature of this extremely compact cyclotron is that it is mounted on a gantry rotating around the patient. The proton beam is extracted at a fixed energy of 250 MeV. As for other superconducting

Fig. 3.13 The Monarch S250 Synchrocyclotron from Mevion

magnets, the large magnetic forces are supported by a special former around the coil. The total consumed power is about 120 kW (Fig. 3.13).

In 2008, IBA started the development of a compact superconducting synchrocyclotron called the "S2C2". With a superconducting NbTi coil, the magnetic field in the center of the cyclotron is 5.7 T, and the size of the cyclotron is reduced to a diameter of 2.5 m. The total weight of the S2C2 is about 50 tons, and the beam energy is constant at 230 MeV. The beam from the S2C2 is pulsed at 1 kHz, and pulses are about 10 μs long. This is due to the synchrocyclotron concept by which the RF-frequency is reduced synchronously with the accelerated proton beam [27]. The first S2C2 has been installed at the Centre de Protonthérapie Antoine-Lacassagne in Nice, France (Fig. 3.14).

Short Note on Superconductors Used in Proton Therapy

Two types of conductors are used in existing proton therapy accelerators so far: NbTi and Nb_3Sn.

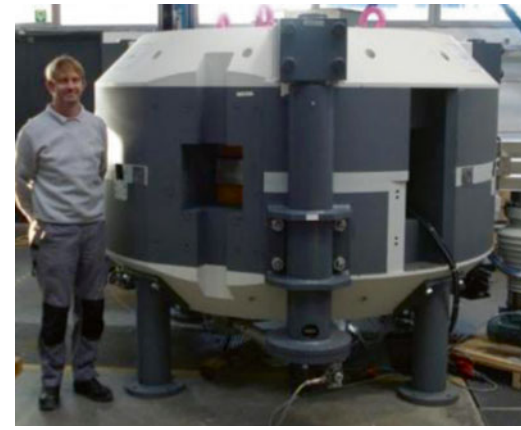

Fig. 3.14 The Superconducting Synchrocyclotron (S2C2) from IBA

The advantage of Nb_3Sn is that it allows for higher magnetic field, offering the opportunity to lower the overall size of the accelerator. The price to pay is an additional complexity in the production process (e.g., thermal treatment), conductor handling (it becomes brittle), and therefore a higher cost.

NbTi, on the other hand, has a simpler production process. Because it is widely used (it is the gold standard for medical applications like magnetic resonance imaging – MRI-magnets), much higher volumes make it cheaper.

Both conductors have different needs in terms of cryogenics and refrigeration. At lower fields, Nb_3Sn could be used at 10 K with much cheaper cryogenerators.

3.4 Future Cyclotrons for Particle Therapy

In this section, we first consider the development of novel cyclotron concepts for proton therapy. Further innovation can be found in a concept presented by SHI, while more radical propositions are found in studies considering ironless cyclotrons. These two concepts will primarily

optimize the weight and size of the cyclotrons, but most probably not their cost. In order to reduce the cost, future solutions may come from novel superconducting materials that will decrease the refrigeration requirement and therefore the cost of cryogenics.

In the second section, we will discuss heavy ion (e.g., carbon) therapy. Currently, all operational heavy ion facilities are synchrotron-based; however this may change as superconducting cyclotrons for proton and carbon acceleration progress.

3.4.1 Proton Therapy

A step forward in cyclotron technology for proton therapy is currently being pursued by Sumitomo Heavy Industries Ltd (SHI). They are developing a compact high-field superconducting AVF cyclotron for proton therapy [31]. With an extraction energy of 230 MeV and an efficiency of higher than 60 % foreseen from calculations, this isochronous cyclotron is relatively standard in its concept: the hill gap is made small around the outer pole radius, and the spiralization of the poles is relatively high in order to ensure good beam stability despite the high average field. The higher field allows size optimization which brings the yoke weight down to about 55 tons, about one quarter of the weight of the SHI normal conducting 230 MeV cyclotron. There is an advantage to reducing the machine weight as it not only reduces the cost of the machine and size of the facility (space) required, it also facilitates transportation and makes installation of the medical facility much easier.

The design also uses NbTi superconducting coils but at the higher central magnetic field of 3.2 T. This central field corresponds to an average magnetic field close to beam extraction of about 4 T. The nice feature of this machine is that it will be just a little larger than the IBA S2C2 (5.17 T at extraction) but still isochronous. This indicates the frontier field and size between isochronous cyclotrons and synchrocyclotrons which use iron yokes (Fig. 3.15).

At the beginning of this chapter, we mentioned that iron magnetization brings a limitation to iron-yoke isochronous cyclotrons. In addition, we just mentioned that the new SHI design is probably at the lower limit in terms of weight and size, because of the beam dynamics during acceleration. For synchrocyclotrons, the Mevion accelerator is also probably close to the weight limit, for reasons of extraction optics.

As the size of (synchro-)cyclotrons is limited to a given range, an interesting path for further weight reduction comes from Massachusetts Institute of Technology [32]. Their work demonstrates how multiple sets of superconducting coils can be used to replace the iron return yoke and pole pieces of a conventional cyclotron (Fig. 3.16).

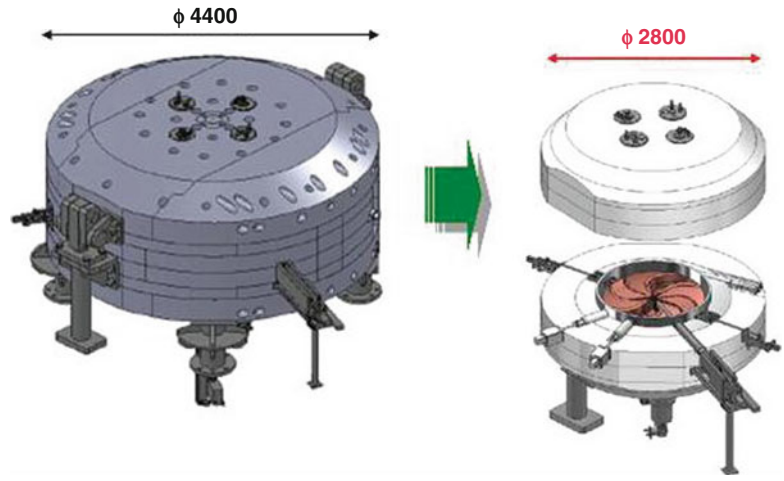

Fig. 3.15 Schematic view of the Sumitomo normal conducting P235 (*left*) and superconducting cyclotrons (*right*) for proton therapy [31]

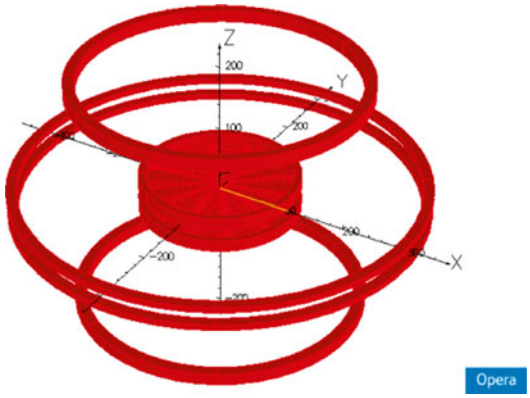

Fig. 3.16 3D illustration of a coil assembly in an iron-free cyclotron modeled by MIT [33]. The iron-free design includes the main field coil, field shaping coils, and shielding coils. Various combinations of superconducting/normal conducting coils can be designed according to the desired machine characteristics. In the above picture, a hybrid design is no smaller than a normal conducting one but saves on overall machine weight

Coil number, location, and current are used as optimization parameters for the required field profile and active shielding requirements of the machine. This ironless cyclotron design study has been shown to offer several significant advantages in the form of cyclotron weight reduction, increased portability (e.g., for the use in gantry mounted systems), enhanced shielding, and structural efficiency.

In comparison to the commercial Mevion Monarch 250 synchrocyclotron for proton therapy [34], the weight of the cyclotron magnet system is reduced by a factor of 6 by using the superconducting ironless design. The study also discusses the potential of smoothly varying the output beam energy without the use of an external energy degrader. This would be made possible due to a full linearity of the magnetic field with the coil current, as opposed to iron-yoke cyclotrons where the nonlinearity of the magnetization is a disadvantage. As is the case for synchrotron-based particle therapy facility, variable beam energy would in turn reduce the production of secondary radiation and, as a consequence, radiation shielding requirement in the patient treatment environment. Iron-free designs may also offer increased tuning ease during mass production, in the fashion of magnetic resonance magnets, and increased access to the midplane. The drawbacks discussed in the study include an increase in the peak field in the coil winding and an increase in stored magnetic energy. However such changes depend on the initial choice of optimization constraints. The design study is illustrative at this stage but expresses good indications for the feasibility of this approach in future applications.

Looking at future trends for cyclotron developments, it is also interesting to mention the conceptual magnetic design of a "next-generation" high-temperature superconducting (HTS) cyclotron for particle therapy – a feasibility study carried out by the Research Centre for Nuclear Physics in Osaka, Japan [35]. This concept applies the quality improvements seen in HTS tapes over recent years to coils for the use in medical accelerators. The aim is also a yoke-free, ultra compact, efficient, and high-energy AVF (azimuthally varying field) cyclotron with much reduced power consumption. Bean-shaped coils above and below the beam chamber are implemented in order to create a suitable AVF magnetic field structure needed for beam stability. The concept is still in early stages of development, and the technical difficulties of realizing any iron-free cyclotron requiring rapid energy variations for clinical treatment are not trivial.

3.4.2 Heavy Ion Therapy

Today, most proton therapy facilities use cyclotrons as their preferred solution for reasons of simplicity, reliability, smaller size and cost, and the ability to modulate the beam current at kHz frequencies. There is a reason to believe that the success of cyclotrons in proton therapy will also apply to other heavy ion therapies in future years, in particular to carbon ion therapy.

In addition to the ballistic accuracy of proton beams, other ions, such as carbon, have the additional advantage of a different biological interaction with cells which can be very effective even against types of cancer cells that resist usual radiations. Over the past few years, an increasing

interest in carbon-based therapy has been seen, leading to ideas about developing a cyclotron-based solution similar to the current offerings in proton therapy.

The IBA-JINR (Joint Institute of Nuclear Research, Dubna, Russia) 400 MeV/u superconducting isochronous cyclotron is the first cyclotron concept designed to deliver protons, carbon, and alpha-ions for cancer treatment. Accelerating several different beams with a single cyclotron imposes severe constraints on the magnetic field structure which can be overcome by a careful design. This challenge is met by the design of the IBA-JINR effort but has a consequence on the machine size and weight.

To understand this consequence, it is important to note that carbon ions and alpha particles will be accelerated to 400 MeV/u and extracted by electrostatic deflector, whereas protons (as H2+) will be accelerated to 265 MeV/u and extracted by stripping. Electrostatic deflection is the extraction technique used, for example, on IBA's Cyclone®230 or Varian's ProBeam® cyclotrons. It is a technique that is compatible with the extraction of any type of ions. Stripping extraction, on the contrary, is compatible only with the extraction of ions or molecules that still have electrons in orbit. The idea is to remove, or "strip", these remaining electrons to change the beam curvature radius and therefore extract the beam out of the cyclotron. Now, at relativistic energies, the Lorentz force which bends the beam trajectory inside the cyclotron acts in opposite directions onto nuclei and electrons among the same atom/molecule. As a consequence, electrons can be stripped from an ion or molecule during acceleration, and a good acceleration efficiency is obtained at the cost of a limitation in the magnetic field.

In the case of the IBA-JINR design, this constraint results in a magnet yoke with a diameter of 6.6 m. The total weight of the new machine will be about 700 tons. The magnetic field in the machine will be 4.5 T in the hills and 2.45 T in the valleys. The superconducting coils will be enclosed in a cryostat. All other parts of the cyclotron will be warm.

If one compares the overall size of a cyclotron or synchrotron-based facility, one can see that the cyclotron plus a compact carbon gantry can be installed in the same space and for the same cost as for a carbon synchrotron [36]. This shows that despite the consequent size of the 400 MeV/u cyclotron when compared to its proton-only counterparts, it still has the potential to be attractive, especially as it promises the ease of use and user-friendliness of cyclotrons (Fig. 3.17).

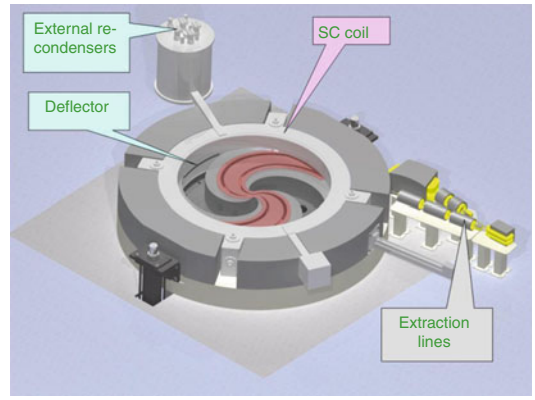

Fig. 3.17 View of the IBA-JINR 400 MeV/u cyclotron for carbon therapy. The H+ and C6+ beam lines are combined into one beam line outside of the cyclotron. Cooling is achieved using liquid helium

In conclusion, it is evident that development of the cyclotron, from conception to widespread adoption in physics and cancer therapy, has been prolific. Continued activity, evolution, and fresh interpretations bring new energy into this field driven by a market demand for smaller and more affordable machines. Developing features and customizations aim to provide an ever more precise, compact, and affordable therapy to patients worldwide.

Bibliography

1. Livingston MS, Lawrence EO. The production of high speed light ions without the use of high voltages. Phys Rev. 1932;40:19–35.
2. Veksler V. Concerning some new methods of acceleration of relativistic particles. Phys Rev. 1945;9:153.
3. McMillan EM. The synchrotron – a proposed high energy particle accelerator. Phys Rev. 1945;68:143.
4. Umezawa M. Indianapolis. HITACHI proton beam therapy system. 2013. Particle Beam Therapy Symposium, 55th AAPM Annual Meeting, Indianapolis, Indiana.

5. Thomas LH. The paths of ions in the cyclotron. Phys Rev. 1938;54:580.
6. Heyn FA, Tat KK. Operation of a radial sector fixed frequency proton cyclotron. Rev Sci Instrum. 1958;29:662.
7. Christofilos N. 2736799 USA, 10 Mar 1950.
8. Courant ED, Livingston MS, Snyder HS. The strong-focusing synchrotron – a new high energy accelerator. Phys Rev. 1952;88:1190–6.
9. Kerst DW, Terwilliger KM, Jones LW, Symon KR. A fixed field – alternating gradient accelerator with spirally ridged poles MURA-DWK/KMT/LWJ/KRS-3. Midwest Universities Research Assoc. s.l.: Unpublished. 1954.
10. Dunn PD, Mullett LB, Pickavance TG, Walkinshaw W, Wilkins JJ, editors. Accelerator Studies at A.E.R.E. Harwell, Symposium on high-energy accelerators and pion physics, vol. 1. Geneva: Edouard Regenstreiff; 1956. p. 11–23.
11. Hiramoto K, Coutrakon G. Synchrotron technology for particle therapy system. 2010. PTCOG 49 Educational Workshop, Chiba, Japan.
12. Bohm D, Foldy LL. Theory of the synchrocyclotron. Phys Rev. 1947;72:649–61.
13. Bohm D, Foldy LL. Theory of synchrotron. Phys Rev. 1946;70:249.
14. Wilson RR. Radiological use of fast protons. Radiology. 1946;47(5):487–91.
15. Lawrence Radiation Laboratory. LRL Accelerators. Berkeley, California 2010.
16. McMillan EM. Synchrocyclotron. s.l.: patent US 2615129A. 1947.
17. The Svedberg Laboratory Historical Notes. [Online] http://www.tsl.uu.se/About_TSL/Historical_notes/.
18. Published work from Harvard Cyclotron Laboratory. [Online] http://users.physics.harvard.edu/~wilson/cyclotron/cyclotron_publications.html.
19. Wilson RR. A brief history of the Harvard University Cyclotrons. [Online] 2003. http://users.physics.harvard.edu/~wilson/cyclotron/history.html.
20. Optivus Proton Therapy Inc. History of Proton Therapy, California 2008.
21. Mills F, et al. Technical assessment of the Loma Linda University Proton Therapy Accelerator. Batavia: Fermi National Accelerator Laboratory; 1989.
22. Jongen Y, Laisne A, Lannoye G. France N. Preliminary design of a reduced cost proton therapy facility using a compact, high field isochronous cyclotron. European Particle Accelerator Conference. Nice, France 1990.
23. Jongen Y. Review on cyclotrons for cancer therapy. Lanzhou: International Conference on Cyclotrons and their Applications. 2010.
24. Schillo M, et al. Compact superconducting 250 MeV proton cyclotron for the PSI PROSCAN proton therapy project. In: Cyclotrons and their applications. East Lansing: S.n.; 2001.
25. Antaya T. High-field superconducting synchrocyclotron. PCT/US2007/001628. 19 Jan 2007.
26. World's First MEVION S250 Proton Therapy Treatment Delivered at Barnes-Jewish Hospital. [Online] Mevion Medical Systems Inc., 19 Dec 2013. [Cited: 06 27, 2014.] http://www.mevion.com/archived-news/105--worlds-first-mevion-s250-proton-therapy-treatment-delivered-at-barnes-jewish-hospital.
27. Kleeven W. The IBA superconducting synchrocyclotron project S2C2. Vancouver: Cyclotrons. 2013.
28. Ion Beam Applications. [Online] http://www.iba-protontherapy.com/proteusone-0.
29. Kumata Y. Particle Therapy Technologies. 55th AAPM annual meeting, Indianapolis, Indiana 2013. p. 1.
30. Rocken H. Commissioning and Testing of Varian's 250 MeV Superconducting ProBeam® Cyclotrons for Proton Therapy. Villigen: European Cyclotron Progress Meeting. 2012.
31. Tsutsui H, Hashimoto A, Mikami Y, Mitsubori H, Mitsumoto T, Touchi Y, Ueda T, Uno K, Watazawa K, Yajima S, Yoshida J, Yumoto K, Sumitomo Heavy Industries. Design Study of a Superconducting AVF Cyclotron for Proton Therapy. Ltd. Vancouver: Cyclotrons. 2013.
32. Radovinsky A, Minervini JV, Miller CE, Bromberg L, Michael P, Maggiore M. Superconducting magnets for ultra light and magnetically shielded, compact cyclotrons for medical, scientific, and security applications. IEEE Tran Appl Supercond. 2014;24:3.
33. Radovinsky AL, Minervini JV, Michael PC, Bromberg L. Variable energy acceleration in a single iron-free. http://www.psfc.mit.edu/library1/catalog/reports/2010/13rr/13rr009/13rr009_full.pdf. [Online] September 2013.
34. Mevion Medical Systems. [Online] www.mevion.com.
35. Ueda H. Conceptual design of next generation HTS cyclotron. Osaka: IEEE Trans Appl Supercond. 2013;23:13.
36. Jongen Y. Cyclotrons from protons to Carbon for Hadron Therapy. Pasadena: PAC; 2013.

Development of C-Ion Radiotherapy Technologies in Japan

4

Koji Noda

4.1 Introduction

Heavy-ion beams are very suitable for deeply seated cancer treatment not only owing to their high-dose localization around the Bragg peak but also owing to the high biological effect in this region. National Institute of Radiological Sciences (NIRS), therefore, proposed to construct "Heavy-Ion Medical Accelerator in Chiba" (HIMAC) [1], which was approved by the Japanese government in 1984. The HIMAC facility was completed in October 1993 as the world's first heavy-ion accelerator facility dedicated to medical use. Since 1994, NIRS has conducted the cancer treatment and related researches with HIMAC. The HIMAC treatment chose a carbon ion, based on the fast-neutron radiotherapy (RT) experience at NIRS. As a beam delivery method, HIMAC has adopted a single beam-wobbling method because it offers the robustness toward beam errors and the easy dose management. The treatment protocols were significantly increased after the respiratory-gated irradiation method was developed for treatments of moving tumors. As a result of the accumulated numbers of protocols, in 2003, the Japanese government approved the carbon-ion RT with HIMAC as a highly advanced medical technology. Because of this recognition, NIRS proposed a standard carbon-ion RT facility in Japan [2] in order to boost applications of carbon-ion RT, with emphasis being placed on a downsized version so as to reduce cost. The design study and R&D works for the proposed facility was carried out in 2004 and 2005. The fruits of this work were realized in the Gunma University, carbon ion therapy facility which has been successfully commissioned since 2010.

NIRS, further, has been engaged in a "new treatment research project" [3] since April 2006 for the further development of HIMAC treatments. One of the most important purposes in this project is to realize an "adaptive cancer radiotherapy," which can accurately treat tumors even with changing sizes and shapes during a treatment period. The pencil-beam 3D scanning method has been well known to be very suitable for the adaptive cancer RT. The 3D scanning, however, has not been applied to the treatment of the moving tumor because of difficulty in dose delivery management. For treatments, both the static and moving tumors, therefore, NIRS has developed a phase-controlled rescanning with gated irradiation [4] to move toward the goal of adaptive cancer RT. The new treatment research facility was constructed in order to evaluate the developed technology through a clinical study. The facility, which is connected with the existing HIMAC accelerator complex, has three treatment rooms: two rooms equipped with both horizontal

K. Noda, PhD
Department of Accelerator and Medical Physics,
National Institute of Radiological Sciences,
Chiba, Japan
e-mail: noda_k@nirs.go.jp

A.K. Rath, N. Sahoo (eds.), *Particle Radiotherapy: Emerging Technology for Treatment of Cancer*,
DOI 10.1007/978-81-322-2622-2_4

and vertical beam delivery systems, while one room with a rotating gantry. As the first stage, one of three treatment rooms has been opened with the pencil-beam 3D scanning since May 2011, utilizing a range shifter as an energy degrader for slice change. As the second stage, the second room has been also operated since September 2012. In this stage, the hybrid energy scanning [5], which is combined with the thin range shifter with 11 energy steps through the synchrotron, has been applied toward more accurate treatment. A preclinical study for the phase-controlled rescanning [6, 7] is completed and a clinical study with this technology is about to be started. As the third stage, a compact heavy-ion rotating gantry, which will be installed in the third room, has been developed with the superconducting technology, in order to realize the intensity-modulated carbon-ion RT (IMCT) combined with the pencil-beam 3D scanning [8, 9]. The IMCT will bring the shorter-course treatment owing to higher-dose concentration.

This chapter describes developments of the beam delivery technologies including the new 3D scanning technique and rotating gantry and introduces the carbon-ion RT facilities in Japan based on the developments and studies at HIMAC.

4.2 Development of Beam Delivery Technologies in HIMAC

4.2.1 HIMAC

HIMAC was designed and constructed on the basis of radiological requirements. The ion species ranged from He to Ar in the early stage of the HIMAC operation, while those from H (proton) to Xe have been delivered at present not only for the heavy-ion RT but also for its related physics and biological experiments. The beam energy was designed to be varied from 100 to 800 MeV/n for efficient treatment. HIMAC consists of an injector linac cascade, dual synchrotron rings with independent vertical and horizontal beam lines, and three treatment rooms equipped with the beam delivery system. For carbon-ion RT, a C^{2+} beam, produced by the 10-GHz ECR (electron cyclotron resonance) ion source, is injected to the linac cascade consisting of RFQ and Alvarez linacs and is accelerated up to 6 MeV/n. After the carbon-ion beam is fully stripped with a thin carbon-foil stripper, the beam is then injected into the synchrotron rings. The carbon-ion beam stored by the multi-turn injection is accelerated up to a desired energy and is slowly extracted from the synchrotron. Finally, the carbon beam extracted from the synchrotron is delivered to the beam delivery system. Figure 4.1 shows a bird's-eye view of the HIMAC facility.

The HIMAC facility has employed a single beam-wobbling method, which is one of the passive beam delivery methods [10], as shown in Fig. 4.2. This beam delivery method consists of two components; a single beam-wobbling system for a lateral dose spread and a ridge-filter method for the creation of spreadout Bragg peak (SOBP). A pair of beam-wobbling magnets (wobbler) moves the beam in a circular orbit with high frequency so as to generate a pseudo-stationary broad beam in conjunction with a heavy-metal scatterer. An exchangeable ridge filter modulates the beam range in the field to spread out the Bragg peak longitudinally. A range shifter system inserts variable-thickness energy absorbers to adjust the beam range. A multi-leaf collimator (MLC) with movable metal elements and/or a customized patient collimator defines the field aperture. A patient compensator, a sculptured plastic device, compensates the beam ranges so that the beam range conforms with the distal part of the target volume in the field.

In the HIMAC beam delivery system, the wobbling frequency is set to be 56.4 Hz, and the ridge filter consisting of identical aluminum bar ridges spreads the beam range to give a uniform biological dose to the SOBP region. In the case of a heavy-ion beam, the SOBP is composed of various LET components with different weighting factors at each depth. The cell survival rate under a mixed LET radiation field can be described by a formalism proposed in the theory of dual radiation action on the basis of the Linear Quadratic (LQ) model [11], which was experimentally proven. We finally designed the SOBP of mixed

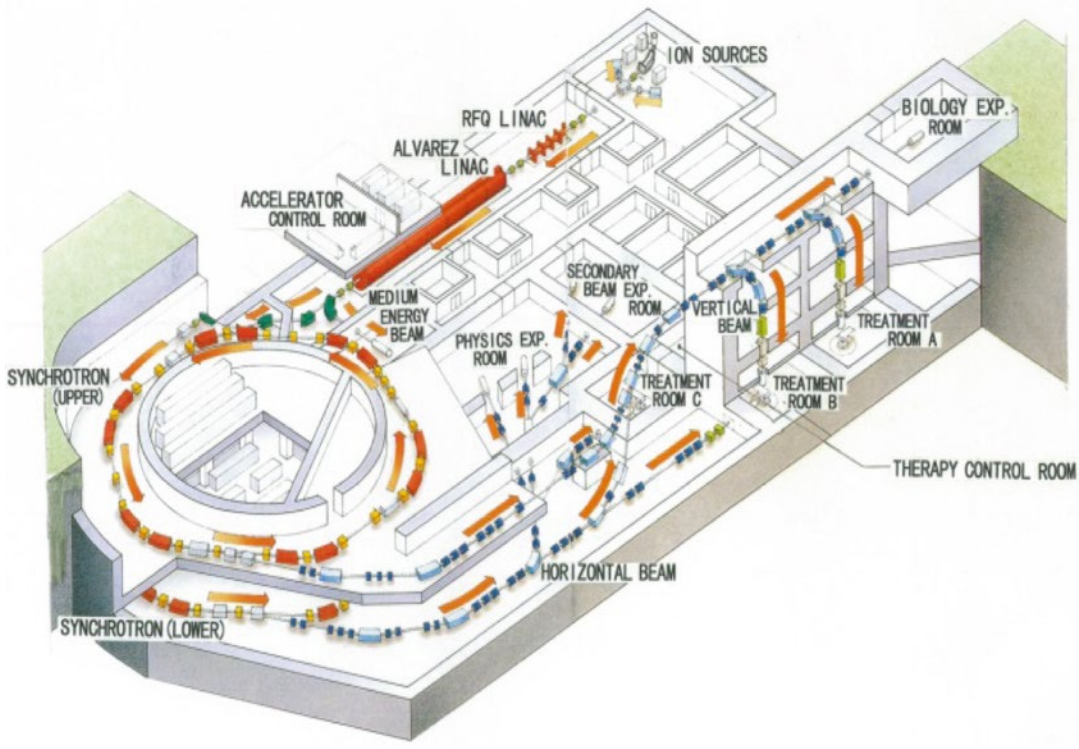

Fig. 4.1 Bird's-eye view of the HIMAC facility

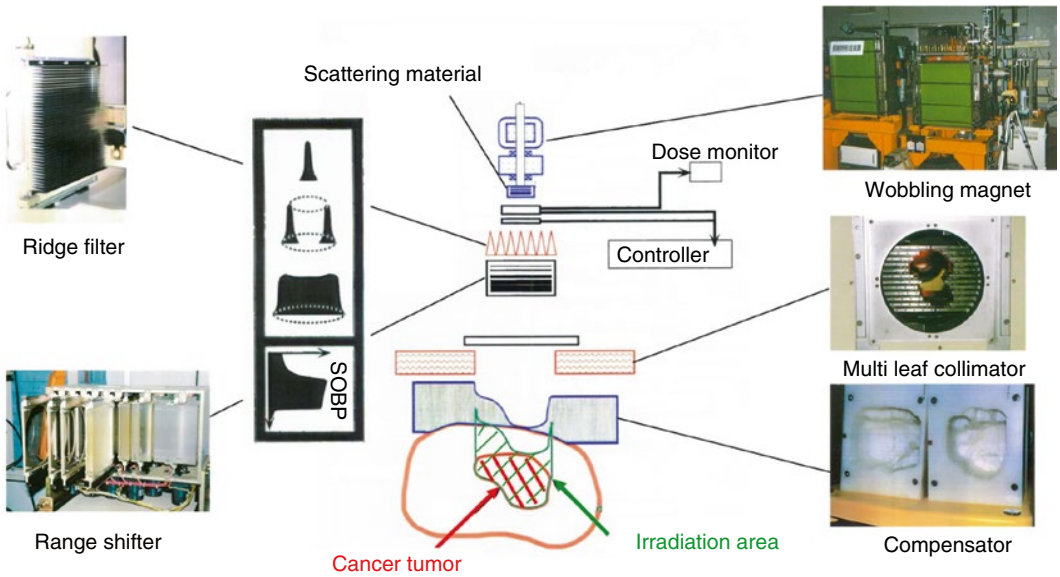

Fig. 4.2 Typical beam delivery system with the beam-wobbling method as one of the broad-beam methods

ions with different LET according to the procedure proposed by Lawrence Berkley National Laboratory (LBNL) [12] and the formalism [11]. At HIMAC, applying the single beam-wobbling with ridge-filter method, the maximum lateral field and the SOBP size are designed to be 22 cm in diameter with ±2.5 % of uniformity and 15 cm at the isocenter, respectively.

The single beam-wobbling method is a very robust method against fluctuations of beam position and/or intensity, compared with a pencil-beam 3D scanning one. The HIMAC beam delivery system, therefore, has employed this method in order to deliver its dose safely and reliably. On the basis of this method, the respiratory-gated and layer-stacking irradiation methods were developed in order to increase the irradiation accuracy, which have been routinely used for treatments in HIMAC. The beam-wobbling method was improved, further, to increase the residual range, and beam utilization efficiency.

4.2.2 Respiratory-Gated Irradiation Method

Damage to normal tissues around tumor is inevitable in treatment of a tumor moving along with a patient's respiration. Therefore, a respiratory-gated irradiation method with a broad beam was developed [13].

Essential design considerations are as follows:

1. A gate signal for permitting irradiation should be accurately generated to enable irradiation only when target is at the desired position. For this purpose, a position-sensitive detector (PSD) with an infrared light source is chosen to generate the respiration signal because of its reliability, stability, and easy setting. Since the organs are normally most stable at the end of expiration, the permitting signal for irradiation should be generated during this phase. The gate signal, on the other hand, is generated by the AND logic between the irradiation-permitting signal and the flattop period than can extract the beam from the synchrotron.
2. An operation pattern of the synchrotron should be optimized to give maximum effective dose rate. A duty factor of the beam delivery in a 0.3-Hz operation pattern, thus, is to increase more than 50 % in order to avoid a beat between the flattop period and the permitting irradiation period.
3. An aborting system of residual beam in the flattop of the synchrotron operation pattern should be provided to avoid unwanted activation. In the beam-aborting system, a beam deceleration scheme was employed and a residual beam is decelerated from a top energy to an injection-energy level.
4. An interlock system for a safe treatment should be used. An interlock function, thus, is added to the interlock system used for treatment of a fixed target so as to work immediately when irradiation dose in a non-permitting-irradiation period exceeds a threshold level.

A block diagram of this system is shown in Fig. 4.3. As shown in the lower-left corner in Fig. 4.3, an infrared-LED sensor is set on the surface of patient body, and its movement is monitored by a position-sensitive detector, which results in obtaining a respiratory signal. The gate signal, which is a permitting signal of irradiation, is generated by AND logic between the respiratory signal and the flattop signal of the synchrotron operation (upper right in Fig. 4.3). The beam should be delivered according to the gate signal produced only when the target is in its designated position (upper left in Fig. 4.3). One of the most essential technologies for the system is a slow beam extraction method having a quick response on the beam on/off compared with a respiration period. For this purpose, the RF-KO slow extraction method [14] was developed and its response on the beam on/off is within 1 ms. This irradiation method has been successfully applied since 1996.

4.2.3 Layer-Stacking Irradiation Method

In the single beam-wobbling method, the fixed SOBP produced by the ridge filter results in undesirable dosage to the normal tissue in front of target, because the thickness of an actual target varies within the irradiation field. In order to suppress the undesirable dosage, thus, the layer-stacking irradiation method was developed [15]. A schematic drawing of this method is shown in

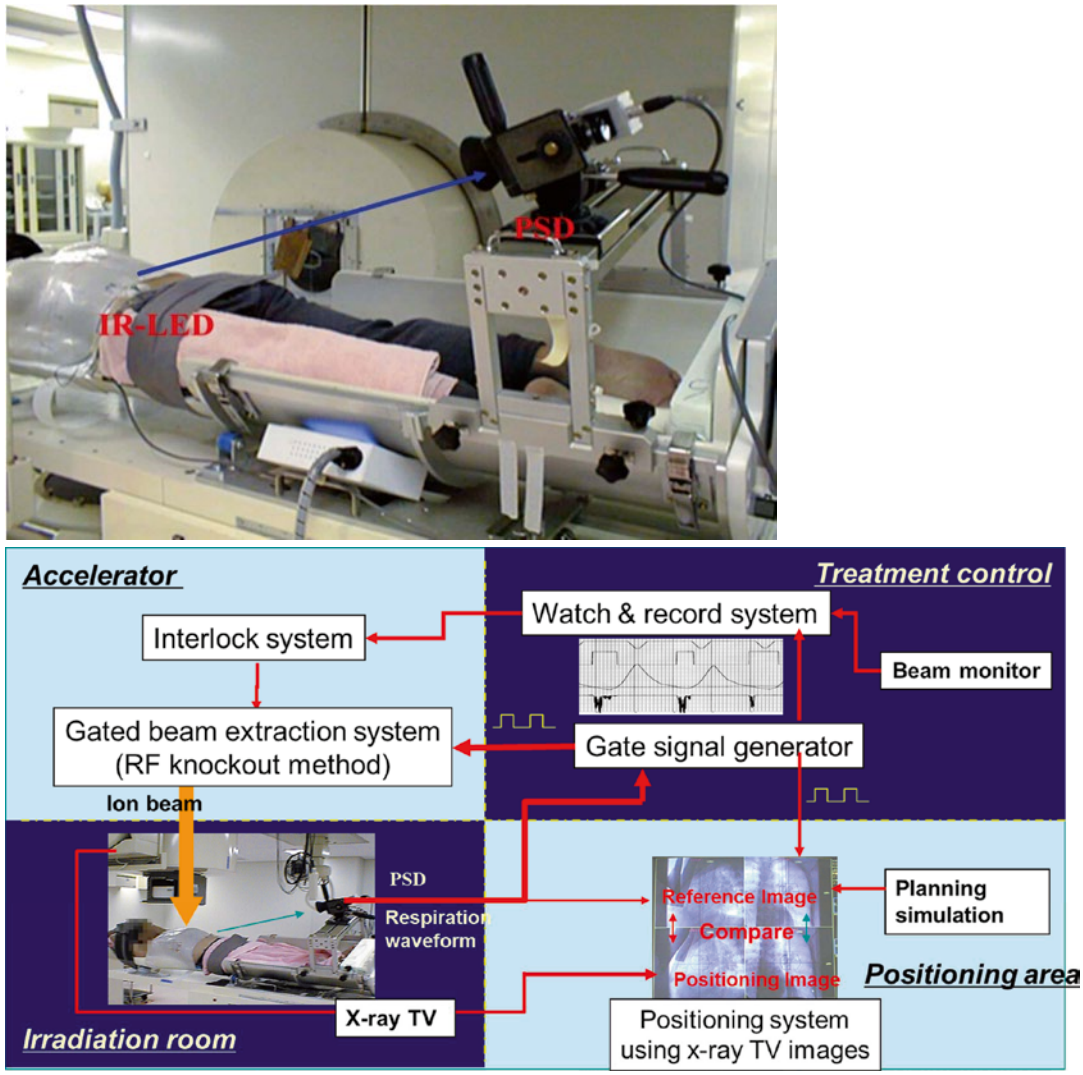

Fig. 4.3 The view of respiratory-gated irradiation in the horizontal beam delivery system in the HIMAC facility

Fig. 4.4. This method is to conform a variable SOBP to a target volume by controlling dynamically the conventional beam-modifying devices. The thin SOBP with several mm in water-equivalent length, which is produced by a ridge filter, is longitudinally positioned over the target volume in a stepwise manner. The target volume is longitudinally divided into slices, to each of which the small SOBP is conformed using the MLC and the range shifter, and a variable SOBP coinciding to the target volume is to be formed. This method has been routinely utilized since 2004. Figure 4.5 shows the simulation result to compare between dose distributions with and without this method. It is obviously found that the undesired dose region is eliminated when the layer-stacking method is applied.

4.2.4 Improvement of Beam-Wobbling Method

The single beam-wobbling method has been utilized for the HIMAC treatment, because this method has offered both the robustness toward beam errors and the easy dose delivery management. However,

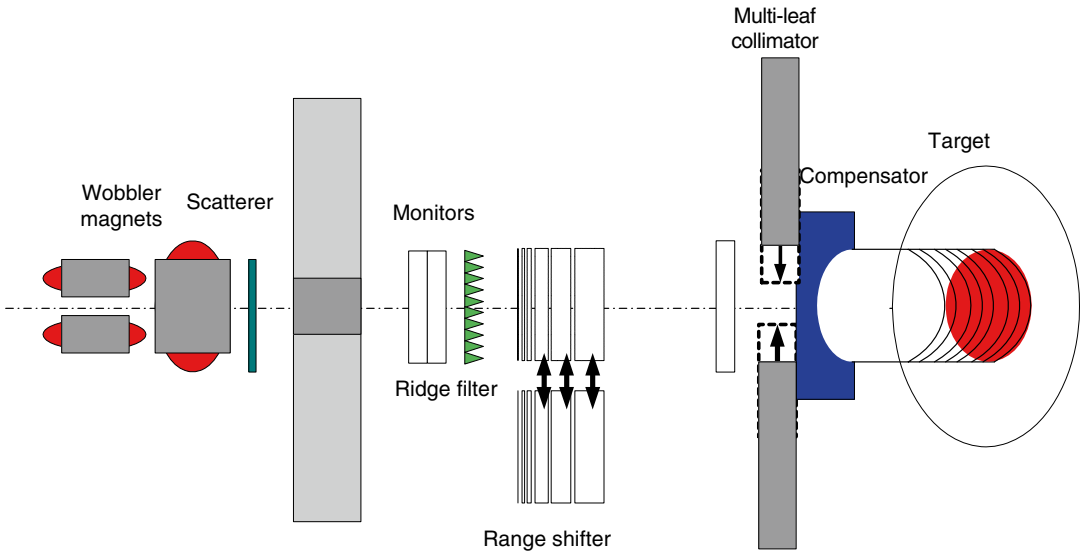

Fig. 4.4 Schematic drawing of the layer-stacking irradiation method

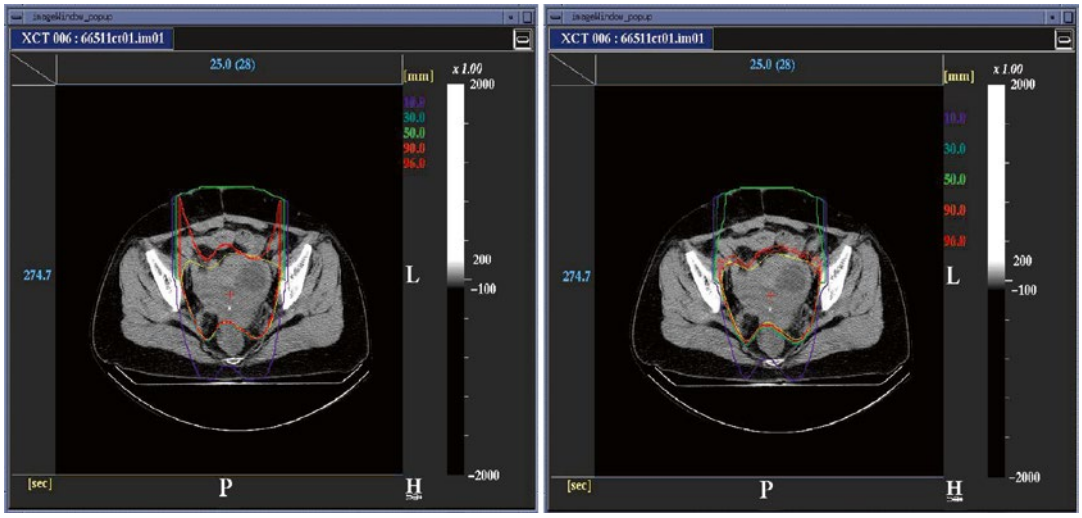

Fig. 4.5 The dose distributions without and with the layer-stacking irradiation method. The *left figure* shows the dose distribution without this method, which can be easily found to have an undesired dose region (*red line*) outside the target. The *right one* shows that this method can eliminate the undesired dose

it is inevitable to lose the residual range due to the scatterer. NIRS, thus, proposed the improved methods, which are spiral beam-wobbling and zigzag beam-wobbling methods [16]. As shown in Fig. 4.6, both the methods employ smaller beam size than that in the single beam-wobbling to deliver a uniform dose distribution in the lateral direction, while the beam moves along on a spiral orbit or on a zigzag one, respectively. The range loss due to passing through the scatterer is smaller because the smaller beam size requires thin scatterer. Consequently, these methods require the lower energy delivered from the accelerator to obtain a required field size, compared with that in the single beam-wobbling method.

The spiral beam-wobbling method should be required the amplitude modulation of the

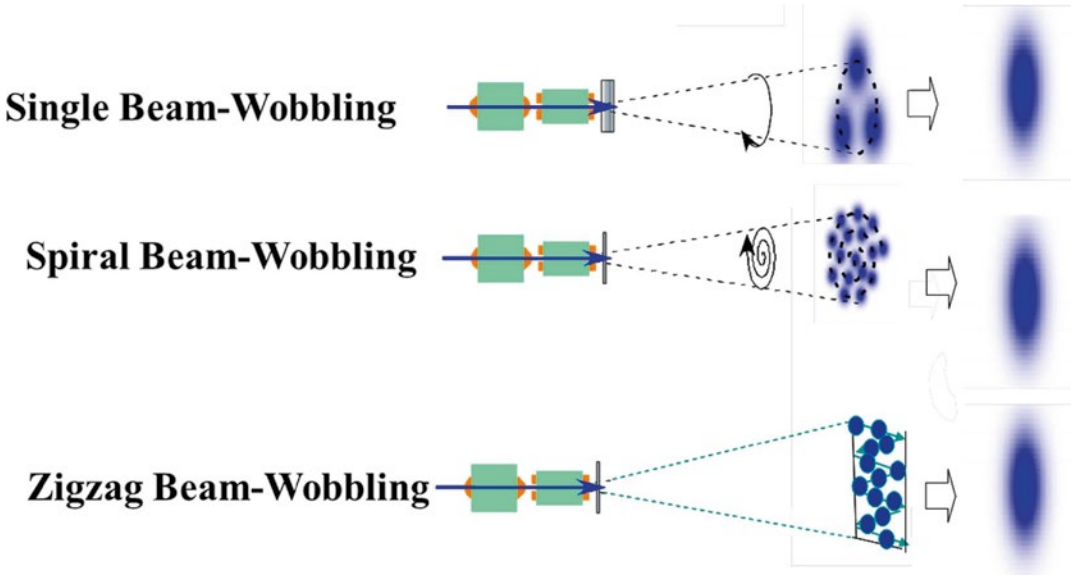

Fig. 4.6 Schematic figures of the single beam-wobbling method, the spiral one and the zigzag one

excitation current of the wobbler magnets, because the wobbling radius is proportional to the square root of time under the condition of a constant irradiation area in unit time. The time structure of the beam slowly extracted from the synchrotron disturbs the uniformity of a dose distribution. An angular frequency of beam wobbling should be optimized in order to avoid such disturbance. As a result of a simulation study [17], both the amplitude modulation and angular frequencies are optimized to be 59 Hz and 23 Hz, respectively.

The zigzag beam-wobbling method is raster scanning with a broad beam. The beam moves along on a zigzag pattern generated by the excitation current with a triangular waveform for the wobbler magnets. The orthogonal wobbler magnets are generally set at the slow and fast wobbling speeds, because beams scan in the irradiation field as uniformly as possible to improve the time characteristic of uniformity in the irradiation field. Changing a phase relation in each magnet, further, one can rotate the field shape. Combing this scheme with a rotatable MLC, one can obtain the higher beam-utilization efficiency in rectangular-like shape, compared with the spiral beam-wobbling method. A regulated zigzag beam-wobbling method, further, was proposed in order to deliver the larger irradiation area than these on both the spiral and zigzag methods. The irradiation field is reduced as the beam size increases when using the nonregulated method, because the dose profile at locations close to the field edge falls off. The regulated beam-wobbling method makes the stay time longer at the locations close to the field edge in order not to reduce the falloff. The regulated wobbling method is expected to lead to expansions of the uniform irradiation field and increased beam efficiency. The performances of these three methods were experimentally verified [16].

4.3 Next-Generation Beam Delivery Technology

In the radiotherapy, one has sometimes observed shrinkage of a tumor size as well as change in its shape during a course of the treatment. In order to keep the sophisticated conformations of the dose distributions even in such cases, a strict requirement has been that treatment planning be carried out just before each fractional irradiation, which is called “adaptive cancer radiotherapy.” For this purpose, a pencil-beam 3D scanning should be employed, as it does not use both the compensa-

tor and patient collimators requiring long manufacturing time. It is also well known that 3D scanning has brought about high treatment accuracy in the case of a fixed target [18–20]. However, this method has not yet been put into practical use for the treatment of a target moving with respiration. Since the HIMAC facility should carry out treatments not only for static targets but also for moving ones, we have developed a 3D scanning method that can treat both moving and static targets. In cooperation with a rotating gantry, furthermore, the 3D scanning method can achieve a higher accuracy of treatment even for a target close to critical organs by the IMPT [8], as compared with conventional carbon-ion RT. On the basis of these new developments, we have also designed and developed a rotating gantry incorporating the 3D scanning method [21].

4.3.1 Pencil-Beam 3D Scanning for Moving-Tumor Treatment

Pencil-beam scanning is an irradiation method to paint the dose distribution with a small beam and narrow Bragg peak, which allows us to take full advantage of the heavy particles. This irradiation scheme is schematically shown in Fig. 4.7. The pencil beam is laterally scanned so as to form a lateral irradiation field with orthogonal scanning dipole magnets and is then longitudinally positioned at different depths by either a range shifter or by energy change from the accelerator. The beam scanning path and the number of particles per location have been precisely determined in treatment planning to deliver the planned dose distribution. The scanning magnets therefore need to be controlled as a function of the number of particles detected by the dose monitor system. Fast and synchronous control of the dose monitor, magnetic scanning, and beam extraction systems with precision and resolution better than 1 % and 1 ms is normally required for clinically practical beam deliveries at HIMAC.

There are two approaches for lateral beam scanning, the spot- and raster-scanning methods. In the spot-scanning method, the scan path is quantized into spots and beam is delivered on a spot-by-spot basis. This method is sometimes referred to as a “dose-driven scanning” method since the dose at any given spot is determined fully by the dose delivered at that spot and the beam is turned off after the dose is fully delivered. In this method, the switching speed and precision of beam extraction are crucial, and it is generally difficult to form fine dose distribution

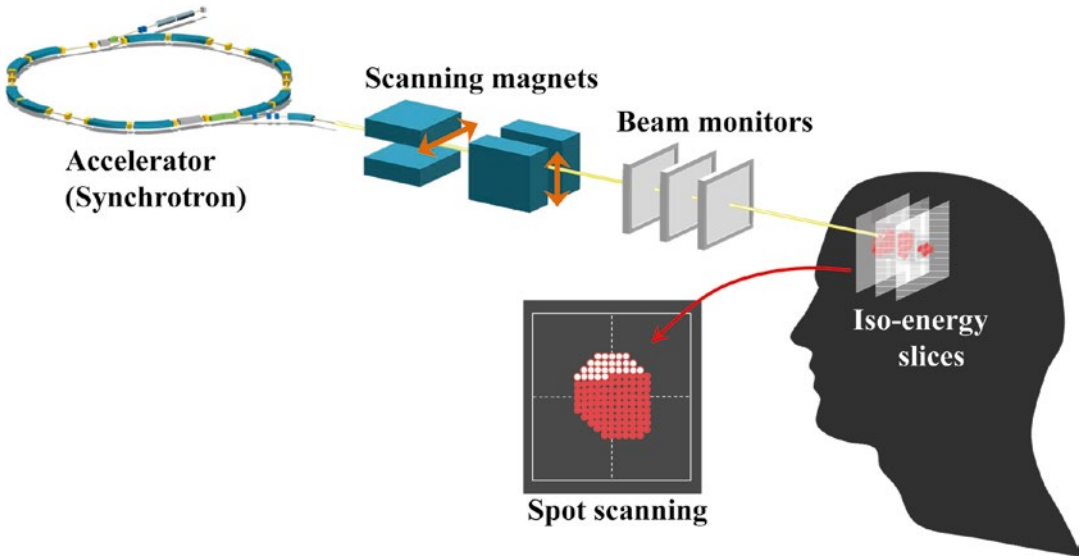

Fig. 4.7 Image view of 3D scanning

with a large number of spots delivered within a tolerable duration. In the raster-scanning method, the pencil beam is delivered continuously during magnetic scanning, which is controlled as a function of the number of particles delivered. This method is a variation of the dose-driven spot-scanning method, in that the beam is not turned off between spots, but the beam that is on, while it is moving from one spot to another, is included in the dose to each spot. This will greatly ease the requirements for the beam extraction system. In treatment planning and beam control, the concept of discrete spots may still be used, but the extra dose delivered in transitions between spots must be mitigated or explicitly counted in plan optimization. Another scheme, which is called "hybrid raster scanning," was recently developed and has been in practical use [5]. The hybrid raster scanning is essentially same with the dose-driven scanning, but the beam is continually delivered even during the spot position change. During the slice change, on the other hand, the beam delivery is stopped during each slice change.

In the pencil-beam 3D scanning, the beam-utilization efficiency increases to almost 100 %, which is much higher than that of the broad-beam method such as the single beam-wobbling method. The beam intensity is thus estimated to decrease by a factor of 3–5, compared with the broad-beam methods. For scanning beams, however, the dose-rate limitation is determined by considering the following: (1) the quantity of an extra dose due to the finite time to turn off the beam delivery in the spot-scanning method and (2) the amount of extra dose delivered when the beam is moving between positions in the raster-scanning method in which the beam is not turned off. In both cases, the dose is proportional to the beam intensity delivered.

4.3.1.1 Phase-Controlled Rescanning Method (Lateral Scan)

Toward the adaptive cancer radiotherapy for both the static and the moving target, a new 3D scanning technique with a pencil beam was required. NIRS, therefore, proposed phase-controlled rescanning (PCR) with a pencil beam [4]. In the PCR method, as schematically shown in Fig. 4.8, rescanning completes irradiation on one iso-energy slice during one respiratory-gated period. Since the three-dimensional movement of the target is close to "zero" on average, a uniform dose distribution can be obtained even under irradiation on the moving target.

The PCR method requires mainly two technologies: (1) intensity-modulation technique for a constant irradiation time on each iso-energy slice having a different cross section, as shown in Fig. 4.9 and (2) fast pencil-beam scanning technique for completing several-times rescanning within a tolerable time.

1. Intensity modulation
   A spill control system was developed [22] in order to deliver the beam with intensity modulation, based on the improvement of the RF-KO slow extraction method. The core part of this system requires the following functions: (1) calculation and output of an AM signal according to request signals from an irradiation system, (2) real-time processing with a time resolution less than 1 ms, and (3) feed-forward and feedback controls to realize the extracted intensity as requested. This system allows us to control dynamically the beam intensity almost as required.
2. Fast 3D scanning
   For the fast pencil-beam 3D scanning, three key technologies were developed as follows: (1) new treatment planning system (TPS) for the hybrid raster scanning, (2) extended flat-top operation of the synchrotron, and (3) high-speed scanning magnet.

1. New TPS [23]
   A new TPS has been developed for fast 3D scanning with a pencil beam. The biological dose distribution of a pencil beam is obtained by combining the measured physical dose distribution and the RBE obtained through measured α and β values in the LQ model. Using the biological dose distribution, the new TPS optimizes the assignment of spot positions and their weights so as to give the prescribed dose on a target and to significantly reduce the dose on surrounding normal tissues. A hybrid

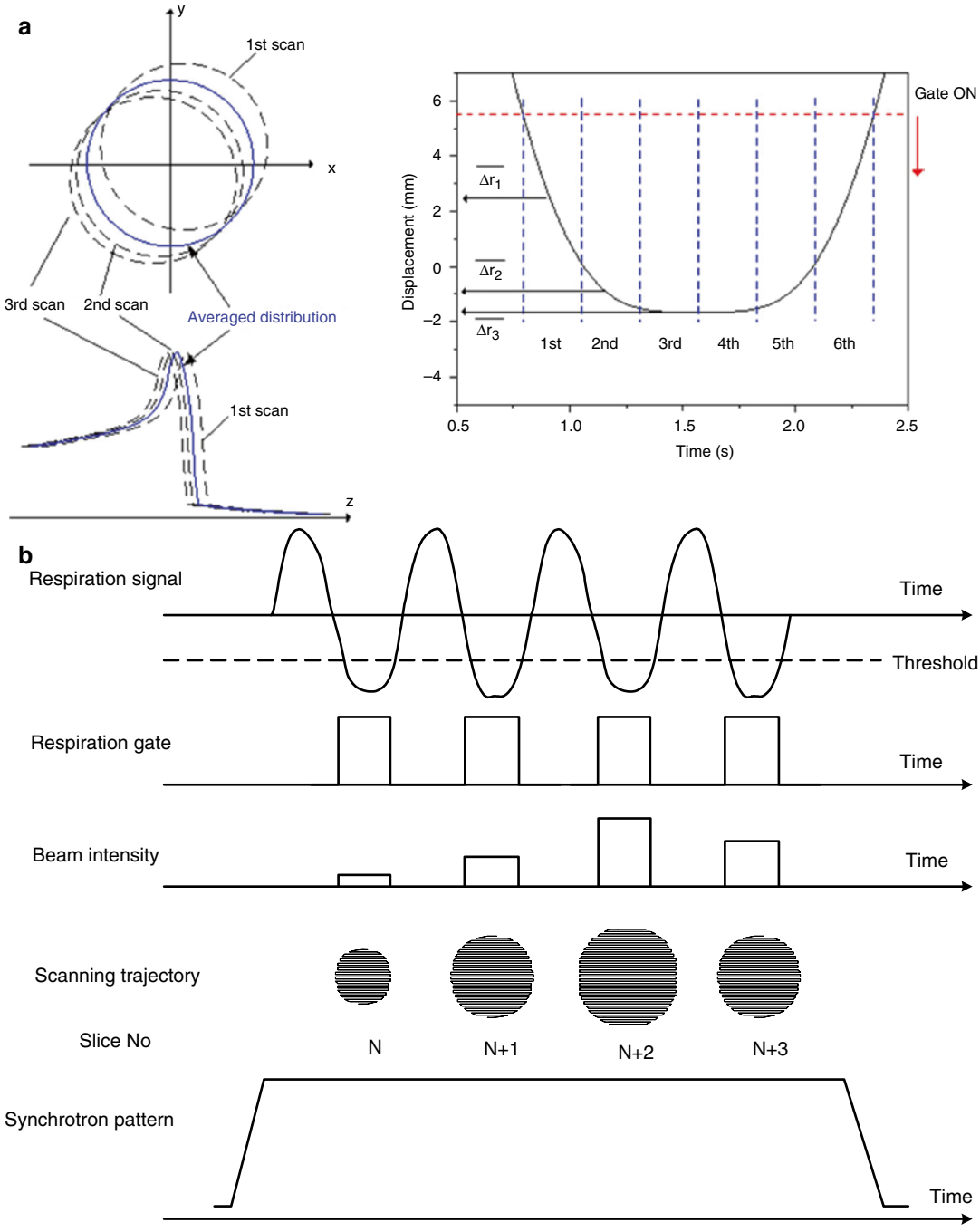

Fig. 4.8 (**a**) Principle of phase-controlled rescanning (PCR) method and (**b**) schematic diagram of phase-controlled rescanning (PCR) method

raster scanning is employed, instead of spot scanning, in order to save the beam-off period during spot position movement. In the hybrid raster scanning, on the other hand, it is inevitably necessary to deliver an extra dose to the position between the spot positions, which disturbs the dose distribution. It is noted that its disturbance is proportional to the extra

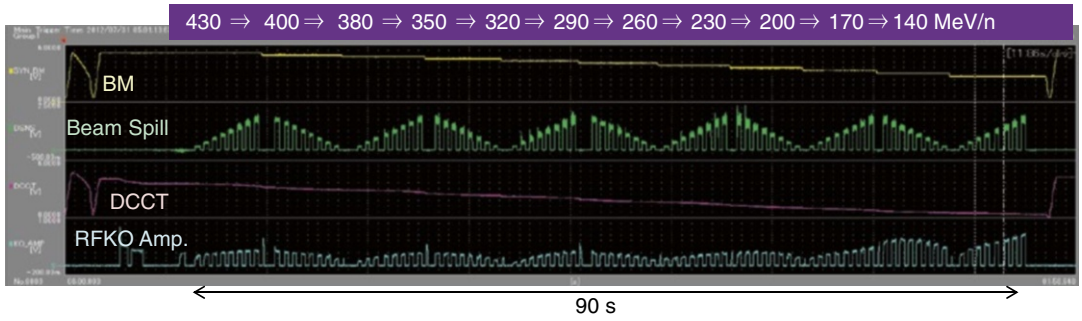

Fig. 4.9 Intensity modulation in multiple-energy operation with extended flattop. From upper trace, the exciting current of bending magnets corresponding to the multi-energy operation, the beam spill (the time structure of the extracted beam), the signal of DCCT (DC current transformer) corresponding to the circulating beam intensity and RF-KO signal

dose. As a result, it was not easy to increase the beam intensity delivered to obtain good dose distribution, because the extra dose is proportional to the beam intensity delivered. The HIMAC synchrotron, however, has the high reproducibility and uniformities in the time structure of the extracted beam through the spill control system. One, thus, can predict the extra dose and incorporate its contribution to the treatment planning. Consequently, the beam intensity can be increased without disturbing the dose distribution, which results in the shorter irradiation time. By applying a modified "travelling-salesman problem," the path length of raster scanning could be shortened by 20–30 %. Finally, the new TPS can increase the scanning speed totally by a factor of about 5.

2. Extended FT operation
   Owing to a high beam-utilization efficiency of around 100 % in the scanning method and to an intensity upgrade to 2×10^{10} carbon ions, one can complete a single-fractional irradiation of almost all treatment procedures in a single-operation cycle of the synchrotron. This single-cycle operation, which can be realized by using a clock-stop technique in the flattop period, can increase the treatment efficiency especially for the respiratory-gated irradiation. Thus, we have proposed the extended flattop operation of the synchrotron. In this operation mode, the stability of the beam was tested, and it was verified that the position and profile stability were less than ±0.5 mm at the isocenter in more than 100 s of the extended flattop operation. This extended flattop operation can shorten the irradiation time by a factor of 2. This operation scheme can also make the intensity modulation easy.
3. High-speed scanning magnet
   The scanning speed is designed to be 100 and 50 mm/ms in the horizontal and vertical directions, respectively, which are faster by around one order than that in the conventional one. In order to increase the scanning speed, we designed a scanning magnet having slits in both ends of the magnetic poles, according to thermal analysis, including an eddy-current loss and a hysteresis loss. The power supply of the scanning magnet was designed for fast scanning, and this consists of two stage circuits; the first stage for voltage forcing by IGBT switching elements and the second stage for the flattop-current control by FET switching ones. As a result of the test, the temperature rise was measured to be around 30 degrees maximum, which is consistent with our thermal analysis.

4.3.1.2 Depth Scan

The PCR method as well as the conventional 3D scanning has essentially required an iso-energy slice change for the depth scanning. For the first stage of HIMAC scanning treatment in 2011, the range shifter as the energy degrader, set just in front of a patient, has been utilized to change the

slice, because of saving the commissioning time of the HIMAC accelerator. It has been well known, however, that the variable energy operation by accelerator itself has great advantages over that by the energy degrader: keeping the spot size small, suppressing secondary neutron yield, increasing RBE owing to reducing fragmentation, and shorting irradiation time owing to high-speed slice change. Since the HIMAC synchrotron with one-cycle operation can deliver enough high intensity of the carbon-ion beam for one-fraction irradiation with applying the 3D scanning, NIRS has developed the multiple-energy operation with one-cycle operation of the HIMAC synchrotron. In this method, the energy of the extracted beam can be changed by stepwise energy pattern at the flattop of synchrotron operation. The duration of the flattop can be arbitrarily determined by a clock on/off in the flattop period, as shown in Fig. 4.10.

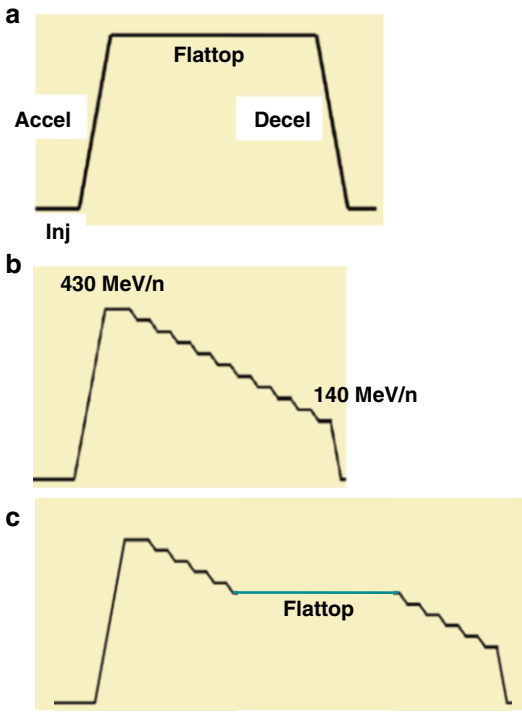

Fig. 4.10 Schematic diagram of variable energy operation at HIMAC. (**a**) Conventional operation pattern, (**b**) variable energy operation pattern, and (**c**) extended flattop with arbitrary energy by the clock on/off

As the first step, an eleven-step energy operation from 430 to 140 MeV/n was developed [24], which has been routinely utilized for the hybrid depth scanning, since 2012. In the hybrid depth scanning, range of more than 3 cm is changed by the energy change with the synchrotron, while that of less than 3 cm with the thin energy degrader. Figure 4.11 shows the simulation results of the range shifter scan and the hybrid depth scan, respectively. It is obviously found that the hybrid depth scan gives better DVH than the range shifter scan. As the second step, the 201-step energy pattern, which can change the energy ranging from 430 to 56 MeV/n, has been developed. The energy change in one step corresponds to a range shift of 2 or 3 mm, and it will take less than 100 ms for one slice change [24]. The bare tune in each energy level is designed so as to keep constant, while each separatrix size is increased with decreasing energy by changing the sextupole field of the separatrix exciter. Both the betatron tune and beam position changes during the multiple-energy operation are adjusted with the design values. Further, a simulated irradiation on a prostate cancer that was treated with the hybrid depth scanning was carried out with 201-step multiple-energy operation. As the result, it was verified that 201-step multiple-energy operation can be well operated as same manner as the hybrid depth scanning. The 201-step multiple-energy operation will be applied to the clinical study from 2015.

4.3.1.3 Experimental Study

As shown in Fig. 4.12, a test irradiation port for the fast 3D scanning experiment was designed and constructed in order to verify the design goal concerning the physical dose distribution for both the static and moving targets and the survival curve of HSG cell line.

Figure 4.13 shows the measured result of the physical dose distribution simulated on a prostate cancer treatment. The red lines show the physical dose distribution designed in the lateral and distal one, respectively, while the black ones the biological ones. As compared between the red lines and the measured ones (symbols), it is found that

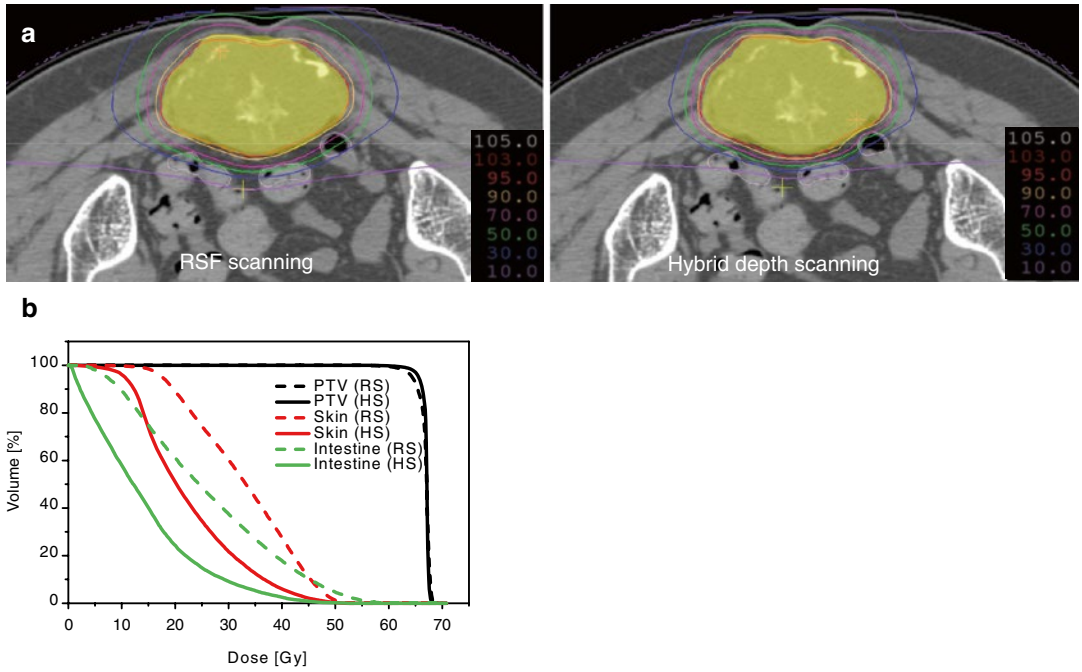

Fig. 4.11 (**a**) Treatment planning images: left shows the range shifter scanning and right hybrid depth scanning. (**b**) DVH figures. The *dashed lines* show results in range shifter scan and *solid lines* the hybrid depth scan: *red* is skin and *green* intestines

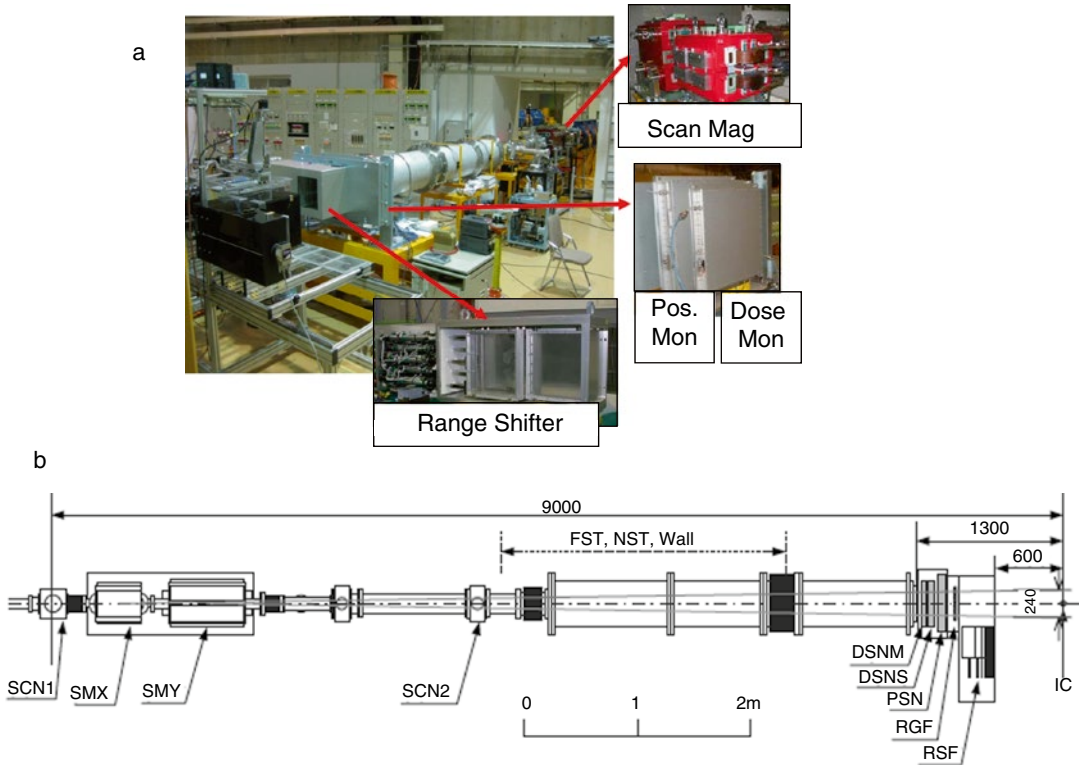

Fig. 4.12 A test irradiation port for the fast 3D scanning experiment

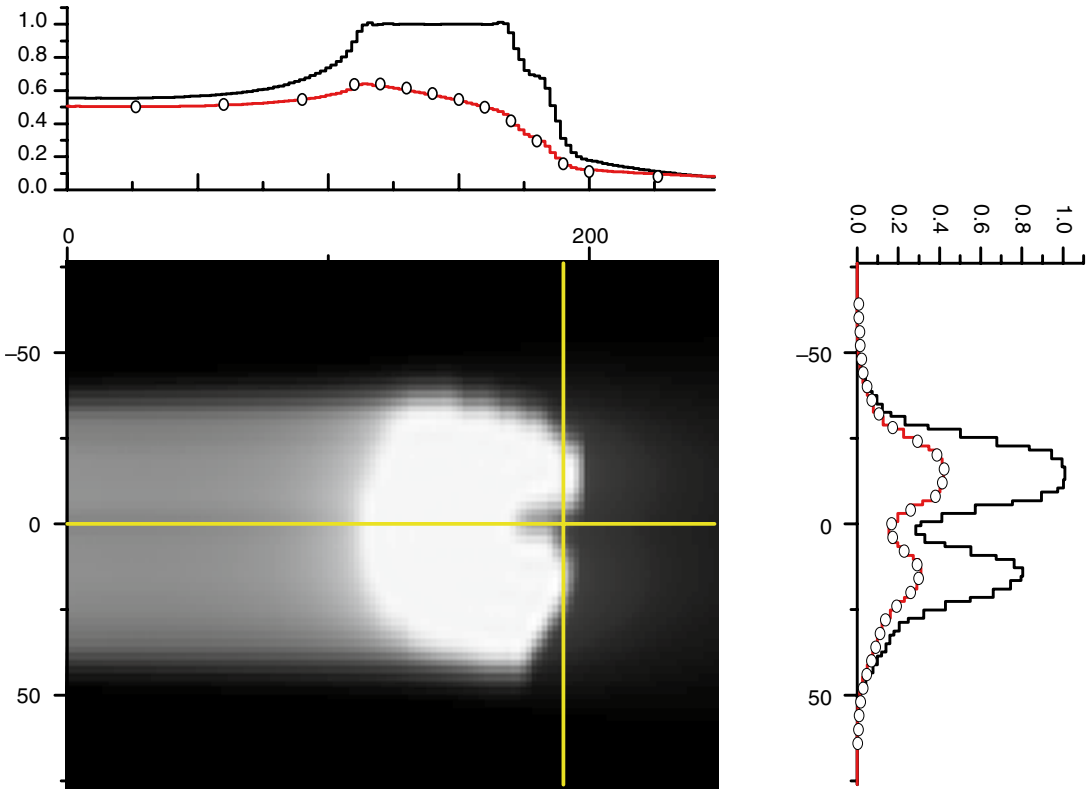

Fig. 4.13 The measured result of the physical dose distribution simulated on a prostate cancer treatment. The *red lines* show the physical dose distribution designed in the lateral and distal one, respectively, while the *black* ones are the biological dose distributions

the measured values are in good agreement with the designed distribution.

Figure 4.14 shows the experimental result of moving target irradiation. This experiment was carried out by using moving phantom with 20 pinpoint ion chambers. Without rescanning, as shown in Fig. 4.13a, the deviations between the measured and design dose are very large and unacceptable for the treatment. It is obviously found from Fig. 4.13b that the dose deviations with eight times rescanning can be reduced to small values within ±2.5 %, which is acceptable for the treatment.

Figure 4.15 shows the result of the biological experiment with the HSG cell line, where the solid line is the designed survival curve and symbols are the measured survival ratios. It is evident from the figure that the predictions of the proposed model agree very well with the results of the biological experiment.

4.3.2 Rotating Gantry

A rotating-gantry system allows wide choices of beam orientation, compared with a fixed port irradiation system. In the clinical study with HIMAC, since the beam can be delivered from either horizontal or vertical direction, the patient is fixed in supine, prone, and often rolled positions by typically 10°–20° from the horizontal plane in order to achieve a better combination of beams. This situation often adds to the patient's discomfort, complicates the treatment planning, and makes precise positioning difficult. A rotating-gantry system, which allows 360° rotation around the patient, will resolve many of these problems, and it is the standard for conventional x-ray teletherapy systems. A rotating gantry for carbon-ion RT, on the other hand, is much larger, as its size is typically 10 m in diameter much larger than commercialized proton RT systems, because the requirement for beam

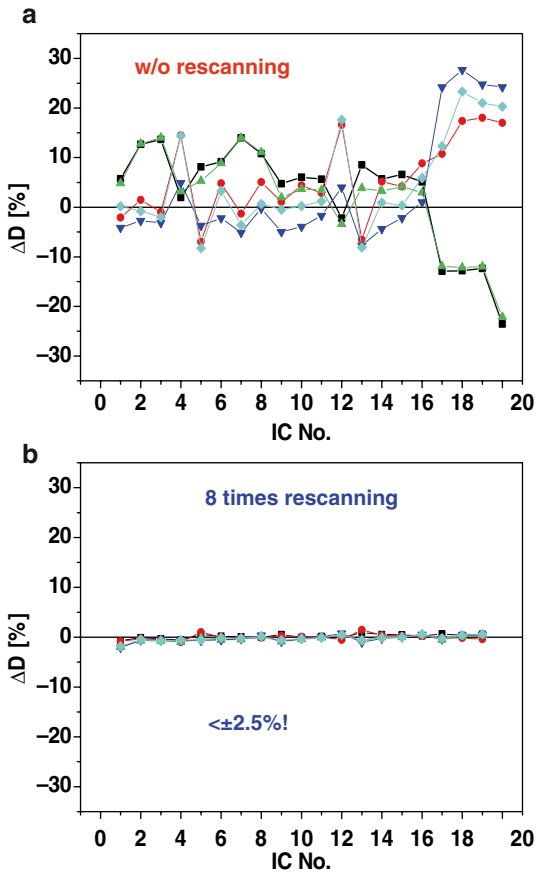

Fig. 4.14 The experimental result of moving target irradiation without (**a**) and with (**b**) rescanning

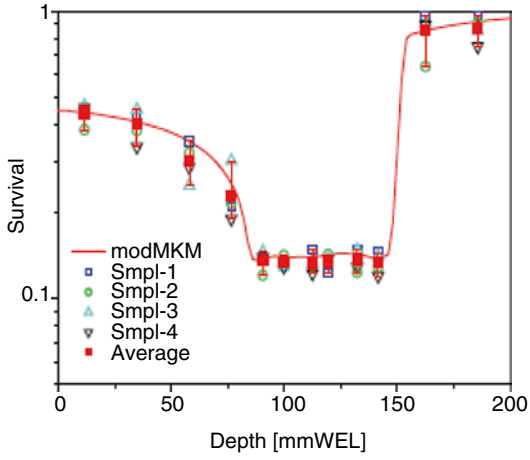

Fig. 4.15 Biological experiment with the HSG cell line, where the *solid line* is the designed survival curve and *symbols* are the measured survival ratios

bending is a few times more severe. The HIT (Heidelberg Ion Therapy) facility [25] in Germany has the only heavy-ion rotating-gantry system existing today.

An isocentric superconducting rotating gantry is being developed [21]. This rotating gantry is designed to transport carbon ions having 430 MeV/n to an isocenter with irradiation angles of over ±180 degrees and is further capable of performing the fast 3D scanning with a scan size of approximately 20 cm square at the isocenter. Figures 4.16 and 4.17 show a layout of the rotating gantry and the magnet assignment in the gantry, respectively. The gantry consists of ten combined-function superconducting magnets, a pair of the scanning magnets, and two pairs of beam profile monitor and steering magnets, allowing a compact geometry – the length and the radius of the gantry are approximately 13 and 5.5 m, respectively.

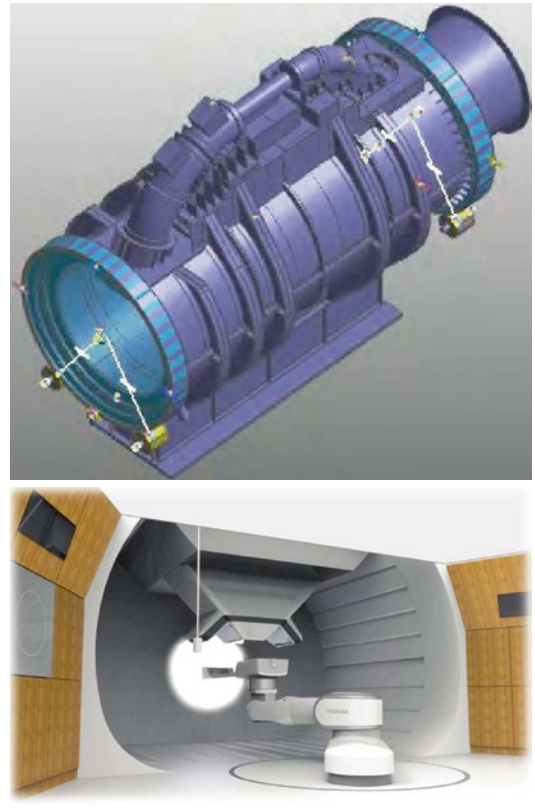

Fig. 4.16 The layout of the carbon-ion rotating gantry. *Upper* is a bird's-eye view and *lower* is the inside treatment room

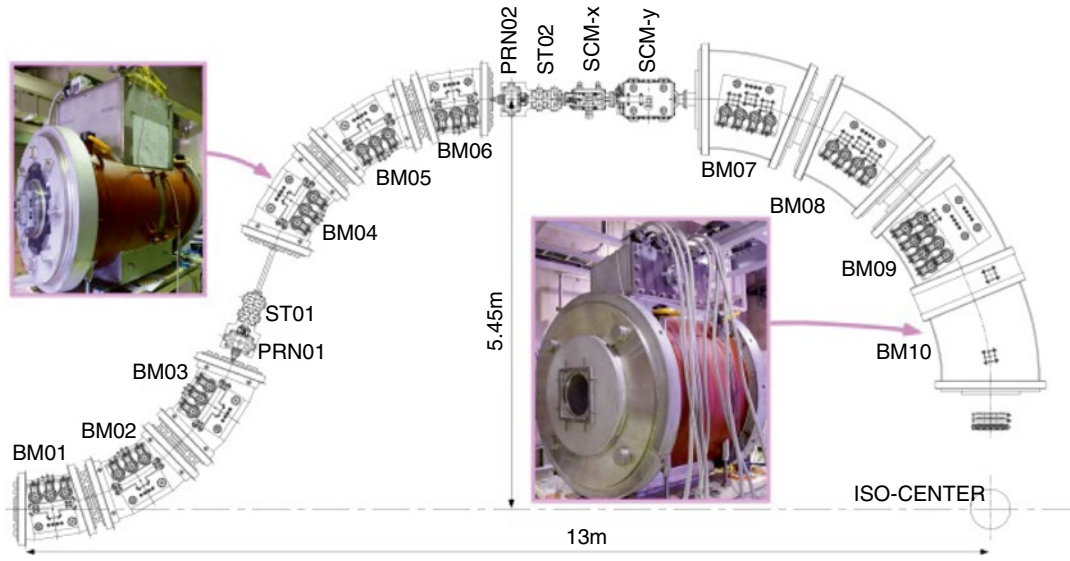

Fig. 4.17 Assignment of superconducting magnets in the rotating gantry

Before manufacturing all magnets, the test-superconducting magnet was designed and manufactured in order to verify a stability of a superconducting state under the mechanical rotation and vibrations on a rotating gantry and a stability of temperature under the fast slewing of the magnetic field to follow the multiple-energy operation. As the result of verification, no quenching phenomenon was observed in each test. Following these tests, the magnetic-field measurements for both dipole and quadrupole fields were made. It was verified that the overall results agreed with the calculated ones; however, the precise analysis revealed that the dipole field, as provided by only exciting the dipole coil, has a slight quadrupole component. Owing to the small magnitude of this unexpected quadrupole component, this component has to be adjusted by the quadrupole coil.

In the 3D scanning with the rotating gantry, the delivered beam-spot size and beam distribution inside the spot at the isocenter should be kept constant independently of the rotating angle. Therefore, NIRS proposed a compensation method of an asymmetric phase-space distribution for a slowly extracted beam from the synchrotron [26], which utilizes a multiple scattering through a thin foil set in a position having an optimized beta function along a transport line before the gantry entrance. The proposed method is an essential technology for an efficient treatment through the 3D scanning with the rotating gantry. From an experiment result, it is found that the design parameters should be optimized with taking account of undesired multipole fields in the transport line as well as the extracted beam characteristics from the synchrotron. For the purpose, thus, a beam model is designed. The beam model parameters are obtained by fitting with the measured beam profile data.

4.3.3 New Treatment Research Facility

The next-generation beam delivery technologies have been developed as the new treatment research project in NIRS, since 2006. These technologies should be finally verified by the clinical study. NIRS, therefore, constructed the new treatment research facility, which is connected with the existing HIMAC accelerator. In the treatment hall, placed beneath the facility, three treatment rooms are prepared in order to treat more than 800 patients per year. Two of them are equipped with fixed beam delivery systems in both the horizontal and vertical directions, while the other one is equipped with a rotating gantry. A

treatment-simulation room is also prepared for patient positioning as a rehearsal place and for observing any changes of target size and shape with x-ray CT during the entire treatment. Furthermore, six rooms are devoted to patient preparation just before irradiation. A bird's-eye view of the new treatment research facility with the HIMAC is shown in Fig. 4.18.

In order to carry out the clinical study in a manner identical to the existing HIMAC treatment, the required residual range should be more than 25 cm. Thus, the maximum ion energy is designed to be 430 MeV/n in the fixed beam delivery system, corresponding to the residual range of 30 cm in a carbon-ion beam and that of 22 cm in an oxygen-ion beam. The maximum lateral field and SOBP sizes are 22 cm × 22 cm and 15 cm, respectively, in order to cover all treatments with the HIMAC. The rotating gantry system employs a maximum energy of 430 MeV/n, a maximum lateral field of more than 18 cm × 18 cm, and a maximum SOBP size of 15 cm.

After the preclinical study using the beam delivery system in the new treatment research facility constructed, the clinical study has been conducted since May 2011. In the first year, one of the treatment rooms in the new facility opened for 11 patients from May to July 2011. In this stage, the treatments of all patients were carried out with the range shifter scan, and their irradiation areas were verified by PET imaging with the autoactivation method. After preparing the second room, as the second stage, 535 patients were treated through the half-day (3 h) operation with two treatment rooms from September 2012 to August 2014. In this stage, the hybrid depth scan has been applied for slice change. As the third stage, the respiratory-gated irradiation with the PCR method is scheduled for the moving-tumor treatment. Further, the treatment with the rotating gantry will be initiated from 2016 after the commissioning in 2015.

4.4 Standard Carbon-Ion RT Facility

For widespread use of carbon-ion RT in Japan, NIRS designed a standard carbon-ion RT facility, which was a downsized version of the HIMAC facility, in order to reduce the construction cost. NIRS, further, developed the key technologies for these facilities from 2004 and 2005. GHMC (Gunma University Heavy-Ion Medical Center), in collaborating with NIRS, started construction of a pilot facility of standard carbon-ion RT facility in 2006, which can be downsized to one-third compared with the HIMAC facility. Treatments with the pilot facility have been successfully carried out since March 2010.

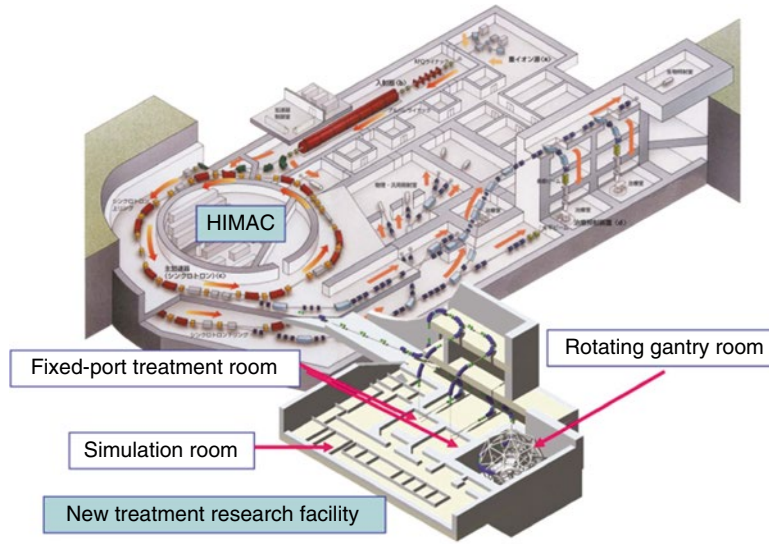

Fig. 4.18 The bird's-eye view of the new treatment research facility with HIMAC

4.4.1 Design Consideration

The statistics for the 15-year treatment period with HIMAC were utilized to determine the specifications, which may indicate reasonable clinical requirements of treatment beam properties for carbon-ion RT.

4.4.1.1 Residual Range

The residual range is defined as the water-equivalent depth that the beam can penetrate after it has passed through the necessary beam-modifying devices. It is found from the HIMAC treatment statistics that a residual range of 25 cm in water may cover most of the patients. The residual range depends not only on the beam energy but also on the field-formation method. In the broad-beam methods such as the beam-wobbling and double-scatterer methods, range loss is caused mainly by the scatterer. The maximum residual range is estimated to be 26 cm. In the pencil-beam scanning method, on the other hand, range loss can be minimized, and for HIMAC, the residual range is typically 27 cm in water for a 400 MeV/n carbon beam.

4.4.1.2 Field Size and SOBP

A lateral-field diameter of 22 cm and a longitudinal-field extent or SOBP size of 15 cm can cover almost all types of patients treated with HIMAC. A larger field size of more than 20 cm is required mainly for the treatment of oblong tumors. In such cases, it is important to maintain the field length rather than the diameter. The field-patching method has been employed for a target size of more than 22 cm in diameter. The SOBP size should range from 4 to 15 cm.

4.4.1.3 Dose Rate

For HIMAC, the irradiation dose rate is required to be 5 GyE/min/*l* so as to complete the fractional irradiation course within a tolerable time [1]. When one gives a certain biological dose, the ion number delivered to the surface of a patient is inversely proportional to the surface physical dose (LET) and the ratio (R) of biological dose on the mid-SOBP and the physical dose to the surface. For example, the LET of 400 MeV/n carbon-ion is around 10 keV/μm, and the R of carbon-ion is estimated to be 2.2–2.3. In carbon-ion RT using broad-beam methods, the dose rate of 5 GyE/min/*l* (10 cm × 10 cm × 10 cm) corresponds to around 10^9 particles per second (pps) of beam intensity required at the entrance of a beam delivery system, under a beam-utilization efficiency of around 20 % in the beam delivery system.

4.4.1.4 Number of Annual Treatments

The number of annual treatments should be increased as high as possible, due to an economical reason. The number of annual treatments N_T is obtained as

$$N_T = \left(Ns \times Nroom\right) / F, \tag{4.1}$$

where Ns is the number of annual sessions per room, Nroom the number of treatment rooms, and F the average fraction number. The Ns, further, is given as

$$N_S = H_T \times D_W / T_{OCC}, \tag{4.2}$$

where H_T is the daily treatment hours, DW the annual working days, and T_{OCC} one fractional treatment time corresponding to an occupancy time of a treatment room per patient. The H_T is given by subtracting the daily QA hours from the daily working hours.

$$\begin{aligned} T_{OCC} = {} & Tpos\left(\text{positioning time}\right) \\ & + Tirr\left(\text{irradiation time}\right) \\ & + Tsetup\left(\text{setup time}\right). \end{aligned}$$

Assuming the F of 12, the H_T of 6 h, the D_W of 240 days, the T_{OCC} of 25 min, and Nroom of 3, the N_T is estimated to be 864 pts per year. It is noted that this Tocc value is given without the automatic patient positioning technique. When one utilizes the automatic patient positioning technique, the N_T is expected to be increased to 1080 pts/year under the T_{OCC} of 20 min. Estimations of the annual treatment numbers under various conditions are summarized in Table 4.1.

4.4.2 Pilot Facility

Just after completing a design study and R&D works for standard-type C-ion RT facility in Japan, in 2006, it was approved by Japanese gov-

Table 4.1 Estimation of annual treatment number under various conditions, H: Horizontal beam line; V: Vertical beam line; R: Fully rotational beam line

	Conventional	Auto-pos and 3D scan	Auto-pos and 3D scan and R-gantry
N_{room}	3; H&V, H,V	3; H&V, H,V	2: H & R-Gantry
T_{occ}	22	14	14/11
$Ns \times N_{room}$	11,700	18,500	14,000
N_T:	980	1,540	1,170

Table 4.2 Specifications of standard C-ion RT facility

Ion species	Carbon
Energy	400–140 MeV/n
Range/SOBP/lateral size	250/40–150/220 mm
Max. dose rate	5 GyE/min/*l*
Beam intensity	$1.2 \cdot 10^9$pps
Treatment room	3: H&V, H, V
Irradiation method	Gating/layer stacking

ernment that a pilot facility was constructed in Gunma University. According to the design consideration mentioned in the previous section, the specifications of a pilot facility are determined as summarized in Table 4.2.

On the basis of the design study and R&D works for the standard C-ion RT facility in Japan [2], its pilot facility was designed as follows. The facility consists of an ECR ion source, an RFQ and an APF-IH linac cascade, a synchrotron ring, three treatment rooms, and one experimental room for basic research. In this pilot facility, a C^{4+} beam, which is generated by a compact 10-GHz ERC source, is accelerated to 4 MeV/n through the injector cascade consisted of the RFQ and APF-IH linacs. After the C^{4+} beam is fully stripped by a thin carbon foil, the C^{6+} beam is injected into the synchrotron through the multi-turn injection scheme and is accelerated up to a maximum of 400 MeV/n. All magnets in the beam transport lines are made of laminated steel in order to permit a change in the beam line within 1 min. The beam delivery system employs a spiral beam-wobbling method for forming uniform lateral dose distribution with a relatively thin scatterer.

Gunma University constructed of the pilot facility, in collaboration with NIRS. The GHMC (Gunma University Heavy-Ion Medical Center) has successfully carried out totally 985 treatments from March 2010 to December 2013.

4.4.3 Following Projects

Following the pilot facility at GHMC, two additional projects for carbon-ion RT have been progressed in Japan: the Saga-HIMAT (Saga heavy-ion medical accelerator in Tosu) project and the Kanagawa Prefectural one.

The Saga-HIMAT project [27] has constructed a carbon-ion RT facility since February 2010, based on the GHMC facility design. This facility has successfully carried out the cancer treatment since August 2013. Although this facility has three treatment rooms, two of them have been opened with the spiral beam-wobbling method as the first-step operation: the one will be equipped with both the horizontal and vertical beam delivery systems, while the other with both the horizontal and 45° beam delivery systems. As the next step, the third room will be opened, using both the horizontal and vertical beam delivery systems with the fast 3D rescanning method developed by NIRS. The bird's-eye view is shown in Fig. 4.19.

The Kanagawa Prefectural Government has also constructed the carbon-ion RT facility as i-ROCK (Ion-Beam Radiation Oncology Center in Kanagawa) project in the Kanagawa Prefectural Cancer Center. The accelerator system is designed based on the GHMC facility design, but the maximum energy is increased to be 430 MeV/n. The beam delivery system has employed the NIRS scanning design. The i-ROCK prepares four treatment rooms (2:H&V, 2:H), as shown in Fig. 4.20.

4.5 Summary

More than 600,000 persons are diagnosed with cancer every year in Japan, and it is forecasted that this number will continue to rise. In such a situation, following the GHMC facility as a pilot facility of standard version, Saga-HIMAT has been operated since August 2013, and i-ROCK will be opened in 2015. They are constructed

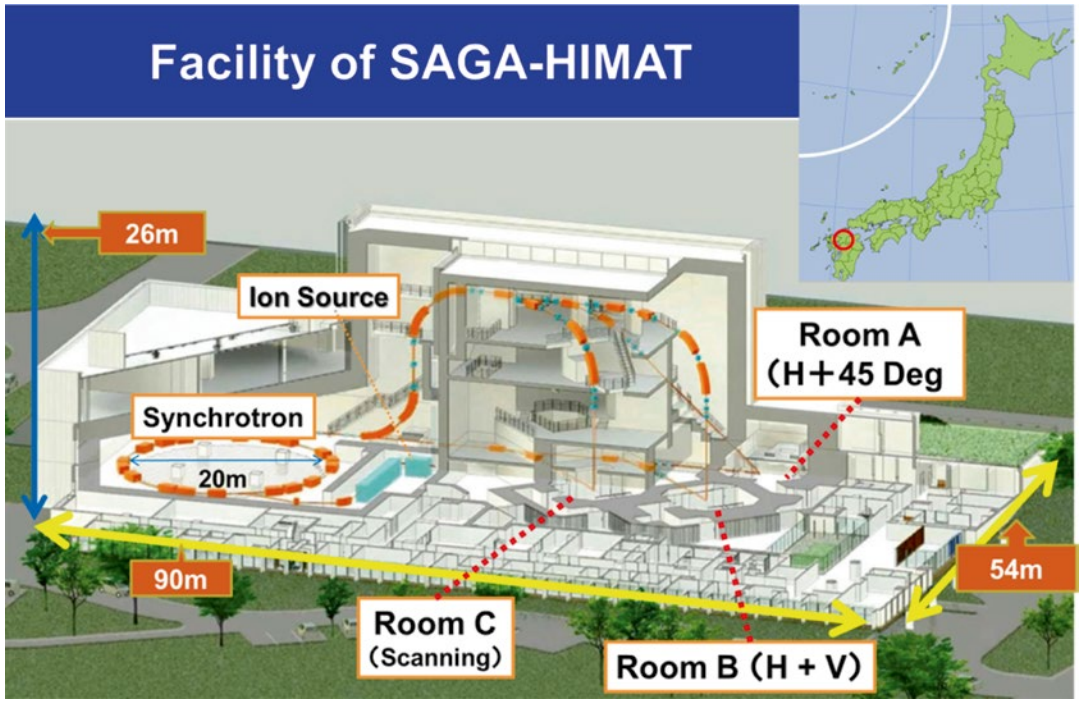

Fig. 4.19 Facility layout of Saga-HIMAT

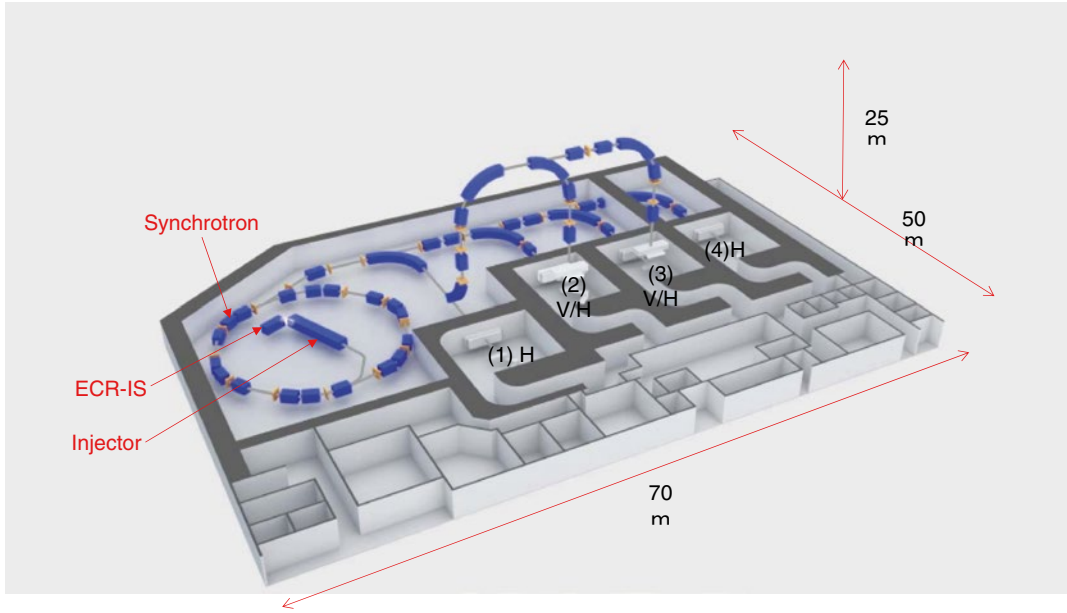

Fig. 4.20 Facility layout of i-ROCK

utilizing both the accelerator and beam delivery technologies developed by NIRS-HIMAC, which are also expected to boost applications of carbon-ion radiotherapy in Japan.

References

1. Hirao Y, Ogawa H, Yamada S, Sato Y, Yamada T, Sato K, Itano A, Kanazawa M, Noda K, Kawachi K, Endo M, Kanai T, Kohno T, Sudou M, Minohara S, Kitagawa A, Soga F, Takada E, Watanabe S, Endo K, Kumada M, Matsumoto S. Heavy ion synchrotron for medical use. Nucl Phys. 1992;A538:541c–50.
2. Noda K, Furukawa T, Fujisawa T, Iwata Y, Kanai T, Kanazawa M, Kitagawa A, Komori M, Minohara S, Murakami T, Muramatsu M, Satou S, Takei Y, Tashiro M, Torikoshi M, Yamada S, Yusa K. New accelerator facility for carbon-ion caner-therapy. J Radiat Res. 2007;48:A43–54.
3. Noda K, Furukawa T, Fujimoto T, Inaniwa T, Iwata Y, Kanai T, Kanazawa M, Minohara S, Miyoshi T, Murakami T, Sano Y, Sato S, Takada E, Takei Y, Torikai K, Torikoshi M. New treatment facility for heavy-ion cancer therapy at HIMAC. Nucl Instrum Methods B. 2008;266:2182–5.
4. Furukawa T, Inaniwa T, Sato S, Minohara S, Noda K, Kanai T. Design study of a raster scanning system for moving target irradiation in heavy-ion radiotherapy. Med Phys. 2007;34(3):1085–97.
5. Inaniwa T, Furukawa T, Kanematsu N, Mori S, Mizushima K, Sato S, Toshito T, Shirai T, Noda K. Evaluation of hybrid depth scanning for carbon-ion radiotherapy. Med Phys. 2012;39(5):2820–5.
6. Furukawa T, Inaniwa T, Sato S, Shirai T, Mori S, Takeshita E, Mizushima K, Himukai T, Noda K. Moving target irradiation with fast rescanning and gating in particle therapy. Med Phys. 2010;37(9):4874–9.
7. Furukawa T, Inaniwa T, Sato S, Shirai T, Takei Y, Takeshita E, Mizushima K, Iwata Y, Himukai T, Mori S, Fukuda S, Minohara S, Takada E, Murakami T, Noda K. Performance of the NIRS fast scanning system for heavy-ion radiotherapy. Med Phys. 2010;37(11):5672–82.
8. Lomax AJ. Intensity modulation methods for proton radiotherapy. Phys Med Biol. 1999;44:185–205.
9. Inaniwa T, Kanematsu N, Furukawa T, Hasegawa A. A robust algorithm of intensity modulated proton therapy for critical tissue sparing and target coverage. Phys Med Biol. 2011;56:4749–70.
10. Torikoshi M, Monohara S, Kanematsu N, Komori M, Kanazawa M, Noda K, Miyahara N, Itoh H, Endo M, Kanai T. Irradiation system for HIMAC. J Radiat Res. 2007;48:A15–25.
11. Kanai T, Furusawa Y, Fukutsu K, Itsukaichi H, Eguchi-Kasai K, Ohara H. Irradiation of mixed beam and designing of spread-out Bragg peak for heavy-ion radiotherapy. Radiat Res. 1997;147:78–85.
12. Chu WT, Ludewigt BA, Renner TR. Instrumentation for treatment of cancer using proton and light-ion beams. Rev Sci Instrum. 1993;64(1993):2055–122.
13. Minohara S, Kanai T, Endo M, Noda K, Kanazawa M. Respiration gated irradiation system for heavy-ion radiotherapy. Int J Radiol Oncol Biol Phys. 2000;47:1097–103.
14. Noda K, Kanazawa M, Itano A, Takada E, Torikoshi M, Araki N, Yoshizawa J, Sato K, Yamada S, Ogawa H, Itoh H, Noda A, Tomizawa M, Yoshizawa M. Slow beam extraction by a transverse RF field with AM and FM. Nucl Inst Methods Phys Res A. 1996;374:269–77.
15. Kanai T, Kanematsu N, Minohara S, Komori M, Torikoshi M, Asakura H, Ikeda N, Uno T, Takei T. Commissioning of a conformal irradiation system for heavy-ion radiotherapy using a layer-stacking method. Med Phys. 2006;33:2989.
16. Yonai S, Kanematsu N, Komori M, Kanai T, Takei Y, Takahashi O, Isobe Y, Tashiro M, Koikegami H, Tomita H. Evaluation of beam wobbling methods for heavy-ion radiotherapy. Med Phys. 2008;35:927.
17. Komori M, Furukawa T, Kanai T, Noda K. Optimization of spiral wobbler system for heavy-ion radiotherapy. Jpn J Appl Phys. 2004;43:6463–7.
18. Kanai T, Kawachi K, Kumamoto Y, Ogawa H, Yamada T, Matsuzawa H, Inada T. Spot scanning system for proton radiotherapy. Med Phys. 1980;7:365–9.
19. Pedroni E, Bacher R, Blattmann H, Boehringer T, Coray A, Lomax A, Lin S, Munkel G, Scheib S, Schneider U, Tourovsky A. The 200-Mev proton therapy project at the Paul Scherrer Institute: conceptual design and practical realization. Med Phys. 1995;22:37–53.
20. Haberer T, Becher W, Shardt D, Kraft G. Magnetic scanning system for heavy ion therapy. Nucl Instrum Methods A. 1993;330:296–305.
21. Iwata Y, Noda K, Shirai T, Murakami T, Furukawa T, Mori S, Fujita T, Itano A, Shouda K, Mizushima K, Fujimoto T, Ogitsu T, Obana T, Amemiya N, Orikasa T, Takami S, Takayama S, Watanabe I. Design of a superconducting rotating gantry for heavy-ion therapy. Phys Rev ST Accel Beams. 2012;15:044701.
22. Sato S, Furukawa T, Noda K. Dynamic intensity control system with RF-knockout slow-extraction in the HIMAC synchrotron. Nucl Instr Methods A. 2007;574:226.
23. Inaniwa T, Furukawa T, Sato S, Tomitani T, Kobayashi M, Minohara S, Noda K, Kanai T. Development of treatment planning for scanning irradiation at HIMAC. Nucl Instrum Methods B. 2008;266:2194.
24. Iwata Y, Kadowaki T, Uchiyama H, Fujimoto T, Takada E, Shirai T, Furukawa T, Mizushima K, Takeshita E, Katagiri K, Sato S, Sano Y, Noda K. Multiple-energy operation with extended flattops at HIMAC. Nucl Intsrum Methods A. 2010;624:33.
25. Eickhoff H, Haberer Th, Schlitt B, Weinrich U. Hicat-the german hospital-based light ion cancer therapy project. Proc. EPAC04, 2004;290–4.
26. Furukawa T, Noda K. Compensation of the asymmetric phase–space distribution for a slowly extracted beam from a synchrotron. Nucl Intsrum Methods A. 2006;565:430.
27. Kanazawa M, et al. Saga-HIMAT project for carbon ion radiotherapy. Proceedings of 8th annual meeting of Particle Accelerator Society of Japan, Tsukuba, p.161–4.

5 Physical Rationale for Proton Therapy and Elements to Build a Clinical Center

A. Mazal, N. Fournier-Bidoz, F. Goudjil, S. Delacroix, C. Nauraye, L. DeMarzi, C. Mabit, I. Pasquié, M. Robilliard, A. Patriarca, C. Wessels, C. Alapetite, S. Helfre, H. Mammar, S. Bolle, V. Calugarou, L. Feuvret, J.L. Habrand, L. Desjardins, R. Dendale, and A. Fourquet

5.1 Introduction

In this chapter we present:

I. The physical bases of proton therapy, going from microscopic concepts to macroscopic features
II. The technology and the logistics, which evolve to more and more compact and cheaper facilities with the capability to perform adaptive radiation therapy
III. The most usual clinical indications, moving toward (nearly) all indications of radiation therapy
IV. Some research orientations, rediscovering physics, and radiation biology
V. Basic elements to conceive and build a clinical center
VI. Conclusions: The need to learn from others and also to innovate

A. Mazal (✉) • N. Fournier-Bidoz • F. Goudjil
S. Delacroix • C. Nauraye • L. DeMarzi • C. Mabit
I. Pasquié • M. Robilliard • A. Patriarca • C. Wessels
C. Alapetite • S. Helfre • H. Mammar • V. Calugarou
L. Desjardins • R. Dendale • A. Fourquet
Department of Radiation Oncology, Institut Curie, Paris, France
e-mail: alejandro.mazal@curie.fr

S. Bolle
Department of Radiation Oncology, Institut Gustave Roussy, Villejuif, France

L. Feuvret
Department of Radiation Oncology, Hôpitaux de Paris – Pitié Salpêtrière, Paris, France

J.L. Habrand
Department of Radiation Oncology, Centre François Baclesse, Caen, France

5.2 Physical Bases of Proton Therapy

After a seminal paper from Wilson on the potential use of protons to treat cancer [1], Koehler and Raju presented a visionary graph (Fig. 5.1 [2]) showing the physical selectivity of different types of beams versus their biological properties, represented by the linear energy transfer (LET) or density of ionization. A third variable was also shown: the importance of the cost to produce those kinds of tools.

While protons are at present rapidly evolving, the use of pions has been already stopped, and neutrons are nearly disappearing, but they provide a full set of data on radiobiology for the use of particles heavier than protons. Several reviews have been published these last years concerning the basis, indications, and the technology in proton therapy [3].

When considering the basic physical interactions of charged particles with matter, we can

A.K. Rath, N. Sahoo (eds.), *Particle Radiotherapy: Emerging Technology for Treatment of Cancer*,
DOI 10.1007/978-81-322-2622-2_5

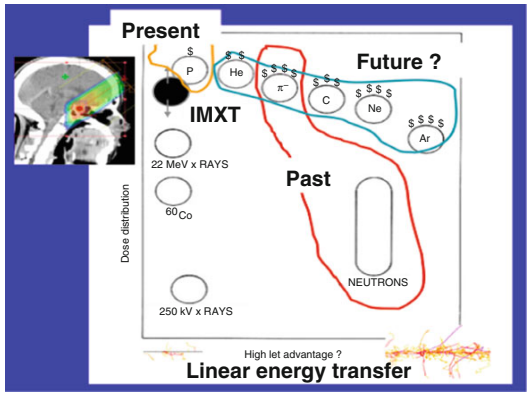

Fig. 5.1 Physical selectivity vs. linear energy transfer (*LET*) (radiobiological advantage) and cost for different types of beams and techniques (Modified from Raju [2])

take into account mainly three "collisions" in the range of energies for clinical applications (up to around 250 MeV for protons):

1. Nuclear interactions
2. Inelastic collisions with electrons
3. Multiple Coulomb scattering by the nucleus

5.2.1 The Nuclear Interactions

The inelastic collisions of the incident protons and heavier ions with the nucleus of the atoms at the target (Fig. 5.2) generate the following as secondary particles and with some associated consequences.

(a) Neutrons (that will add secondary dose to patients and will be at the origin of large shielding in the accelerator, beam transport components, and treatment rooms)
(b) Fragments (that will create a "tail" of dose in depth with high biological effects)
(c) Scattered protons at large angles (increasing the lateral penumbra of clinical beams)
(d) Activation of accelerators, beam lines, and devices (affecting servicing and decommissioning) as well as tissues in the patient (leading to methods for in vivo dosimetry and/or range verification based on PET measurements or gamma prompt detection)

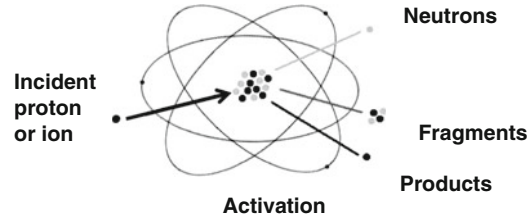

Fig. 5.2 Nuclear interactions through inelastic collisions between an incident charged particle and a nucleus in the range of energies used for clinics (e.g., up to 250 MeV with protons), producing secondary particles and activation

As a consequence of these nuclear interactions, the number of incident particles is reduced when entering a matter (e.g., the patient). A typical value is a reduction in the flux of particles of 1 % per cm of water equivalent tissues (Fig. 5.3).

5.2.2 The Inelastic Collisions with Electrons: The Dose and the Bragg Peak

The collisions of the incident protons with the electrons of the matter produce ionization and excitation (Fig. 5.4) and thereby what is of interest in clinical applications: the energy deposition reported to a volume, defined as the dose.

When analyzing the particle trajectories in a media such as the tissues, it is of the highest interest to evaluate the stopping power ($S = dE/dx$), the amount of energy released per unit of length.

The mathematical expression of the stopping power has a dependence on the inverse of the speed of the particle squared, what in practice means is that it increases when the speed decreases, creating its maximum at the end of the range of particle.

As a combination of the decrease in the number of particles in depth in the tissues and the increase of the stopping power also with depth, the deposited dose has an entrance plateau followed by a peak (called the Bragg peak). After the peak, there is a sharp descending gradient till no dose is delivered in the tissues (Fig. 5.5). The depth of this peak can be increased by increasing the energy of the incident particle.

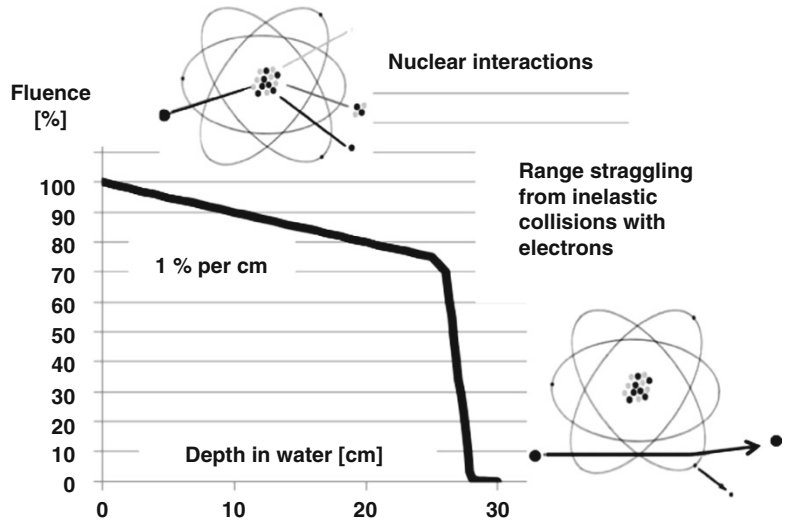

Fig. 5.3 Particle flux reduction in depth in tissues from nuclear interactions of incident accelerated protons. At the end of the initial slope, all the remaining particles have lost enough energy with interactions with the electrons to stop at a given range. The variations in the individual ranges give the final slope for what is called "range straggling"

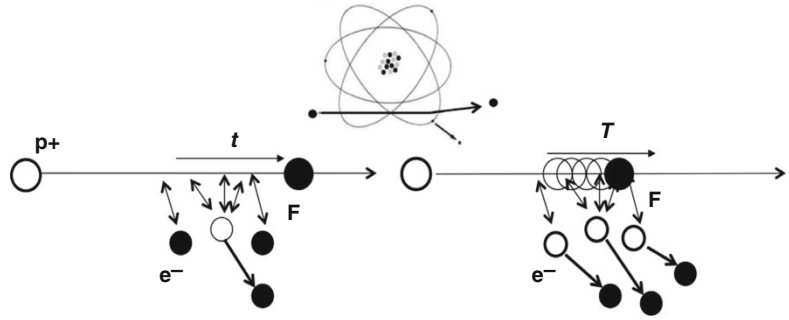

Fig. 5.4 Variation of stopping power with depth. At the entrance of a body, the particles have higher energies, so a (fast) particle spent less time (t) close to the electrons than at the end of the range, when the energy and the speed are lower and the interaction time (T) is longer. In consequence, the "stopping power" is higher at the end of the range, and a larger number of ionizations are produced

Indeed, all charged particles, from electrons to heavy ions (both used for clinical applications), have a Bragg peak but with some different final appearance. For electrons, the scattering of particles hides the peak. For heavier ions, the nuclear interactions create a "tail" after the peak (Fig. 5.6a).

For all the particles heavier than electrons, it is necessary in clinics to increase the region covered by the peak in the target with a weighted superposition of peaks of different energies (Fig. 5.6b). The resulting dose distribution is called a "spread out Bragg peak" or SOBP. A flat dose is obtained at the target, with the negative consequence of increasing the entrance dose.

The additional interest for heavier particles comes from the biological effect related to the high density of ionization in their track and the possibility to produce a differential effect on tumor and healthy tissues.

5.2.3 The Multiple Coulomb Scattering

The elastic scatter of the incident protons by the nucleus cumulates small deviations of the incident particle when traversing matter (Fig. 5.7). This effect is used with scattering foils of high atomic number (e.g., lead) to build "passive

lines." But it also increases the lateral penumbra for both passive and pencil beam scanned beams in tissue. At depths in tissues larger than 20 cm, the penumbra is larger for a proton beam than for a 6–8 MV photon beam as those used for conformal IMRT with fixed or rotational beams.

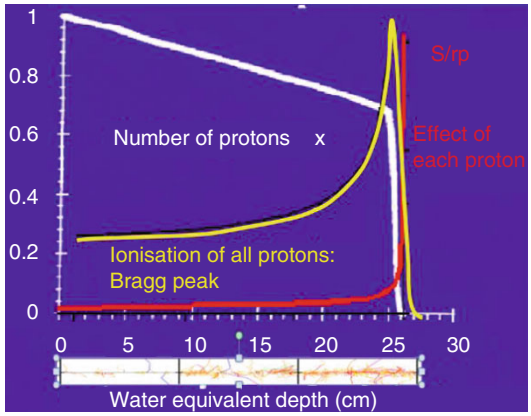

Fig. 5.5 The Bragg peak in the depth dose curve (*in yellow*) in water for a high-energy proton beam (around 200 MeV). The shape is a combination of the number of particles (*in white*) and the stopping power (*in red*). Y-axis is the fraction of the maximum value of the quantity plotted

5.3 Technology and Logistics to Plan and Deliver Proton Therapy

5.3.1 The Beam Characteristics and the Treatment Planning System

From the physical basis described previously, different treatment planning systems have been developed [4]. When simulating a single modulated beam, it is possible to evaluate the advantages and limits of proton beams compared to photon beams, which are traditionally used in clinical applications (Fig. 5.8):

- A proton beam has the advantages of a flat entrance plateau (without a maximum in the beam path), a flat homogeneous dose at the target, a high gradient after the target, and, mainly, no dose after the target.
- But it has limits such as the high entrance dose, the neutron dose around the target, the uncertainty in the range, and the increased lateral penumbra in depth.

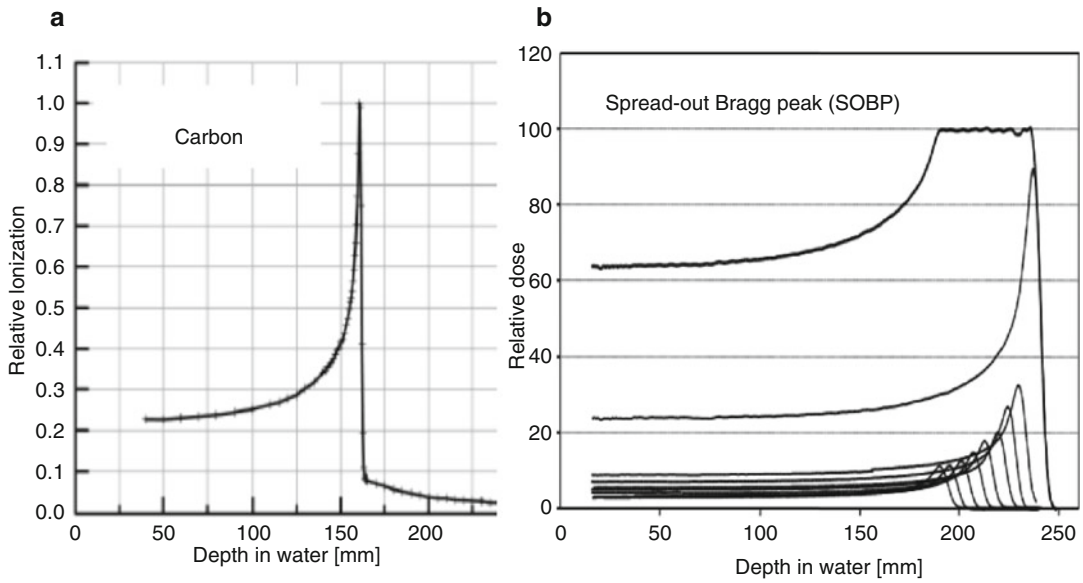

Fig. 5.6 (**a**) Bragg peak for a carbon beam, showing the fractionation tail after the peak (Extracted from M. Moyers, PTCOG meeting 2008); (**b**) superposition of Bragg peaks of proton beams with different energies to build a spread out Bragg peak (SOBP) covering a target with a given thickness in depth (Modified from H. Kooy, personal communication, 2013)

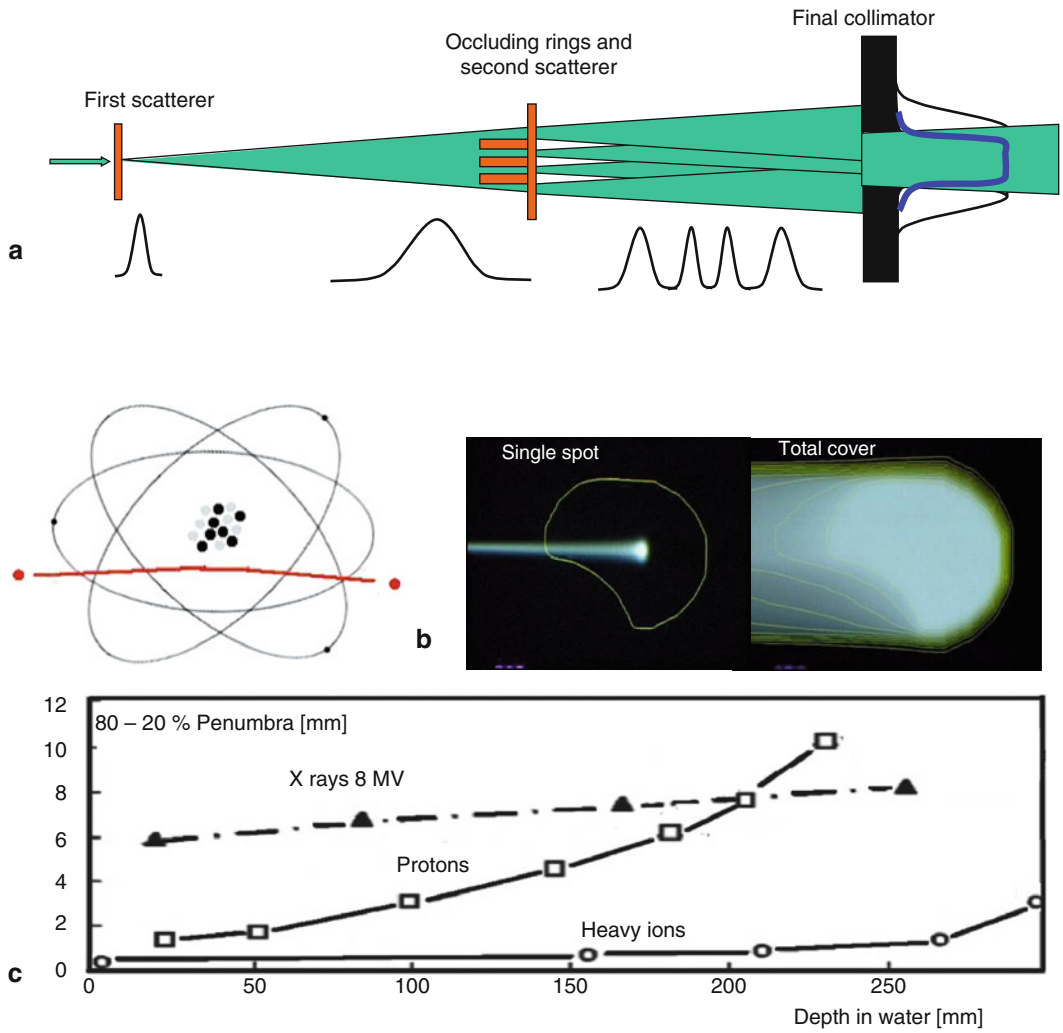

Fig. 5.7 Effect of multiple Coulomb scattering by the nucleus. (**a**) The deviation of the incident particles can be used to build "passive lines" by increasing the initial small Gaussian beam size with simple or double scattering systems. (**b**) The mushroom shape of a pencil beam, given by the multiple scatter, will be scanned to cover a given target. (**c**) Final lateral penumbra (20–80 % on lateral profiles) vs. depth in tissue for protons and heavier ions compared to photon beams used in radiation therapy. Mixed graphs (Courtesy from T. Lomax, PSI, N. Schreuder, and own figures)

In general, several beam directions are adopted (Fig. 5.9), each one with an optimized range, modulation, and compensation (or equivalent dynamic approaches).

5.3.2 The Technological Development

The approach to increase the use of protons in radiation therapy could not have been possible without a very strong development in technology of accelerators, beam transport, delivery, and control systems (Fig. 5.10). The first pioneering facilities in the 1960s used to work with very large accelerators [5] originally conceived for research in physics and built mainly by research laboratories in cooperation with specific companies. In the 1990s, the first clinically oriented devices are conceived in more compact models driven by industrial companies. As an example of this evolution, the synchrocyclotron

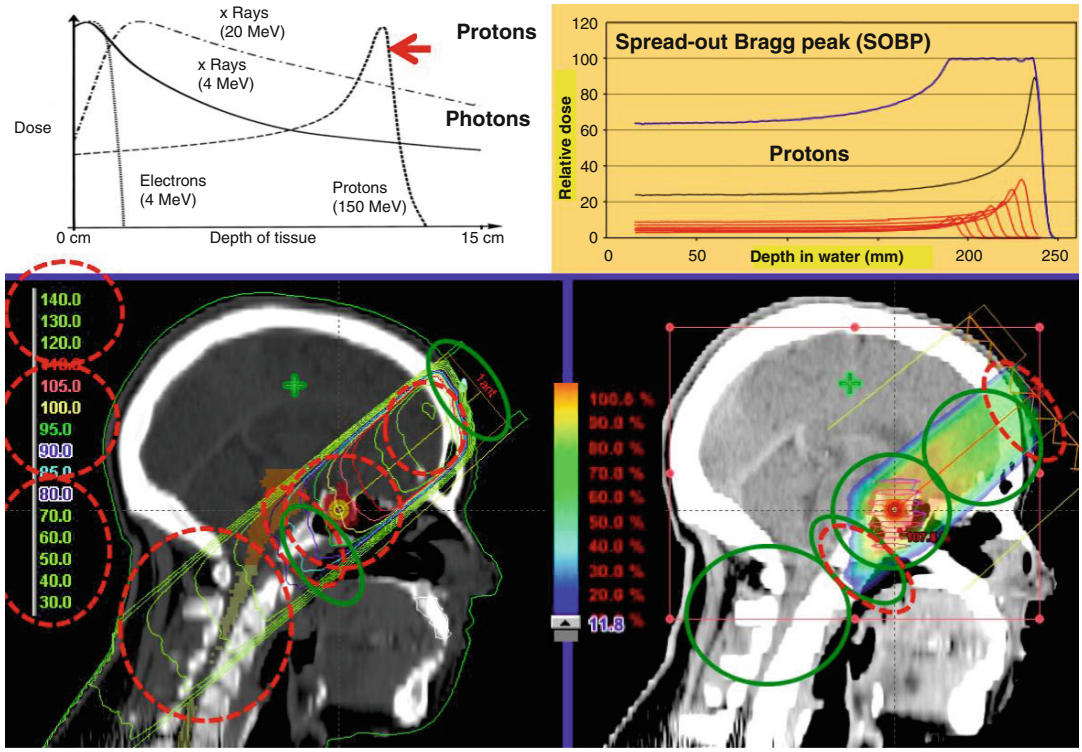

Fig. 5.8 Some advantages (*in green circles*) and limits (*in red*) of a single beam of energy modulated protons (spread out Bragg peak) (*at the right*), compared to a single photon beam (*at the left*) incidents on an intracranial target at the base of the skull. (SOBP: courtesy of N. Schreuder, Software: Eclipse, Data: IBA, calculations: A. Mazal)

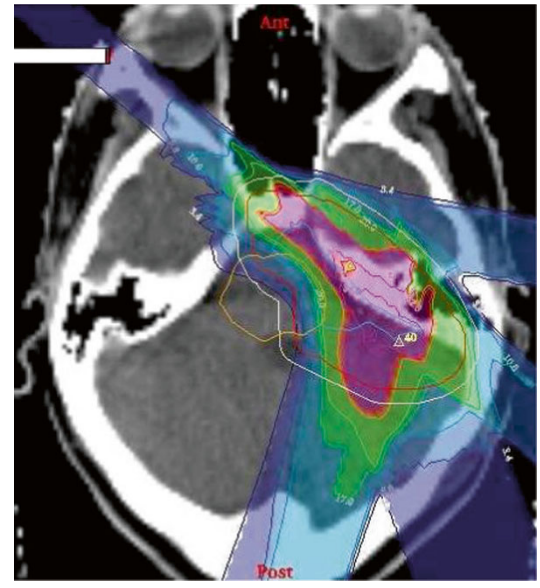

Fig. 5.9 Combination of different incidences of proton beams in anatomical regions with complex inhomogeneities. A treatment plan can include combination of photons and protons as well as "patches" where one beam irradiates part of the target and its distal edge superposes the lateral penumbra of a second beam that irradiates the rest of the target (Calcs L. de Marzi. Software Dosisoft)

in Orsay, France, with 900 ton of weight for the magnetic circuit, was built initially by Philips in 1958, reshaped by the Nuclear Physics Institute in 1975, adapted for clinics in 1991, and replaced in 2010 by a new, more compact system.

Clinical particle accelerators are completed with beam transport systems toward several treatment rooms with fixed lines (horizontal, vertical, oblique) or isocentric gantries (able to turn the beam around the patients [8]). They can deliver the beam in the required direction toward the patient. For both fixed and gantry lines, there is a beam modifying system called "nozzle" to shape and monitor the beam (Fig. 5.10).

The technical evolution of proton therapy at present goes toward more and more compact machines, mainly based on cryogenics and very high magnetic fields, conceived in their simplest and cheaper approach to provide beam toward a single treatment room. Other solutions are under development based on high gradients of electric fields to produce compact linacs for proton therapy.

More futuristic and still to be economically and clinically proven, at least two axes of the study have been developed:

(a) The dielectric wall accelerator (DWA), conceived at the Lawrence Livermore Laboratory in USA, using strong isolators and light-based excitation of dielectrics to produce the particle acceleration through "Blumline cells" with expected gradients of 100 MeV/m [6]
(b) The laser-based proton acceleration, where high-intensity pulses of a laser beam incident on a target produce a mechanical separation of charges and electric fields of TV/m in a very small space [7]

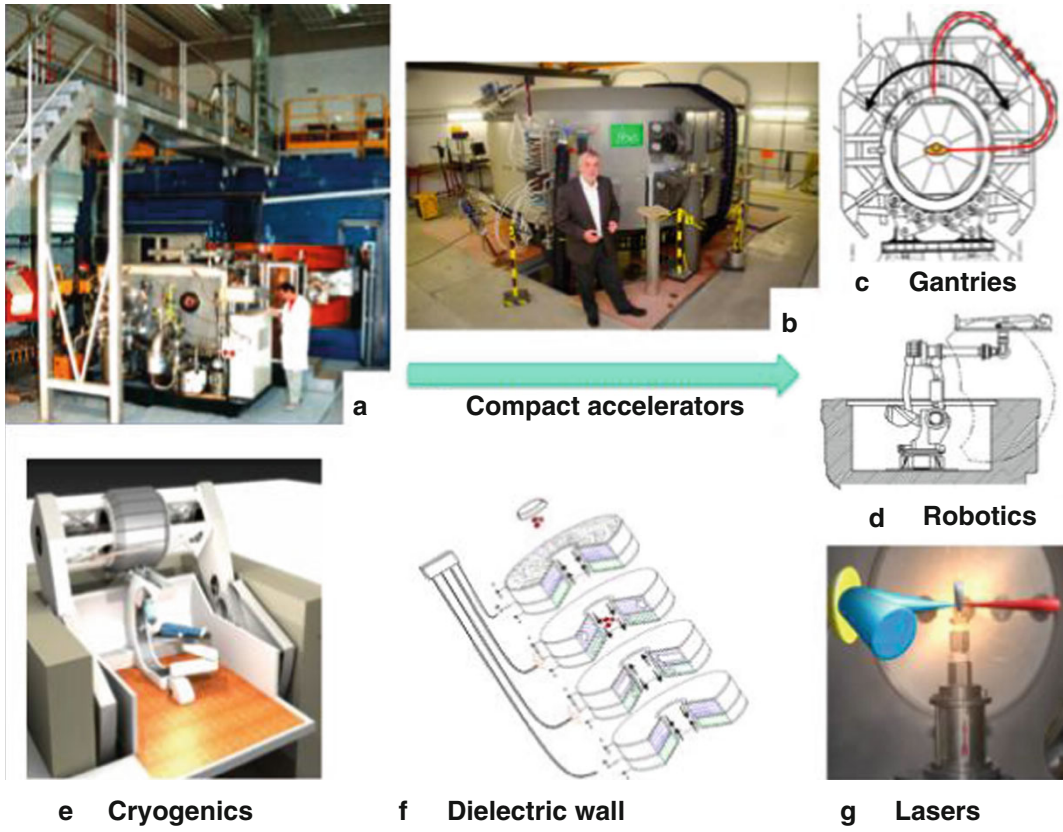

Fig. 5.10 Technical evolution of accelerators and beam transport for proton therapy: (**a**) 900 T synchrocyclotron from Orsay, devoted to clinical applications since 1991, (**b**) cyclotron producing 230 MeV protons developed for proton therapy by the industry (Courtesy of IBA), (**c**) isocentric gantry to transport the beam in any direction around the patient, (**d**) robotic patient positioning system at Orsay, (**e**) compact cryogenic accelerator mounted on the gantry for single treatment room approach (Mevion, USA), (**f**) principle of dielectric wall cells to produce compact linear accelerators [6], and (**g**) high-intensity laser-based proton acceleration principle [7]

Both approaches still need to be fully developed, and the feasibility of their clinical use has still not been attained.

5.3.3 The Patient Positioning: Robotics and Imaging

The planning and delivery of a high precision dose distribution with particles or photons would not be possible without a corresponding image-guided system. The roots of such a system are the existing imaging devices as those in use in a diagnostic department (Fig. 5.11). From these original images, there is a phase of calculation and simulation of a treatment by combining multimodalities, setting a segmentation of target and critical organs, and modeling the beams. At the end of this process, imaging systems are also installed and used at the treatment room itself to set up and monitor the patient positioning, giving the required tools to implement adaptive therapy (Fig. 5.12). The imaging system is complemented with the use of robotic approaches for patient positioning [9], providing a full 6D capability with ancillary tools and functions such as multiple supports (couch, chairs, phantoms, detectors), trajectories, compensation of loads, etc.

5.3.4 The Management of the Range Uncertainty

A particular source of uncertainty when treating with protons is the real position of the distal falloff when crossing complex inhomogeneities in the

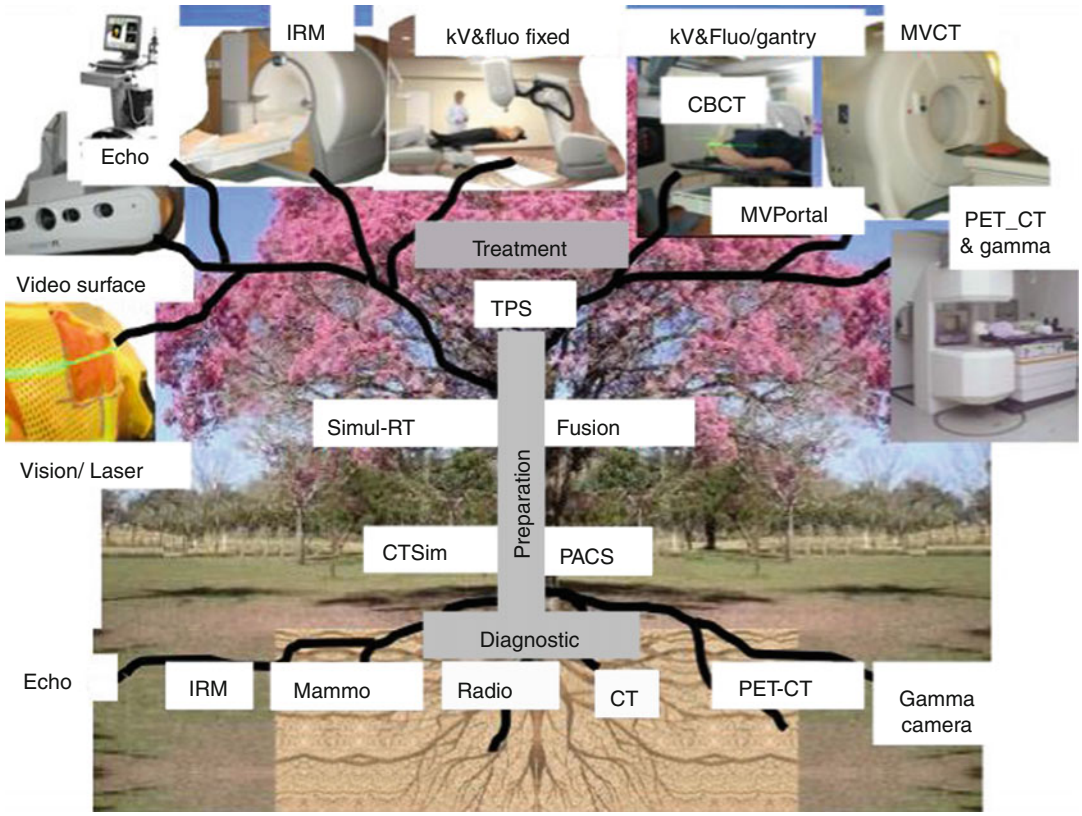

Fig. 5.11 Image-guided radiation therapy (IGRT) represented by a tree scheme; the images are produced since the diagnostic phase of a treatment (*the roots*), passing through the preparation of the treatment and ending at the treatment room (*the branches*), for patient positioning and dose monitoring. The functionality of each system evolves to warrant the quality of the full process, increasing the resolution, reducing the dose, including 4D acquisition, and providing the tools to adapt the treatment when needed, in particular for changes in the anatomy, tumor response, and practical issues on beam delivery

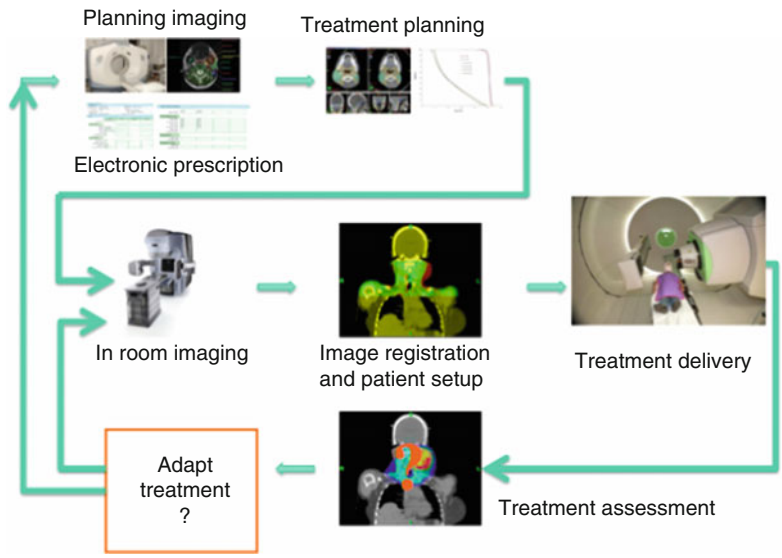

Fig. 5.12 The workflow of adaptive radiation therapy (Courtesy G. Olivera & D. Galmarini, 21st Century, USA)

body [10]. Several systems under development or already in clinical use to reduce these uncertainties and take them into account when planning, delivering, and adapting the treatment (Fig. 5.13) are described below.

(a) The use of the latest advances in imaging such as reconstructing tools and the use of dual energy CT acquisition: They reduce artifacts and provide a more accurate relationship between Hounsfield units and stopping power, optimizing the calculation of the proton beam range in clinical images.
(b) The evaluation of the tissue activation by nuclear interactions of the charged particles: Initially proposed for carbon beams, through the use of a PET camera in or outside the treatment room, the concept has been extended also to proton beams. By comparing the calculated image of activation with the measured one, it is possible to infer if the delivered dose is the one aimed at.
(c) The detection of prompt gammas also produced by nuclear interactions, with a single or multiple slits camera: With this approach, it is possible to estimate the position of each individual Bragg peak delivered with pencil beam scanning.
(d) The acquisition of high-energy proton radiography, with a beam able to cross through the patient with a very small dose: With this approach, the integrated stopping power can be estimated for each ray. By multiplying the incidences, it is possible to reconstruct a proton tomographic image.
(e) Preparing for the worst case: Due to the sharp dose falloff, a misalignment might lead to significant underdosage of the tumor volume or severe overdosage of the normal tissue. Expecting such a misalignment using probabilistic approaches, it is possible to create a plan that guaranties the "success" of a treatment. The so-called robust optimization has nevertheless a trade-off, which can be phrased in a single question: won't we do worse in the absence of the worst-case scenario [11]?

5.4 Most Usual Clinical Applications

The clinical applications for proton therapy are presented here only as an introduction to what is developed in the following chapters of this book. They include at present two groups of locations:

(a) Well-accepted sites where protons are considered the tool of choice (Fig. 5.14): ophthalmic tumors (uveal and iris melanomas and choroidal hemangiomas [12–15]), base of the skull chordomas and chondrosarcomas

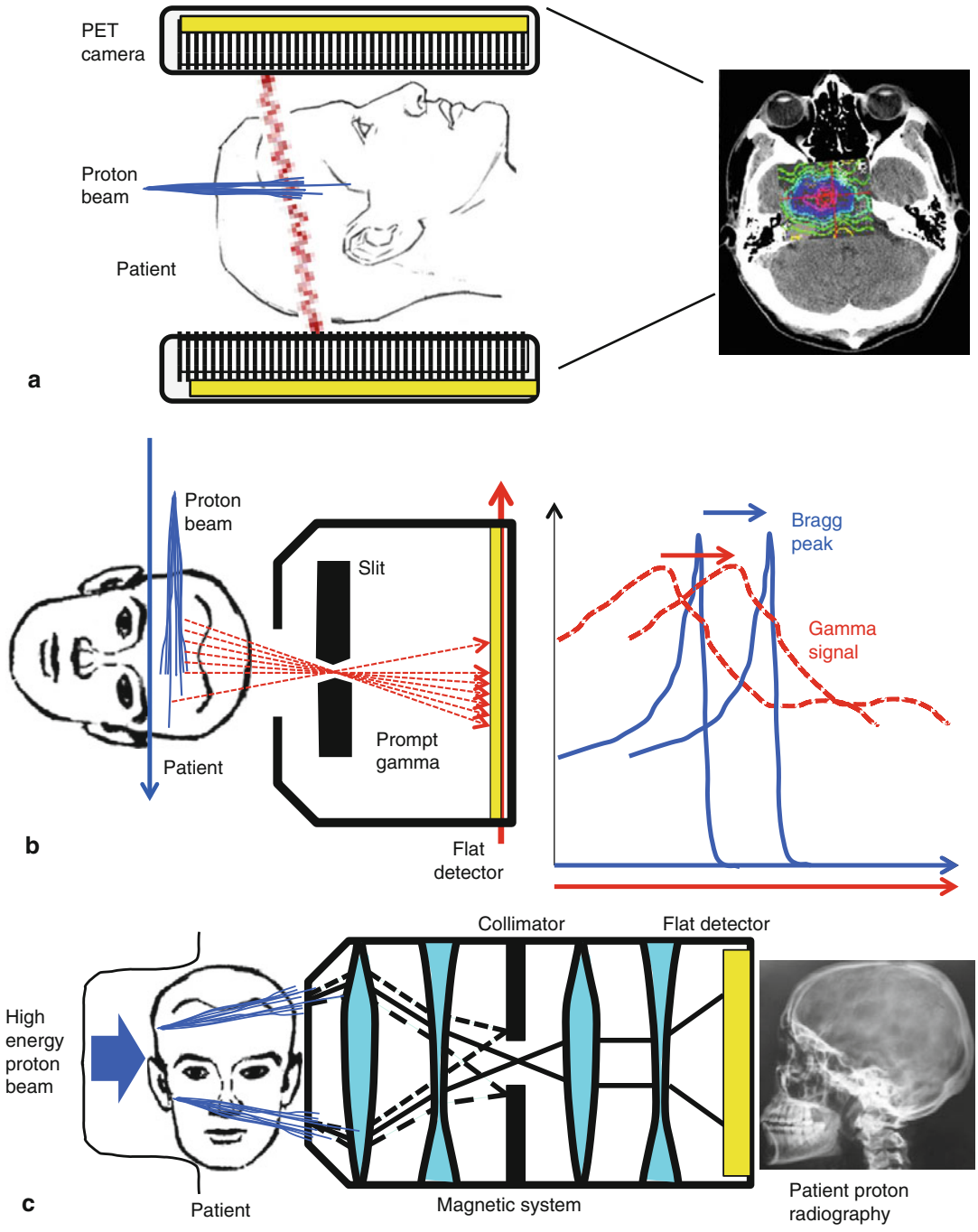

Fig. 5.13 Proposed systems to reduce the uncertainties in dose delivery with particle therapy. (**a**) PET measurement of tissue activation by nuclear interactions of the particle beam (Data from W. Enghardt and coworkers, Darmstadt, Germany); (**b**) measurement of the prompt gamma produced also by nuclear interactions of the particle beam in tissues (Data from F. Roellinghoff and coworkers, IBA, Belgium); (**c**) proton radiography with high-energy proton beams (Data from M. Prall and coworkers, GSI, Germany)

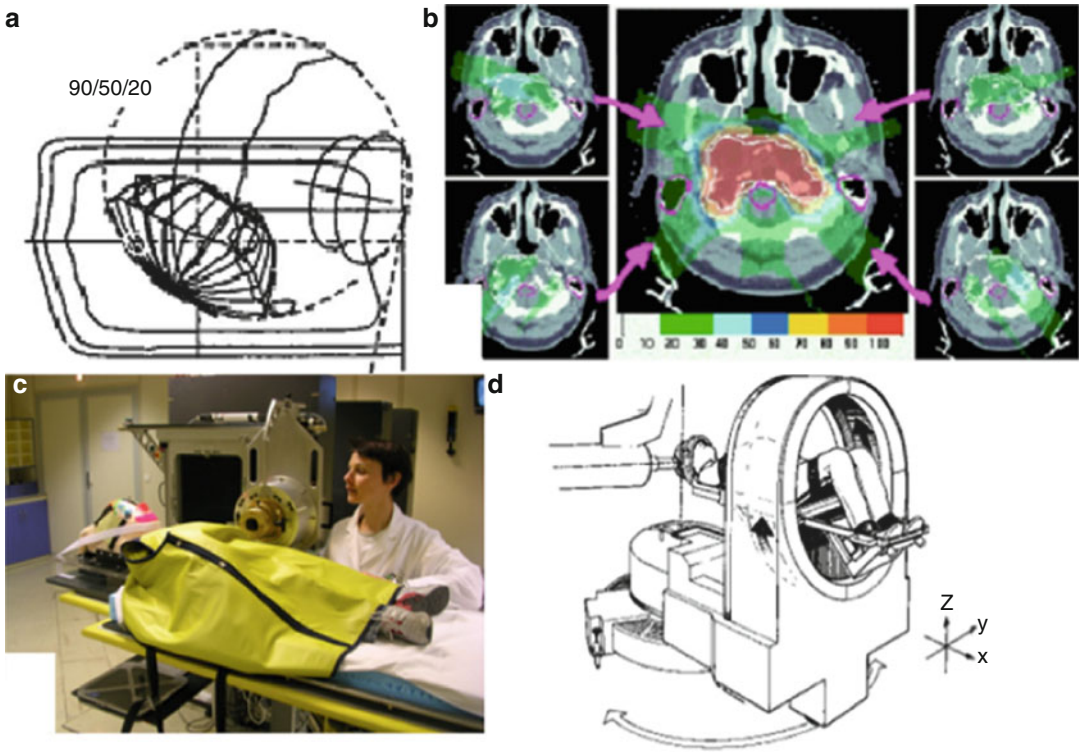

Fig. 5.14 Main recognized clinical indications of proton therapy for some rare diseases. (**a**) Uveal melanoma, (**b**) base of the skull chordomas and chondrosarcomas (Figure courtesy of Trofimov, Boston, USA), (**c**) pediatrics, and (**d**) radiosurgery (Figure courtesy of M. Bousiere, Boston, USA)

[16, 17], pediatrics (in particular CNS tumors [18]), and radiosurgery (in particular for intracranial targets [19])

(b) Other sites, including more common oncological diseases, with already a wide application or under clinical study: the head and neck, lung, sarcomas of the pelvis, prostate, breast, etc.

The rationale for these studies is both the high conformation of the dose distribution to the target, allowing dose escalation studies, and the minimal integral dose to all the other tissues, improving the tolerance to the treatment.

For most of them, the highest rates of local control in radiation therapy have been obtained with proton therapy with the lowest rate of treatment-related complications.

For some cases of radioresistant tumors (e.g., salivary glands and sarcomas), carbon therapy is achieving even better results and shorter treatments with hypo-fractionation, based not only on their physical selectivity but mainly on their biological properties from their high density of ionization and related high RBE (relative biological effectiveness). In other cases, trials are undergoing comparing proton therapy with the most advanced approaches with photon beams (IMRT with IGRT). These clinical studies are complemented with cost-benefit analysis to find the correct place of proton therapy compared to other approaches. A survey of protocols under application can be found at the Particle Therapy Cooperative Group web site (www.ptcog.ch).

5.5 Proton Therapy Research and Development in Physics and Biology

The research and development in the field of proton therapy includes a wide scope of subjects from clinical protocols and translational research

to developments in physics and technology, including a new visit to the bases of radiation biology.

In physics and technology, there is a great effort to reduce the cost and complexity of the clinical use of protons, starting from basic principles or through cumulated experience. As it has been partially presented, research and developmental works are oriented toward the conception of compact systems (using cryogenics to produce high magnetic fields, compact linacs, compact gantries, fast and compact scanning systems) to optimize the practical use of clinical beams (e.g., reducing the uncertainties in the range, optimizing the quality assurance, improving the beam modeling, using robotics for patient positioning and all the tools for image-guided radiation therapy, optimizing the patient throughput).

It is in the field of radiation biology where the most important and innovative improvements can be expected. At the very first level, it is necessary to continue the studies on the radiobiological effectiveness of protons [20, 21] and, mainly, of heavier ions. The use of biological target volumes estimating tumor growth and/or hypoxia through PET imaging but also drug uptake for concomitant treatments is an important field of development, all of them as a pretreatment evaluation and/or in adaptive radiation therapy with both photons and charged particle therapy.

In this global chapter, we want also to show at least three fields of ongoing work in R&D by teams related to the Institut Curie proton center in Orsay, France (Fig. 5.15):

(a) The evaluation of proton mini-beam radiation, such as those produced with synchrotron radiation [22];
(b) The study of potential effect of nanoparticles combined with proton therapy [23];
(c) The use of very high dose rates irradiating clinical targets in very short times with continuous or with pulsed radiation including protons [24, 25].

All of them are in initial phases of R&D or implementation (in vivo, in vitro, phase I of clinical trials, etc.) with photons, electrons, protons, and heavier ions. They should be evaluated carefully for their potential positive and negative effects in radiation therapy.

5.6 Basic Elements to Conceive and to Build a Clinical Center

Based on the previous rationale, different scenarios can be conceived when starting a project to build a proton therapy center. They are determined by the clinical and epidemiological scope of the project, the environment, the partners, the financial resources, and a wide number of other factors. Even if standard technical products are available today, the time to conceive, build, and ramp up the clinical operation of a new center is still longer than usual times for linacs, e.g., in the order of 2 years (or much more) to cover all the phases of a project (Figs. 5.16 and 5.17).

The real starting point is to have a political and financial support, taking into account both the investment and the operating cost, based on a clinical and scientific first scope of the project. It is necessary to evaluate in detail the clinical goals and the technical specifications (including all the existing options) as well as the building, the shielding, the clinical environment, the services, and the ancillary tools (planning and dosimetry system, imaging, accessories, etc.).

A first typical choice is to decide if there is an interest for a proton center or if heavier ions are under consideration. A second choice is to quantify the capacity of the project, leading to a single or multiple treatment rooms, including or not special lines (e.g., ophthalmic, radiosurgery, fixed lines, etc.), and the number of gantries. A third theoretical choice could follow which is related to the type of technology for the accelerator (e.g., synchrotron, cyclotron, synchrocyclotron, linacs, all with or without cryogenic approaches) and the types of gantries. But indeed the usual choices during the present calls for bids are essentially related to a global offer around functional specifications, servicing, and financial concerns (with small

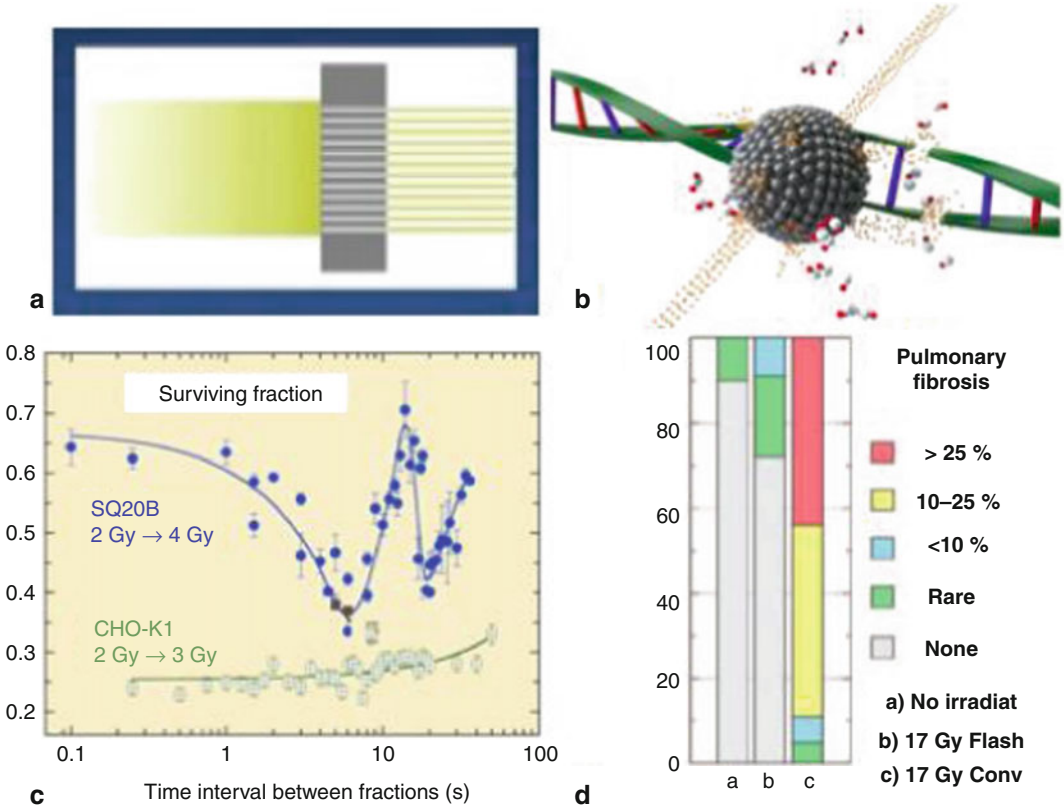

Fig. 5.15 Ongoing research examples with proton beams at the Institut Curie with partners: (**a**) use of microbeams [22], (**b**) use of nanoparticles [23], (**c**) effect of pulsed beams on cell lines [24], and (**d**) differential fibrosis with high ("flash") and low ("conventional") dose rates [25]. All figures modified from original cited references and data provided by authors

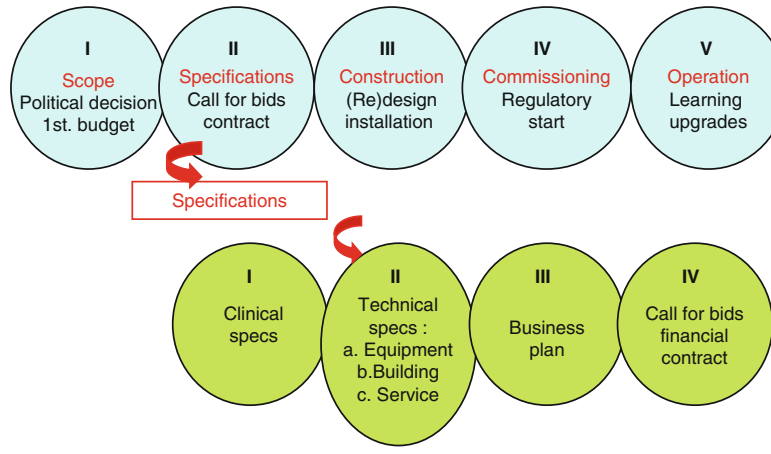

Fig. 5.16 Phases of a project, in some kind of topical linear and sequential approach, showing some of the essential steps from scope to operation, usually with iterations and a large margin of options

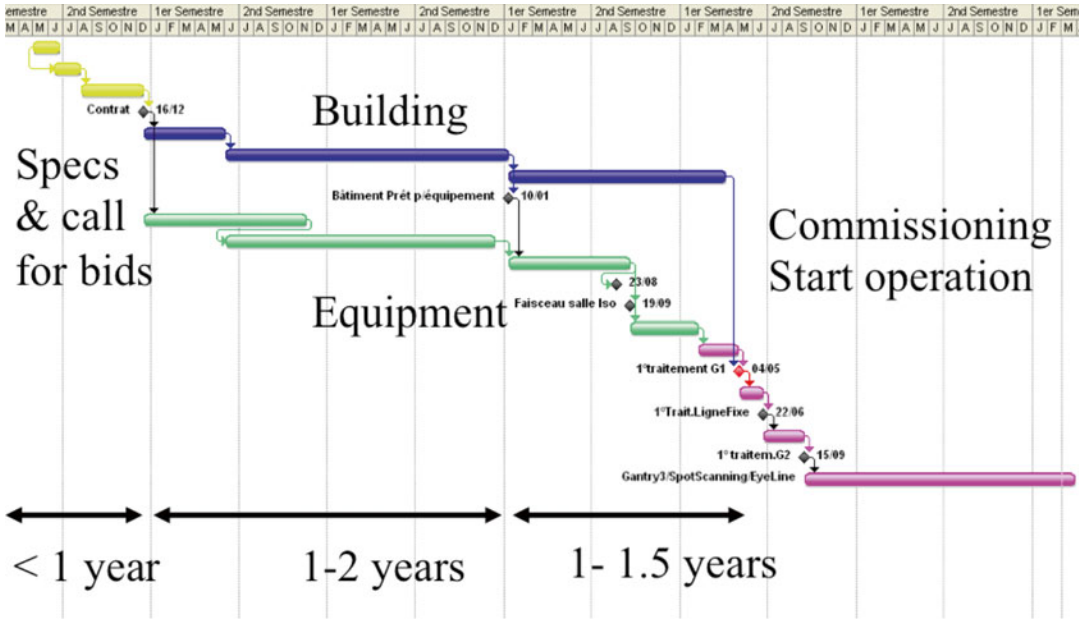

Fig. 5.17 Typical schedule for a multiroom proton therapy project from specification to operation, including building construction and equipment fabrication in parallel, followed by installation and commissioning. The time scale is being reduced with experience, industrial optimization, and shorter commissioning times

differences, all the accelerators are in principle able to provide the present specifications for clinics). Concerning the delivery and beam shaping systems, the present projects are evolving from passive approaches to scanned pencil beam, in order to perform intensity modulation with protons.

The business plan balancing costs and resources must be a realistic one, without extrapolation on the potential case mix and capacity, taking into account the use of the beam not only for clinics but also for quality assurance, maintenance, and, eventually, research projects. A single institution today is able to drive a project; in some other cases, the project is the base for a regional or national network of partners and referring centers. Present call for bids are at the international level, around ten companies can answer and present proposals (much more than for linacs!). It is important to evaluate the long-term prospective of servicing, engagement, and survival of those companies. In some cases, as the scenarios are wide and complex, the selection process follows a competitive dialogue, optimizing and converging on the specifications and eliminating vendors until the choice of a preferred one, before a final choice, usually announced to the (still small) community of particle therapy centers. The contract (Fig. 5.18) and the cost must take into account different risk factors, the updates, and upgrades for such a state-of-the-art and long-term equipment.

While the construction has most of the usual issues of radiation therapy buildings, there are some specific requirements provided by the vendors of the equipment that must be known through a "building interface" set of specifications, carefully verified before delivering the equipment. The installation is followed by phases of setup, validation, verification, acceptance, and commissioning with a progressive participation of the user. A formal transfer of property and responsibility from the vendor to the user is done at the end of the acceptance test procedures. These tests (performance, methodology, tolerances, etc.) are part of the contractual documents.

As this may be a rather new approach in radiation therapy in a community, mainly in those

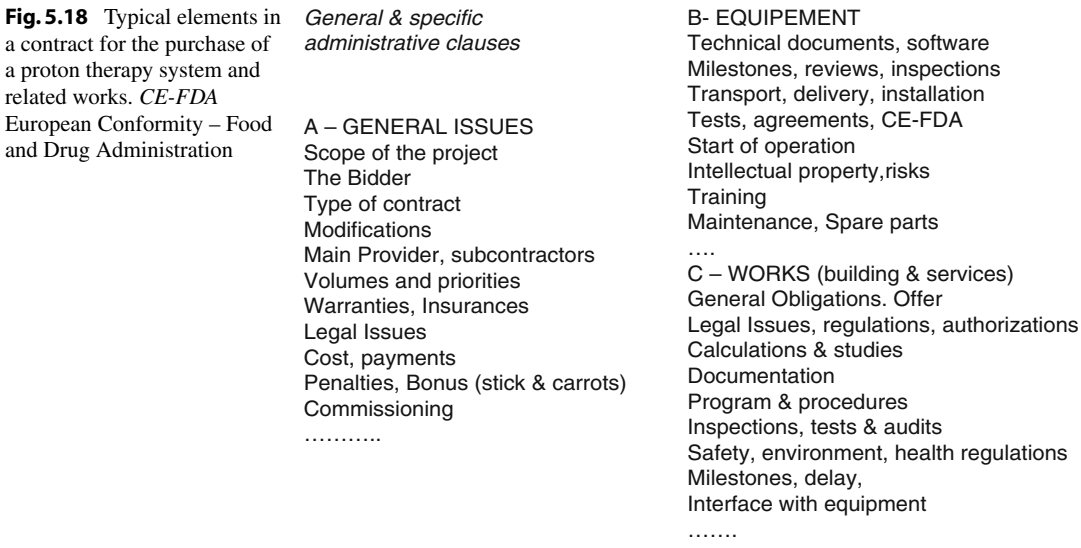

Fig. 5.18 Typical elements in a contract for the purchase of a proton therapy system and related works. *CE-FDA* European Conformity – Food and Drug Administration

countries where the first center(s) are being installed, it is important to agree at the very initial phase of the project with the regulatory authorities about the specific requirements to start testing and operation.

The start of clinical operation is a milestone that shows the achievement of parallel processes including training for all the teams (MDs, medical physicists, technical staffs, radiographers, etc.), logistics (patient workflow, quality assurance, service, building, administration, etc.), integration (oncology information system, treatment planning, record and verification systems, immobilization, image-guided therapy, management of movements and adaptive therapy, workshop, etc.), agreements (FDA/CE marking, agreement from local regulatory authorities, reimbursements, etc.), etc.

During the first months (years) of operation, there will be a "learning curve," increasing the number of patients, the complexity of clinical cases, and the optimization of tools and human resources. It is important to keep pace with upgrades, taking also into account the evolution of alternative approaches with external radiation therapy with photons and brachytherapy and promoting a synergy in their use, including the conception of clinical protocols, specific approaches such as hypo-fractionated treatments, concomitant treatments, translational research, and revisiting radiation biology.

Conclusions

The physical properties of the interactions of protons with matter have been at the origin of their interest to treat cancer, among different approaches in radiation therapy. While the interactions of protons with electrons are of clinical interest, the nuclear interactions and the scattering are indeed mostly limiting factors that must be taken into account when planning and delivering protons for therapy.

The most important limitation today to promote the use of protons is the cost to implement and use a facility, it is even more for projects aiming to use heavier ions. In order to reduce the cost, efforts are oriented toward conceiving compact facilities, not only reducing the size, the weight, and the cost of the accelerators but also optimizing the gantries and the logistics to improve the patient throughput.

Among the fields of development nowadays, we can mention the management of uncertainties (in the range, in the dose, in the positioning, and in the variation of the targets and tissues) and the development of clinical protocols for nearly most of the clinical sites

in radiation oncology. Efforts are also oriented towards the study of biological effects both for the native beams and also in treatments with modifiers of the sensitivity or the tolerance of healthy tissues. Therefore, the use of protons and heavier charged particles is strongly linked to research and development on different fields such as clinics, translational research, physics, technology, biology, computing, robotics, radiation protection, and socioeconomy through cost-benefit studies.

The improvement in imaging and calculating tools, coupled with a reduction in the global cost of the facilities and the results of historical cases and new clinical trials, has led to a recent increase in the interest on the use of protons in therapy. While the pioneer sites based on research centers on physics have already stopped operating or are closing, the new hospital-driven projects are increasing. More than 40 centers are working at present, at least a similar number of new facilities are planned or in a building phase (Fig. 5.19 and www.ptcog.ch), and the number is increasing exponentially. The new centers will be based on the experience of the existing centers but also will foster innovation and increase in the clinical data available for evaluation of the benefit of this approach.

Building and operating a new center is still a challenging project, but besides the investment cost, it converges toward the level of complexity of any advanced technique in radiation therapy. Proton therapy can be considered as a valuable tool among the available techniques in radiation therapy. Its correct place will be determined through multidisciplinary clinical trials, protocols, and continuous development.

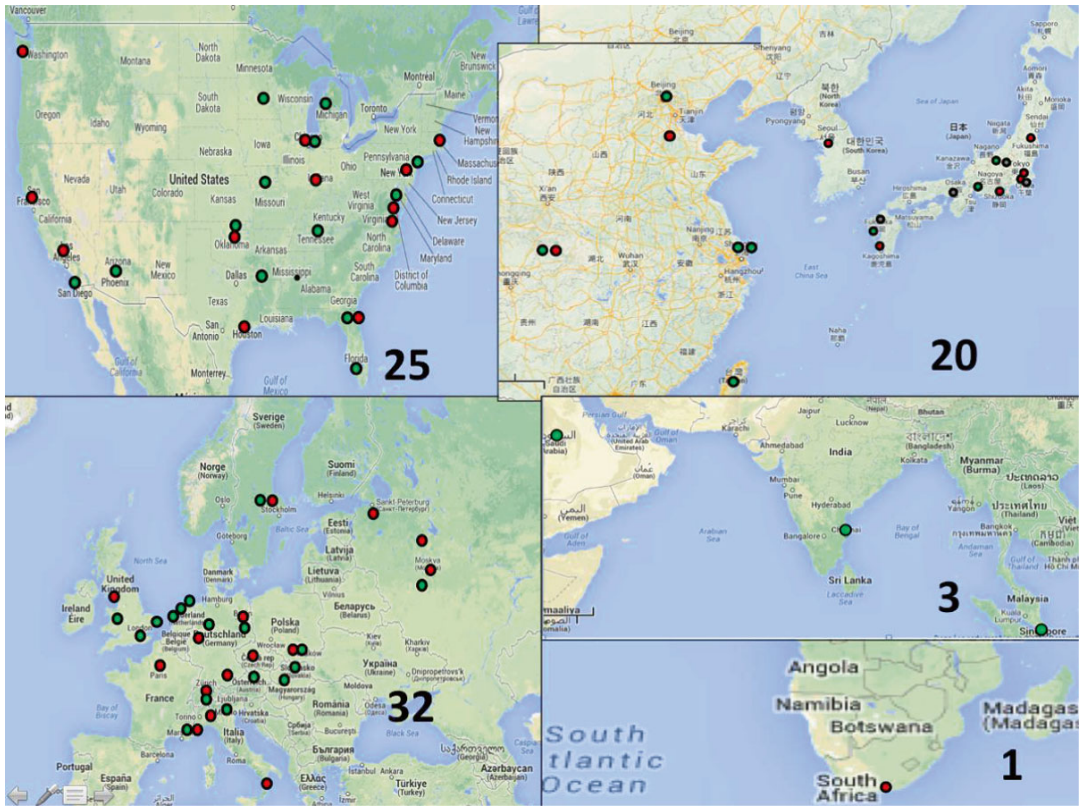

Fig. 5.19 Existing (*red dots*) and planned (*green dots*) facilities in the world as declared in the PTCOG web site at the end of 2013 (Data from www.ptcog.ch)

Acknowledgments N. Schreuder, H. Kooy, T. Lomax, Y. Jongen, V. Malka, R. Mackie, JC. Rosenwald, G. Olivera, D. Galmarini, W. Enghardt, F. Roellinghoff, M. Prall, M. Durante, A. Trofimov, M. Boussiere, Y. Prezado, E. Porcel, V. Favaudon.

References

1. Wilson RR. Radiological use of fast protons. Radiology. 1946;47:487–91.
2. Raju MR. Heavy particle radiotherapy. New York: Academic Press; 1980. p. 7–71.
3. Mazal A, Habrand JL, Delacroix S, Datchary J, Dendale R, Desjardins L, Ferrand R, Malka V, Fourquet A. Protontherapy: basis, indications and new technologies. Bull Cancer. 2010;97(7):831–46.
4. Lomax AJ, Bortfeld T, Goitein G, Debus J, Dykstra C, Tercier PA, Coucke PA, Mirimanoff RO. A treatment planning inter-comparison of proton and intensity modulated photon radiotherapy. Radiother Oncol. 1999;51(3):257–71.
5. Rosenblatt J. Particle acceleration. London: Methuen & Co Ltd; 1968.
6. Caporaso GJ, Sampayan SE, Kirbie HC. Dielectric-wall linear accelerator with a high voltage fast rise time switch that includes a pair of electrodes between which are laminated alternating layers of isolated conductors and insulators, U.S. Patent 5,821,705, A, 1998.
7. Malka V, Faure J, Fritzler S, Glinec Y. Electron and proton beams produced by ultrashort laser pulses. In: Lasers and nuclei/Lecture notes in physics, Vol. 694. Springer Verlag Berlin Heidelberg and European Communities; 2006. p. 81–90.
8. Pedroni E, Bacher R, Blattmann H, Böhringer T, Coray A, Lomax A, Lin S, Munkel G, Scheib S, Schneider U, et al. The 200-MeV proton therapy project at the Paul Scherrer Institute: conceptual design and practical realization. Med Phys. 1995;22(1):37–53.
9. Mazal A, Rosenwald JC, Ferrand R, Delacroix S, Nauraye C, Aligne C, Schlienger P, Habrand JL. Robots in high precision patient positioning for conformal radiotherapy. World Congress on Medical Physics and Biomedical Engineering: Sept. 1997, Nice. Med Biol Eng Comput. 1997;35: 824.
10. Knopf AC, Lomax A. In vivo proton range verification: a review. Phys Med Biol. 2013;58:R131–60.
11. Chen W, Unkelbach J, Trofimov A, Madden T, Kooy H, Bortfeld T, Craft D. Including robustness in multi-criteria optimization for intensity-modulated proton therapy. Phys Med Biol. 2012;57(3):591–608.
12. Desjardins L, Levy C, d'Hermies F, Frau E, Schlienger P, Habrand JL, Mammar H, Schwartz L, Mazal A, Delacroix S, Nauraye C, Ferrand R, Asselain B. Initial results of proton therapy in choroidal melanoma at the d'Orsay Center for Proton Therapy; the first 464 cases. Cancer Radiother. 1997;1(3):222–6.
13. Dendale R, Lumbroso-Le Rouic L, Noel G, Feuvret L, Levy C, Delacroix S, Meyer A, Nauraye C, Mazal A, Mammar H, Garcia P, D'Hermies F, Frau E, Plancher C, Asselain B, Schlienger P, Mazeron JJ, Desjardins L. Proton beam radiotherapy for uveal melanoma: results of Curie Institut-Orsay proton therapy center (ICPO). Int J Radiat Oncol Biol Phys. 2006;65(3):780–7.
14. Levy-Gabriel C, Rouic LL, Plancher C, Dendale R, Delacroix S, Asselain B, Habrand J-L, Desjardins L. Long term results of low dose proton beam therapy for circumscribed choroidal hemangiomas. Retina. 2009;29(2):170–5.
15. Lumbroso-Le Rouic L, Delacroix S, Dendale R, Levy-Gabriel C, Feuvret L, Noel G, Plancher C, Nauraye C, Garcia P, Calugaru V, Asselain B, Desjardins L. Proton Beam therapy for iris melanoma. Eye (Lond). 2006;20(11):1300–5.
16. Munzenrider JE, Liebsch NJ. Proton therapy for tumors of the skull base. Strahlenther Onkol. 1999;175(2 Supplement):57–63.
17. Noel G, Feuvret L, Calugaru V, Dhermain F, Mammar H, Haie-Meder C, Ponvert D, Hasboun D, Ferrand R, Nauraye C, Boisserie G, Beaudre A, Gaboriaud G, Mazal A, Habrand JL, Mazeron JJ. Chordomas of the base of the skull and upper cervical spine. One hundred patients irradiated bu a #D conformal technique combining photon and proton beams. Acta Oncol. 2005;44(7):700–8.
18. Kirsch DG, Tarbell NJ. Conformal radiation therapy for childhood CNS tumors. Oncologist. 2004;9(4):442–50.
19. Kjellberg RN, Sweet WH, Preston WM, et al. The Bragg peak of a proton beam in intracranial therapy of tumors. Trans Am Neurol Assoc. 1962;87:216–8.
20. Calugaru V, Nauraye C, Noël G, Giocanti N, Favaudon V, Mégnin-Chanet F. Radiobiological characterization of two therapeutic proton beams with different initial energy spectra used at the Institut Curie Proton Therapy Center in Orsay. Int J Radiat Oncol Biol Phys. 2011;81(4):1136–43.
21. Calugaru V, Nauraye C, Cordelieres FP, Biard D, De Marzi L, Hall J, Favaudon V, Megnin-Chanet F. Involvement of the Artemis protein in the relative biological efficiency observed with the 76 MeV proton beam used at the Institut Curie proton therapy center in Orsay. Int J Radiat Oncol Biol Phys. 2014;90(1):36–43.
22. Prezado Y, Fois GR. Proton-minibeam radiation therapy: a proof of concept. Med Phys. 2013;40(3):031712.
23. Porcel E, et al. Platinum nanoparticles: a promising material for future cancer therapy? Nanotechnology. 2010;21:085103.
24. Ponette V, Giocanti N, Tourbez H, Balosso J, Hennequin C, Favaudon V. Pulse exposure to ionizing radiation elicits rapid changes in cellular radiosensitivity. C R Acad Sci III. 1996;319(6):505–9.
25. Favaudon V, Caplier L, Monceau V, Pouzoulet F, Sayarath M, Fouillade C, Poupon MF, Brito I, Hupé P, Bourhis J, Hall J, Fontaine JJ, Vozenin MC. Ultrahigh dose-rate FLASH irradiation increases the differential response between normal and tumor tissue in mice. Sci Transl Med. 2014;6:245ra93.

Radiation Dosimetry of Proton Beams

6

Narayan Sahoo, Gabriel O. Sawakuchi, Michael T. Gillin, and Xiaorong R. Zhu

This chapter aims to review the currently practiced radiation dosimetry principles and procedures for passively scattered and magnetically scanned proton pencil beam spots (PPBS). Usefulness and limitations of various dose measuring devices, like ion chambers, films, solid-state detectors, gel, and plastic and liquid scintillators that are used in proton dosimetry are reviewed. Absolute or reference dosimetry procedures using calorimeter, ion chambers and Faraday cup are described. Relative dosimetry techniques for beam data collection are presented. Monitor unit calculation procedure for patient treatment fields for passively scattered fields using simple dosimetry factors is discussed. The detector size effects in the measurement of PPBS profiles and integral depth-dose are described. The importance of the contribution of low-dose envelopes present in PPBS profiles to 3-D dose distribution is discussed, and possible ways to measure and account for them in the modeling of PPBS in the treatment planning system are outlined. The feasibility of 3-D dosimetry using gel and liquid scintillators is discussed. Our experience at the Proton Therapy Center at Houston with the dosimetry of passively scattered and discrete spot-scanned proton beams including dose verification of patient treatment fields with intensity-modulated proton therapy is presented.

6.1 Introduction

Like any other modality used for radiation therapy, accurate and reproducible dosimetry is important for proton therapy for delivering the prescribed dose. The procedure for determination of absorbed dose for patient treatment fields at any proton therapy facility must be consistent with established national and international standards for meaningful comparison of treatment outcomes. Dose monitor in the proton beam nozzles needs proper calibration to ensure that prescribed dose is delivered to the patient. International dosimetry protocols are used to calibrate the dose monitor under reference conditions specified by these protocols. Dose distributions under non-reference conditions are determined from relative dose distribution measurements using suitable detectors and applying correction factors that may be necessary to account for the deviation from the standard reference conditions used in the monitor calibration protocol. Patient treatment field dose distribution calculations are usually carried out in treatment planning

N. Sahoo, PhD (✉) • G.O. Sawakuchi, PhD
M.T. Gillin, PhD • X.R. Zhu, PhD
Department of Radiation Physics, UT MD Anderson Cancer Center, 1515 HolcombeBlvd, Unit-1150, Houston, TX 77030, USA
e-mail: nsahoo@mdanderson.org

A.K. Rath, N. Sahoo (eds.), *Particle Radiotherapy: Emerging Technology for Treatment of Cancer*,
DOI 10.1007/978-81-322-2622-2_6

system using suitable beam models. Accurate beam modeling requires proton beam dosimetry data like Bragg peak depth-dose curve data for various energy options, transverse relative fluence distributions, and dose profiles at various depths. Spread out Bragg peak (SOBP) depth-dose curves are also needed for beam modeling and verification. Although 3-D dose measurements are ideal to get a complete picture of the dose distribution for patient treatment fields, it is not yet feasible. Instead, 2-D dose distributions at a number of depths are used to validate the dose calculation by treatment planning systems. It is also useful for patient treatment field dosimetry quality assurance to measure absolute dose at different points of the irradiated volume, relative depth-dose curves, and transverse profiles. Proper choice of the detectors is important for accurate dosimetry. Detectors are usually selected depending on the type of measurement to be made and the nature of the irradiating fields. This chapter describes the detectors commonly used for proton beam dosimetry, important features of the dosimetry protocols used for the dose monitor chamber calibration under reference conditions, practical aspects of measurements of beam profiles, depth-dose curves, both Bragg peak and SOBP, and 2-D dose distribution. Dosimetry measurements both for passive or double-scattered and spot-scanned proton beams are covered.

6.2 Dosimeters Used in Proton Beam Dosimetry

All the detectors used for dosimetry of photon and electron beams can be used for dosimetry of proton beams with the application of proper beam specific correction factors. Calorimeter; Faraday cup; ionization chambers; films, both radiographic and radiochromic; diodes; diamond detectors; TLDs; OSLDs; radiophotoluminescent glass dosimeters; alanine detectors; scintillators, both plastic and liquid; amorphous silicon detectors; gas electron multiplier (GEM chamber); and gel dosimeters are all found to be useful to measure dose distribution for proton beams. Absolute dose measurements are possible only with calorimeters, Faraday cup, and ion chambers. All other detectors are used for relative dose measurements. Faraday cup has a distinct use in charge particle therapy to determine the particle fluence. All the detectors, except calorimeter and Faraday cup, can measure point doses; 1-D dose distributions can be measured by ion chamber, film, diodes, diamond detectors, OSLD strips, scintillators, amorphous silicon detectors, GEM chamber, and gel dosimeters. 2-D dose distributions can be measured by ion chamber arrays, films, diode arrays, scintillation screen, amorphous silicon detectors, GEM chamber, and gel dosimeters. 3-D dose measurements are in principle possible with gel dosimeters and liquid scintillators. All dosimeters used for relative dose measurements in proton beam have varying degrees of energy and linear energy transfer dependence, being minimal and negligible for ion chambers. Thus, they should be used after proper characterization of their response to proton beam and should only be used where the LET or energy dependence is either negligible or a correction can be applied to account for the over or under response with proton energy and LET. An excellent review of the various detectors used for proton beam dosimetry is given [1] by Karger et al.

6.3 Dosimetry under Reference Condition

Dosimetry under reference condition is required to calibrate the main dose monitor of the proton beam delivery system, in which the dose per MU is determined as accurately as possible. The dose calibration should be traceable to a primary or secondary national or international standard. However, no primary standard exits for proton beams. Calorimetry-based standards are being developed at primary standard laboratories in Canada and the UK. Until such a standard is available, the dose monitor calibration of clinical proton beams under reference conditions is carried out following national or international protocols, primarily using ion chambers.

6.3.1 Calorimeter

Absolute dose measurement with calorimeter is based on the measurement of heat generated in a

core material or calorimeter phantom irradiated with the beam being calibrated. If a material of known specific heat (C) is irradiated in adiabatic condition, the absorbed energy is converted to heat, and the temperature of the material will increase by ΔT, then dose = 4.186*C*ΔT. The temperature rise is measured by using thermistor and a Wheatstone bridge as described in many standard dosimetry books and in a chapter in the AAPM 2009 summer school proceedings by McEween [2]. Although the theory of calorimetry is simple, it is hard in practice mainly due to the difficulty in accurately measuring small temperature changes. For example, 2 Gy of dose leads to a temperature rise of only 0.5 mK in water. Thus, for less than 0.5 % uncertainties in the measured dose, one should be able to measure temperature change of 2.5 μK. Additionally, there are uncertainties in thermistor calibration and corrections need to be applied for (1) deviation from adiabatic condition, (2) the existence of thermal defect in which part of the energy does not appear as heat, (3) non-tissue equivalence of the core material, and (4) nonuniform heat distribution due to high dose gradient in the distal dose fall-off region of proton Bragg peak and dynamics of proton beam dose delivery. Currently, calorimeters are only used by national standard laboratories for investigational purpose with an aim to establish a primary standard for proton beams and to check the adequacy of the ion chamber-based beam calibration.

6.3.2 Proton Beam Calibration with Ionization Chamber

Ion chambers are most widely used in practice for proton beam calibration as has been the case for external photon and electron beam therapy. The first step in the dose determination with an ionization chamber is to obtain the ion chamber charge to dose calibration factor (calibration coefficient) for the specific beam to be calibrated. However, as mentioned earlier, there are no primary standards for proton beams and the chamber calibration coefficient is obtained from ion chamber ^{60}Co beam calibration coefficient. The most recent protocol for proton beam calibration is the IAEA Technical Report Series 398 [3]. Use of this protocol is also recommended in the ICRU report number 78 [4] dealing with all aspects of proton beam therapy, although some of the older proton therapy centers may still be using the earlier ICRU 59 protocol [5]. A comprehensive review and comparison of the older ICRU 59 and newer IAEA TRS 398 protocols for proton beam calibration with ion chamber are given in ICRU report number 78 [4]. Only the important practical aspects of the IAEA TRS 398 report are described in this chapter and readers are encouraged to review the original IAEA TRS 398 and ICRU 78 for detailed discussion of the proton beam calibration protocols.

6.3.2.1 Proton Beam Dose Monitor Calibration Using IAEA TRS 398 Protocol

A waterproof cylindrical or parallel plane chamber with ^{60}Co dose to water per unit charge calibration factor from an accredited calibration laboratory (ADCL), a water tank with appropriate ion chamber holder, a calibrated high-precision electrometer, good cables to connect the chamber to electrometer, a thermometer, and a barometer are needed to carry out proton beam dose monitor calibration following the IAEA TRS 398 protocol. A reference condition has to be decided before the start of the calibration process as per the recommendation of the protocol given in its Table 10.II. Beam quality for proton beams is specified in terms of residual range (R_{res}), which is defined as $R_{res} = Z_{ref} - R_p$. The Z_{ref} is the depth of the reference point where the chamber is located and R_p is the practical range, the depth of the distal 10 % dose, of the beam as shown in Fig. 10.1b in IAEA TRS 398. The R_p is determined from measured depth-dose curve of the SOBP used for calibration. Usually, the chamber is placed at the center of the SOBP for a modulated beam. The beam quality factor (K_Q) for proton beam of quality Q is defined in the following equation.

$$K_Q = \frac{\left(W_{air} . S_{w,air} . P_{wall} . P_{cel} . P_{cav}\right)_Q}{\left(W_{air} . S_{w,air} . P_{wall} . P_{cel} . P_{cav}\right)_{^{60}Co}}$$

Quantities for ^{60}Co in the in the denominator of the above equation are well established. For protons, there are some uncertainties. According IAEA TRS 398, $W_{air/e}$ for protons is 34.23 ± 0.14 J C^{-1}. Water to air stopping power ratios are obtained from Monte Carlo simulation. P_{wall}, the correction factor for non-water equivalence of the wall of the ion chamber; P_{cel}, the correction factor for the presence of the central electrode; and P_{cav}, the correction factor for perturbation of proton fluence distribution due to the presence of the ion chamber are assumed to be unity for protons. Table 10.3 of the IAEA TRS 398 lists the beam quality factor for a number of widely used ion chambers as a function of R_{res}. The determination of the dose per monitor unit (MU) follows the following simple steps.

1. Measurement of charge generated in ion chamber for fixed amount of MU.
2. Correction for the measured charge for environmental conditions like temperature and pressure, which is usually different from the condition associated with the chamber calibration factor.
3. Determination of chamber polarity factor by measuring the charge for same MU at both positive and negative applied bias to the chamber.
4. Determination of ion recombination factor (K_s), which is usually done following the two-voltage method. The charge is measured for the same number of MU for high voltage and then with a lower voltage. The K_s is determined from the formula provided in Table IV.1 of the IAEA TRS 398 report depending on the type of beam to be calibrated.
5. Final step is the determination of dose per MU using the following equation:

$$D_W = M.N_{DW},60_{Co}.K_Q, \qquad (6.1)$$

where, Dw is the dose to water,

M is charge generated in ion chamber corrected for temperature and pressure (K_{TP}), polarity (K_p) and ion recombination (K_s),

N_{DW}, 60_{Co} is the dose to water calibration coefficient of the ion chamber for the ^{60}Co beam, and

K_Q is the beam quality factor.

A work sheet is provided in IAEA TRS 398 to record different factors needed to determine the dose per MU and to record the results of dose monitor calibration.

Usually a unit of MU corresponds to a certain amount of charge collected by the main dose monitor or back-up dose monitor. The dose per MU can be adjusted to desired value by changing the amount of charge to be used to define the MU and measuring the dose per MU using the IAEA TRS 398 protocol as outlined above.

6.3.2.2 Calibration of the Dose Monitors for Proton Pencil Beam Spots

Same reference condition like the passive scattered modulated proton beam can be used to calibrate the dose monitor of spot-scanned proton pencil beam delivery system. A broad field with uniform dose distribution in a large volume has to be created using a suitable spot distribution and the depth-dose curve for this field needs to be measured to determine the R_{res} before the calibration is carried out. The dose uniformity in the reference volume is also to be confirmed with measurement in a number of different locations. For example, the reference condition used at UT MD Anderson Cancer Center Proton Therapy Center in Houston, USA, which will be referred as PTCH hereafter, is uniform dose of 217.13 cGy to 1 liter volume irradiated with a broad beam of 10 cm × 10 cm and nominal SOBP width of 10 cm created with the superposition of 6760 spots with 18 different energies from 178.6 to 221.8 MeV and 8 mm of inter-spot spacing. The number of digital charge counts per MU was adjusted such that total of 217.13 MU would deliver the 217.13 cGy.

Alternatively, a broad field of monoenergetic proton spots can be used to do the monitor chamber calibration at a reference depth chosen in the plateau region. The IAEA TRS 398 protocol recommended value for plateau calibration is 3 cm in water. The relationship between MU and dose is complex in discrete spot-scanned proton beams. The dose at any location depends on the contribution of the all the spots of the broad field. The delivery of the desired dose to a volume requires that the entire spot pattern must be delivered. A single MU merely represents a certain amount of charge collected by the main dose monitor; its relation to dose distribution will depend on the ener-

gies and locations of spots. The purpose of the dose monitor calibration under the reference condition is to define the amount of digital charge count per MU and to check its constancy during periodic QA measurements. Once the number of digital charge count per MU is established, it is used for dosimetric characterization of PPBS in terms of dose/MU, to configure the PPBS in treatment planning system and for dose verification of broad fields. As described by Pedroni et al. [6] and Tilly et al. [7], if the treatment planning system requires MU per proton, then it would be necessary to use a Faraday cup to count the number of protons in one MU to establish this factor as described in the next section. It is a customary practice to verify the dose for treatment fields of spot scanned proton pencil beams calculated by the treatment planning system using a suitable measuring device like ion chamber or ion chamber array.

6.3.3 Fluence-Based Reference Dosimetry

Dose to a medium like water can be determined from the knowledge of the incident particle fluence (ϕ) and collision stopping power ($S_w(Z)/\rho_w$) in water at the depth of interest (Z) using the following equation:

$$D_w(Z) = \phi . \frac{S_w(Z)}{\rho_w}. \qquad (6.2)$$

Fluence can be measured by a Faraday cup or sample activation [1].

A Faraday cup, named after Michael Faraday, is a metallic cup designed to count charged particles in vacuum [8]. The construction of the Faraday cup ensures that only the primary charged particles can enter the cup and be counted. The number of charged particles (N) can be determined from the measured current or charge Q and the knowledge of the charge per particle (Ze), which is 1e for protons.

$$\text{Thus, } N = \frac{Q}{Ze}.$$

Suppose the incident proton beam is completely stopped in the Faraday cup and is uniformly distributed in an area A. Then the fluence of the charged particle, $\phi = N/A$, and the dose from this incident beam can be calculated using Eq. (6.2). The determination of collision stopping power also requires the knowledge of the spectral fluence of the incident proton beam. One of the possible methods to determine the spectral fluence of a polyenergetic beam is Monte-Carlo simulation of the beam line.

Incident proton fluence can also be determined from sample activation measurements in which a sample with known number, N, of ^{12}C atoms is irradiated for a known time interval t. The proton fluence can be derived from measuring ^{11}C activity and the knowledge of the reaction cross sections and decay constants. This is very useful for high dose per pulse proton beams, but has more uncertainties compared to other methods. The estimated uncertainties of various methods used for reference dosimetry are the following [1, 3]:

- Water calorimetry: 0.6 %
- Graphite calorimetry: 1.4 %
- Ion chamber: 2.3 %
- Faraday cup: 2.3 %
- Activation-based dosimetry: 3.5 %

6.4 Proton Beam Dosimetry under Non-reference Conditions

National and international protocols like IAEA TRS 398 provide the guideline for dose measurement under reference conditions for therapeutic radiation beams including protons. The treatment fields seldom match the reference conditions. Thus, the clinical dosimetry of therapeutic radiation beams always involves measurements under non-reference conditions but related to the reference condition.

6.4.1 Passive Scattering Proton Beam Dosimetry under Non-reference Conditions

Proton field parameters for passively scattered proton beams leading to a different dose/MU at any point under non-reference condition compared to that from the reference condition are beam

Table 6.1 Dosimetry factors to quantify the changes in dose/MU at a point of interest under non-reference condition

Changed parameter from reference condition	Associated dosimetry factor
Beam energy	Relative output factor (ROF)
SOBP width	SOBP factor, SOBPF
Range shifter thickness	Range shifter factor (RSF)
Distance of the point of interest from the center of SOBP	Off-center factor (OCF)
Distance of the point of interest from the central axis of the field	Off-axis factor (OAF)
Source to point of interest distance	Inverse square factor (ISF)
Field size	Field size factor (FSF)
Compensator and patient scatter factor	Compensator and patient scatter factor (CPSF)

energy or range, SOBP width, thickness of range shifters, location of the point of interest relative to the center of SOBP, location of the point of interest relative to the central axis of the beam, source to calibration point distance, field size, and compensator and patient scatter factor. Effect of each of these changes can be quantified in terms of special dosimetry factors [9] as given in Table 6.1.

One can determine these factors by measurement with an ionization chamber in water and use them for dose/MU determination for the specific proton fields of passively scattered beam. These parameters are also useful for simple calculation of point doses in passive scattered proton fields. 3-D dose distribution using these parameters will be too cumbersome and impractical. Semiempirical model-based dose calculation algorithms like pencil beam algorithms are used instead in modern treatment planning systems. However, they are found to be useful in determining the monitor units of treatment fields as discussed in Sec. 6.4.3.

6.4.2 Proton Dose Calculation Using the Semiempirical Analytical Methods

Proton dose distribution for a broad proton field of any shape and size can be calculated [10] either through the use of radiation transport formalism for the protons in the incident beam or by semiempirical analytical methods based on the analytical modeling of proton interaction with devices used for beam spreading and shaping and the irradiated media, and measured data to determine the parameters used in the model. The radiation transport methods, which are expected to be the most accurate, can be Monte Carlo simulation-based or deterministic solution of the Boltzmann transportation equation. However, these calculations are very computationally intensive and are not routinely used in dose calculation for clinical treatment planning. The deterministic dose calculation based on solving the Boltzmann transportation equation is still in research and developmental stage, but the Monte Carlo simulation-based dose calculation is widely used [11] in the proton beam dosimetry necessary to provide the dose distribution information in the situation where analytical methods have limited accuracy. In routine clinical practice, the dose into different media is calculated using the pencil beam algorithm. In this algorithm, a broad incident beam is divided into narrow pencil beams and the dose is calculated convolving the central axis depth-dose of the beamlet [12, 13], $I(Z)$, with the lateral beam profile, $K(r,\phi,\sigma(z))$, and is given by

$$D(r,\phi,z) = \sum_{p} I_p(z).K_p\left(r,\phi,\sigma(z)\right). \quad (6.3)$$

The lateral distribution of the beamlet is modeled by a Gaussian distribution with root mean square (RMS) spread $\sigma(z)$ and sum p is carried over all the beamlets of the broad beam. The $\sigma(z)$, which is also known as lateral beam spread parameter, is obtained from RMS of lateral spread parameters due to various responsible scattering processes, like multiple coulomb scattering, large-angle scattering, and nuclear interactions, involved in proton beam interaction with the beam-modifying devices and media of passage of the beam. Detail description of the dose calculation algorithm is outside the scope of this chapter. One of the key components of the implementation of the dose calculation algorithms is that they require high-quality measured beam data for depth-dose curves and lateral profiles both to extract the

pencil beam parameters and to validate the beam model. The validation of the model of the proton beam delivery system nozzle used in Monte Carlo simulation also requires high-quality beam data of the depth-dose curves and lateral beam profiles. The 3-D distribution can be constructed from the measured depth-dose curves and beam profiles or from calculated dose distribution using an appropriate dose computation model.

6.4.3 Depth-Dose Measurement

Depth-dose curves, which are dose profiles in the beam longitudinal direction are usually measured using suitable ionization chambers in computerized 3-D water tank beam scanning systems. The depth dose measurement in broad fields of passive scattering proton beam is similar to the measurements for collecting beam data for photon or electron beams. A parallel plate ionization chamber is recommended for depth-dose distribution measurement by the IAEA TRS 398 protocol [3]. Because of the uncertainties in the effective point of measurement for cylindrical chambers, their use in the high-dose-gradient regions of depth-dose curve should be avoided.

The ionization chamber measures the ionization as a function of depth, which needs to be converted to dose as a function of depth because of possible change in the stopping power ratio $S_{w,air}$ with depth and the change of the ion chamber perturbation factors. Per IAEA TRS 398 protocol, the perturbation factors are assumed to have a value of unity, but it recommends to check any variation of ion recombination and polarity effect with depth. The values of the stopping power ratio $S_{w,air}$ as a function of residual range (R_{res}) at the depth of the measurement are obtained using the following equation [3]:

$$S_{w/air} = a + b\,R_{res} + c\,/\,R_{res}, \qquad (6.4)$$

with $a = 1.137$, $b = -4.3 \times 10^{-5}$, and $c = 1.84 \times 10^{-3}$.

In practice, the variation of the $S_{w/air}$ with depth is minimal and is nearly constant for the range of clinical proton energies. Thus, the difference between the normalized percentage depth-dose curve and normalized depth-ionization curve is negligibly small for the range of proton energies used in the clinic for patient treatment as can be seen in the following figure (Fig. 6.1).

Special care needs to be taken while measuring the depth-dose distribution for small proton beam fields. As recommended in the IAEA TRS 398 protocol, if the field size is smaller than twice the diameter of the parallel plate chamber, then a smaller detector like mini ionization chamber, diode, or diamond detector should be used. Appropriate stopping power ratios, for example, water to air for mini ionization chamber, water to silicon for diode, or water to graphite for diamond detector, then are used to convert the detector response to dose to

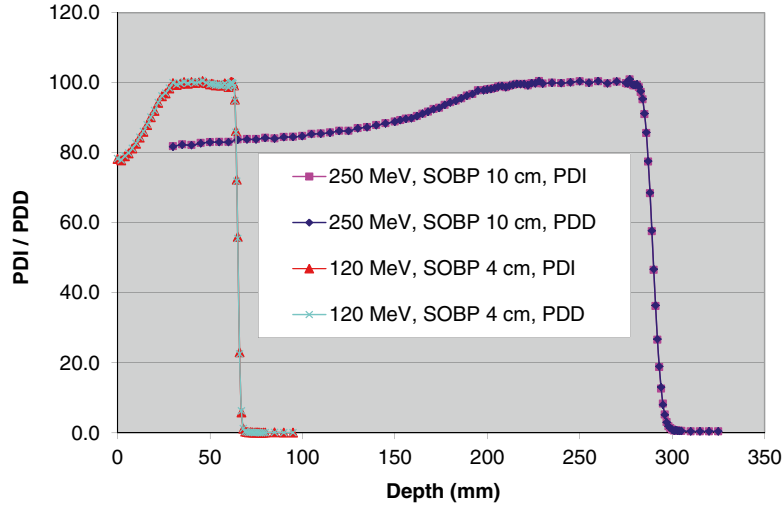

Fig. 6.1 Comparison of percentage depth-ionization (PDI) and percentage depth-dose curves (PDD) measured at PTCH for two passively scattered proton beams

water. It is recommended that the suitability of these detectors be checked by comparing the depth-dose distribution measured by these detectors with that measured by a parallel plate ionization chamber for an appropriate large field size.

While performing depth-dose measurements with ion chamber and water tank beam scanning system, consideration should be given to suitable scanning parameters, like the time of integration at each point of measurement and spatial spacing of the measurement points. For SOBP fields that are generated with rotating range modulation wheels (RMW), the adequacy of the time of integration should be studied to ensure that artifacts of incomplete rotations of the RMW are not present in the measured depth-dose curves.

Although parallel plate ionization chambers remain the detector of choice for measurement of depth-dose distributions, use of films [14, 15] and imaging plates [16] was also explored to measure the depth-dose curves of proton beams. These measurements require suitable detector response to dose calibration factors and corrections both for LET dependence of the detector response and for quenching. They are useful for quick measurement of depth-dose distribution for constancy checks of the delivery system. A multilayer ionization chamber array, like the Zebra from IBA (IBA Dosimetry GmbH, Schwarzenbruck. Germany), is also found to be suitable for rapid online depth-dose measurements in passive scattering beam [17].

6.4.4 Transverse Profile Measurements

Small-volume ionization chambers in water tank beam scanning system provide high-quality transverse profiles also known as lateral profiles, of proton beam fields. These measurements require scans with high spatial resolution in the high gradient region to determine the field penumbra and may need some correction for the detector size effect. Since the variation of proton LET in the transverse direction is minimal, other dosimeters like film, diode, diamond detectors, and luminescent screens with CCD camera can be used for measuring dose or fluence profiles perpendicular to the beam direction [1]. A suitable calibration curve is used for converting the detector response to dose, if it is not directly proportional to the dose, as in the case of the film. Ionization chamber arrays are also used to measure the lateral profiles but may have limited spatial resolution due to the large inter-chamber separation. Additionally, large detector sizes in the commercially available ionization chamber arrays may not provide accurate field penumbras due to volume averaging effects. They are very useful for constancy check of the delivery system functionality.

6.4.5 Scanned Proton Pencil Beam Spot (PPBS) Dosimetry under Non-reference Conditions

A broad field to provide the required 3-D dose distribution is created by the superposition of a number of spots of different energies spread over the irradiated volume. Thus, the dose at any point of interest is determined from the sum of dose from each spot used to create the broad field. The dose from each pencil beam at any point of interest can be obtained using Eq. (6.3). Usually, the 3-D dose distribution in the media of interest is calculated in the treatment planning system using a semiempirical analytical model. Commissioning the treatment planning system for PPBS [18] includes generating the required input data such as planar integral depth-doses in Gy•mm^2/MU for each energy and lateral in-air fluence profiles of the pencil beam spot for selected energies and adjusting the model parameters to match the measured data. Knowledge of spot depth-dose distribution and lateral dose profiles of each individual spot is needed to determine the dose for any broad field created by these spots and forms the core of the dosimetry of PPBS as described the following sections.

6.4.5.1 Dosimetry of PPBS

Dosimetry of the PPBS involves experimental characterization of the spot dose distribution in terms of in-air fluence, spot size, in-water dose

profiles, peak spot dose, and planar integral spot dose (PISD). The general shape of the PPBS is close to a Gaussian function and the FWHM of the spot fluence or dose profiles depend on the initial energy and depth of measurement. As the FWHM of the narrowest PPBS can be smaller than 10 mm, measurement of profiles, peak spot dose, and central axis percentage depth-dose is challenging. Various devices like film, small-volume ionization chamber, diodes, optically simulated luminescent detectors, and other solid-state detectors can be used to measure the fluence and dose profiles of PPBS. Some practical measurements to obtain PPBS profile and depth-dose data are described in detail in the following paragraphs.

6.4.5.2 Spot Profile Measurement

There are published reports of spot profile measurements carried out at different facilities using the scanning proton pencil beam. The details of in-air fluence and in-water dose lateral profile measurements carried out for commissioning of the scanning proton beam at PTCH are described in a paper by Sawakuchi et al. [19]. A PTW PinPoint chamber (Model 3014, PTW-Freiburg, Freiburg, Germany) with 0.1 cm radius and 0.5 cm height was used in a PTW MP3 3-D water tank beam scanning system to measure the lateral fluence and dose profiles. Another PTW PinPoint chamber was used as a reference chamber in performing the scans. The reference chamber was placed at an upstream location in the beam path and as far away as possible from the central axis to minimize the perturbation in the fluence or dose at the field chamber from the particles scattered by the reference chamber. An adaptive step size was used at various locations of the profile, namely, 0.1 cm, in the high gradient region and 1 cm in the low gradient regions of the profile. At each point integrated charge for 4 s was measured. Relative dose measurement was extended several centimeters from the central axis until its value became a factor of 10^4 lower than the central axis value. The reliability of the ionization chamber (IC) measured profile was studied by comparing them with those measured with Gafchromic EBT films (International Specialty Products, Wayne, NJ) and optically stimulated luminescent detector (OSLD) strips (Luxel, Landauer, Inc., Crystal Growth Division, Stillwater, OK). The application of OSLD strips for profile measurements is relatively new and is described in a recent publication by Yukihara et al. [20]. The use of OSLD strips for measuring PPBS profiles was therefore experimental in nature. Figure 6.2 shows a comparison of the in-air profiles measured with EBT film, OSLD, and ionization chamber.

As described in the paper by Sawakuchi et al. [19], lateral profiles measured by IC, OSLD, and EBT film are in excellent agreement in the central region. In the low-dose tail regions, the agreement between the OSLD and IC measured profile data remained excellent, but the EBT data differed substantially from both. This disagreement is expected because the dose in these region is outside the measurable range of EBT films. The

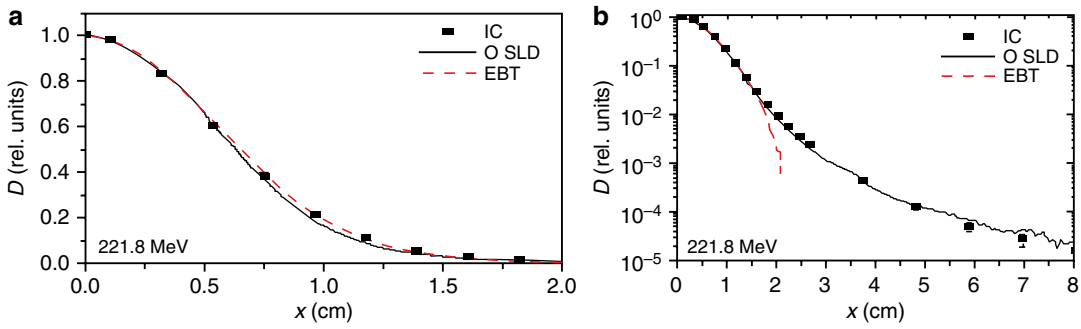

Fig. 6.2 Comparison of in-air profiles measured by ion chamber (IC), OSLD strips, and EBT film for the 221.8 MeV PPBS at PTCH. (**a**) Data are plotted in linear scale, (**b**) same data are plotted in semi-logarithmic scale. (reproduced from Sawakuchi et al., [19] © Institute of Physics and Engineering in Medicine. Reproduced by permission of IOP Publishing. All rights reserved)

agreement between the IC and film data in the central region demonstrated that a small-volume IC can be used with a reference chamber to measure the relatively narrow profiles. Good agreement with OSLD data in the low-dose regions gives additional support that IC data in the low-dose region can also be reliable. Small ion chamber was used to measure the lateral profiles of PPBS in water as part of our effort on experimental characterization of the spot beams.

The effect of the IC size was also studied using an analytical deconvolution procedure [21]. The measured profiles were fitted to a linear combination of Gaussian functions and were deconvolved with a Gaussian detector response kernel $K(x) = A.\exp(-x^2/2\sigma_\kappa^2)$ with σ_κ being equal to the radius of the IC. The deconvolved profiles are also given by the sum of Gaussians with modified $\sigma^2 = \sigma_m^2 - \sigma_\kappa^2$, where σ_m is the shape parameter of the Gaussian in the measured profiles. The full width at half maxima (FWHM) and full width at 0.01 of the maxima (FW0.01M) of the profiles with and without the detector size corrections were compared to quantify the effect of the IC size on the in-air fluence and in-water dose profiles of PPBS. A negligibly small detector size effect was observed both in the in-air and in-water profiles of PPBS with the three energies used in this study. The differences in the uncorrected and corrected FWHM and FW0.01M for in-air and in-water profiles were found to be less than 0.5 mm. This simple analytical deconvolution procedure indicated that the detector size has a rather small effect on the Gaussian-like lateral profiles of PPBS measured with small ion chambers. Similar results were also reported by Schwaab et al. [22], who used a parabolic function for their detector response function. This observation was thought to be a consequence of the small second gradient of the lateral profile function in most of the region beyond the peak of the Gaussian-like functions.

6.4.5.3 The Planar Integral Depth-Dose for PPBS

The planar integral depth-doses in Gy•mm^2/MU, also known as integral depth-dose (IDD), for each energy and spot are measured using a large parallel plate ion chamber like the PTW Bragg peak chamber (BPC) [18]. The required calibration factor to convert the ionization chamber reading of the BPC to dose can be obtained by performing the cross calibration of this chamber with an ADCL-calibrated farmer type chamber in a broad field larger than the size of the BPC. Because of the time and personnel required to measure the IDD for a large selection of energies, Monte Carlo simulation is often used to generate the needed beam data for the treatment planning system. The measured data for selected energies can be used to validate the Monte Carlo-generated data. The Monte Carlo-generated relative planar integral depth-dose for different proton energies can be converted to corresponding absolute dose in Gy•mm^2/MU values using the measured data by the BPC.

In determining the IDD either by measurement using a large area ionization chamber or by Monte Carlo simulation, the size of the chamber or the scoring region should be large enough to include the dose from the long tails of the spots also known as the low-dose envelopes or nuclear halo dose. These tails are present both in the low-energy spot profiles because of increased large-angle scattering in the beam line components and the irradiation media and in the high energy spots from the dose deposited far away from the central axis by the secondary particles generated by the nuclear interaction in the irradiation media. The adequacy of the scoring volume size in Monte Carlo simulation can be assured by doing a convergence test of the calculated IDD as a function of size of the scoring volume [18] as shown in Fig. 6.3.

The correction factors for the integral depth-dose measured by the Bragg peak chamber due to its size limitation could be determined by Monte Carlo simulation or by determining a long tail dose correction factor (LTDCF) from the measured lateral profiles by an area integration method described by Anand et al. [23]. The adequacy of the analytical representation of the spot profiles in the treatment planning system to correctly account for the low-dose envelope has to be examined by verification of calculated dose by measurements by creating suitable spot

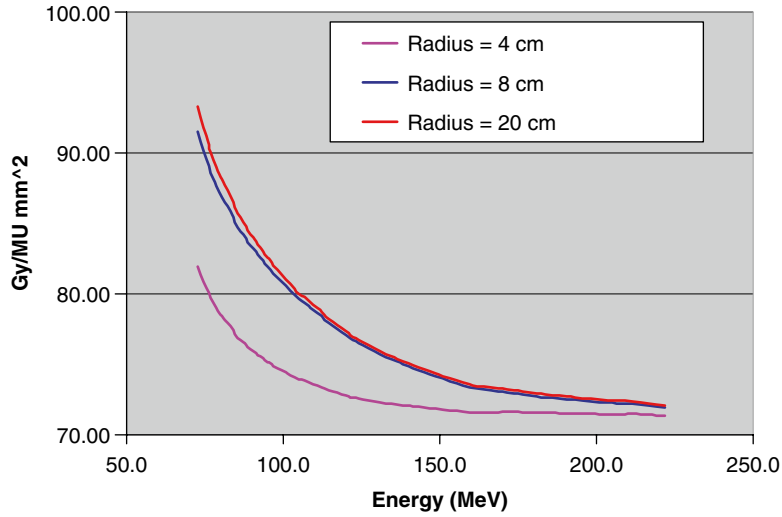

Fig. 6.3 The variation of IDD at 2 cm depth as a function of scoring volume radius in Monte Carlo simulation of PTCH scanned proton beams [18]

patterns where the dose from the tails of large number of spots can contribute to the dose at the point of measurement as described by Pedroni et al. [6] and Sawakuchiet al. [19]. These tests involve the comparison of calculated dose by the treatment planning system at a point as a function of field size with measured dose. It has been shown [6, 23] that the neglect of low-dose envelopes either in the IDD or the lateral profiles of the PPBS may lead to underestimation of the calculated dose in the treatment planning system by as much as 14 %. It has been shown [6] that use of a separate Gaussian function representing the low-dose envelope to model the incident spot profiles in the treatment planning system improves the agreement between the calculated and measured dose.

6.4.6 Monitor Unit Determination for Passive Scattering Proton Fields

The determination of MU of a passive scattering proton field to deliver the required dose at the point of interest is an important dosimetry task. There are a small number of methods available in the literature to determine the MU for the passive scattering fields [9, 24–26]. One of them is based on the dosimetry factors that quantify the change in dose/MU (d/MU) of the field under consideration relative to the reference field used for dose monitor chamber calibration as described in Sec. 6.4.1 and has some similarity with the formalism used for photon and electron fields.

If the dose from the treatment plan at the point of interest is D_{Plan} and the $(d/\text{MU})_{\text{Plan}}$ at this point calculate using the parameters in Table 6.1, then one can write

$$\left(\frac{d}{\text{MU}}\right)_{\text{Plan}} = \left(\begin{matrix}\text{ROF.SOBPF.RSF.}\\ \text{OCF.OAF.FSF.ISF}\end{matrix}\right).\text{CPSF}, \quad (6.5)$$

$$\text{MU} = \frac{D_{\text{Plan}}}{\left(\frac{d}{\text{MU}}\right)_{\text{Plan}}}. \quad (6.6)$$

The determination of the MU using the above equation requires the knowledge of the *CPSF* in addition to the measured dosimetry parameter in water phantom given in Table 6.1. Since the *CPSF* is not readily available from the patient treatment plan, one has to determine by taking the ratio of the dose in the patient plan and dose at the same water equivalent depth and geometrical setup in a water phantom for the same proton fluence of the field under consideration without the compensator. This can be avoided by calculating the dose in a water phantom for the treatment field proton fluence without the compensator

and determining the dose at the point of interest and then using the dose/MU in the water phantom without the compensator (referred as no compensator (nc) in the equations) $\left(\left(\frac{d}{\mathrm{MU}}\right)_{\mathrm{water-nc}}\right)$ to determine the MU because of the relationship given in Eq. (6.8).

The terms in the parenthesis in the right-hand side of the Eq. (6.5) are equal to the $\left(\frac{d}{\mathrm{MU}}\right)_{\mathrm{water-nc}}$ for the same proton fluence in the patient treatment plan for the field for which the MU is being calculated. The *CPSF* is the contribution of the compensator scatter factor and patient scatter factor in the patient treatment plan. Thus,

$$\left(\frac{d}{\mathrm{MU}}\right)_{\mathrm{Plan}} = \left(\frac{d}{\mathrm{MU}}\right)_{\mathrm{water-nc}} .\mathrm{CPSF}. \quad (6.7)$$

Similarly, one can also write $D_{\mathrm{Plan}} = D_{\mathrm{water\text{-}nc}} \times$ CPSF.

$$\text{Thus, MU} = \frac{D_{\mathrm{Plan}}}{\left(\frac{d}{\mathrm{MU}}\right)_{\mathrm{Plan}}} = \frac{D_{\mathrm{water-nc}} .\mathrm{CPSF}}{\left(\frac{d}{\mathrm{MU}}\right)_{\mathrm{water-nc}}} .\mathrm{CPSF} = \frac{D_{\mathrm{water-nc}}}{\left(\frac{d}{\mathrm{MU}}\right)_{\mathrm{water-nc}}}. \quad (6.8)$$

The MU for the treatment field can also be verified by carrying out a measurement of the dose/MU in a water phantom without the compensator and using the dose at the point of interest calculated in the water phantom for the treatment field without compensator. Such type of calculation is easily done using the treatment planning system, like using the verification plan capability of the Varian Eclipse treatment planning system (Varian Medical Systems, Palo Alto, CA, USA).

Other semiempirical methods for dose/MU calculation for passive scattering proton beam fields are also being used and have been described in published literature. One of these semiempirical methods is by Kooy et al. [25, 26] and it uses the relationship given in Eq. (6.9) between a factor $r = (R-M)/R$, a function of range R and modulation width M of the SOBP, and the output factor ψ_c and the SOBP entrance dose $D_{0,c}$ of the reference calibration field to determine the output factor for other options:

$$\psi(r) = \frac{\mathrm{CF}.\psi_c.D_{0,c}}{100/\left(1+a_0.r^{a_1}\right)}. \quad (6.9)$$

The parameters CF, a_0, and a_1 in Eq. (6.9) for every option are determined empirically by measuring the output as a function of r. The modulation width for the calculation of the output factor was taken to be the distance between the distal 90 % dose and proximal 98 % dose levels of the SOBP. Additional correction factor, shown in Eq. (6.10) below, was used [25] to take into account the shift of the effective source position due to the change in the range of the beam by range shifters to improve the accuracy of the calculated output factor using Eq. (6.9).

$$\psi'(R,M) = \left(s_0 + s_1\left(R - R_L\right)\right).\psi(r) \quad (6.10)$$

The parameters s_0 and s_1 are determined by measuring the ψ' for fixed r for three different ranges for every option of the delivery system. R_L is the lowest range for the option. The Eqs. (6.9) and (6.10) were further refined by Lin et al. [27] to address interbeamline modulation width variability.

The methods described above are also applicable for determining the monitor units for uniform scanning proton beam fields where the beam is spread laterally by a magnetically scanned proton beam and longitudinally by energy layer stacking. The output of a uniform scanning field depends on the range, modulation or SOBP width, scanning area, field size, and snout position [28, 29]. Dosimetry factors similar to the ones described in Table 6.1 can be measured and used to determine the MU of the treatment fields of uniform scanning proton fields.

A sector integration-based method was developed by Zhao et al. [30] to calculate the dose/MU for arbitrarily shaped fields using the measured dose/MU as a function of energy, spread-out Bragg peak width, and aperture diameter.

The aperture is divided into a number of sectors, whose output is known from measured data and the output of the field is calculated from the area-weighted sum of all the sectors in the field. This method has the advantage of including the effect of aperture size and shape on dose/MU compared to other methods. A Monte Carlo simulation-based method can also be used to determine the output factors (dose/MU) of passive scattered proton treatment fields in CT-based patient geometry as shown by Paganetti [31]. The Monte Carlo simulation method has the advantage of taking into account all the possible proton interaction in the patient compared to other methods based on measured data in water phantom.

6.4.7 Monitor Units for Fields of Scanned Proton Pencil Beam Spots (PPBS)

Broad treatment fields of scanning proton pencil beam are built up by a large number of pencil beam spots of different energies directed toward different locations within the irradiated volume. The PPBS is characterized by its depth-dose distribution, integral depth-dose (IDD) in terms of Gy•mm^2/MU, and spot lateral dose profile in terms of Gy/MU. The dose at any point in the irradiation volume from 1 MU of each spot is calculated using these terms and summed over all the spots in the field using Eq. (6.3). The relative weights of each spot to achieve the desired dose distribution in the irradiated volume are determined by inverse planning and optimization. The spot MU is determined by the relative weights of the spot and the prescribed total dose. If the optimization is carried out for number of protons in each spot, then the MU for each spot is determined from the number of protons per MU established during the monitor chamber calibration. For example, if N is the number of protons needed for one spot and n is number of protons per MU, then MU for this spot $= N/n$. The total monitor unit to be delivered for the field to deposit the desired dose distribution in the irradiated volume is the sum of the monitor units of each spot in the broad field. The relationship between the dose at any location and total MU does not have the same linear relationship that exits for a passive scattering proton beam field. The total MU of a scanning proton beam field depends on the total irradiation volume and dose given to this volume. The dose given to a point, a plane, or volume from the scanning proton beam field is usually verified by suitable measurements to confirm the accuracy of dose calculation method as described in the next section.

6.4.8 Patient Treatment Field Dose Verification

The proton treatment delivery systems have many dynamic components, like range modulation wheels in passive scattering beam, scanned PPBS, and uniformly scanned proton beam in addition to patient-specific treatment devices like apertures and compensators. The dose calculation in the treatment planning systems is carried out using semiempirical analytical dose calculation algorithms, which may have limitations in accurately calculating the delivered dose distribution to the patient. Therefore, verification of calculated dose distribution by measurements is desirable for proton therapy. The amount and types of measurement depend on the complexity of the treatment fields and the accumulated experience with such measurements. These measurements involve point dose measurements with ion chamber to verify the accuracy of the MU of the treatment field to deliver the planned dose and depth-dose distribution measurements with ion chamber or multilayer ion chambers to verify the dose distribution in the beam longitudinal direction, especially the dose around distal range of the proton beam and planar dose measurement with ion chamber array or film [32] or other 2-D detectors like scintillation screens with CCD camera at selected depths [6]. These measurements are usually carried out as part of a patient treatment field-specific dose verification quality assurance program with established tol-

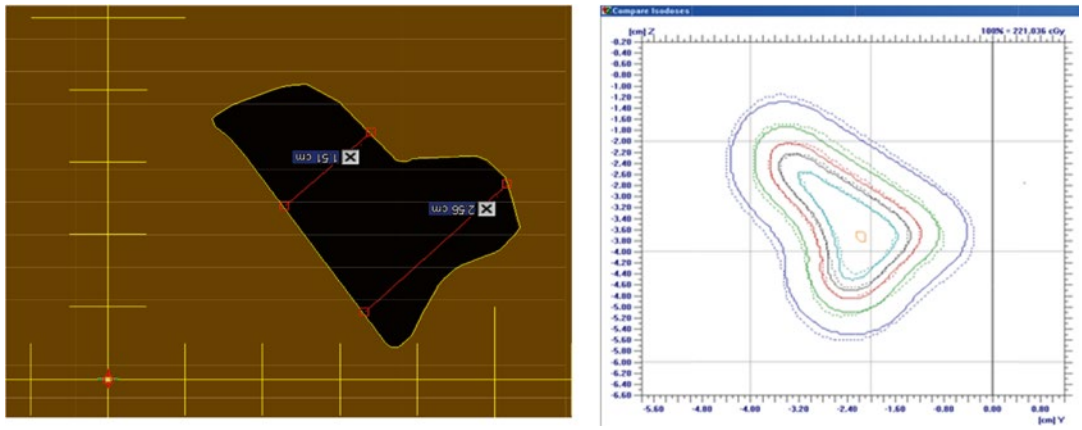

Fig. 6.4 Comparison of measured and calculated 2-D dose distribution of a passive scattering irregular field used for patient treatment at PTCH. Solid lines represent measurement and dashed lines represent calculation by the treatment planning system

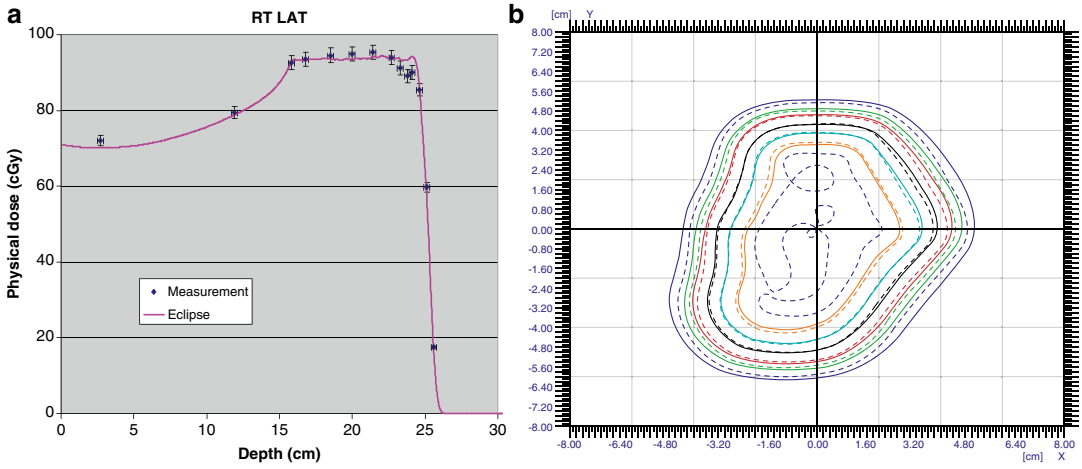

Fig. 6.5 Comparison of measured and calculated depth-dose distribution (**a**) and 2-D dose distribution (*solid lines* represent measurement and *dashed line* represent calculation by the treatment planning system) (**b**) of a prostatic scanning proton beam field used for patient treatment at PTCH (reproduced from Zhu et al., [32] with permission)

erance levels for accepting the results of comparison of the measured and calculated dose distribution. Gamma index analysis is used for comparison of measured and calculated 2-D planar dose distribution. Figure 6.4 shows a comparison of a planar dose distribution of an irregular field at an off-axis location of a passively scattered proton field measured with a radiographic film in plastic water phantom.

Figure 6.5a shows comparison of calculated depth-dose distribution of a scanning proton beam field for prostatic target created by single-field optimization with that measured with a Markus chamber (Model 34045, PTW-Freiburg, Freiburg, Germany) in a water phantom. Figure 6.5b shows comparison of the measured and calculated 2-D dose distribution of the same field measured using a 2-D ion chambers array (MatriXX from IBA Dosimetry, Schwarzenbruck Germany) in plastic water phantom (CIRS, Norfolk, VA, USA).

Figures 6.6 (a) and (b) show the comparison of calculated and measured depth-dose and planar dose distribution of a complex multi-field optimized scanning proton beam field, also

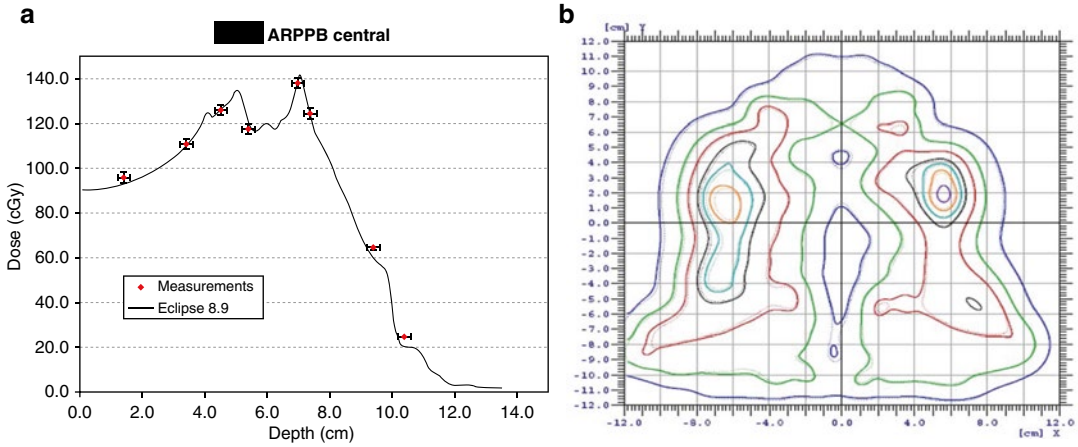

Fig. 6.6 Comparison of measured and calculated depth-dose distribution (**a**) and 2-D dose distribution (**b**) of a IMPT field used to treat a target in the head and neck at PTCH. In (**b**), solid lines represent measurement and dashed lines represent calculation by the treatment planning system

known as intensity-modulated proton therapy (IMPT) field for treating a target in the head and neck. The dose distribution was measured with a 2-D chamber array in plastic water phantom.

Figure 6.7 shows the comparison of calculated 2-D dose distribution of a complex IMPT field with that measured with scintillation plate and CCD camera [6].

These examples show that dosimetric tools are available to carry out dose verification of complex treatment fields. However, these verification measurements are done to verify dose distribution in homogeneous media, where dose calculation in the treatment planning systems is more accurate than the dose distribution calculated in inhomogeneous media in the patient. Limited amount of dose verification measurements is carried out for inhomogeneous phantom designed by the Imaging and Radiation Oncology Core QA Center in Houston, formerly known as Radiological Physics Center, as part of their credentialing process to enroll patients in clinical trials involving proton therapy. TLDs and EBT films are used to verify point and 2-D dose distribution respectively with established dose and distance agreement criteria. More work remains to be done to devise methods for verification of dose distribution in inhomogeneous media. This is a challenging task for measurement, but is feasible through Monte Carlo simulation. Once the beam model for Monte Carlo simulation is validated in situation where dose can be accurately measured, the Monte Carlo simulation can then be used to calculate dose in the patient CT images. This Monte-Carlo calculated dose distribution can be compared with planned dose distribution from the treatment planning system as part of an independent dose check quality assurance program.

Another challenge in proton therapy dose distribution verification is the presence of high dose gradient in the distal edge of the field. Although multiple ion chambers or ion chamber arrays can be used to verify point doses in different locations in the irradiated volume as described by Karger et al. [1], a complete knowledge of the 3-D dose distribution requires high-resolution 3-D dose measurement tools, which are not currently available. However, a number of 3-D dosimeters are currently being investigated for their potential use. BANG polymeric gels and PRESAGE radiochromic polymer dosimeters have the potential to provide 3-D dose distribution information for verification of IMPT fields [1, 33]. However, they are still investigational [34] and, as described by Krager et al. [1], have limitations due to LET and energy dependence, effect of preparation variability on their response and single use, and they require off-line evaluation and analysis. A 3-D dosimetry system using liquid scintillators and CCD cameras is being investigated by Beddar et al. [35, 36] and shows promise to measure the 3-D dose distribution in real time.

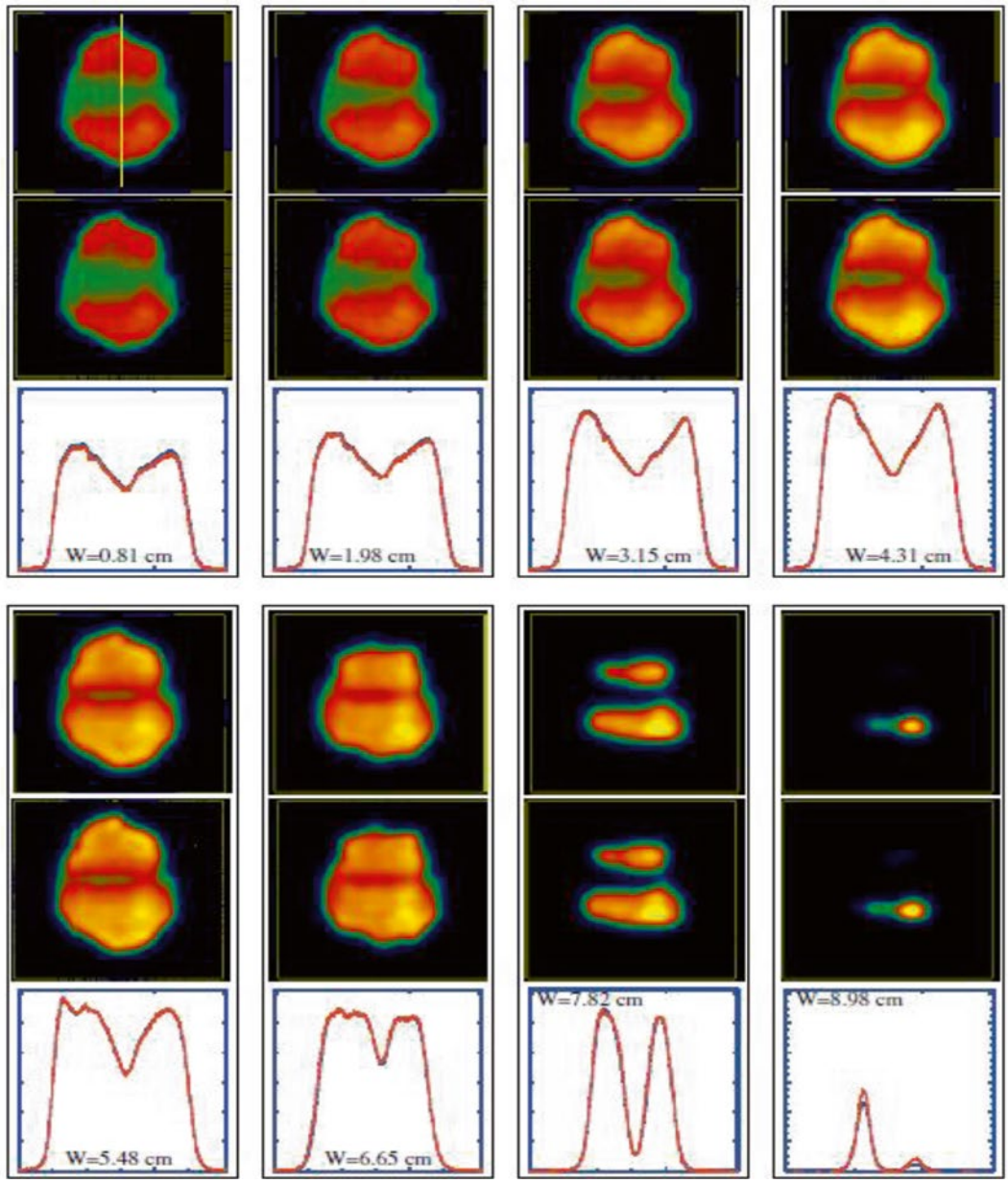

Fig. 6.7 Comparison of 2-D dose distribution of a IMPT field measured by scintillation screen and CCD (middle panel of each group) with calculated dose (top panel of each group) (reproduced from Pedroni et al. [6] © Institute of Physics and Engineering in Medicine. Reproduced by permission of IOP Publishing. All rights reserved)

6.4.9 Phantoms for Proton Dosimetry

Water is the required phantom for proton beam dosimetry under reference conditions [3]. However, it may not be always convenient to use the water phantom for frequent dosimetry measurements and plastic solid phantoms are often used instead. The water equivalent thickness of the plastic material needs to be determined by measurement of the relative stopping power of the plastic with respect to water before their use for

dosimetry measurements. The dose measured using the plastic phantoms can differ from that measured in water at the corresponding water equivalent depth due to the difference in the proton scattering properties of the plastic material compared to that for water leading to a change in the proton fluence at the point of measurement. Correction factors need to be determined to obtain the dose to water from measurements using plastic phantoms as part of the commissioning process of these phantoms for proton beam dosimetry.

6.4.10 Summary

The procedure for the determination of dose of proton beams under reference condition is well established in the IAEA TRS 398 protocol [3] and ICRU report 78 [4], even though a primary standard for proton beam dosimetry is not currently available. Many of the dosimeters used for measurement of point doses and 2-D doses in photon and electron beams can be used for similar measurements in proton beam after proper characterization of their response to the proton beam, especially the LET dependence of the dosimeter response. Ion chambers and ion chamber arrays remain the dosimeters of choice, but TLDs, OSLDs, films, and scintillation screens with CCD cameras are found to be useful in many situations and are being used for proton beam dosimetry. Suitable formalisms are available to determine the dose in non-reference conditions after the dose monitor is calibrated to define the standard for the MU both for the fields of passive scattering and pencil beam scanning proton beams. Dose verification measurements for patient treatment proton beam fields in water-like medium using the ion chamber, film, ion chamber arrays, and scintillation screen-CCD camera-based system are well established and are being routinely performed to assure that the dose from the proton treatment fields is delivered per the treatment plan. Development of a primary standard for the proton beam, research and developmental work on 3-D dosimetry, dose verification measurements in inhomogeneous phantoms, and Monte Carlo simulation-based dose verification in patient CT image sets are expected to remain the focus of future work in radiation dosimetry of proton beams.

Acknowledgement The authors would like to acknowledge the help of the members of the clinical physics group at the PTCH in the dosimetry measurements and analysis of the data presented in some of the figures in this chapter.

References

1. Krager CP, Jakel O, Palmans H, Kanai T. Dosimetry for ion beam radiotherapy. Phys Med Biol. 2010;55:R193–234.
2. McEween M (2009) In "Clinical dosimetry measurements in radiotherapy (2009 AAPM Summer School)". Medical physics monograph No. 34. Edited by Rodgers DWO and Cygler JE. Medical Physics Publishing, Madison, Wisconsin. APPM 2009 Summer School Proceedings.
3. IAEA. Absorbed dose determination in external beam radiotherapy: an international code of practice for dosimetry based on standards of absorbed dose to water. Technical report series, vol. 398. Vienna: International Atomic Energy Agency; 2000.
4. ICRU 78. Prescribing, recording, and reporting proton-beam therapy (ICRU report 78) (Bethesda, MD: International Commission on Radiation Units and Measurements).
5. ICRU 59. Clinical proton dosimetry–Part I: Beam production, beam delivery and measurement of absorbed dose ICRU report no. 59 (Bethesda.MD: International Commission on Radiation Units and Measurements).
6. Pedroni E, Scheib S, Böhringer T, Coray A, Grossmann M, Lin S, Lomax A. Experimental characterization and physical modeling of the dose distribution of scanned proton pencil beams. Phys Med Biol. 2005;50:541–61.
7. Tilly N, Grusell E, Kimstrand P, Lorin S, Gajewski K, Pettersson M, Bäcklund A, Glimelius B. Development and verification of the pulsed scanned proton beam at The Svedberg Laboratory in Uppsala. Phys Med Biol. 2007;52:2741–54.
8. Grusell E, Isacsson U, Montelius A, Medin J. Faraday cup dosimetry in a proton therapy beam without collimation. Phys Med Biol. 1995;40:1831–40.
9. Sahoo N, Zhu XR, Arjomandy B, Ciangaru G, Lii M, Amos R, Wu R, Gillin MT. A procedure for calculation of monitor units for passively scattered proton radiotherapy beams. Med Phys. 2008;35:5088–97.
10. Carlsson AK, Andreo P, Brahme A. Monte Carlo and analytical calculation of proton pencil beams for computerized treatment plan optimization. Phys Med Biol. 1997;42:1033–53.
11. Paganetti H. Monte Carlo simulations will change the way we treat patients with proton beams today. Br J Radiol. 2014;87(1040):20140293.

12. Hong L, Goitein M, Bucciolini M, Comiskey R, Gottschalk B, Rosenthal S, Serago C, Urie M. A pencil beam algorithm for proton dose calculations. Phys Med Biol. 1996;41(8):1305–30.
13. Schaffner B, Pedroni E, Lomax A. Dose calculation models for proton treatment planning using a dynamic beam delivery system: an attempt to include density heterogeneity effects in the analytical dose calculation. Phys Med Biol. 1999;44:27–41.
14. Zhao L, Das IJ. Gafchromic EBT film dosimetry in proton beams. Phys Med Biol. 2010;55:N291–301.
15. Arjomandy B, Tailor R, Zhao L, Devic S. EBT2 film as a depth-dose measurement tool for radiotherapy beams over a wide range of energies and modalities. Med Phys. 2012;39:912–21.
16. Nohtomi A, Terunuma T, Kohno R, Takada Y, Hayakawa Y, Maruhashi A, Sakae T. Response characteristics of an imaging plate to clinical proton beams. Nucl Inst Methods Phys Res A. 1999;424:569–74.
17. Dhanesar S, Sahoo N, Kerr M, Taylor MB, Summers P, Zhu XR, Poenisch F, Gillin M. Quality assurance of proton beams using a multilayer ionization chamber system. Med Phys. 2013;40:092102.
18. Gillin MT, Sahoo N, Bues M, Ciangaru G, Sawakuchi G, Poenisch F, Arjomandy B, Martin C, Titt U, Suzuki K, Smith AR, Zhu XR. Commissioning of the discrete spot scanning proton beam delivery system at the University of Texas M.D. Anderson Cancer Center, Proton Therapy Center, Houston. Med Phys. 2010;37:154–63.
19. Sawakuchi GO, Zhu XR, Poenisch F, Suzuki K, Ciangaru G, Titt U, Anand A, Mohan R, Gillin MT, Sahoo N. Experimental characterization of the low-dose envelope of spot scanning proton beams. Phys Med Biol. 2010;55:3467–78.
20. Yukihara EG, Gasparian PBR, Sawakuchi GO, Ruan C, Ahmad S, Kalavagunta C, Clouse WJ, Sahoo N, Titt U. Medical applications of optically stimulated luminescence dosimeters (OSLDs). Radiation Measurements 2010; 45:658–662.
21. Sahoo N, Ciangaru G, Sawakuchi GO, Anand A, Poenisch F, Suzuki K, Mohan R, Gillin M, Zhu X. Study of the magnitude of detector size effect in the measured lateral profiles of proton pencil beam spots. Med Phy (abstract). 2010;37:3293.
22. Schwaab J, Brons S, Fieres J, Parodi K. Experimental characterization of lateral profiles of scanned proton and carbon ion pencil beams for improved beam models in ion therapy treatment planning. Phys Med Biol. 2011;56(24):7813–27.
23. Anand A, Sahoo N, Zhu XR, Sawakuchi GO, Poenisch F, Amos RA, Ciangaru G, Titt U, Suzuki K, Mohan R, Gillin MT. A procedure to determine the planar integral spot dose values of proton pencil beam spots. Med Phys. 2012;39:891–900.
24. Moyers MF. "Proton Therapy". In: Van Dyk J, editor. Modern Technology of Radiation Oncology. Wisconsin: Medical Physics Publishing; 1999. p. 863–4.
25. Kooy HM, Schaefer M, Rosenthal S, Bortfeld T. Monitor unit calculations for range-modulated spread-out Bragg peak field. Phys Med Biol. 2003;48:2797–808.
26. Kooy HM, Rosenthal SJ, Engelsman M, Mazal A, Slopsema RL, Paganetti H, Flanz JB. The prediction of output factors for spread-out proton Bragg peak fields in clinical practice. Phys Med Biol. 2005;50:5847–56.
27. Lin L, Shen J, Ainsley CG, Solberg TD, McDonough JE. Implementation of an improved dose-per-MU model for double-scattered proton beams to address interbeamline modulation width variability. J Appl Clin Med Phys. 2014;15(3):297–304.
28. Zheng Y, Ramirez E, Mascia A, Ding X, Okoth B, Zeidan O, Hsi W, Harris B, Schreuder AN, Keole S. Commissioning of output factors for uniform scanning proton beams. Med Phys. 2011;38:2299–306.
29. Zhao Q, Wu H, Cheng CW, Das IJ. Dose monitoring and output correction for the effects of scanning field changes with uniform scanning proton beam. Med Phys. 2011;38:4655–61.
30. Zhao Q, Wu H, Wolanski M, Pack D, Johnstone PA, Das IJ. A sector-integration method for dose/MU calculation in a uniform scanning proton beam. Phys Med Biol. 2010;55:N87–95.
31. Paganetti H. Monte Carlo calculations for absolute dosimetry to determine machine outputs for proton therapy fields. Phys Med Biol. 2006;51:2801–12.
32. Zhu XR, Poenisch F, Song X, Johnson JL, Ciangaru G, Taylor MB, Lii M, Martin C, Arjomandy B, Lee AK, Choi S, Nguyen QN, Gillin MT, Sahoo N. Patient-specific quality assurance for prostate cancer patients receiving spot scanning proton therapy using single-field uniform dose. Int J Radiat Oncol Biol Phys. 2011;81:552–9.
33. Zeidan OA, Sriprisan SI, Lopatiuk-Tirpak O, Kupelian PA, Meeks SL, Hsi WC, Li Z, Palta JR, Maryanski MJ. Dosimetric evaluation of a novel polymer gel dosimeter for proton therapy. Med Phys. 2010;37:2145–52.
34. Deene YD, Vandecasteele J. On the reliability of 3D gel dosimetry. Journal of Physics: conference series 2013;444: 012015.
35. Beddar S, Archambault L, Sahoo N, Poenisch F, Chen GT, Gillin MT, Mohan R. Exploration of the potential of liquid scintillators for real-time 3D dosimetry of intensity modulated proton beams. Med Phys. 2009;36:1736–43.
36. Archambault L, Poenisch F, Sahoo N, Robertson D, Lee A, Gillin MT, Mohan R, Beddar S. Verification of proton range, position, and intensity in IMPT with a 3D liquid scintillator detector system. Med Phys. 2012;39:1239–46.

Clinical Pencil Beam Scanning: Present and Future Practices

7

Marco Schwarz, Carlo Algranati, Lamberto Widesott, Paolo Farace, Stefano Lorentini, Roberto Righetto, Daniele Ravanelli, and Francesco Fracchiolla

7.1 Selecting Pencil Beam Scanning as the Beam Delivery Technique

Pencil beam scanning (PBS) is often taken for granted as the main beam delivery technique in proton therapy, but the reality is more nuanced. While the first experiences in proton therapy with scanned beams date back to the late 1990s at Paul Scherrer Institute (PSI) in Switzerland [13], commercial gantry-based solutions for PBS became available around 2008–2010. Currently, only a minority of centers solely rely on PBS to deliver treatments, and it is likely that most treatments are still performed with either passive scattering or uniform scanning. Still, a rapid transition towards PBS is ongoing and it is probably safe to say that the vast majority of, if not all, facilities due to start in the near future will be PBS only.

Why is PBS so appealing? The main reasons are essentially twofold:

1. The increased dose conformity and, generally, the additional degrees of freedom available with PBS in shaping the dose distributions with respect to scattered beams. Scattered beams produce dose distributions lacking in proximal conformity and they make it highly impractical to create intentionally heterogenous dose distribution in the targets, such as those needed to deliver simultaneously integrated boost (SIB) treatments or to achieve a so-called "dose painting" [1]. In addition, the lack of proximal conformality of passively scattered protons may have clear clinical downsides, such as the increased skin dose (see, e.g., [10]) and thus the need to combine proton with photon treatments in order to reduce the occurrence of cutaneous side effects. Creating superior dose distributions in the high-dose region is of course primarily interesting for improved treatment quality, but it also helps proton therapy keep the pace (or have a slight edge) with respect to photon therapy; that, thanks to intensity-modulated techniques, is now capable of producing exquisitely conformal dose distributions.
2. PBS requires little or no patient-/field-specific hardware, such as the apertures and compensators used with scattered beams. This has two positive consequences:
   1. Beam apertures, being made with high Z material such as brass and being positioned close to the patient, are associated to an unwanted neutron dose. Such dose is typically not as high as initially feared [8, 24], but it is obvious that removing any source of unnecessary irradiation is beneficial and

M. Schwarz (✉) • C. Algranati • L. Widesott
P. Farace • S. Lorentini • R. Righetto • D. Ravanelli
Francesco Fracchiolla
Protontherapy Department, Trento Hospital,
Via Al Desert 14, Trento 38123, Italy
e-mail: marco.schwarz@apss.tn.it

A.K. Rath, N. Sahoo (eds.), *Particle Radiotherapy: Emerging Technology for Treatment of Cancer*,
DOI 10.1007/978-81-322-2622-2_7

that aperture-free PBS-based proton therapy results in a very low level of neutron dose [17].
2. Without the need of entering the room at every field to change apertures and compensators, the time needed to treat a patient with PBS will generally decrease.

If this beam delivery technique is so interesting, then why did it take so long for PBS to be widely available? First of all, it is because of the complex technology needed to deliver PBS beams fast and safely in clinical practice. Building a passively scattered proton beamline is far from trivial, but PBS poses new challenges on both the beam transport and delivery hardware (e.g., magnets) and software (e.g., treatment control and safety system) that must be able to continuously adjust and check the beam properties on a millisecond time scale [4].

Then, in the early days of PBS, there was a lot of emphasis on achieving spot sizes as small as reasonably possible, thus setting strict requirements on the beam properties. While one may argue that a small size is not the only thing that matters in PBS, it remains true that 3–4 mm beams are often needed to create dose distributions that are truly superior to state-of-the-art photon therapy (Fig. 7.1) [22].

While defining the technical requirement for a PBS-based facility, one faces specific questions that require a compromise between conflicting needs. For instance:

1. Which *maximum proton energy*? This is not a PBS-specific question but needs be addressed nonetheless. The current trend is for maximum energies in the 230 MeV range or lower, corresponding to a penetration depth in water of about 32 cm. In the interest of cost, there is an incentive in decreasing this limit even further. However, one should consider that one thing is achieving energies to *treat* lesions in any location and it is a different thing to have energies high enough to *image with protons*, which is a candidate solution for accurate in vivo range estimation (see, e.g., [18]). In the interest of proton imaging, the maximum available energy should actually be increased, not decreased.
2. Which *minimum proton energy*? This is a PBS-specific question and it does have a significant impact on the clinical workflow. PBS is a technique which is *mostly* but *not entirely* free of beam-specific hardware, and a beam absorber (a.k.a. range shifter) is the beam modifier most likely to be needed in PBS. Such a device is needed because there is a limit to the lowest proton energy that can be safely and effectively transported through the beamline to the isocenter. Most commercially available proton therapy systems allow a minimum energy between 100 MeV (corresponding to a range of about 7.8 cm in water) and 60–70 MeV (3.1–4.1 cm). Obviously, the lower the minimum energy, the better. In addi-

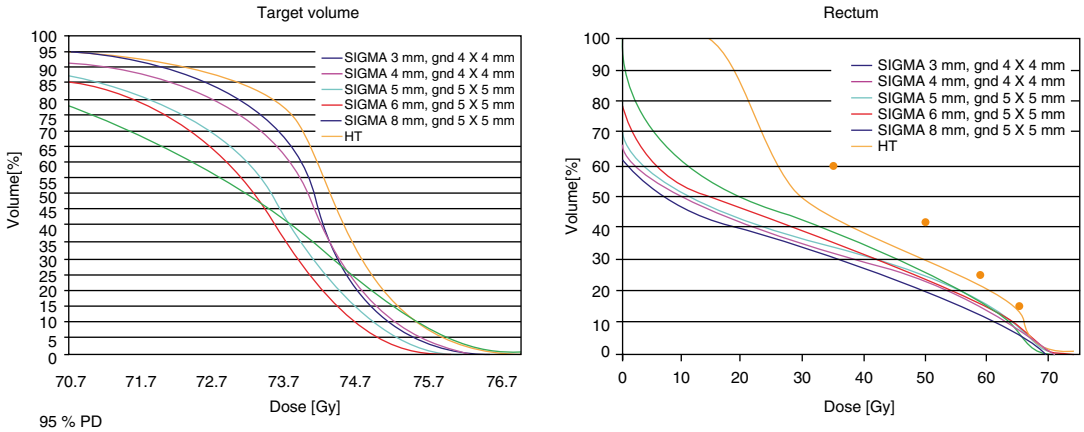

Fig. 7.1 Effect of pencil beam size on the dose distribution. Dose volume histograms (DVH) for the target volume (prostate) and the rectum obtained with different pencil beam size and spot spacing are compared with DVH obtained with state of the art photon radiotherapy technique (helical tomotherapy (HT)).[22]

tion to setting a low minimum energy, one should minimize the dosimetric effect of the preabsorber, which acts as an additional source of scatter for the beam, either by moving it as close as possible to the patient or to use it only for the energy layers where it is required.

3. Which *maximum field size*? The maximum field size available in several PBS facilities nowadays it is quite large (e.g., 30×40 cm^2), but this size is probably determined by the needs of scattered beams rather than PBS. There is of course a price to pay for large fields (in terms of both money and equipment size/weight), and in principle PBS treatments could rely on the routine use of abutting fields. As a consequence, there is a trend in new facilities relying entirely on PBS to accept smaller field sizes, e.g., 20×20 cm^2. One must however take into account that in order to routinely rely on field abutment, appropriate planning techniques are needed, which are not the standard in all treatment planning systems (TPSs).
4. Are beam *apertures* necessary? The pencil beam size can change by more than a factor 2 between high energies and low energies (Fig. 7.2). Therefore, when a sharp lateral penumbra is needed at shallow depths, apertures may have a role. Apertures, however, are associated with increased complexity both in terms of workflow (they should be inserted/removed at every field and they require a movable holder in order to have them as close as possible to the patient) and dose calculation (the dose contribution from scatter in the aperture may not be accurately estimated by pencil beam algorithms).
5. How *fast* should the *energy change* between neighboring layers? Several strategies to minimize the so-called interplay effects between beam delivery and respiratory motion have been proposed through the years, such as beam tracking, volumetric repainting, and gating, but none of them have established themselves as the standard in clinical practice. With the exception of PSI, where energy changes in the range of 80 ms have been obtained, most current commercial solutions for PBS are associated with energy changes in the 1–2 s range, which may severely decrease the benefits of volumetric repainting [2].
6. Are *multiple spot sizes* needed? The initial effort in PBS development was aimed at achieving spot size as small as possible. Then the question came whether using the smallest spot size, which is surely beneficial for most patients, is the best possible solution in all cases. The arguments in favor of the selected use of larger spot size are essentially twofold:
   1. Larger spot sizes result in a reduced total number of spots, i.e., a shorter beam-on time, which may be beneficial with very large target volumes. Given that in-layer

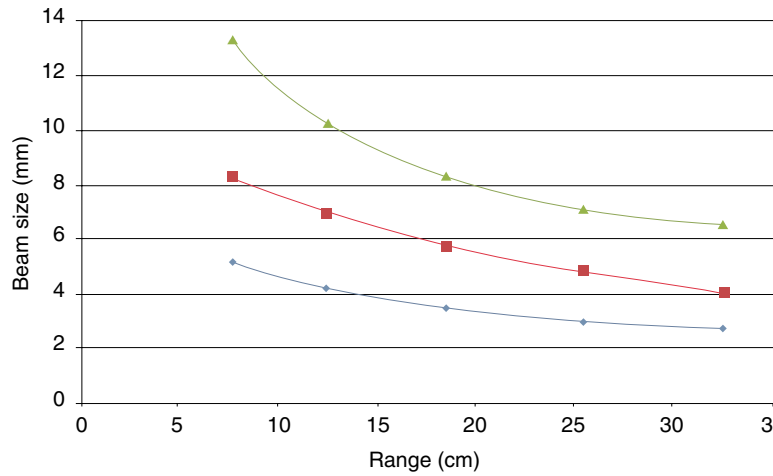

Fig. 7.2 Spot size (1 sigma in air at isocenter) as a function of beam range available in Trento

dead times, to move a spot from one position to the next, are typically much smaller than dead times between layers (when the beam energy should be changed), of course the relative decrease in beam-on time is larger for smaller energy switching times.
2. Larger spot size may produce dose distributions that are less sensitive with respect to intrafraction motion [7].

7.2 Commissioning a Pencil Beam Scanning Facility

Comparing pencil beam scanning with other beam delivery techniques (see, e.g., [3]), one current difficulty with PBS in clinical practice is that, due to the relative novelty of the techniques, the commissioning procedure are not fully established and are therefore quite time consuming. In this section we'll summarize the work performed at our center to characterize our PBS system. While some details of what we'll discuss are specific to our technical configuration, we'll mostly focus on aspects that are vendor independent and that should therefore be characterized in any PBS facility.

Our center hosts a cyclotron-based beam production and delivery system serving two isocentric gantries (Figs. 7.3 and 7.4). The main technical characteristics relevant for the beam commissioning are shown in Table 7.1. The terminal part of the beam delivery system (the so-called nozzle (Fig. 7.5)) is designed for pencil beam only, so vacuum extends as far downstream as possible, PBS-specific beam focusing elements are present beside the scanning magnets, and the beam does not interact with any material prior to hitting the beam monitor chambers (IC2 and 3) and the exit window. The overall water equivalent thickness of the nozzle is therefore small.

7.2.1 Spot Size, Shape, and Geometrical Accuracy

Since our facility is one of the very first where PBS-only beam delivery systems are available on the gantry of an IBA machine, we went through an extensive set of measurements to characterize spot size and shape as a function of (a) energy, (b) position in the transversal plane, and (c) gantry angle. The beam properties in the transverse plane were typically measured

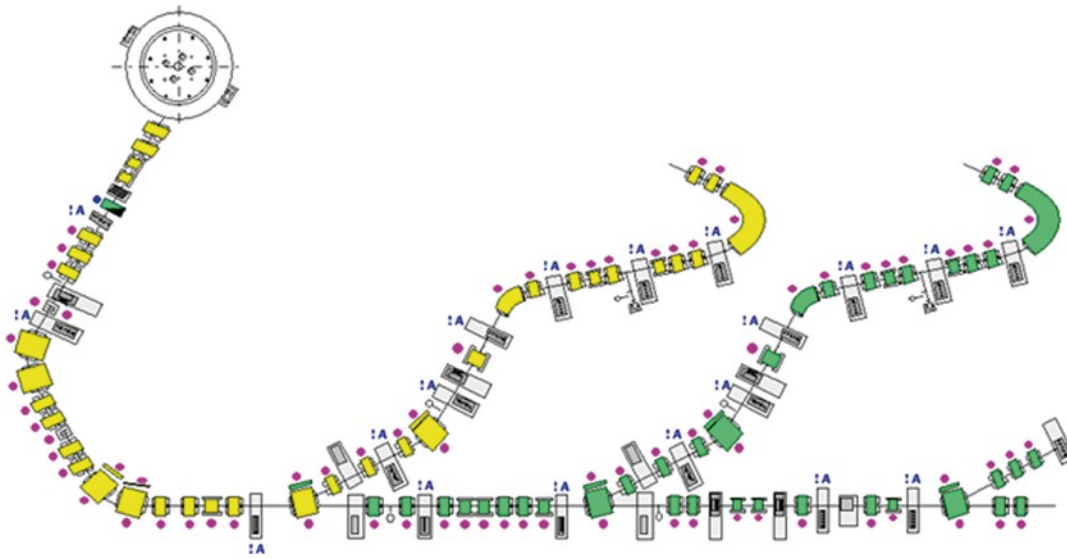

Fig. 7.3 Schematic layout of the PT center in Trento, where one cyclotron serves two gantry rooms and one fixed line room. Picture courtesy of IBA

Fig. 7.4 One of the two gantries available at the PT center in Trento

Table 7.1 Summary of the main beam characteristics of the PBS system installed in Trento

Type of accelerator	Cyclotron
Maximum beam range at isocenter	32 cm
Minimum range at isocenter without beam modifiers	4.1 cm
Minimum spot size (in air) at maximum range	2.5 mm
Minimum spot size (in air) at minimum range	7.0 mm
Time needed for energy change between neighboring layers	≤2.0 s
Number of available spot sizes per range	3
Time to deliver 2G to a $10 \times 10 \times 10$ cm^3 volume	<60 s
Maximum field size	30×40 cm^2
Spot position accuracy	≤1 mm

with a scintillation detector coupled with a CCD camera (Fig. 7.5). The measurements did allow us to assess the normality of the spots as a function of beam energy, position, and gantry angle and to evaluate the fluctuations in spot size for each energy as a function of position and gantry angle (see example in Fig. 7.10). Overall, the range of variations was typically within 10 % of the spot size, which is considered to be adequate from a clinical perspective. Of course a crucial test for pencil beam scanning is the capability of the beam delivery system to accurately place the spots in absolute terms, not only relative to one. To assess such accuracy, we had to take account for a specific feature of our system, where the reference for beam alignment is the same as for patient alignment, i.e., two orthogonal pairs of X-ray tubes and flat panel detectors (Fig. 7.11). This means that whenever a geometrical property needed to be assessed (e.g., isocentricity), one should first evaluate beam and X-ray separately and then combine these measurements by testing the colinearity between beam and X-ray imaging system. Concerning the gantry, our commissioning procedure started with an assessment of mechanical isocentricity (see an example of the performances in Fig. 7.8). We then moved to a "star shot" test to evaluate the beam isocentricity. Since the beam is magnetically steered, this property is in principle a function of the energy, so such test was repeated for a number of representative energies (see an example of the results in Fig. 7.9). Last but not least, the overall beam-pointing accuracy depends on the performance of the patient positioning system that had to be characterized for all possible couch angles, isocenter position, and a broad set of weights (Fig. 7.10).

7.2.2 Monitor Chamber Calibration

The aim of monitor chamber calibration is to establish a direct relationship between the number of protons delivered and the monitor units (MUs) read by the monitor chambers in the nozzle (IC2/3; see Fig. 7.11). Whenever a reference measurement of absolute dose is needed in radiation therapy, a code of practice has to be followed. Mainly for historical reasons (no PBS techniques were developed when the current code of practice, i.e., IAEA Code of Practice TRS 398, was written), there are no reference conditions of measurement specifically defined for active beam delivery techniques in proton therapy.

However, several studies were published where such conditions are proposed [6, 9, 14]. In our facility we used two methods inspired by the methods of PSI [14] and GSI [9].

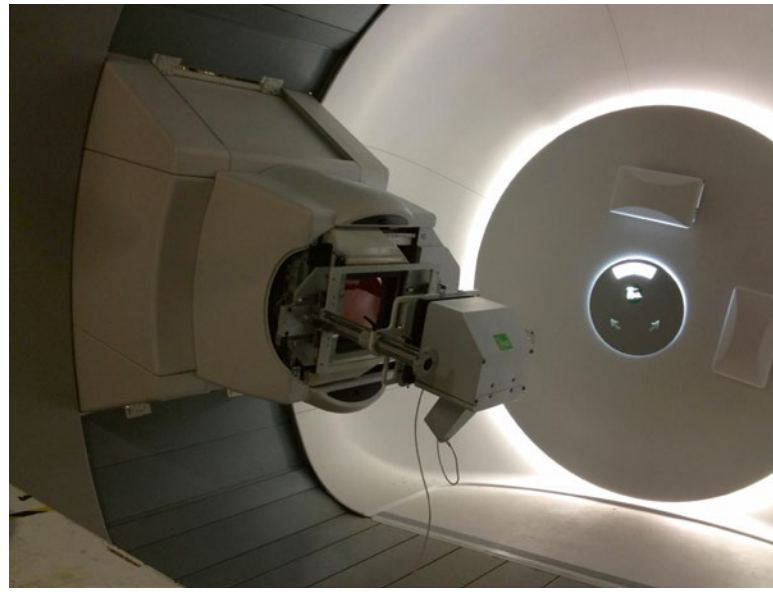

Fig. 7.5 Experimental setup to measure spot properties in the transverse plane for different gantry angles, energy, and position in the plane

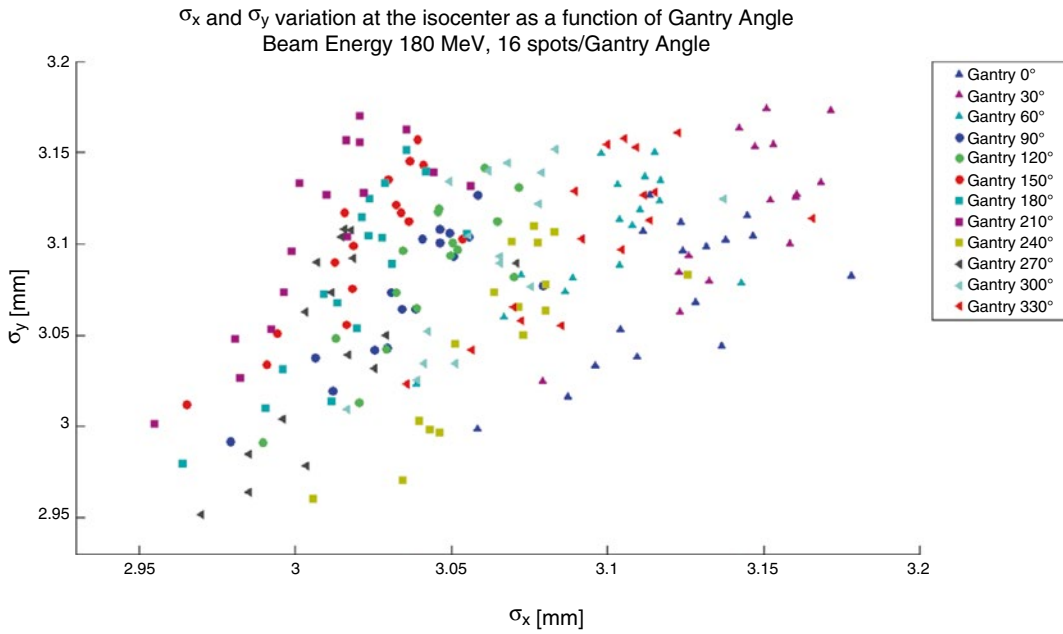

Fig. 7.6 Variation in spot size in the isocenter plane as a function of position in the plane and gantry angle

The first method is based on a Faraday cup (Fig. 7.12) where 10^{-4} mbar of vacuum was created and high voltage (HV) (≈1200 V) was applied in order to have the maximum yield from the device. The incoming protons hitting the thin entrance window travel along the vacuum space until they hit a copper block at the end of the vacuum. The vacuum is used to prevent protons interacting in this space, while the HV is applied in order to eliminate electron contamination in the signal. Protons reaching the copper block are absorbed and their charge is registered with an electrometer. Dividing this value by the proton charge, the *number* of protons hitting the entrance

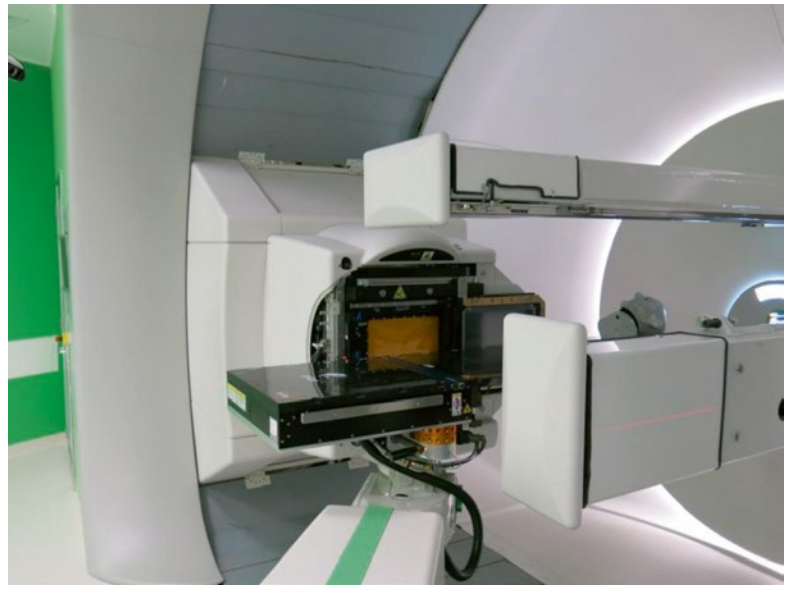

Fig. 7.7 X-ray-based beam and patient alignment system. The two flat panels are extracted, thus being in imaging position. The X-ray tubes are located within the nozzle and behind the rolling floor

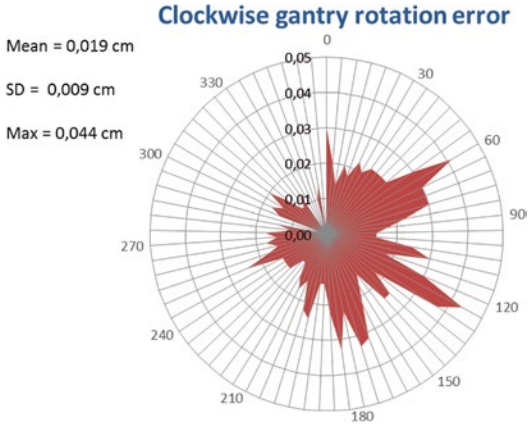

Fig. 7.8 Mechanical isocentricity of the gantry: The difference (in cm) between nominal and intended gantry position is shown as a function of the gantry angle. All differences are within 0.5 mm

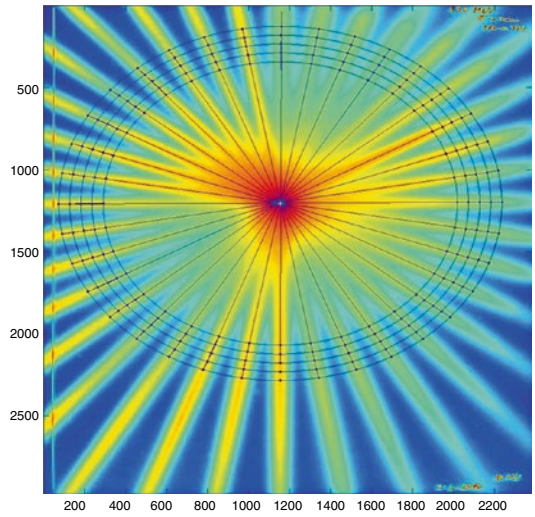

Fig. 7.9 Results of the "star shot" test for 150 MeV protons and gantry angles from 180° to 350°

window can be derived. Since not all protons hitting the entrance window reach the copper (due to interactions with the entrance window itself), a Monte Carlo simulation of the exact geometry of the Faraday cup was performed to evaluate these losses at three different energies (70, 160, and 220 MeV). The correction factors estimated are 1.20 %, 0.84 %, and 0.79 % for the three energies, respectively. We then delivered single spots of 1MU/spot with 15 different energies (from 70 to 220 MeV with an energy step of 10 MeV). The results are summarized in Fig. 7.13.

The second method combines ionization chamber (Advanced Markus – IBA Dosimetry) measurements and Monte Carlo simulations (TOPAS [15]). The chamber was placed at 2 cm depth in a water phantom and mono-energetic layers (10×10 cm^2, 0.25 cm of spot spacing and 1MU/spot) were delivered in order to determine the absolute dose value in the plateau region of

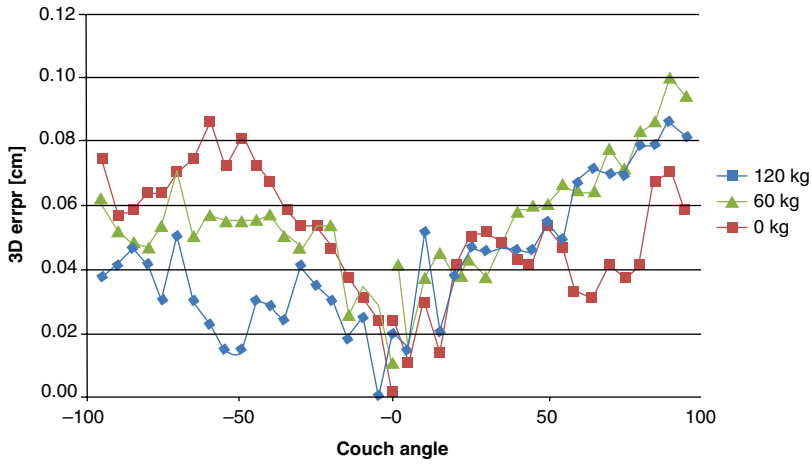

Fig. 7.10 Geometrical accuracy of the patient positioning system

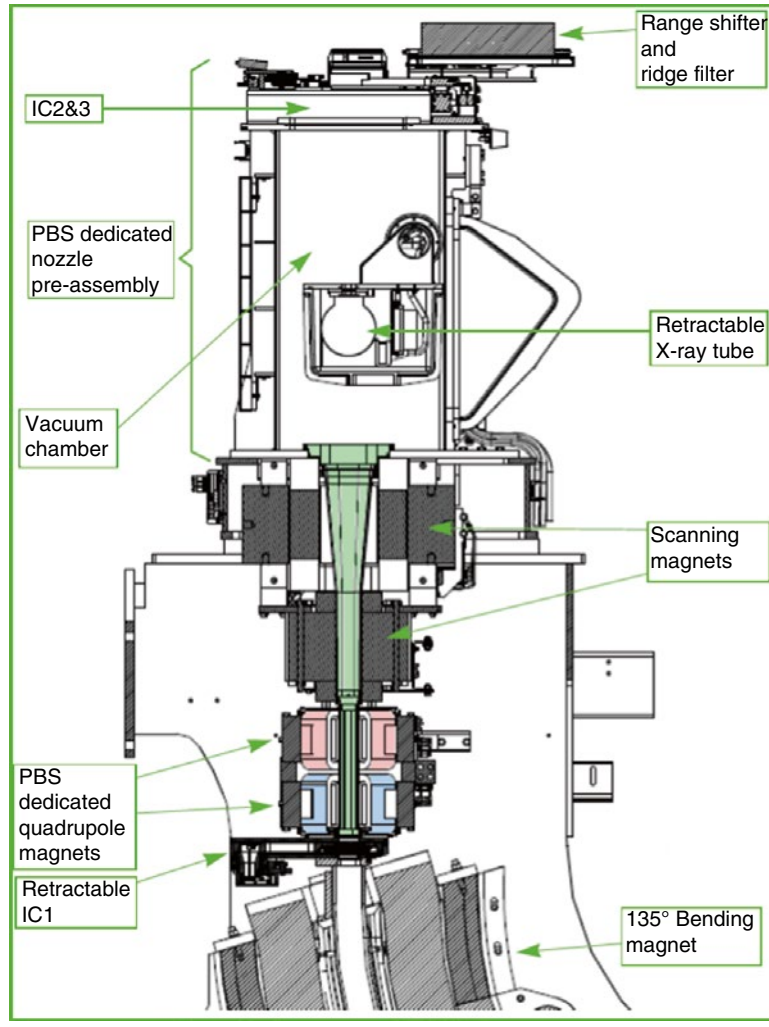

Fig. 7.11 Schematic representation of the "nozzle": In this picture, the beam direction is from the *bottom* to the *top*, i.e., the isocenter is 30–40 cm from the range shifter (Picture courtesy of IBA)

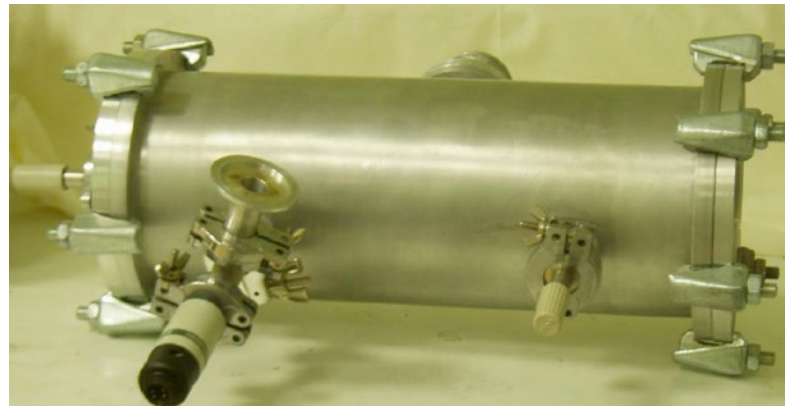

Fig. 7.12 Faraday cup (Courtesy of E. Grussel)

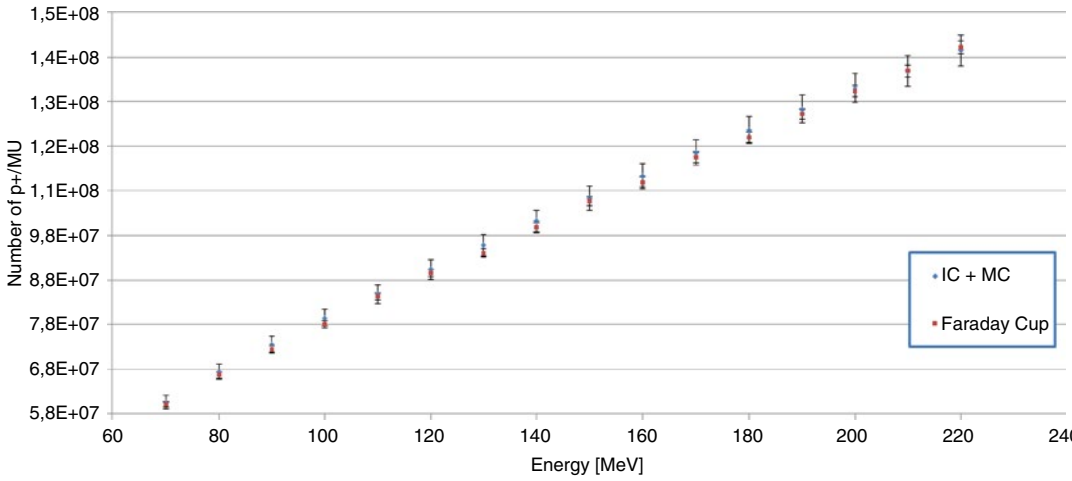

Fig. 7.13 Comparison between the two methods used to calibrate the monitor chambers

the Bragg peak where there is a small dependence with respect to chamber positioning errors, thus making the measurement geometry reliable. The experimental setup is shown in Fig. 7.14.

The same setup was simulated in our Monte Carlo code until a statistical uncertainty better than 0.05 % was reached. Knowing the number of primary protons simulated, the dose at 2 cm in water simulated and measured, we used the following formula to obtain the number of protons/spot delivered:

$$N^{p}_{IC+MC} = N^{p}_{MC} \frac{D_{IC}}{D_{MC}}$$

where N^{p}_{IC+MC} is the number of protons actually delivered, $N_{MC}{}^{p}$ the number of primary histories in the Monte Carlo simulation, and D_{IC} and D_{MC} the dose measured and simulated, respectively. The results are shown in the graph of Fig. 7.13.

7.3 Treatment Planning System

Typically, the data needed to create a scanning beam model in a treatment planning system are the following:

1. A set of integral depth dose (IDD) curves from minimum to maximum energy, typically in steps of 5–10 MeV (Fig. 7.15). These depth dose curves are acquired in a "small beam vs. large detector geometry," in our case with an 8 cm diameter parallel plate ionization chamber. The large size of this detector aims at collecting the whole signal due to proton interactions in water. Comparison with Monte

Carlo calculations shows that this size is actually not enough to acquire signal due to the small but nonzero contributions of protons with a large scattering angle. As a consequence, we corrected our experimental data with Monte Carlo calculations, thus achieving a better agreement with measurements and calculations.

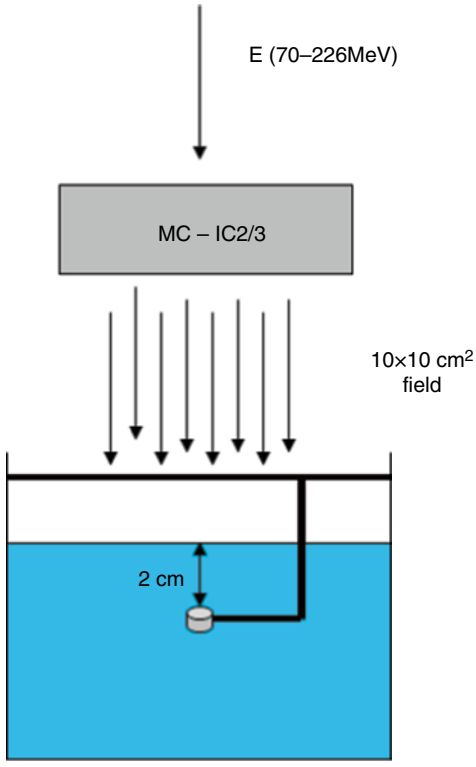

Fig. 7.14 IC measurements setup

2. For each spot belonging to different energy options, its energy, size, symmetry and shape should be provided via the measurement of the transversal properties of the central spot. Here it is interesting to notice that beam modeling makes an important assumption, i.e., variations in spot size with respect to gantry angle and position in the transverse plane are negligible for the sake of dose calculation. This significantly reduces the number of measurements to acquire for the sake of beam modeling, but a large number of measurements (see, e.g., Fig. 7.6) have to be taken to verify this assumption. Additionally, if the machine's performance is such that this assumption does not hold, there is no way to correct for it. Spot size and shape has to be measured for a number of distances (in our case five) with respect to the snout end, in order to model divergence effects.
3. For each energy, data about the beam output should be provided in order for the TPS to calculate the monitor units needed to deliver a given absolute dose. In our case, the information was acquired via a reference ionization

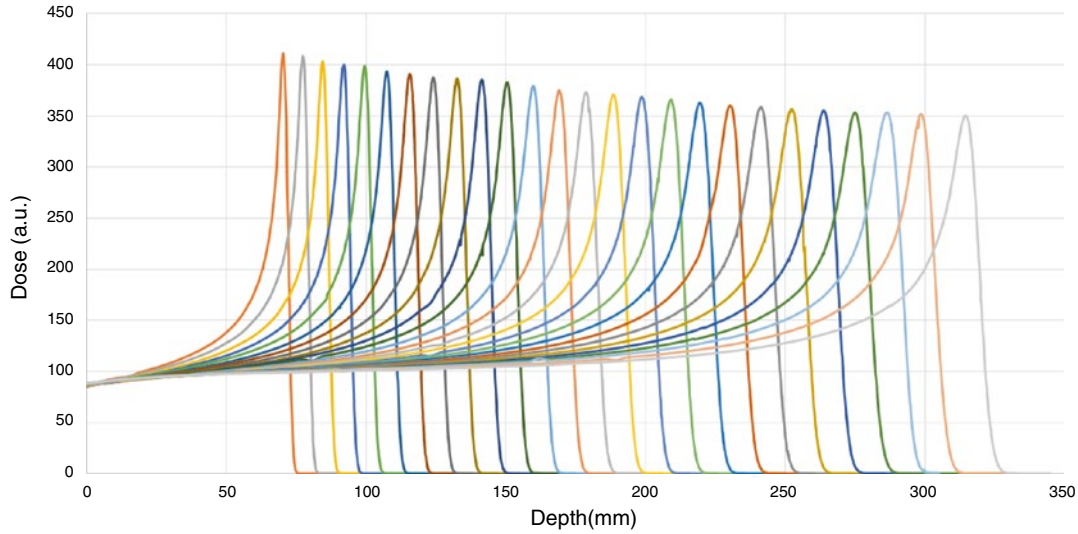

Fig. 7.15 Set of integral depth dose curves needed for beam characterization in the TPS

chamber, making measurements of dose associated with a monoenergetic layer with a fixed number of monitor units. The ionization chamber was positioned at 2 cm depth in water, a depth associated with a shallow dose gradient along the depth for all energies we measured. In such a way, we could acquire measurements that were not too sensitive with respect to small uncertainties in the chamber position.

4. The preabsorber/range shifter is modeled in a different way according to any given TPS. Taking into account the effect of a preabsorber is not trivial, particularly when it is located at some distance from the patient (in our case, the maximum distance between preabsorber and isocenter is about 40 cm), as a small error in modeling large-angle scatter may translate to a larger error in the calculated dose. In our case, data to characterize the physical properties of the range shifter were needed, while actual beam measurements were used for verification but not for characterization.

The beam model, once available, was tested via a set of comparison between measurements and calculations. Such comparisons started from elementary beam properties (e.g., spot size in air) and then built up in terms of complexity and clinical significance, e.g., moving to the dose distribution to a single spot in water, then to monoenergetic 2D layers, then to "box-like" dose distributions, up to planning and delivery of clinically realistic plans in heterogeneous phantoms ("end-to-end tests") that will be briefly described here. The main advantage of an end-to-end test is the possibility of having a measurements assessing the agreement between calculated and measured dose when all steps of the clinical workflow are included: CT scan, CT calibration curve, dose calculation, patient alignment, and treatment delivery. Since the clinical indications to be initially treated in our center are intracranial lesions, we carried out our tests using an anthropomorphic phantom with quite a detailed representation of the human anatomy (Fig. 7.16). After the phantom was scanned in our CT unit and a CT calibration curve was available, we asked a radiation oncologist to draw the target contours representative for a number of clinical indications (e.g., neurinoma, meningioma, glioma, base of skull chordoma), we designed a treatment plan using clinically applied dosimetric constraints to target and organs and risk, we aligned the phantom with the same protocols used in the clinic, and we delivered the plan. By measuring the delivered dose at three depths in the phantom with dose-calibrated gafchromic films, we could assess the overall agreement between prescription and delivery for our treatment chain (see example of the results in Fig. 7.17). The difference between calculation and measurements are such that the gamma index passing rate with 3 %/3 mm dose and distance to agreement parameters is typically above 95 %, with a maximum of the gamma value below 1.5. The largest discrepancies between measurements and calculations are typically found at shallower depths when a

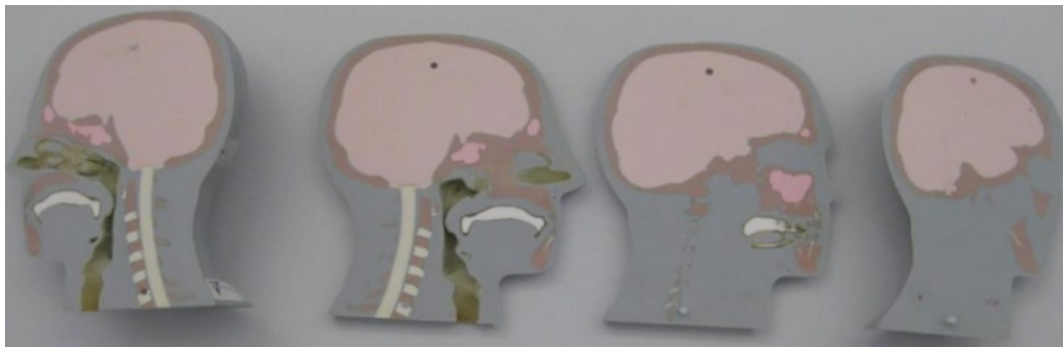

Fig. 7.16 Anthropomorphic phantom used in end-to-end tests

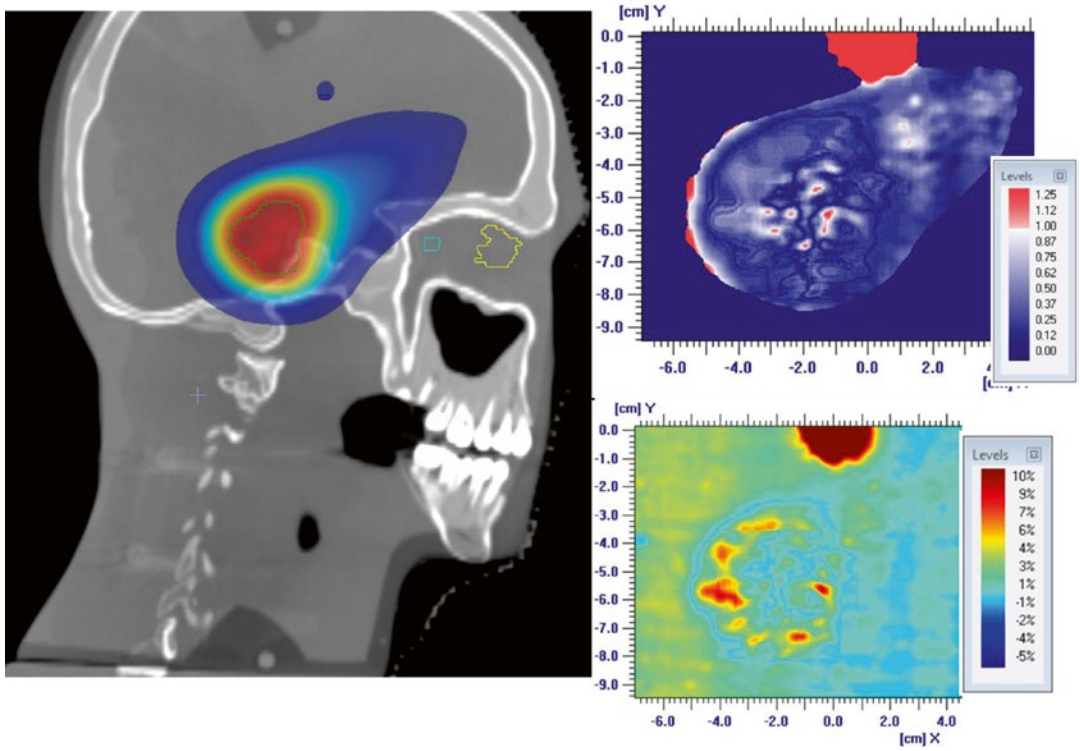

Fig. 7.17 Results of an end-to-end test. Dose calculation in the anthropomorphic phantom (*left*), gamma analysis (*upper right*), dose difference (*bottom right*)

preabsorber is used, and the more distant the preabsorber from the patient, the higher the differences.

7.3.1 Plan Robustness Analysis

The end-to-end test shortly presented in the previous paragraph tells about differences between prescribed and delivered dose and gives information about the likely uncertainties with respect to the nominal plan. However, this test does not allow to estimate the effects of setup error and range uncertainties on the delivered dose. For a fully satisfactory inclusion of range and setup uncertainties in the planning procedure, methods such as robust optimization are probably the only viable solution in the long term (see section 7.4.1 and Chap. 10 for more details). While we wait for robust optimization to be routinely available in commercial treatment planning systems, we should at least find methods to evaluate the robustness of plans generated with conventional planning techniques and that are being delivered in clinical practice.

In photon therapy, the common practice still consists of defining the goals to be achieved by treatment plan optimization via the nominal target and organs at risk (OAR) doses. This approach, albeit improvable, is acceptable given the physical properties of photons. If proton therapy with PBS aims at becoming a treatment option for most/all lesions currently treatable with photons, the planning procedure should handle setup errors and organ motion in a more appropriate way also in the phase of plan evaluation and dose reporting. In photon therapy, there are examples showing the potential of probabilistic dose reporting (see, e.g., [19]), i.e., an approach where the results of treatment planning are presented in terms of probability distributions of relevant dosimetric indices in a population. As a consequence, the dose in the target is not reported as, say, the minimum dose in the PTV, but as a probability that the minimum dose in the

CTV will be greater or equal than a threshold. The computational burden needed to calculate the probability distributions is usually manageable with current computers, so there are no technical obstacles for the introduction of probabilistic dose reporting in clinical practice.

Another field where probabilistic dose reporting should become common practice is the comparison between proton and photon dose distributions. Treatment planning studies comparing protons and photons are carried out quite often these days, and so far it is common practice to compare target dose distributions using the PTV, which might overestimate the benefits of protons in case the PTV is defined in the same way as for photon therapy, or it might underestimated them in case it is defined too conservatively. The use of probabilistic dose reporting would lead to more fair comparisons between the two radiotherapy techniques.

This is the reason why we developed an in-house software that allows to quantify the likely effect of uncertainties on the delivered dose distribution. The concept behind this software is quite simple, i.e., to add to the nominal plan quantitative information about the likely spread of the most relevant dosimetric indices as a consequence of geometrical and range uncertainties. In order to obtain such an information, a relative large set of dose recalculation is involved, typically between 200 and 250, in order to sample the space of the possible combination between uncertainties. At the moment our software does simulate translational setup errors and range errors, but rotational errors and uncertainties due to anatomy changes are not taken into account (yet). One common issue with this kind of uncertainty analysis is how to display the results in an informative yet concise way. In our software tool, we implemented several visualization methods, such as dose volume histogram band, worst-case scenario, maximum dose difference (see example in Fig. 7.18), and probability distribution of single dosimetric indices, and we haven't come up yet with a single visualization that satisfies all needs.

7.4 Improving Treatment Planning and Delivery

7.4.1 Robust Optimization

Currently, most treatment planning techniques with pencil beam scanning are based on the use of a planning target volume (PTV), which is an appropriate tool to take into account geometrical uncertainties in plan optimization and reporting as long as:

1. The PTV margins are appropriately set, given the level of uncertainties one wants to be protected against.
2. The dose distribution in the PTV is as homogeneous as possible.
3. The dose distribution in the PTV is invariant for uncertainties within the level one wants to be protected against (e.g., typically 3–10 mm according to the disease site).

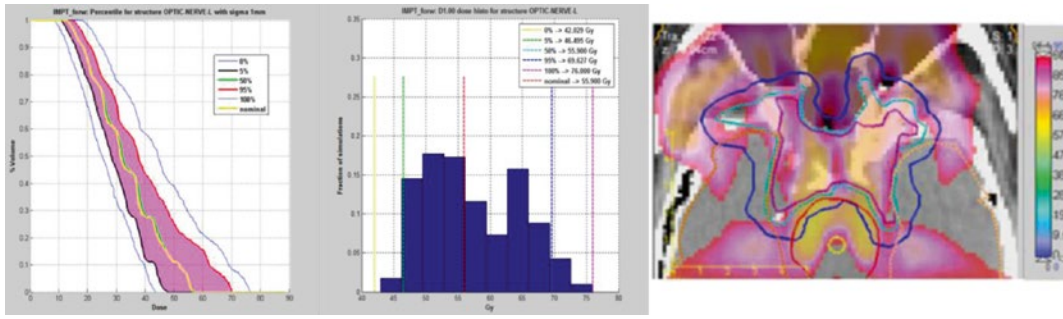

Fig. 7.18 Methods to visualize the results of robustness analysis applied to the intensity modulated proton therapy (IMPT) plan of a base of skull lesion: On the *left*, a DVH band for the optic nerve, in the center the probability distribution of maximum dose in the optic nerve, on the *right* the probability that a voxel will receive a dose different from the nominal plan by more than 2 Gy

While the first two conditions can be ensured via planning protocols, the last assumption is in general not true with protons.

The effect of range uncertainties and setup errors is an issue regardless whether passive scattering or PBS is applied; pencil beam scanning, however, is potentially more affected by this problem for two main reasons:

(a) For any given IMPT field, dose heterogeneities are present not only at the edges of the target volume but also within the target itself; while with scattering and single-field optimization range uncertainties and setup errors are in general going to result in dose fluctuations at the target edges, IMPT dose distributions are based on the assumption that anywhere within the target a homogeneous dose may be achieved via the sum of (highly) modulated fields.
(b) Since spot weights are defined via computer optimization, and since cost function are composed only by dosimetric parameters, anything that minimizes the residual cost will be "accepted" by the minimization algorithm. As long as a cost component related to range uncertainty is not present in the cost functions, there is no way to explicit control the effect of range uncertainty in an IMPT dose distribution.

At the moment, the potential dosimetric errors due to the application of IMPT are mostly being handled in an implicit (or defensive) way, e.g., preferring single-field optimization (SFO) when IMPT is not strictly needed. Details of SFO and IMPT treatment planning with scanning proton pencil beam is given in Chapter 12.

The problem is then how to "steer" the optimization of IMPT plans to take into account additional parameters other than dosimetric indices on a nominal plan. Better optimization approaches are needed for IMPT to become a treatment option for most treatment sites, so the issue of assessing and ensuring plan "robustness" has then become a "hot topic," at least in research studies. Plan robustness can be defined as a metric quantifying the extent to which a delivered dose distribution will change with respect to the planned dose distribution when either positioning errors and/or range errors and/or anatomy changes occur during the treatment course.

From the optimization point of view, one can see robustness as an issue related to uncertainty in the input data. This uncertainty should be taken into account in the cost function, and different approaches have been developed in the recent years to accomplish that.

These robust optimization methods can be divided into two broad categories:

1. These are approaches assuming previous knowledge of the probability distribution of errors. Most proposal for robust optimization in photons use this approach. A robust plan may then be obtained either via "coverage probability" approaches (see, e.g., [20]), where each voxel has an assigned probability of presence for the target or an OAR, or via the optimization of the expectation value of tumor control and normal tissue complication probabilities [23]. Under this assumption, the quantity to be minimized is not a nominal plan but rather the expected value of the residual cost over the possible values of range uncertainties and setup errors weighted according to their probability. For proton therapy, robust optimization based on probabilistic planning has been proposed by Unkelbach et al. [21].
2. These are approaches that do not make assumptions of the probability distribution of errors. Pflugfelder and colleagues [16] implemented a so-called worst-case optimization, initially proposed by Lomax et al. [12] and applied this to the evaluation of plan robustness (e.g., [11]). The basic concept of worst-case optimization is the following: via the simulation of range uncertainties and positioning errors, one can obtain for each voxel the worst-case scenario (e.g., minimum dose for a target voxel and maximum dose for an OAR voxel). The dose distribution composed by all worst-case voxels is then included in the cost function.

The worst-case optimization is well manageable from the computational point of view and can provide robust dose distributions. On the other hand, the worst case dose distribution may be (and typically is) unphysical, because the weight configuration that creates the worst dose in the i-th voxel may or may not be the same that creates the worst dose in the j-th voxel. This means that it

has the risk of being overly conservative, thus deteriorating the nominal dose distribution beyond what is actually needed. Fredriksson et al. more recently proposed a method to achieve plan robustness through minimax optimization [5]. The main difference with respect to the work of Pflugfelder et al. [16] is that only physically realizable dose distributions are considered, i.e., the correlation between uncertainties in different voxels is taken into account. As a result, dose distributions tend to achieve a better compromise between target coverage and OAR sparing compared to alternative methods such as SFO plans or plans obtained by overriding the CT number of low-density tissue (e.g., the lung).

7.5 Treatment of Moving Tumors

From both a dosimetric and clinical perspective, proton therapy is an appealing treatment option for tumors in the liver or in the lung, sites that are both affected by respiratory motion. Unfortunately, it is likely that the technical hurdles yet unsolved in the treatment of moving targets is probably the Achilles' heel of PBS when compared to proton therapy delivered with passive scattering and uniform scanning ("wobbling"). For PBS to become a mature technique on moving targets, two main developments should occur and be available on a large scale via commercial solutions:

1. Treatment planning platforms where the timing of the delivery is taken into account in the dose calculation and with the effects reflected on a dose distribution. In other words, it should be possible to combine 4D patient anatomy representation (e.g., via 4D CT) together with delivery sequences where time information is available in principle for every spot (or at least every layer), in such a way that the interplay effects are evaluated at the level of each patient. Such an evaluation should then allow the user to decide if rescanning is needed and which type and level of rescanning is the most appropriate. For instance, one should be able to answer for a specific patient a question such as: is it better to perform 3 volumetric rescans of the 20 % highest weighted spots, or 4 in-layer rescans of the 2 most distal layers?
2. In the phase of treatment delivery, one needs a high degree of freedom in beam delivery (e.g., energy changes fast enough to allow for volumetric repainting) and an imaging/monitoring tool to follow (and in principle account or adapt to) the patient breathing motion (e.g., the combination of surface detection tools for continuous motion detection to trigger gating combined with periodic fluoroscopic imaging to verify the relation between internal motion and surface motion).

Last but not least, there are anatomical changes that occur on the time scale of seconds (e.g., those due to breathing), but there are also potentially significant anatomy changes happening over the time scale of days to weeks that call for adaptive treatment techniques in protons even more than in photons. This is not a specific problem of pencil beam scanning, but it is rather a potentially serious issue of proton therapy regardless of the beam delivery technique. It is fair to say that when it comes to soft tissue imaging for both patient positioning and treatment adaptation, proton therapy is in the paradoxical situation of lagging behind state-of-the-art photon therapy even though these tools are more crucial for protons than for photons. Cone beam CT (CBCT), a tool which is now routine in several photon clinics, is at its very early steps of clinical implementation in proton therapy, and it is possible that the image quality achievable with CBCT will remain suboptimal for the sake of proton dose recalculation. This is the reason why CBCT may not be as successful in protons as it is in photon therapy. Alternative methods, such as the installation of a diagnostic quality CT in the gantry room, are being investigated in several centers, and the first results about their suitability for proton therapy will be available in the next few years.

References

1. Bentzen S. Theragnostic imaging for radiation oncology: dose-painting by numbers. Lancet Oncol. 2005;6(2):112–7.
2. Bernatowicz K, Lomax AJ, Knopf A. Comparative study of layered and volumetric rescanning for differ-

ent scanning speeds of proton beam in liver patients. Phys Med Biol. 2013;58(22):7905.
3. Engelsman M, Schwarz M, Dong L. Physics controversies in proton therapy. Sem Rad Oncol. 2013;23:88–96.
4. Flanz J. Particle beam scanning. In: Paganetti H, editor. Proton therapy physics. Boca Raton(FL): CRC Press; 2012.
5. Fredriksson A, Forsgren A, Hardemark B. Minimax optimization for handling range and setup uncertainties in proton therapy. Med Phys. 2011;38:1672.
6. Gillin MT, Sahoo N, Bues M, Ciangaru G, Sawakuchi G, Poenisch F, Arjomandy B, Martin C, Titt U, Suzuki K, Smith AR, Zhu XR. Commissioning of the discrete spot scanning proton beam delivery system at the University of Texas M.D. Anderson Cancer Center, Proton Therapy Center, Houston. Med Phys. 2010;37(1):154–63.
7. Grassberger C, Dowdell S, Lomax AJ, et al. Motion interplay as a function of patient parameters and spot size in spot scanning proton therapy for lung cancer. Int J Radiat Oncol Biol Phys. 2013;86(2):380–6.
8. Hall EJ. Intensity-modulated radiation therapy, protons, and the risk of second cancers. Int J Radiat Oncol Biol Phys. 2006;65(1):1–7.
9. Jäkel O, Hartmann GH, Karger CP, Heeg P. A calibration procedure for beam monitors in a scanned beam of heavy charged particles. Med Phys. 2004;31(5):1009–13.
10. Kozak KR, Smith BL, Adams J, et al. Accelerated partial-breast irradiation using proton beams: initial clinical experience. Int J Radiat Oncol Biol Phys. 2006;66(3):691–8.
11. Lomax AJ. Intensity modulated proton therapy and its sensitivity to treatment uncertainties 1: the potential effects of calculational uncertainties. Phys Med Biol. 2008;53(4):1027–42.
12. Lomax AJ, Pedroni E, Rutz H, et al. The clinical potential of intensity modulated proton therapy. Z Med Phys. 2004;14:147–52.
13. Pedroni E, Böhringer T, Coray A, et al. Initial experience of using an active beam delivery technique at PSI. Strahlenther Onkol. 1999;175(Suppl II):18–20.
14. Pedroni E, Scheib S, Böhringer T, Coray A, Grossmann M, Linand S, Lomax A. Experimental characterization and physical modelling of the dose distribution of scanned proton pencil beams. Phys Med Biol. 2005;50:541–61.
15. Perl J, Shin J, Schümann J, Faddegon B, Paganetti H. TOPAS – an innovative proton Monte Carlo platform for research and clinical applications. Med Phys. 2012;39:6818–37.
16. Pflugfelder D, Wilkens JJ, Oelfke U. Worst case optimization: a method to account for uncertainties in the optimization of intensity modulated proton therapy. Phys Med Biol. 2008;53(6):1689–700.
17. Schneider U, Lomax A, Pemler P, et al. The impact of IMRT and proton radiotherapy on secondary cancer incidence. Strahlenther Onkol. 2006;182:647–52.
18. Schulte RW, Bashkirov V, Loss Klock MC, et al. Density resolution of proton computed tomography. Med Phys. 2005;32(4):1035–46.
19. Schwarz M, van der Geer J, Van Herk M, et al. Impact of geometrical uncertainties on 3D CRT and IMRT dose distributions for lung cancer treatment. Int J Radiat Oncol Biol Phys. 2006;65:1260–9.
20. Stroom JC, de Boer HC, Huizenga H, et al. Inclusion of geometrical uncertainties in radiotherapy treatment planning by means of coverage probability. Int J Radiat Oncol Biol Phys. 1999;43:905–19.
21. Unkelbach J, Bortfeld T, Martin BC, et al. Reducing the sensitivity of IMPT treatment plans to setup errors and range uncertainties via probabilistic treatment planning. Med Phys. 2009;36(1):149–63.
22. Widesott L, Lomax AJ, Schwarz M. Is there a single spot size and grid for intensity modulated proton therapy? Simulation of head and neck, prostate and mesothelioma cases. Med Phys. 2012;39(3):1298–308.
23. Witte MG, van der Geer J, Schneider C, et al. IMRT optimization including random and systematic geometric errors based on the expectation of TCP and NTCP. Med Phys. 2007;34(9):3544.
24. Xu XG, Bednarz B, Paganetti H. A review of dosimetry studies on external-beam radiation treatment with respect to second cancer induction. Phys Med Biol. 2008;53:R193–241.

Treatment Planning for Protons: An Essay

8

Hanne Kooy

8.1 A Brief History of Protons at the Harvard Cyclotron Laboratory

The first proton radiotherapy patient was treated in 1957 at the Berkeley Radiation Laboratory. At the Harvard Cyclotron Laboratory, treatments commenced shortly after in the early 1960s under the direction of the Massachusetts General Hospital neurosurgeon Dr. Raymond Kjellberg. Neurosurgeons were well equipped to use the precision of proton beams without the availability of 3D imaging technologies such as CT. Their appreciation of the 3D cranial anatomy projected on X-rays sufficed to treat neoplasms such as pituitary abnormalities and arterial venous malformations. Both Dr. Kjellberg in Boston and Dr. Leksell in Stockholm pioneered the use of protons in the cranial anatomy. Dr. Kjellberg's program, however, had ready access to the proton beam at the HCL (Fig. 8.1). Dr. Leksell's program did not have ready access which led to the invention of the Leksell Gamma Knife as an alternative therapeutic system for stereotactic radiosurgery. Protons were thus the first modality used in cranial stereotactic radiosurgery, while the Gamma Knife made cranial stereotactic radiosurgery a standard modality.

A second program for eye treatments commenced under the direction of Dr. Evangelos Gragoudas from the Massachusetts Eye and Ear Infirmary in Boston. Again, the static and visually apparent anatomy of the eye and neoplasm afforded effective use of localized proton radiation.

Both programs were effective without the use of volumetric imaging or dose calculations; both were sufficiently served by manual calculation processes.

A third program in large-field "conventional" radiotherapy commenced in 1974 under the aegis of Dr. Herman Suit from the department of radiation oncology at Massachusetts General Hospital. The introduction of this program did require the use of volumetric data sets. Dr. Michael Goitein was one of the first to combine volumetric image data provided by the now available CT scanners and computational algorithms in a treatment planning system, dubbed Rx, for proton radiotherapy. Rx presented the physician and physicist with the necessary information and confidence to treat internal neoplasms reconstructed from the volumetric data.

All three programs continued at the HCL until 2001 and were transferred, uninterrupted, to the Northeast Proton Therapy Center (now the F.H. Burr Proton Therapy Center) on the campus of the Massachusetts General Hospital, the

H. Kooy, PhD
Department of Radiation Oncology, Massachusetts General Hospital, Harvard Medical School, Boston, MA, USA
e-mail: hanne.kooy@gmail.com

A.K. Rath, N. Sahoo (eds.), *Particle Radiotherapy: Emerging Technology for Treatment of Cancer*,
DOI 10.1007/978-81-322-2622-2_8

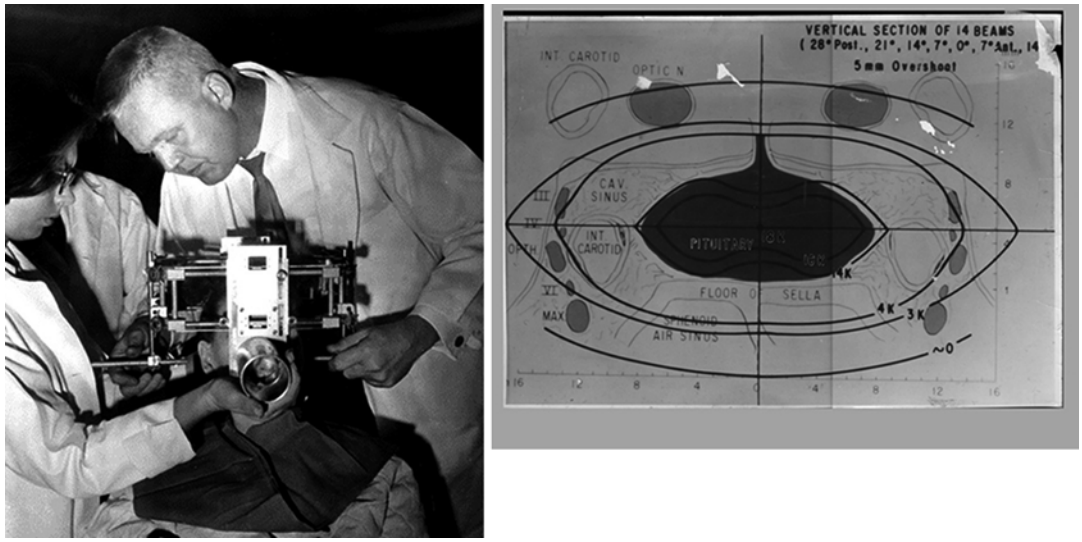

Fig. 8.1 Dr Raymond Kjellberg (and assistant) manipulating the stereotactic frame for a proton radiosurgery patient (*left*). An example dose calculation (not for this patient) shows the dose hand calculation for a pituitary lesion using 14 proton beams that penetrate beyond the target volume, but their composite dose creates a focal region with sharp penumbra

second (the first was Loma Linda CA) proton facility within a hospital.

8.2 Implication for Modern Radiotherapy

The precision of proton beams requires concomitant precision in treatment planning capabilities, in treatment delivery, and in patient positioning. Thus, proton radiotherapy in the 1980s already required and implemented these now assumed obvious requirements for precision radiotherapy. The limitation in proton energy up to 160 MeV at the HCL necessitated a focus on precisely those neoplasms that proved particularly suited for early application of proton radiotherapy: those in the head and neck, in the cranium, and soft tissue sarcomas. It is indisputable that proton radiotherapy, as demonstrated in those sites and especially for chordomas, proved the axiom of radiotherapy: increasing dose while sparing normal tissue increases cure. It should be noted that the HCL did not, per se, demonstrate the superiority of protons. It primarily demonstrated that when precision in dose delivery is achieved, outcome can be improved. It secondarily demonstrated that protons well achieve such precision.

It was the well-understood physics of proton interactions in matter, i.e., scatter and energy loss, that allowed the precise manipulation of scattered and modulated (in energy and intensity) protons by mechanical means to create spread-out Bragg peak, SOBP, fields of variable range, and modulation. The use of apertures and range compensators, as modeled in the Rx treatment planning system, provided highly conformal 3D SOBP dose fields where the aperture served to provide lateral conformance, as in photon fields, and the range compensator served to provide distal target conformance to "stop" the proton field beyond the distal surface of the target.

Proton radiotherapy at HCL in the early 1980s was in sharp contrast to the parallel practice of radiotherapy. The first relied on now assumed obvious practices in precision therapy (Fig. 8.2), while the latter relied on X-ray simulation and simple 2D calculation methods. It would take two decades until photon radiotherapy would "catch up" and achieve the clinical performance of 1980 proton radiotherapy. Our question now is

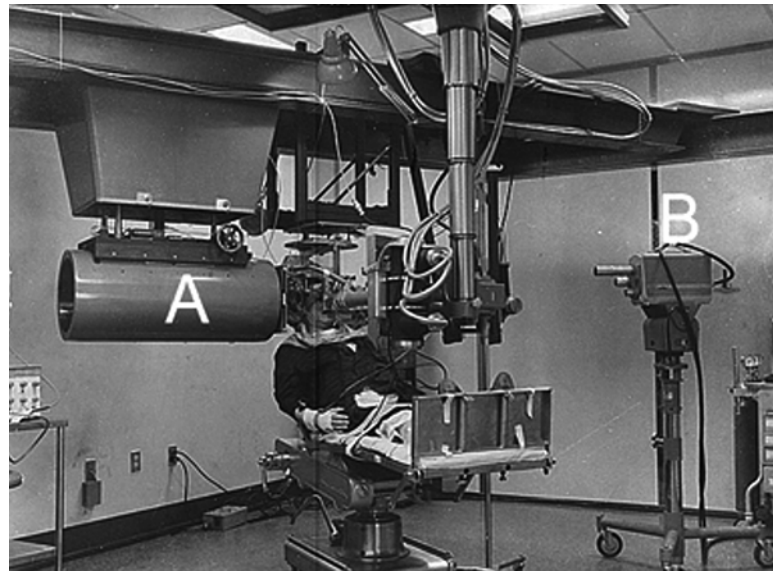

Fig. 8.2 Patient setup and verification in the stereotactic treatment room at the Harvard Cyclotron Laboratory. A water-filled variable range shifter (*A*) permitted variable penetration into the cranium, while X-ray (*B*) permitted setup verification. The treatment technology thus implemented now assumed standards of precision

whether photon radiotherapy can maintain parity to proton radiotherapy to further the modern aims of radiotherapy.

8.3 Aims of Modern Radiotherapy and Proton Radiotherapy

Modern radiotherapy aims to optimize the response to radiation by minimizing dose to non-involved tissue to decrease normal tissue complications and to increase in target dose. These aims require improved differential imaging and identification of inter-target disease, improved localization (even in real time) with on-treatment imaging and target dose modulation, improved patient-specific response, and, now most importantly, improved quality of life for the patient.

These requirements require the application of in vivo and biological imaging capabilities, more advanced treatment planning and delivery systems, and, significantly, better understanding and utilization of differential biological response in the target and healthy tissues. Only some of these are furthered by external beam radiotherapy in the treatment management of the patient. All, however, need to synchronize over the course of treatment. It is this synchronization that is not promoted by the current treatment planning architectures. Instead, treatment planning for modern radiotherapy must be deployed in an architecture that permits its functions to be distributed and accessed in their appropriate operational location. Current treatment planning systems are inconsistent with this requirement.

Radiotherapy operates in a safe zone of dose fractionation imposed by dose toxicity of the, at least originally, large volumes of irradiated healthy tissues. Modern conformal dose treatments reduce the volume of irradiated healthy tissues and offer the opportunity to increase fraction doses and modulate dose within a target. If such opportunity benefits the patient, proton and ion radiotherapy outperform photon radiotherapy.

It is recognized that physical, chemical, and genetic regional differences can exist within a single target. It is assumed that in such regions, differential dose delivery in terms of local ionization differentials (i.e., different lineal energy transfer, LET, distributions) can improve response through enhanced local biological response. Ion radiotherapy has a twofold advantage compared to photon radiotherapy. The application of different doses to different regions within a target will benefit from that modality that can achieve the sharpest regional dose gradients. The use of modulated LET

distributions can only be achieved with ion radiotherapy. Thus, proton and ion radiotherapy outperform photon radiotherapy where spatial and biological differentials are expected to improve outcome.

Imaging requirements prior and during treatment are core to the aims of modern radiotherapy. The original workflow model assumed that the treatment planning process preceded and remained static over a set of treatment delivery sessions. Treatment planning occurred as a stand-alone activity whose result was the treatment plan and the patient setup reference geometry to be applied and referenced daily. The daily effort to minimize inaccuracies and achieve presumed compliance was to reposition the patient to this static representation. Thus, the mitigation of all inaccuracies, and assumed worst case, had to be incorporated in the treatment plan to achieve acceptable dose coverage (and avoidance) over the time course of treatment. This process led to the definition of the planning target volume (PTV) as a geometric expansion of the target. This PTV expansion sufficed for photon treatments as the photon dose distribution in patient is invariant with respect to the patient's anatomy and geometric setup which equates dosimetric accuracy. An PTV expansion, or a pure geometric registration of the patient, does not suffice in proton treatments as the dose distributions is sensitive to geometry, and thus, geometry and dosimetry are strongly coupled, and one cannot serve as a surrogate for the other. Whereas geometric setup certainly serves as the best first corrective action, it does not in and of itself guarantee dosimetric accuracy even in XRT.

The optimal process re-images and re-plans the patient before treatment delivery and monitors during treatment for compliance to the adapted plan (and in the furthest extreme adapts the radiation field during treatment). Particle beams in these processes offer novel capabilities compared to photon beams. The particle beam, as a unit or as individual particles, can be readily detected in task-specific detection systems. These include geometric ionization chambers for position, solid state imaging planes for indirect spectroscopy of particle interaction products, and Faraday chambers for energy. These unique (compared to a photon beam) methodologies offer unique opportunities to obtain necessary inpatient information during treatment and can enable real-time feedback in the delivery process.

It is important to observe that the control parameters in ion radiotherapy – per spot charge position and energy – are more consistent than those – MLC leaf positions – in photon radiotherapy. For the latter, these leaf positions are an awkward (if necessary) transformation from the physical quantity – fluence – in patient. For ion radiotherapy, the spot parameters represent fluence in patient directly, are the parameters that are used to control the delivery, and are the parameters that are observed directly. There is no transformation from the intended to observed quantities, and treatment delivery observation can be directly translated to the dose in patient and used in a feedback control to maintain the correct dose in the patient under variable circumstances. Thus, particle radiotherapy can achieve better delivery performance when considering the modern aims of radiotherapy.

Effective use of particle radiotherapy is hampered by its label "expensive." Any therapy has to be of course cost-effective. This is, unfortunately, a subjective debate within a society and between societies. Nevertheless, if considered as a debate in terms of cost-benefit in development, deployment, and clinical effectiveness, the outcome should favor particle radiotherapy as many of the aims are better (and thus likely cheaper) achieved with particle radiotherapy. Looking back, of course, one should question that because proton radiotherapy in the 1980s was superior to photon radiotherapy and because the cost to achieve parity between the two modalities has been significant over three decades, perhaps we should have adapted protons more broadly earlier. We should pose the same question now where significant expenditures will be made to achieve the latest aims of radiotherapy and where ion radiotherapy may significantly improve on the achievement and efficacy of those aims.

8.4 Requirements for Treatment Planning

It is necessary to challenge the current model for treatment planning given the above stated aims and the necessary integration of up-to-date technologies in the treatment management processes. There are three facets in the current model. The first continues to emphasize the pretreatment static (over time) treatment plan model without explicit consideration of the dynamics of the possible daily changes in treatment or other changes incurred by clinical realities. The second perpetuates the deployment of treatment planning systems with a 1980s model of a "workstation" with a functionally overburdened software application that aims to achieve too many workflow steps within its confines. The third emphasizes algorithmic components but not computational architectures that promote data management, communication, and workflow processes.

The deployment of a single, heavy, and shrink-wrapped application makes it difficult and contrived to move the various functions that accommodate the adaptive radiotherapy workflow to their optimal locations. In contrast, modern computing paradigms emphasize service-oriented architectures that promote logical decomposition of computational and data management domains and promote distributed access to these services. These architectures are based on distributed and disjointed processes connected by communication protocols.

Of particular interest are radiotherapy data management requirements characterized by large data sets and numerous temporal, logical, and computational associations between data. For example, a dose computation result should adapt when a treatment field parameter changes. The consequences of time have to be incorporated to model both motion effects and to model changes over the course of treatment.

Data management for radiotherapy has been often managed at the operating system file system level where individual patients are mapped to directories and patient data to sub-directories and files. Associations between data (i.e., a beam dependency of a dose calculation) were typically not represented or implicit, and the state (i.e., the dose up to date vis-à-vis the beam state) was assumed. Relational databases have been commercially popular and readily available but are ill suited to radiotherapy data representations. Relational databases impose a rigid schema structure on the data and are coded to perform relational queries on large datasets of the type which are not useful for radiotherapy data (i.e., one is generally not interested in finding all patients with a gantry angle between 0° and 10°). Thus, neither the data casting nor the framework and its significant overhead are useful.

Instead, radiotherapy data is best managed by hierarchical structures linked by key-value association pairs to manage links between data instances. These key-value pairs and the desired query operations are better managed by much simpler systems such as NoSQL databases. Data is contained in XML documents, e.g., that allow for dynamic changes in the data definitions, dynamic management of associations, and ready replication and versioning. Most importantly, such databases readily scale to accommodate the problem and data size and promote distributed architectures.

Modern deployment models, such as cloud computing, are still absent in radiation oncology. It is clear, however, that the large computational requirements readily benefit from such models. A cloud deployment for computational and data management services would be to great benefit for both smaller and larger clinics. It provides affordable access to necessary computing resources on demand and distributed access in a hospital network. It frees clinical centers from the burden to invest in ever increasing computing hardware.

The limitations of the current, functionally monolithic, systems for treatment planning (TPS) and treatment management (TMS) have led to the introduction of ad hoc and institution-specific procedures to implement and manage workflow. After all, the clinical reality may require a patient to receive a new treatment plan which currently is essentially a repeat of the workflow for that patient's treatment plan. Explicit tracking of such a repeat workflow, however, is not rendered in the TPS.

Of great significance is the work of the DICOM radiotherapy Working Group 7 which, in DICOM supplement 147, makes explicit the need for data objects that model the changing state of the patient as a consequence of treatment events and adaptable workflow tasks. In addition, IHE-RO, the Integrated Health Enterprise comprised of committees concerned with vendor and equipment interoperability and workflow within the radiation oncology domain, has defined specific workflow profiles that specify the details of various composite workflow processes necessary to accomplish tasks. An example workflow profile is "Integrated Positioning and Delivery Workflow," which concerns itself with the positioning of a patient prior to treatment delivery, position monitoring (if any) during treatment delivery, and radiation delivery all managed by a single device.

In summary, modern requirements for treatment planning emphasize distributed computing as afforded by service-oriented architecture, explicit modeling of the workflow to dynamically connect the services needed as the treatment session unfolds.

8.5 Case Study

8.5.1 Volumetric Studies

Volumetric treatment planning requires the use of volumetric image studies for both photon (XRT) and proton radiotherapy (pRT). For pRT, the use of CT is axiomatic as CT is the only practical modality for which acceptable conversion from image voxel data, Hounsfield unit for CT, to voxel stopping power has been validated.

Volumetric image studies are necessary to define the physical computational space as represented by volumetric voxel elements and which allows the accurate computational transport of radiation through the patient's anatomy.

Multimodality, cohesively registered, image studies allow the volumetric segmentation into discrete organs for dosimetric analysis of the internal anatomy. Multimodality image studies allow the geometric definition, in a known coordinate system, of target and organs at risk. Special emphasis should be placed on accurate definition especially for the targets; failure negates the inherent precision of proton radiotherapy. Volumetric representations are derived from contour representations on image sections, while their computational representations are dictated by the computational requirements.

XRT and pRT differ notably in the use of a planning target volume (PTV). For XRT, the geometric expansion of a clinical target volume (CTV) into a PTV suffices to account for uncertainties equal to the geometric expansion. The lack of sensitivity of the photon field to these uncertainties, at least within the typical clinical magnitude, removes errors in dose and means that geometric accuracy equates to dosimetric accuracy. Thus, geometric positioning of the patient and geometric tracking of the patient suffice to maintain the dose distribution envelop within the desired specification. For a proton field, the field-patient interactions do depend on local geometry. Thus, geometric positioning does not suffice, or otherwise, and a change in geometry implies a change in dose. The use of a PTV is thus generally excluded. The PTV concept is nevertheless used, especially for spread-out Bragg peak (SOBP) fields. For the latter, the definition is typically obtained after a site-specific study reveals what margins yield in the desired tolerances after assessing dosimetric changes as a function of geometry [1].

Nevertheless, the use of PTV should be voided in favor of statistical approaches that model the treatment dynamics, in terms of geometric uncertainties in setup, patient motion, and patient changes. Bohoslavsky et al. [2], for example, define such a stochastic method and produce a margin prescription that improves on the use of a PTV margin. The improvement is a consequence of the fact that the dynamic consideration assesses the effect of statistical uncertainties, whereas the use of a PTV margin assumes that every treatment has to be within specification and thus represents is the worst case scenario.

The conversion of CT Hounsfield unit to relative (to water) stopping power is necessary as input to a proton dose algorithm, whether implemented as a heuristic (i.e., pencil beam) model or

as a Monte Carlo. This conversion has two basic problems. First, the conversion is based on a population-averaged conversion curve. This standard curve is applied to the CT Hounsfield unit value perhaps corrected or scaled to the specifics of a patient. Second, the conversion ignores details of the actual organ. Thus, different organs may have the same Hounsfield unit but different relative stopping powers. These limitations on the conversion to relative stopping power are an intrinsic limitation for pRT. The fundamental approach requires the use of proton transmission corrected data to allow the patient and site-specific derivation of stopping powers. Alternate methods, such as multispectral CT, are under active investigation to improve this conversion to voxel stopping power.

In practice, these uncertainties in stopping power assessment translate to a range uncertainty on the order of ~3 mm [3] and hence must be considered. For spread-out Bragg peak fields, the range and modulation width are increased by this amount which increases the longitudinal dimension by 6 mm! For pencil beam scanning (PBS) fields, the uncertainty needs to be considered in the optimization process, which is referred as robust optimization, i.e., the optimized result remains insensitive to the uncertainty [4].

8.5.2 Prescription and Course Considerations

The clinician's intent is expressed in statements that quantify the treatment course aims. There is, typically, a dichotomy between these statements and their use in a computational form. Most optimization algorithms are gradient based and use an objective function that is a quadratic summation of terms with heuristic weights to express relative term significance. Each term relates to an organ objective and thus a prescription statement. Such a form may be adequate for XRT where the number of optimization variables, i.e., leaf positions as a substitute for fluence profiles, is relatively (compared to pRT) small and the sensitivity of the optimal plan to these variables is relatively weak; i.e., the objective function has typically a gentle varying minimum region. Even then, such forms often result in plans that, when evaluated by the physician, require heuristic tweaking of the weighting terms or the artificial introduction of "steering" volumes to meet the clinician's demand. Such algorithms therefore do not match well the supposed precision of a prescription.

The clinician's intent must be transformed into a computational form as input to an optimization algorithm. There are two issues. First, the prescription statement needs to be translated in to a computational form representative of the clinician's intent. Second, the nature of the computational form must yield a clinically optimal plan numerically consistent with the clinician's intent.

For prescriptions, we identify constraints and objectives (Fig. 8.3). Constraints are absolute statements such as minimum or maximum doses to a particular structure. Constraints are transparent – a constraint must be met and hence matches well to a computational form. Even so, gradient-based optimization methods often fail to meet the set of constraints. Objectives are clinical desires and often in competition with each other; that is, improving one objective must worsen another objective in a truly optimal plan. Objectives are constrained by the phase space of possibilities that remains after the constraints are satisfied. Objectives are not readily cast in computational form as their values are continuous and interdependent. It is the quantification and computation of objectives that often lack in optimization methods and impose iterations on the "optimal" plan as the clinician's intent is not represented. The use of multi-criteria optimization is a popular technique to manage objectives and inter-objective trade-offs [5].

In addition, we need to consider the time structure of a treatment; one reason already stated is to obviate the artificial use of a PTV. In XRT, the treatment session invariably requires a large set of beams that must be delivered as a single unit. This time structure is therefore invariably invisible and collapsed in a set of repeated identical fractions for a phase of the course. (Of note, we define a phase here as sub-course segment with its specific dose objectives such that all phase dose objectives meet the course dose objec-

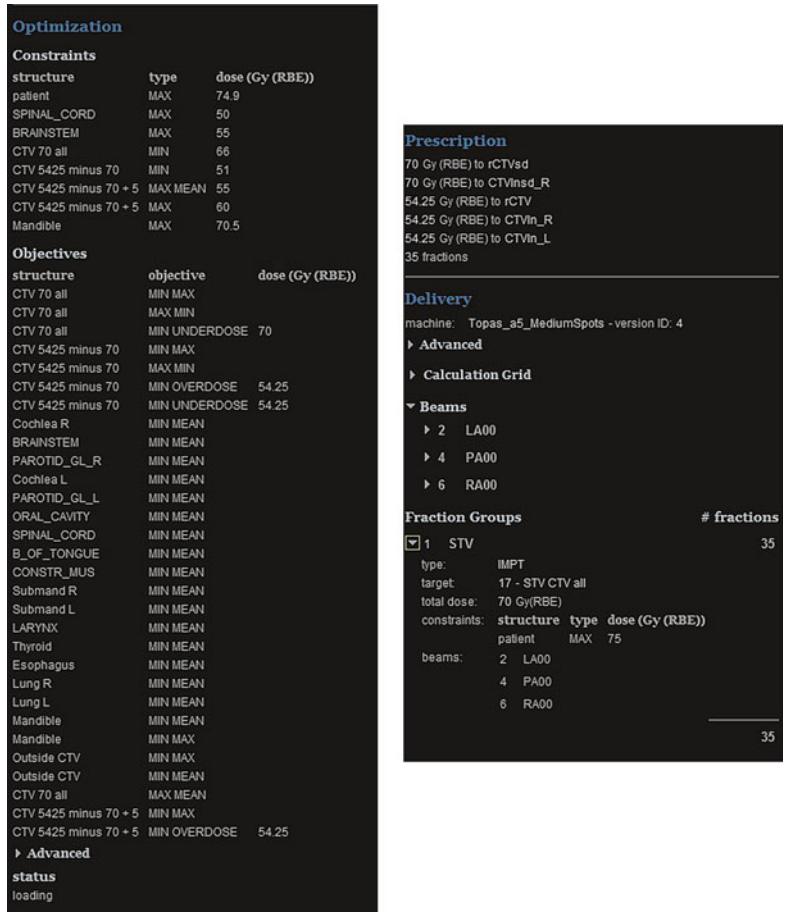

Optimization

Constraints

structure	type	dose (Gy (RBE))
patient	MAX	74.9
SPINAL_CORD	MAX	50
BRAINSTEM	MAX	55
CTV 70 all	MIN	66
CTV 5425 minus 70	MIN	51
CTV 5425 minus 70 + 5	MAX MEAN	55
CTV 5425 minus 70 + 5	MAX	60
Mandible	MAX	70.5

Objectives

structure	objective	dose (Gy (RBE))
CTV 70 all	MIN MAX	
CTV 70 all	MAX MIN	
CTV 70 all	MIN UNDERDOSE	70
CTV 5425 minus 70	MIN MAX	
CTV 5425 minus 70	MAX MIN	
CTV 5425 minus 70	MIN OVERDOSE	54.25
CTV 5425 minus 70	MIN UNDERDOSE	54.25
Cochlea R	MIN MEAN	
BRAINSTEM	MIN MEAN	
PAROTID_GL_R	MIN MEAN	
Cochlea L	MIN MEAN	
PAROTID_GL_L	MIN MEAN	
ORAL_CAVITY	MIN MEAN	
SPINAL_CORD	MIN MEAN	
B_OF_TONGUE	MIN MEAN	
CONSTR_MUS	MIN MEAN	
Submand R	MIN MEAN	
Submand L	MIN MEAN	
LARYNX	MIN MEAN	
Thyroid	MIN MEAN	
Esophagus	MIN MEAN	
Lung R	MIN MEAN	
Lung L	MIN MEAN	
Mandible	MIN MEAN	
Mandible	MIN MAX	
Outside CTV	MIN MAX	
Outside CTV	MIN MEAN	
CTV 70 all	MAX MEAN	
CTV 5425 minus 70 + 5	MIN MAX	
CTV 5425 minus 70 + 5	MIN OVERDOSE	54.25

▸ Advanced

status

loading

Prescription

70 Gy (RBE) to rCTVsd
70 Gy (RBE) to CTVInsd_R
54.25 Gy (RBE) to rCTV
54.25 Gy (RBE) to CTVIn_R
54.25 Gy (RBE) to CTVIn_L
35 fractions

Delivery

machine: Topas_a5_MediumSpots - version ID: 4

▸ Advanced

▸ Calculation Grid

▾ Beams

▸ 2 LA00

▸ 4 PA00

▸ 6 RA00

Fraction Groups # fractions

▾ 1 STV 35

type: IMPT
target: 17 - STV CTV all
total dose: 70 Gy(RBE)
constraints:

structure	type	dose (Gy (RBE))
patient	MAX	75

beams: 2 LA00, 4 PA00, 6 RA00

35

Fig. 8.3 The prescription, constraints, and objectives are shown for a nasopharynx case. The set provides a clinically complete specification for the multi-criteria optimization schema used in astroid. The prescriptions (total dose and fraction number) translate the total doses computed in the system to the appropriate fraction doses and spot parameters for treatment delivery. The constraints are absolute and must be achieved by the optimization (which otherwise fails to achieve a solution if the constraints cannot be achieved). The objectives represent clinical desires within the bounds of constraints and are optimal trade-offs with respect to each other. That is, improving one objective worsens all others. The system uses fraction groups (see DICOM RT [Ion] Plan Fraction Scheme Module) that permit, for a particular course phase, to define and group subset of beam sets with individual constraints. The fraction group maps the total fraction group dose to individual fraction doses using the number of fractions

tives.) The practice of multi-beam sets within a XRT phase is rare to nonexistent.

The pRT practice does allow for intra-treatment session variability of the beam configuration. Such a configuration may be used for practical reasons, it is quicker to deliver two fields out of four per day, or biological reasons, where specific fractions can satisfy a sub-treatment phase biological objective compared to other fractions for the course phase.

The above observations concerning course and time management are consistent with DICOM Second Generation Radiotherapy (DICOM 2G; DICOM Supplement 147) [6]. DICOM 2G, first, recognizes the limitation of the first-generation objects and, second, makes explicit the above requirements in its data object definitions. The first-generation objects were time collapsed and ignorant of workflow order and simply served to move data between processes. The second-generation objects explicitly

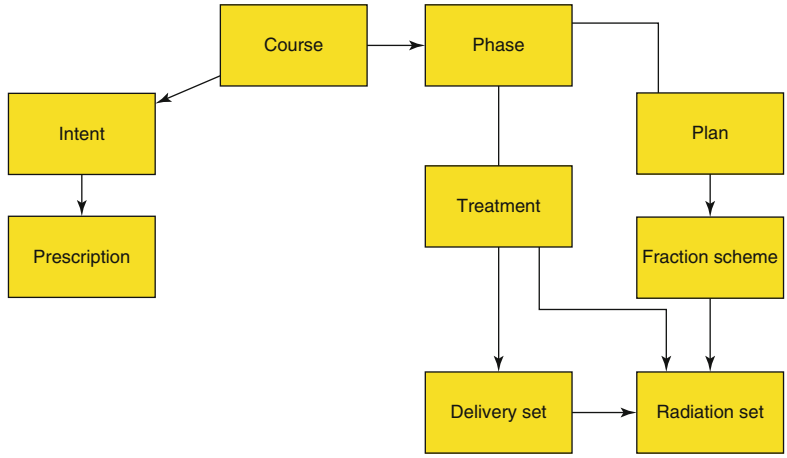

Fig. 8.4 DICOM second-generation object inspired model for treatment planning and delivery. A course defines its intent expressed as prescriptions. A course has one or more phases. Each phase has a plan representation in the treatment planning system and expressed by a fraction scheme (a set of one or more fraction groups) which references radiation sets, a set of beams delivered in a fraction. A phase also has a parallel treatment representation expressed by the actual delivered radiation sets. The ability to represent and act on this model is a key to adaptive radiotherapy and complete documentation of the actual treatment versus planned

model the evolution of a treatment course and its delivery as a function of time. Adaptive radiotherapy (ART) requires DICOM 2G to consistently model and communicate patient changes and adaptations between computational and delivery services.

The second-generation model provides an RT course container structure that locates this course with respect to previous treatment courses and contains (1) prescriptions, (2) treatment phases that capture the time structure and differential objectives of the course, and (3) radiation sets (Fig. 8.4). A radiation set, in turn, captures fractionation schemas and the beams delivered in a fraction. The second-generation model, unlike the first-generation model which aggregated most data in the RT plan object, correctly decomposes data into orthogonal[1] object definitions, manages the time dimension, and captures the dynamics, i.e., variability, of the treatment course.

pRT is well positioned to use the second-generation structure and our planning methodology (astroid, a joint development between Massachusetts General Hospital (MGH), Boston, MA and .decimal, Sanford, FL) explicitly models this structure. Astroid models a treatment course as above and has a radiation set as a fundamental planning unit. The user can model one or more radiation sets as a single set over which a (sub)set of the prescription statements and hence optimization are applied. Thus, optimization directly considers individual fractions and allows interfraction optimization to ensure that combinations of fractions (i.e., radiation sets) achieve a global course objective.

8.5.3 Field Considerations

Even a single proton field may provide the opportunity to achieve the dose objectives in contrast to the numerous fields required in XRT to achieve a measure of conformality. Thus, dose shaping does not rely per se on the number of fields. The choice of the number of fields and the orientation of the fields therefore remains an unsettled issue. Typically, the number of fields ranges from one to four per isocenter, and their orientation is best chosen to provide target coverage with the least lateral dimension, largest target to organ-at-risk

[1] Orthogonal design in data management implies that only a single data object represents a subset of data.

separation, and sharpest lateral penumbral falloff gradient between the target and organ at risk. Integral dose minimization is less of a practical concern as the integral dose is intrinsically low. It should be noted that these considerations are heuristic. The optimal number of beams and their optimal placement is a very difficult computational problem and beyond the current generation of treatment planning systems.

For our case, we assume a class solution and use a 3-field approach consisting of left and right oblique fields (at ±45°) and a posterior field. Field size is typically not a limitation for scanned fields as for scattered fields where elongated targets require multiple isocenters. Multi-isocenter SOBP fields are exceedingly cumbersome as they require feathered match lines.

The next consideration is the placement of "spots" defined as the (hypothetical) terminal point of the proton pencil beam. A spot point is defined in the, e.g., isocentric plane as a coordinate pair and in the longitudinal direction by energy/range. The choice of coordinates in the isocentric plane is typically chosen on a regular, rectangular or hexagonal, spaced grid. The choice of ranges may be constrained by the available ranges of the delivery device and is invariably constrained to sets of constant ranges, so-called energy layers, due to the long (compared to the lateral positioning of spots) time required to change energies. Thus, current systems require as many spots as possible to be delivered at the same energy to minimize dead time between energy switches. The choice of layer spacing is "optimal" when consecutive layers are spaced proportional (or close to) the width of the layer pristine peaks. Pristine peaks, however, sharply decrease in width as a function of lower energy, and this optimal strategy causes a significant pileup of low-energy layers which results in a significant increase in treatment time because, again, energy switching time is a long process (on the order of seconds compared to milliseconds for spot lateral movement). Thus, our pragmatic approach, which contributes less than 2 % to the overall dose heterogeneity, is to space the energy layers by the width of the deepest and thus the broadest peak in the set.

It should be noted that the total number of spots (50,000 in our case for three fields, Fig. 8.5) for our case creates operational requirements for the delivery system. It is a rule of thumb that 10^8 protons deliver 1 Gy(RBE) to 1 cc of volume. The three fields, with a spot $\sigma \sim 5$ mm, deliver about 250×10^{11} protons in 50,000 spots with a mean of 5×10^6 protons/spot and a range of 10^4–10^8 protons/spot. Thus, a delivery system needs a dynamic range of about 10,000 in terms of spot charge control. A priori each spot should be delivered with high accuracy. Often, a specified charge may require the same spot to be delivered multiple times or at low (cyclotron) current to ensure the required charge precision. This, again, is an important treatment delivery system consid-

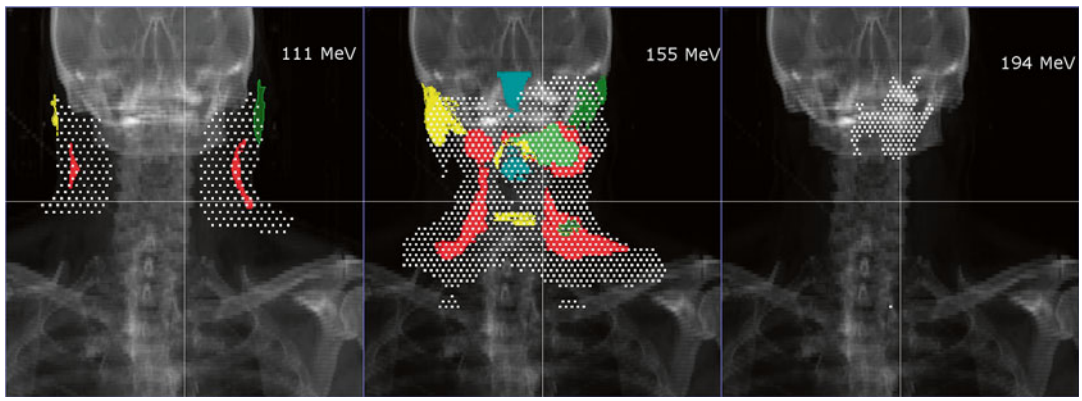

Fig. 8.5 Spot placement for three energy layers (111, 155, and 194 MeV) for the posterior-anterior field. Note that illustration of the respective target and organ-at-risk volumes is contained with the energy layer

eration. The number of protons per spot scales with the spot size when spots are spaced on a regular grid. For a spot with $\sigma \sim 10$ mm, the mean and ranges would be 2×10^7 and 4×10^4–4×10^8. It is, of course, the lowest necessary charge in a problem that drives the performance of the delivery system. The ability of a proton production system, beamline, and scanning system to precisely deliver a spot of the minimum dose is a key performance requirement (Fig. 8.6).

The above spot placement strategy, as is the beam placement strategy, is heuristic. It ensures volumetric coverage of the set of spots but not that this set is optimal either to achieve the desired dose objectives or in terms of delivery. Again, a consideration of optimality for these parameters exceeds current practical computational abilities but is of considerable interest.

The resultant three fields result in 50,000 spots, each defined by a triplet of energy, isocenter plane position, and number of protons. The latter is converted to the reference ionization chamber monitor unit to allow accurate control of the spot dose deposition. It is common to directly quantify the spot intensity by the equipment monitor unit in the treatment planning system. We cannot recommend this practice. Instead, we recommend the use of the number of protons as it is a device-independent and physically well-defined expression of the intensity. Thus, proton plans expressed by number of protons per spot can be readily intercompared between different institutions.

Recent work in spot placement optimization [7] considers optimized placement of spots to minimize the number of spots while achieving prescription objectives. They allow for arbitrary spot placement, i.e., unconstrained in position and energy, and iterate over a set while continuously adding new spots and removing low-weight spots. Their analysis results in fewer spots and more charge per spot, more energy layers (as expected), reduction of dose to organs at risk (because spots can be removed), and (almost) an order of magnitude decrease in optimization

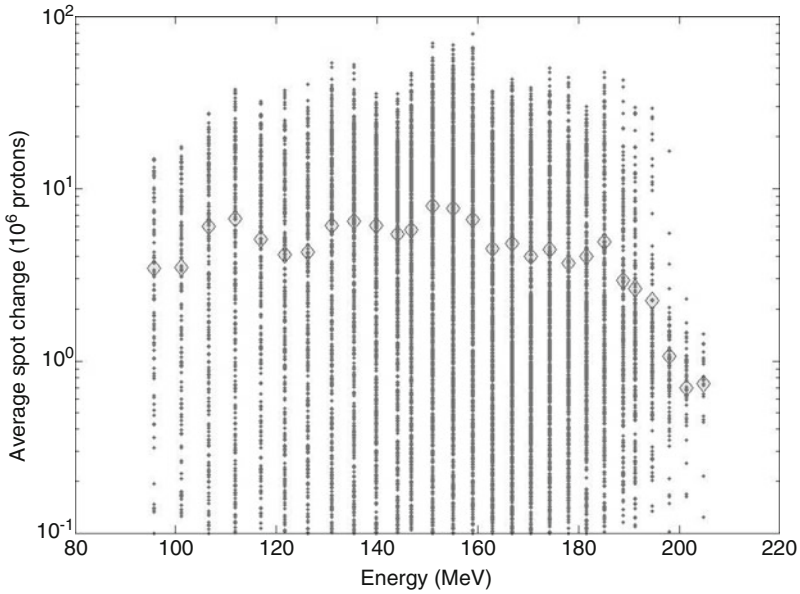

Fig. 8.6 The spot charge distribution within each energy layer (X-axis) for one field containing about 16,000 spots. The spot charge has an average of about 5×10^6 protons per spot. The range varies from (about) 100,000 to 100,000,000 protons per spot, a dynamic range of 1000. The ability for precise charge spot definition is an important requirement of the proton production and delivery system. Considering the spot size of $\sigma \sim 5$ mm, the average spot charge is about $10^6 \cdot mm^{-2}$. That is, if the spot size increases (decreases), the average (and spreads) charge per spot increases (decreases). Thus, smaller spot size further increases the need for high-precision production and delivery

times. In addition, the technique improves as spot size decreases.

This strategy does require that spots can be of arbitrary energy, a capability not available with current generation of treatment planning and delivery systems. The next generation of delivery systems, such as the LIGHT linear accelerator (see Ugo Amaldi http://cds.cern.ch/record/1312611), promises such capability. It should be noted that the current practice of constant and separated energy layers intrinsically reduces the precision of proton target dose conformance by increasing the penumbral region around the target. Target dose inhomogeneity also increases as constant spot placement "misses" small target extensions and hence can cause an increase in local spot intensity as the spot is not well positioned relative to the target. Thus, the ability to place spots where needed and unconstrained by the current artifact of energy layers will improve dose conformance and homogeneity and the ability to use dose painting of targets.

It is, of course, the assessment of the optimal spot intensities that now remains as the core problem of the treatment plan optimization.

8.5.4 Plan Optimization

Our plan has the constraints and objectives listed in Figure 8.3. Our astroid system uses multicriteria optimization ([8] and Fig. 8.7) to create a Pareto surface where each objective spans a dimensional axis and where the axis value range, i.e., minimum and maximum achievable objective value, is determined by the constraint values. That is, the optimization ensures (or fails otherwise) that every constraint is met and subsequently assesses the range of objective values. The objectives are correlated, i.e., their possible value sets span a Pareto surface in the multidimensional objective space, and improving one objective value (such as "minimized lung dose" and within the allowed range, see Fig. 8.6) necessarily worsens all the other objective values. That is, each set of objective values is best when considering the ensemble of values in the set. If the user wishes to improve one objective (say reduce surface dose to the brainstem), the set with that new brainstem objective value out of necessity changes all other objective values. Algorithms that allow the user to change objective values are labeled as "Pareto surface navigation" algorithms and, themselves, are of a class of algorithms under investigation.

The astroid system allows the user to interactively change objective values within the constrained range, and the system will interactively update the dose displays to reflect the new set of objective values. Its navigation algorithm uses the new objective value as a constraint to find the set on the Pareto surface that contains that value.

Thus, the clinical practitioner, in effect, scrolls through all possible trade-offs and assures that each trade-off plan is the best given set of objective values. It is important to note that if the constraint values are changed, a completely different set of trade-offs can be considered. Thus, the Pareto surface optimization does not accommodate trading off a constraint. If so desired, the user can change a particular constraint to an objective and vice versa.

The result for our example case is shown in Fig. 8.8.

8.5.5 Plan Robustness

The dose computation on a static patient representation is considered incomplete for proton radiotherapy where the dose distribution is sensitive to uncertainties in geometry and range [9]. The latter is a consequence of the intrinsic systematic uncertainty in the conversion from CT Hounsfield unit to relative stopping power (among others). Figure 8.9 shows the dose-volume histograms (DVHs) for selected organs at risk and targets.

8.5.6 Dose Quality

The now practical availability of Monte Carlo computational methods will result in a shift, eventually complete, away from empirical pencil beam dose calculation models. Nevertheless, the pencil beam dose calculation models have been the basis for the clinical decision process and, in fact, have been quite accurate (except in

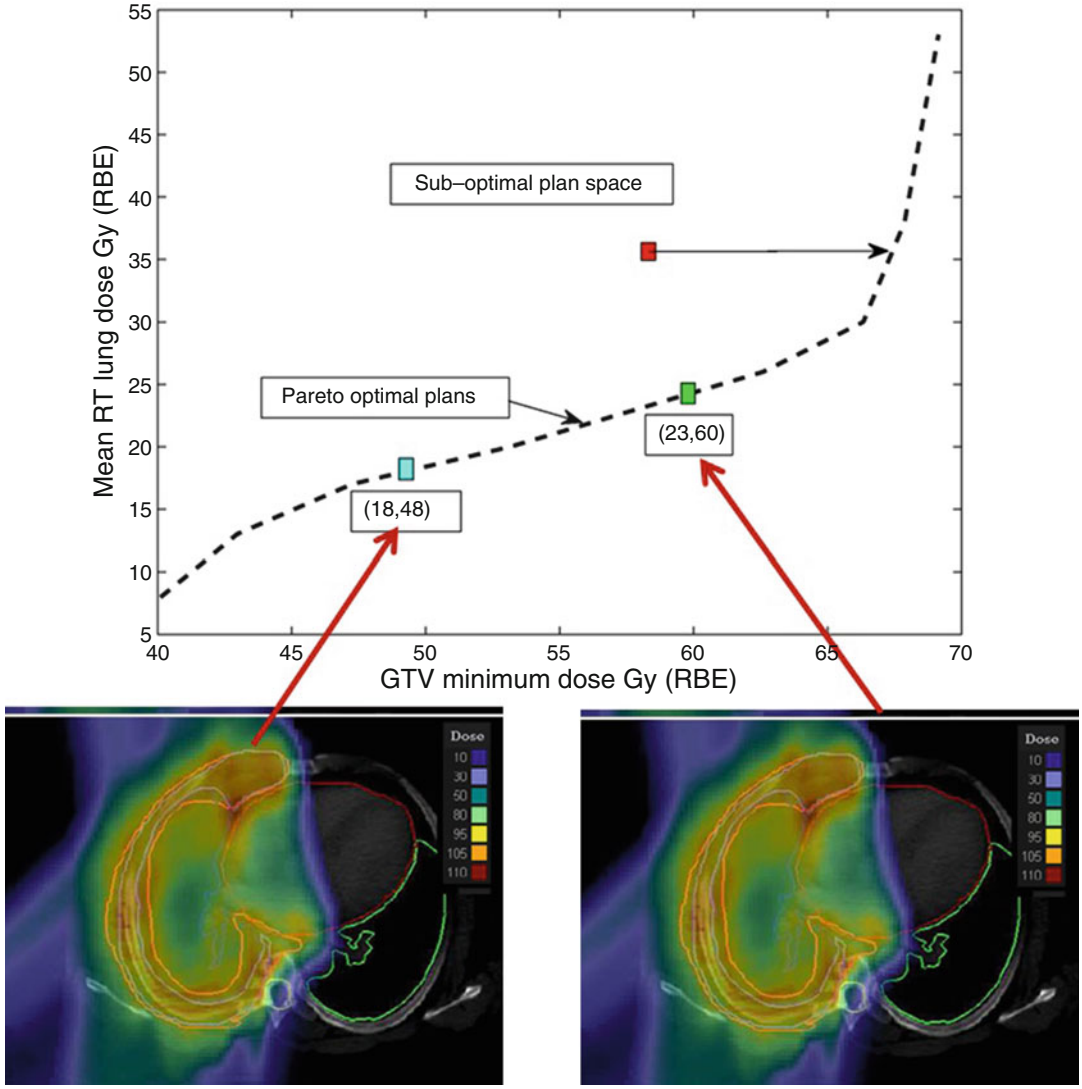

Fig. 8.7 Example trade-off scenario in a 3-field mesothelioma of the right lung pleura. The trade-off considers mean right lung dose (*Y*-axis) versus GTV minimum dose (*X*-axis). The curve that represents the possible trade-off pair values is illustrated in the graph above and forms a curve in the trade-off space. In this space, a hypothetical suboptimal plan (*red square*) lies above the curve. Its suboptimality is indicated by the observation that the GTV minimum dose can be significantly improved while maintaining mean right lung dose. The two isodose distributions represent the two points indicated on the curve. The clinical operator can move along the curve to assess the dosimetric consequence of a particular trade-off value pair

pathological cases such as where metallic implants are present in the patient). Figure 8.10 shows the results of dose computation with three different methods, one with a pencil beam model and two with a Monte Carlo, to illustrate the qualitative and quantitative differences and similarities between the methods.

8.6 Conclusion

Treatment planning requirements given the current aims of radiotherapy are not well implemented by the current commercial treatment planning system architectures. That is, proton radiotherapy permits a more dynamic evolution

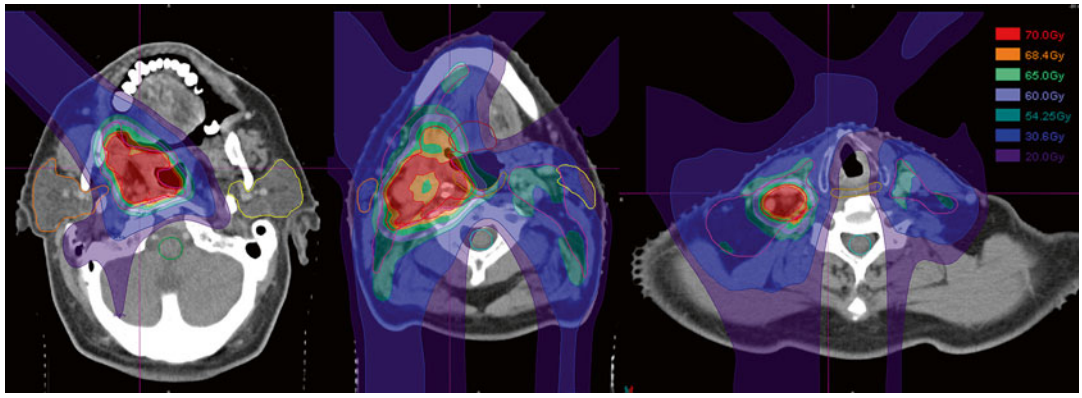

Fig. 8.8 The achieved dose distribution for the nasopharynx case example. The three fields contain about 50,000 spots (determined and placed heuristically without the benefit of spot optimization). Note the ability for both dose avoidance and dose painting (the spot $\sigma \sim 5$ mm)

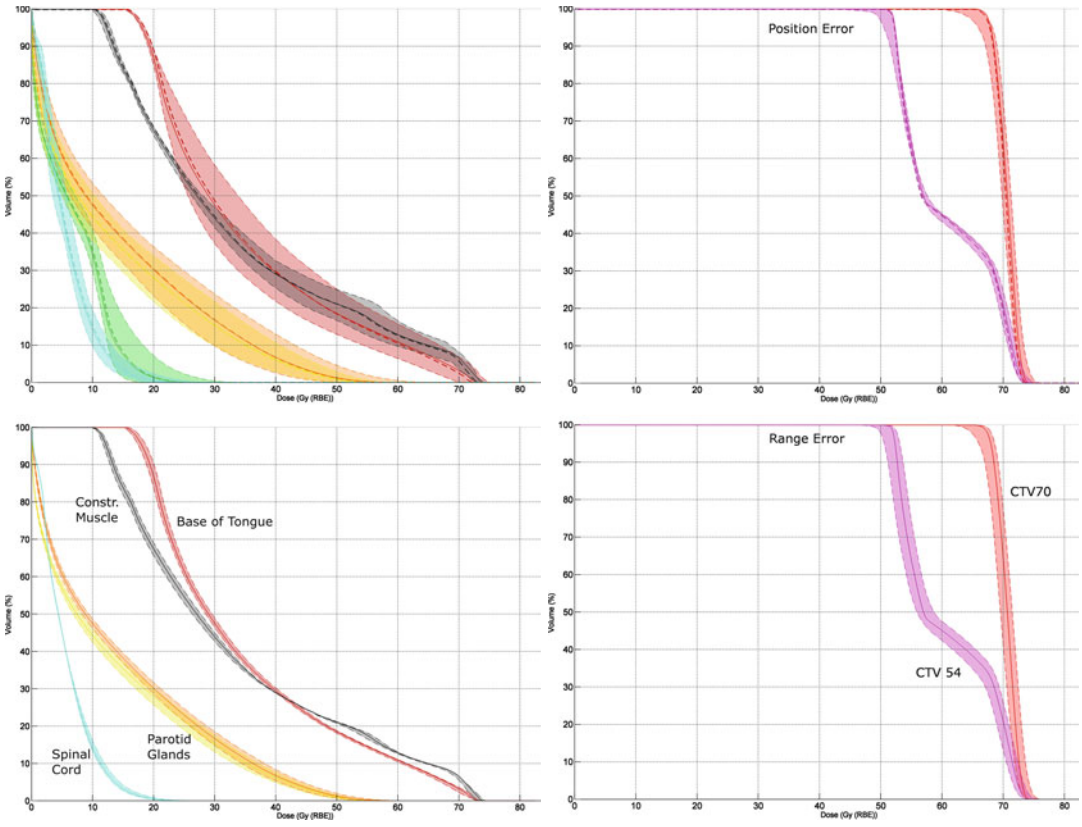

Fig. 8.9 The *left panels* show the DVHs for (selected) organs at risk and the *right* for the two CTV volumes. The *upper panels* show the effect of position error where the dose is recomputed on the error-modified patient with the nominal plan parameters. The *lower panels* show the effect of range over and undershoot of 3 %. The effect of position is more severe on the organs at risk as a consequence of the fact that these organs are invariably in high-dose gradients and thus are susceptible to geometric shifts of that gradient. The target volumes are much less affected. The range error (*lower panels*) has almost no effect on the organs at risk but does affect the targets. The DVHs show the maximum and minimum bands with the *dashed line* representing the mean DVH of the error scenarios and the *solid line* representing the nominal DVH. One must observe that the positioning errors will average out to this mean over the large number of fractions for this site. Thus, the mean (or nominal) DVH is the representative as it is in XRT treatments. The range errors, however, are systematic and must be assessed within the band of the DVH

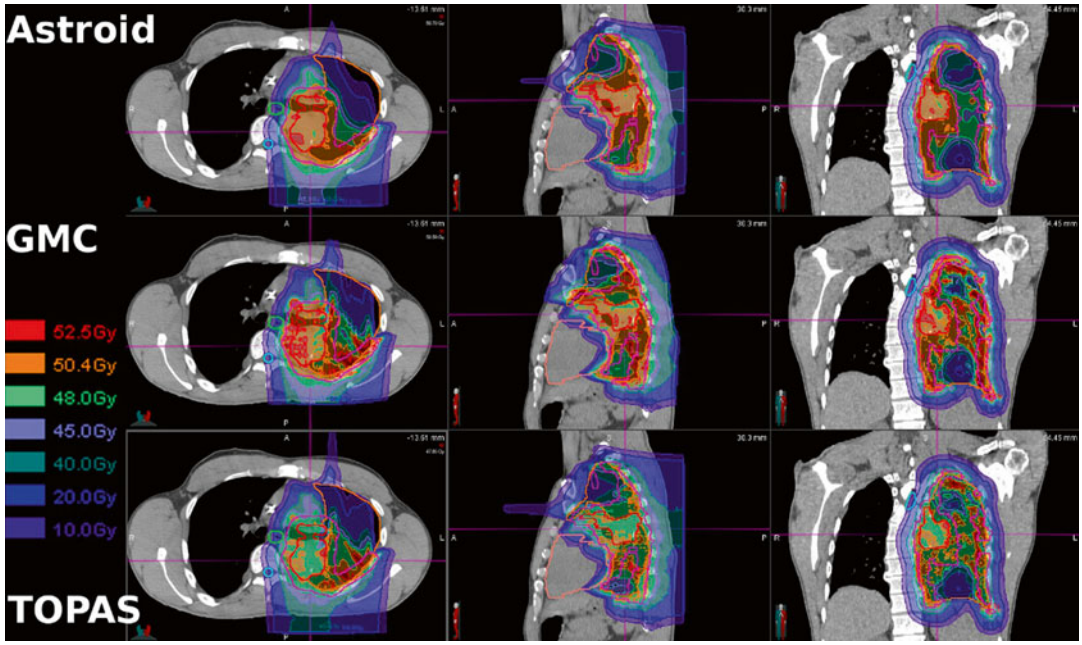

Fig. 8.10 Comparison of dose computation results between a pencil beam model implementation (astroid), a simple primary and secondary scatter Monte Carlo (GMC), and a complete Monte Carlo (TOPAS). Qualitatively, the distributions show the same features in this very heterogeneous geometry. Both Monte Carlos show, albeit with slight differences, more out-scattered protons in the target volume and hence more heterogeneous and lower dose. Monte Carlo calculations are critical as an independent verification. Their clinical accuracy, i.e., how will their differences impact clinical practice, needs to be clearly specified as they will imply changes in a practice established with "less" accurate computational means. Even so, the absolute accuracy of Monte Carlo in the tissue itself also requires more investigation because of patient tissue differences and calibration biases in the Monte Carlo (as in any dose algorithm)

and implementation of a treatment course as multiple radiation sets of only a few fields each can achieve competing dose objectives and thus permit a more tuned and adaptive approach to the planning and delivery process. The DICOM 2G definitions are a complete model for such approaches.

Proton treatment plans are computationally demanding because the number of optimization variables, namely, spot intensities, is very large (on the order of 10,000–100,000 per patient), because the set of "optimal" but competing solutions are (presumably) better, and because a treatment plan must explicitly model the uncertainty space (as compared to the PTV heuristic in XRT). These computational demands will greatly benefit from modern service-oriented and scalable architectures to provide the necessary computational horsepower.

Thus, just as proton radiotherapy in the 1980s led the way toward computational treatment planning systems, proton radiotherapy in the coming decade again will push treatment planning toward more capabilities.

References

1. Engelsman M, Rietzel E, Kooy HM. Four-dimensional proton treatment planning for lung tumors. Int J Radiat Oncol Biol Phys. 2006;64:1589–95.
2. Bohoslavsky R, Witte MG, Janssen TM, van Herk M. Probabilistic objective functions for margin-less IMRT planning. Phys Med Biol. 2013;58:3563–80.
3. Paganetti H. Range uncertainties in proton therapy and the role of Monte Carlo simulations. Phys Med Biol. 2013;2012(57):99–117.
4. Chen W, Unkelbach J, Trofimov A, Madden T, Kooy H, Bortfeld T, Craft D. Including robustness in multi-criteria optimization for intensity-modulated proton therapy. Phys Med Biol. 2012;57:591–608.
5. Halabi T, Craft D, Bortfeld TR. Dose–volume objectives in multi-criteria optimization. Phys Med Biol. 2006;51:3809–18.

6. DICOM Standards Committee, Working Group 7. Radiation therapy. Supplement 147: Second Generation Radiotherapy. Revision 42, March 28, 2014
7. van de Water S, Kraan AC, et al. Improved efficiency of multi-criteria IMPT treatment planning using iterative resampling of randomly placed pencil beams. Phys Med Biol. 2013;58:6969–83.
8. Monz M, Kufer KH, Bortfeld TR, Thieke C. Pareto navigation—algorithmic foundation of interactive multi-criteria IMRT planning. Phys Med Biol. 2008; 53:985–98.
9. Kraan AC, van de Water S, et al. Dose uncertainties in IMPT for oropharyngeal cancer in the presence of anatomical, range, and setup errors. Int J Radiat Oncol Biol Phys. 2013;87:888–96.

Radiation Therapy with Protons and Heavy Ions

9

Oliver Jäkel

9.1 Introduction

The first proton therapy patient was treated in Berkeley at the Lawrence Berkeley Laboratories (LBL) in 1954 and proton therapy celebrates its 60th birthday in 2014 [10]. It is, however, only in the last decade that the number of patients that received proton therapy in dedicated clinical centers is increasing more rapidly. The PTCOG website currently lists 42 proton therapy centers in operation as of August 2014 and 24 new centers currently under construction (see www.ptcog.ch). Heavier ions have also been used first for cancer treatment at LBL in 1957, starting with helium ion treatments and in 1977 with the heavier ions carbon, silicon, neon, and argon [10]. Inspired from the Berkeley experience, the first clinical ion facility in Chiba, Japan, used solely carbon ions for radiotherapy and celebrated its 20th birthday in 2014. Overall 8 facilities worldwide offer carbon treatments, 4 new facilities are under construction (PTCOG lists 3, but an additional facility exists in Marburg), and several projects are in preparation (Japan, Korea, Taiwan, Saudi Arabia). It is expected that also carbon ion therapy will be of increasing importance in the future. In this contribution the differences between protons and heavier ions arising from physical and biological characteristics are highlighted and their implications for therapy planning are discussed. The clinical status of carbon ion therapy is summarized and some possible future developments are outlined.

O. Jäkel, PhD
Department of Medical Physics, German Cancer Research Center, Heidelberg, Germany

Heidelberg Ion Beam Therapy Center, University Hospital Heidelberg, Heidelberg, Germany

e-mail: o.jaekel@dkfz-heidelberg.de

9.2 Physical Characteristics of Heavy Charged Particles

Carbon ions and proton beams have the common feature of a finite range, which can be controlled by selecting the appropriate energy of the therapy beam. The energy loss of charged particles is primarily due to inelastic collisions with target electrons and is described by the Bethe formula (derived by Hands Bethe in 1930), as energy loss per pathlength (dE/dx), or collision stopping power. For relativistic heavy charged particles, the mass collision stopping power as a function of the velocity β of the particle is given by [16]:

$$\frac{S_{\text{coll}}}{\rho} = K \cdot z^2 \cdot \frac{Z}{A} \cdot \frac{1}{\beta^2} \cdot \left[\frac{1}{2} \ln \left(\frac{2 m_e c^2 \cdot \beta^2 \cdot W_{\max}}{I^2 \cdot \left(1 - \beta^2\right)} \right) - \beta^2 + \text{corr} \right] \tag{9.1}$$

where $K = 0.307075$ MeV cm^2 g^{-1}, z is the charge of the projectile ion, Z/A is the average ratio of the

A.K. Rath, N. Sahoo (eds.), *Particle Radiotherapy: Emerging Technology for Treatment of Cancer*,
DOI 10.1007/978-81-322-2622-2_9

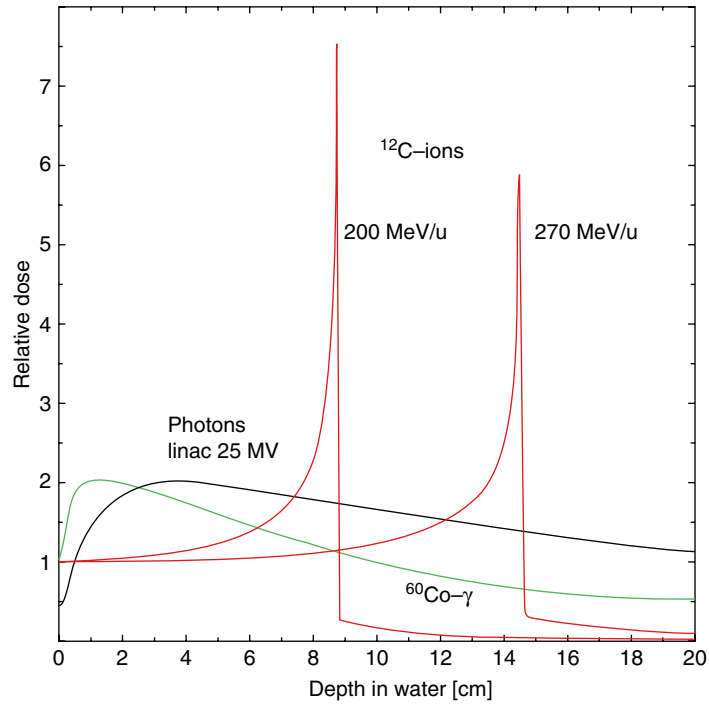

Fig. 9.1 Depth dose curves for ^{60}Co gamma radiation, MV photons, and carbon ions at different energies in water (Reproduced from Ref. [29])

atomic number over the atomic mass of the medium, W_{max} is the maximum energy that the ion can transfer to an electron in a single collision, I is the mean excitation energy of the medium, and *corr* summarizes various corrections (density effect, shell, Barkas and Bloch corrections) which are especially important at very high and low energies. The most important dependence on the projectile is via the charge and velocity: the β^{-2} term leads to a strong increase of energy loss at low energies. This behavior gives rise to a steep increase of the depth dose curve, the so-called Bragg curve. After the Bragg maximum, the energy loss drops rapidly, when the particles have lost all their energy and are stopped. This feature can be seen in the depth dose curve of various particles as compared to X-rays in Fig. 9.1.

The range can be calculated by the continuously slowing down approximation (csda) by integrating the inverse of the stopping power over the energy of the particle:

$$R_{csda} = \int_{E_0}^{0} S_{coll} \cdot dE \qquad (9.2)$$

The difference between protons and heavier ions arises primarily through the z^2-term: the higher charge leads to much increased energy loss; in case of carbon ions as compared to protons, this factor is 36:1. At the same range, the difference is somewhat smaller due to a larger β of carbon as compare to protons. For carbons with a range of 15 cm, the energy loss is about 25 times that of protons with the same range. The Bethe formula is therefore the direct reason why higher energies are needed for carbon ion therapy as compared to proton RT, resulting in larger machines and considerably more expensive facilities.

To understand the importance of a higher energy loss, it is important to realize, where this energy is *deposited* in tissue. Generally the energy transferred to the atomic electrons during collision with protons and ions is very small: the maximum energy that can be transferred is around 1 MeV, but the average energy loss is only around 1 keV. This is due to the very asymmetric energy loss distribution, the so-called Landau distribution, which describes the probability of the energy loss with a certain value (the Bethe formula, only calculates the average energy loss of many ions). Since these values change only slightly for various ions and energies, the energy lost by an ion is generally transferred into a very small region, with a diameter of only nanometer scale. This is in contrast to MV photons,

where energy can be transported away up to several millimeters or even centimeters.

This difference in energy loss patterns is attributed to the linear energy transfer, or LET, defined as the restricted energy loss. The restriction is done by limiting the maximum energy of secondary electrons which are produced in a collision, i.e., by replacing W_{max} in Eq. 9.1 by a cutoff value ΔE. Since the maximum energy transfer in ion beams is anyway small, LET is effectively equivalent to dE/dx in most practical cases. Consequently carbon ions are considered high LET radiation, protons are intermediate, and MV photons are low LET radiation. The higher LET is connected to an increase in biological effectiveness and other specific biological properties (see below).

Two more features of heavier ions are also important for radiotherapy: due to nuclear interactions between projectile and target nuclei, a considerable part of the ions undergo fragmentation reactions. This leads to the buildup of a secondary particle spectrum, consisting mainly of projectile fragments with energies similar to the energy of the incoming ion. Target fragments are less important, due to the relatively low energy transferred by the recoil and the resulting very small ranges. Secondary ions with lower charge but similar velocity as the primary have longer range due to lower energy loss (see Eq. 9.1). This leads to a pronounced tail of light particles beyond the Bragg peak of the primaries as seen in Fig. 9.1.

Besides the secondary ions, there will also be neutrons and gamma rays, which are emitted by de-excitation of nuclei after the collision. Some of this secondary radiation can be used for in vivo monitoring of the irradiation. Likewise some nuclei will be transformed into radioactive isotopes emitting positrons so that also positron emission tomography can be used for a 3D reconstruction of the irradiated volume.

Moreover, nuclear fragmentation leads to a significant loss of primaries with approximately 4 % per cm, i.e., at a depth of 15 cm, nearly half of the primaries are lost. Nevertheless, the energy loss is dominated by carbon ions, due to their significantly higher energy loss according to the Bethe formula.

As the loss of primaries is increasing with increasing atomic number of the projectile, ions which are considerably heavier than carbon are not suitable for radiotherapy. For example, for argon,

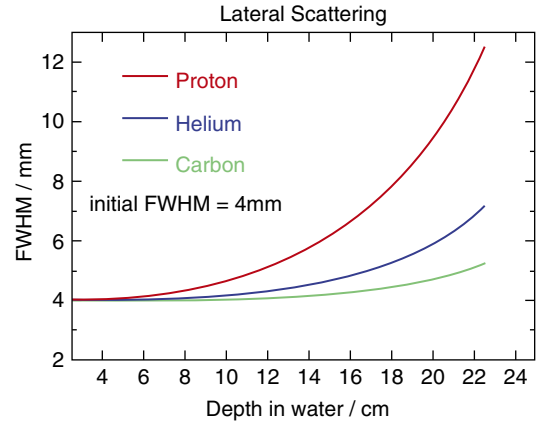

Fig. 9.2 Beam width of proton, helium, and carbon ion beams, expressed as full width half maximum as a function of depth in water. An initial width of 4 mm is assumed (Courtesy of U. Weber)

only 22 % reach a Bragg peak in a depth of 20 cm [27]. This leads to an energy loss which is considerably higher at the entrance than at the Bragg peak.

Finally the increased mass of heavier ions as compared to protons leads to a significant reduction of the lateral penumbra of treatment beams. The reason for this is the smaller deflection of a single ion due to its higher momentum as compared to protons. A single scattering process is described by the differential Rutherford scattering cross section, which describes the cross section as a function of the solid angle Ω, the energy of the projectile E, and the charges of projectile and target nuclei, Z_1 and Z_2:

$$\frac{d\sigma}{d\Omega} \propto \frac{Z_1^2 Z_2^2}{E^2} \cdot \frac{1}{\sin^4 \frac{\Theta}{2}} \tag{9.3}$$

As the probability for large-angle scattering is decreasing rapidly, this leads to the phenomenon of small scattering angles. The process of multiple small scattering events during traversal of thicker layers is described by multiple scattering theories, like the Moliere theory [37]. The dependency on the energy leads to a strong decrease of scattering angles with mass of the projectile. This again is the rationale for the interest in using helium ions, which offer considerable improved lateral penumbra as compared to protons but only a moderate increase of LET and also costs (see [36] for a detailed comparison of carbon ions and protons for radiotherapy).

In Fig. 9.2 an example of the development of the penumbra of various ions is given as a function of depth in water.

9.3 Biological Characteristics of Heavy Charged Particles

Generally, the dose needed to produce a certain biological effect using radiation with a higher LET is lower as compared to photon radiation [19]. This is due to the abovementioned deposition of large amounts of energy into very small volumes around the track. High LET radiation is thus referred to as *densely ionizing*. Since most clinical experience on biological effectiveness of radiation available is for MV X-rays, a concept for transferring these data high LET radiation is needed. Such a concept is the relative biological efficiency (RBE), which is defined as:

$$\mathrm{RBE} = \frac{D_{\mathrm{photon}}}{D_{\mathrm{ion}}}. \tag{9.4}$$

Here, D_{photon} and D_{ion} are the absorbed doses for photons and ion radiation, leading to the same biological effect. The RBE-weighted dose of ion irradiation is used to quantify the dose, which is isoeffective to a photon dose, given as the product of the absorbed dose multiplied by RBE.

Despite the simple definition in Eq. (9.4), RBE is a complex quantity since it depends on LET, dose, particle type, and energy, on the biological system (tissue type) as well as on the biological endpoint (e.g., early vs. late effects). For treatment planning applications, it is generally not possible to model all these dependencies explicitly and approximations have to be made.

There are currently no RBE data derived directly from clinical data of proton or ion beam therapy. Instead models are used, which describe some of the most important dependencies of RBE.

The nature of high LET radiation implies some important differences as compared to the biological effects of X-ray: while the average spacing between energy transfer events along the track is of the order of hundreds of nanometers for low LET, high LET radiation with an LET of 100 keV/µm leads to a mean spacing between events of less than a nanometer. This leads to interaction between ionization events in a single track and results in a higher probability of irreparable damage even from a single track, so-called cluster damage. With increasing LET, the effectiveness will therefore increase until it saturates. For higher LET, RBE will decrease as the effectiveness is constant and the deposited dose increases further with LET. This decrease of RBE at very high LET values is called *overkill effect* and appears around 100–200 keV/µm as seen in a compilation of RBE data in Fig. 9.3 [33] for different cell lines and ions.

For different ions, the RBE as a function of LET is different, with the position of the maximum appearing at higher LET values for particles with higher charge. This is due to the fact

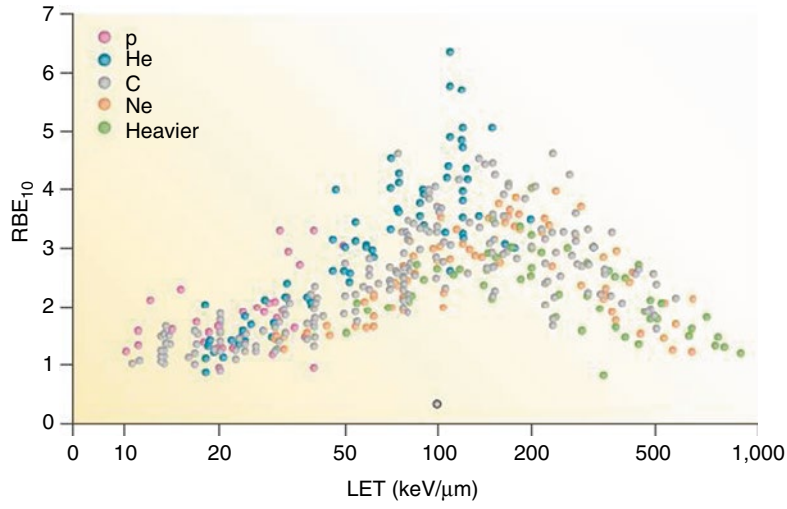

Fig. 9.3 Compilation of RBE data for various ions and cell types (Data from Ref. [33], image reproduced from [23])

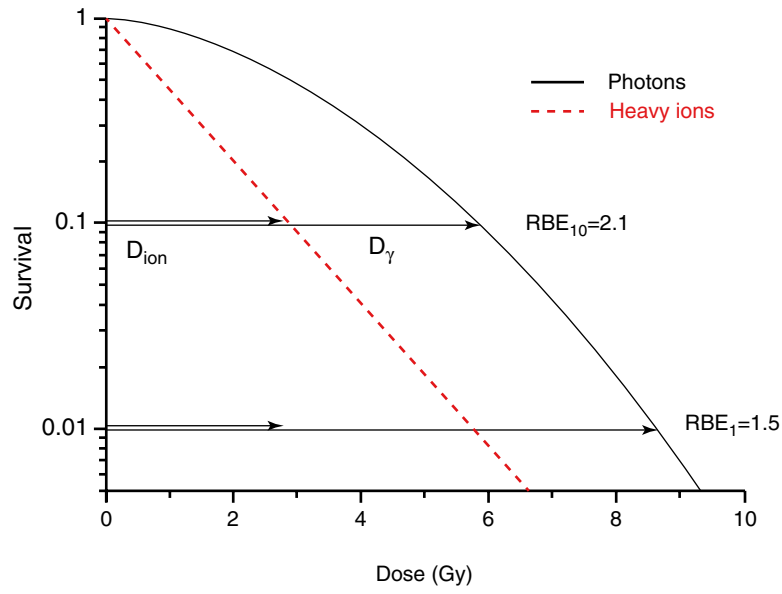

Fig. 9.4 Cell survival curves for photons and ions and determination of RBE for cell inactivation at 10 % and 1 % survival level (Image reproduced from Ref. [29])

that at same LET, lighter particles have lower energy and a smaller track radius, leading to higher energy density in the track as compared to heavier particles.

In addition there is a dose dependency of RBE, which is important when the dose per fraction is changed. The RBE for hypo-fractionated treatments is generally smaller than for more conventional fractionation schemes, with the strength of this dependency being determined by the α/β values of the tissue involved.

The dose dependence of RBE for ions can easily be explained by looking at the cell survival curves (Fig. 9.4): while photon survival curves exhibit the well-known, shoulder, survival curves for ions are getting more and more linear with increasing LET. Due to the nonlinearity of the photon survival curve, the ratio of doses to achieve the same survival level for both radiations is increasing for lower doses. In the very low dose region, the behavior of RBE may be different due to deviations of the survival curve from a purely linear-quadratic form.

Consequently, the ratio of RBE in normal tissues vs. tumor tissue has to be carefully considered, in order to select a fractionation scheme which leads to therapeutic gain, as crossing of RBE values as function of dose my occur (see Fig. 9.5).

When looking at the dependence of RBE on dose, it can be seen that tissues with higher α/β ratio (typically cells with lower repair capacity) exhibit a slower variation with dose as compared to cells with lower α/β ratio (typically cells with higher repair capacity and hence higher radiation resistance). This behavior demonstrates an additional biological benefit, when tumors with low α/β are treated within a tissue of higher α/β at conventional fraction doses around 2Gy. Since the knowledge of α/β ratios especially for tumors is limited, estimates for the values used in treatment planning have to be made carefully (see Ref. [18]). Moreover the RBE may be different for early and late reactions.

Finally there is evidence from in vitro data that the microenvironment of tumor cells is less important for the cell survival in high LET than in low LET radiation. The most important effect may be the oxygen enhancement ratio, which describes a decrease of radiation sensitivity of cells which are poorly oxygenated. This effect is decreasing at higher LET, where no difference can be observed (see Fig. 9.6). This behavior might be highly beneficial in hypoxic tumors, which are difficult to control with conventional radiation. In order to obtain a significant OER effect, it may be necessary to use ions, like oxygen, which provide even higher LET than carbon.

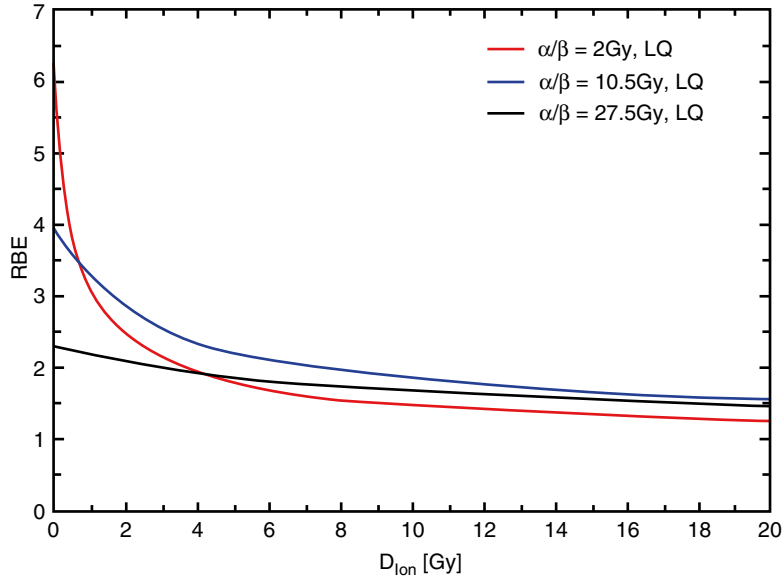

Fig. 9.5 Dose dependence of RBE for three different tissue characteristics as predicted by the simple linear-quadratic approach. Image reproduced from Ref. [8]

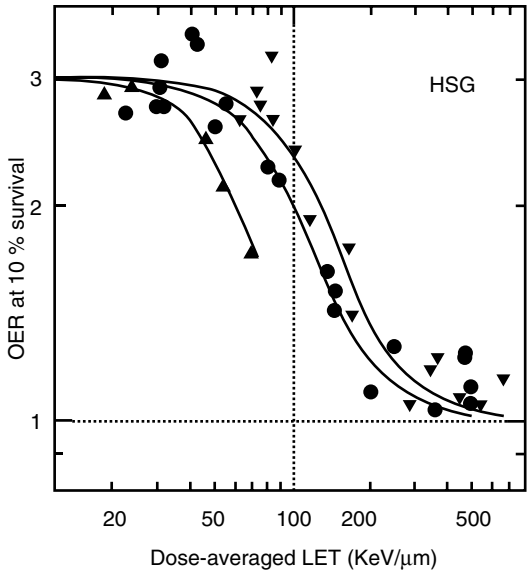

Fig. 9.6 Oxygen-enhancing ration at 10 % survival level measured in vitro for various ions as a function of LET (Image reproduced from Ref. [9])

The oxygen effect seems to show a general trend that high LET radiation, is equally effective for resistant cells, be it due to cell-cycle dependence, oxygenation, or resistant stem cells (see Ref. [23] for details).

9.4 Therapy Planning

Radiotherapy treatment planning for heavier ions is very similar to proton therapy planning from the physical point of view. Typically pencil beam models are used, which describe the three-dimensional dose arising from a single monoenergetic beam in water (see [4, 17, 22]). To describe the depth dose distribution, usually tabulated depth dose curves are used, which either rely completely on measured data or use additional Monte Carlo tools to generate a data base from a few measured data [26]. For the lateral dose distribution, typically a superposition of Gaussians is used, which exhibit widths which are varying with depth. The different terms in such an empirical description refer to the primary beam width, which is evolving due to multiple scattering and at least one additional term, which takes into account large-angle contributions, arising from nuclear fragmentation. The nuclear fragmentation is intrinsically included in the depth dose distribution.

Large differences arise from the modeling of RBE of carbon beam therapy. While for protons a single fixed value for the RBE is used, this is not a valid approach for heavier ions, as outlined above.

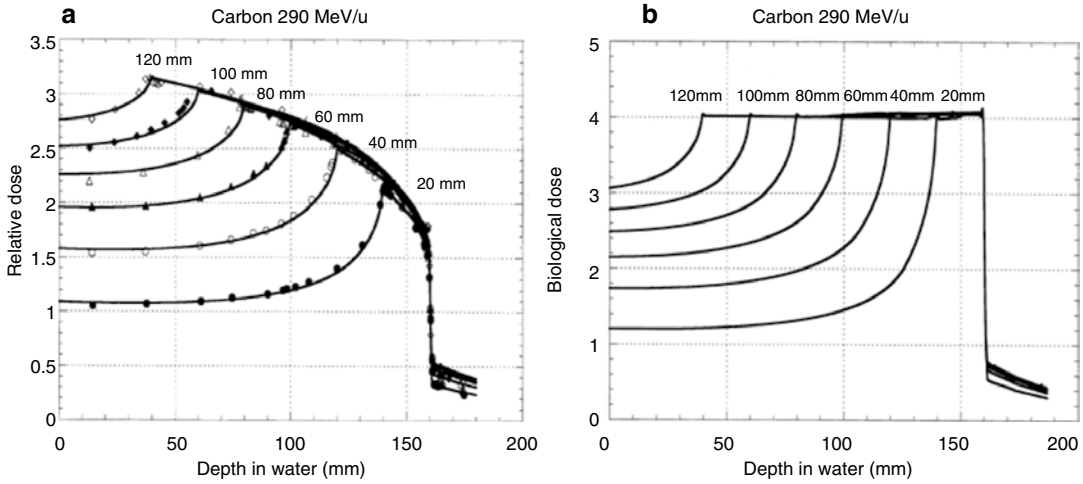

Fig. 9.7 Central axis depth-dose distribution for absorbed dose (**a**) and resulting RBE-weighted depth dose (**b**) for a fixed incoming carbon beam energy and various depth modulations at HIMAC. The decrease in absorbed dose in the SOBP is designed in a way to compensate the increase of RBE toward the distal end (Image reproduced from Ref. [21])

Historically, a depth-dependent RBE was used in Berkeley and Chiba, Japan, as long as only passive delivery techniques where available. In passive techniques, a fixed depth modulation of the treatment field is used. The lateral spread of the treatment field is achieved by a combination of scattering and magnetic deflection (wobbling) elements (see Ref. [21] for details). In such a system, the depth dose is modulated in such a way, as to compensate for the increase of RBE toward the distal end of the target. In Fig. 9.7 the example of various depth dose curves of the HIMAC beamline are shown. The modulation is such that a constant biological effect is produced throughout the target. The design of the modulator therefore reflects the RBE variation and cannot easily be modified.

The selected RBE is strictly valid only for certain fractionation scheme, tumor, and endpoint. Moreover, a superposition of several fields leads to a change of dose and LET and cannot be corrected for. Consequently in these systems, mostly only one field is delivered per day.

More recently, scanning beam delivery system became available, which allow for a more flexible adaption of dose to the target and especially a variable depth modulation, depending on the extension of the tumor in depth (see Refs. [11, 25]). Consequently, also a more flexible RBE modeling is used, which can take into account not only the correct depth variation of RBE but also other dependencies of RBE. Two main models are currently in use for treatment planning:

the local effect model (LEM) and the microkinetic model (MKM). The LEM (see Refs. [6, 7, 30, 31]) assumes that the differences between photons and ions are solely due to the dose distribution on a microscopic scale (expressed as LET). An important ingredient of the LEM is therefore a detailed modeling of the track structure of ions. A second assumption is that radiobiological experience gained with photons can be transferred to ions, by calculating the local damage for ions based on the known damage for photons. As a result, the model can describe the dependencies of RBE for ions and their fragments on the applied dose and for different cell types and endpoints, as long as these are known for photons. The most important input data which are required to calculate RBE values for a certain tumor type or endpoint are the α and β values for photons for the same tumor or endpoint. In addition information on the composition of the particle spectrum is needed, so that a direct integration into a Monte Carlo System is very useful [24].

The MKM (see Refs. [12, 13]) was introduced for the beam scanning system at HIMAC (Refs. [14, 15]). It is based on microdosimetric parameters of ions and links these parameters to macro-

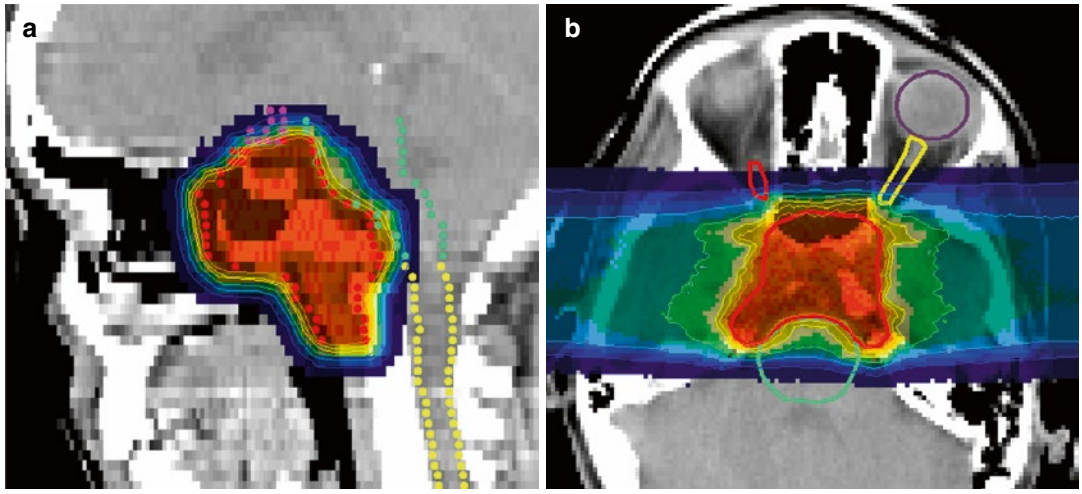

Fig. 9.8 Treatment plans for carbon ion therapy of a patient treated for a skull base chordoma with 20 fractions of 3 Gy (RBE) at GSI. The distribution for the biologically optimized IMPT plan is shown in sagittal (**a**) and transversal view (**b**) (Courtesy of M. Ellerbrock, Heidelberg)

scopic parameters like energy and LET, by using Monte Carlo simulations [28].

The big advantage of such models is that they allow for further modulation of the biological effective doses so that biologically optimized intensity-modulated ion beam therapy becomes feasible [5]. An example of such an optimization procedure is shown in Fig. 9.8.

There is however still an enormous potential in the development of therapy planning for ion beams, which may allow for further optimization of ion beam therapy:

- More detailed biological optimization: in current clinical practice, only fixed α/β values are used for all tissues, this is mainly due to the limited knowledge of α/β values for tumors, but with increasing experience a more detailed modeling may be achievable resulting in improved biological effective dose distributions.
- LET optimization: when the whole target volume is covered by each field, the highest LET always results in the distal part of the target, i.e., in the margin region. Three-dimensional scanning of a target with several fields offers enough degrees of freedom, to redistribute LET while the same dose distribution is maintained (a simple example is given in Ref. [1]). This allows for more stopping particles within the target or in regions which may benefit from the higher LET, like hypoxic regions. More generally beams with different LET may be combined to make optimal use of the high LET radiation (see [2]). This asks for a parallel optimization not only of MV X-rays with ions but potentially also for combinations like p/C, He/C, and C/O, which technically can be delivered at this time at some of the existing facilitates.
- PTV optimization: since the mean LET in a target is decreasing with volume, it is desirable to restrict high LET radiation to small volumes; therefore, techniques should be employed to reduce the volumes to be irradiated with high LET as much as possible. This may even be combined with a reduction of uncertainty in the delivered dose as was shown in Ref. [3]. Clinical results for combined treatments of X-rays and carbon ions show that even a limited carbon treatment may lead greatly improved results [32].
- Optimizing delivery parameters: current planning systems do not yet make use of the potential of modern beam scanning systems, typical parameters which may be varied during delivery are beam width and scan steps and scan directions. Adaption of these parameters may especially lead to much faster delivery of the treatment.

9.5 Clinical Facilities and Research

In the last 5 years, a number of new heavy ion therapy centers came into operation which demonstrated the overall improvement and utilization of technology. The most up-to-date facility is probably the Heidelberg ion beam therapy center, which started clinical operation in 2009. It features a high-resolution 3D beam scanning beam delivery in all three treatment rooms, which allows for 1 mm resolution in 3D. The beam energy can be changed from pulse to pulse from a library of 250 energy levels, similar to the beam intensity and the beam focus (between 3 and 10 mm FWHM for carbon).

The facility is currently providing proton and carbon ion beams for clinical application but already provides helium and oxygen beams with the same scanning functionality for preclinical research. Finally the facility is equipped with the world's first isocentric scanning gantry. Figure 9.9 shows the layout of the facility.

The gantry was commissioned in 2012 and allows for the same field size of 20 by 20 cm^2 as well as the same scan parameters as in the fixed horizontal beam rooms. Patient positioning is facilitated by the use of robotic controlled treatment tables and X-ray systems, which allow for accurate and fast positioning of the patient (see Fig. 9.10). The X-ray system also includes a cone-beam CT functionality.

The most important aspect of the HIT facility is however not a technical but an organizational one: the facility is installed on the campus of Heidelberg University and fully integrated into the existing

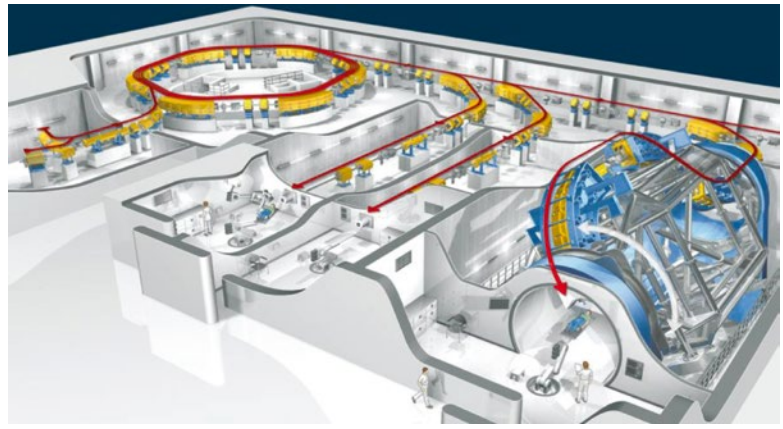

Fig. 9.9 Layout of the HIT facility in Heidelberg. The facility features currently three ion sources, a synchrotron, and two fixed horizontal as well as a gantry treatment room

Fig. 9.10 Treatment room at the HIT facility equipped with a robotic patient positioning and imaging system

oncological services and research centers, like the University Hospital including the Radiation Oncology Services, the National Center for Tumor Diseases (NCT), and the German Cancer Research Center (DKFZ). This allows exploitation of the full potential of ion beams in oncology within clinical trials combining ion beam therapy with other approaches in oncology, like conventional MV-treatment, surgery, chemotherapy, and novel targeted therapies.

There are about 12 clinical trials ongoing (see www.clinicaltrials.gov for a full list), aiming into three directions:

- *Comparison of proton* vs. *carbon ion radiotherapy*
  As carbon ion therapy is connected to higher costs that proton RT, the potential benefit will have to be demonstrated in clinical studies. The clinical results, e.g., for the treatment of skull base chordoma and chondrosarcoma with scanned carbon ions are certainly outstanding. In recently published data [34, 35], 5y (10y) local control (LC) rates of 72 % (54 %) for skull base chordoma patients were found after carbon ion therapy. For chondrosarcoma 88 % (88 %) LC was achieved after 5y (10y) with overall survival being 97.5 % (91.5 %). The only available proton data of similar quality are remarkably similar in local control (within a few percent) although the overall survival was considerably lower (54 % instead of 75 % after 10y for chordoma patients). The problem in this comparison is that the proton data have partially been gained with a combination with photons and (in the case of chondrosarcoma) have been achieved with only low-grade tumors. Two comparative trials which are currently recruiting patients are HIT, try to investigate the difference between both modalities and may provide respective data in the near future.
- *Investigation of novel tumor types*
  Several trials are ongoing at HIT, where the feasibility of using scanning ion beams therapy especially for moving tumors in the liver and pancreas, and for brain tumors like primary and recurrent glioblastoma and atypical meningioma is investigated. This will be important to apply ion beam therapy to a wider range of patients but is at the same time a challenge.
- *Combination of ion beam therapy with chemotherapy*
  Carbon ion therapy obtained excellent results also for LC in adenoid cystic carcinoma (ACCA; see Ref. [32]) but failed to improve OS, due to distant metastasis; it is therefore important to investigate the combined effect of carbon ions and chemotherapy, where little clinical data exist. For ACCa, for example, a combination treatment of conventional IMRT with a carbon boost and concomitant chemotherapy with Erbitux is therefore ongoing [20].

Other combined proton-ion beam facilities using beam scanning technology have been installed in 2013 in Pavia (Italy) and 2014 in Shanghai (China). A third facility was installed in 2012 in Marburg (Germany). This facility is not yet in operation but likely to be so in 2015 in cooperation with Heidelberg University. A facility in Wiener Neustadt (Austria) is under construction and will come into operation in the near future. The largest number of carbon facilities is, however, available in Japan, with currently four operating facilities (Chiba, Hyogo, Gunma, Saga) and two more under construction (Yokohama, Okinawa). Among these, only the HIMAC facility in Chiba has recently been upgraded for beam scanning technology [25].

Generally it is expected that these facilities not only will work on clinical trials and create more evidence for carbon ion therapy but also to provide unique research opportunities in medical physics and radiobiology so that further improvements of the ion beam radiotherapy may be achieved in the future.

References

1. Bassler N, Toftegaard J, Lühr A, et al. LET-painting increases tumour control probability in hypoxic tumours. Acta Oncol. 2014;53(1):25–32.
2. Bassler N, Jäkel O, Søndergaard CS, et al. Dose- and LET-painting with particle therapy. Acta Oncol. 2010;49(7):1170–6. Erratum in Acta Oncol. 2013 52(2):458.

3. Cabal G, Jäkel O. Towards a novel approach for PTV definition in particle therapy. Radiother Oncol. 2013;107(2):227–33.
4. Chen GT, Singh RP, Castro JR, et al. Treatment planning for heavy ion radiotherapy. Int J Radiat Oncol Biol Phys. 1979;5(10):1809–19.
5. Ellerbrock M, Jäkel O, Krämer M, et al. Clinical implementation of intensity modulated heavy ion therapy. Radiother Oncol. 2007;84:129.
6. Elsässer T, Scholz M. Improvement of the local effect model (LEM) – implications of clustered DNA damage. Radiat Prot Dosimetry. 2006;122:475–7.
7. Elsässer T, Scholz M. Cluster effects within the local effect model. Radiat Res. 2007;167:319–29.
8. Friedrich T, Scholz U, Durante M, et al. RBE of ion beams in hypofractionated radiotherapy (SBRT). Phys Med. 2014;30:588–9.
9. Furusawa Y, Fukutsu K, Aoki M, et al. Inactivation of aerobic and hypoxic cells from three different cell lines by accelerated (3)He-, (12)C- and (20)Ne-ion beams. Radiat Res. 2000;154(5):485–96.
10. Giap H, Giap B. Historical perspective and evolution of charged particle therapy. Transl Cancer Res. 2012;1(3):27–136.
11. Haberer T, Debus J, Eickhoff H, et al. The Heidelberg Ion Therapy Center. Radiother Oncol. 2004;73 Suppl 2:S186–90.
12. Hawkins RB. A microdosimetric – kinetic model of cell death from exposure to ionizing radiation of any LET, with experimental and clinical applications. Int J Radiat Biol. 1996;69:739–95.
13. Hawkins RB. A microdosmimetric – kinetic model for the effect of non-Poisson distribution of lethal lesions on the variation of RBE with LET. Radiat Res. 2003;160:61–9.
14. Inaniwa T, Furukawa T, Tomitani T, et al. Optimization for fast-scanning irradiation in particle therapy. Med Phys. 2007;34:3302–11.
15. Inaniwa T, et al. Treatment planning for a scanned carbon beam with a modified microdosimetric kinetic model. Phys Med Biol. 2010;55:6721–37.
16. International Commission on Radiation Units and Measurements. Stopping of ions heavier than Helium (Report 73). J ICRU 5. 2005.
17. Jäkel O, Krämer M, Karger CP, et al. Treatment planning for heavy ion radiotherapy: clinical implementation and application. Phys Med Biol. 2001;46: 1101–16.
18. Jäkel O, Schulz-Ertner D, Debus J. Specifying carbon ion doses for radiotherapy: the Heidelberg approach. J Radiat Res. 2007;48:A87–95.
19. Jäkel O. The relative biological effectiveness of proton and ion beams. Z Med Phys. 2008;18(4):276–85.
20. Jensen AD, Krauss J, Potthoff K, et al. Phase II study of induction chemotherapy with TPF followed by radioimmunotherapy with Cetuximab and intensity-modulated radiotherapy (IMRT) in combination with a carbon ion boost for locally advanced tumours of the oro-, hypopharynx and larynx – TPF-C-HIT. BMC Cancer. 2011;11:182.
21. Kanai T, Endo M, Minohara S, et al. Biophysical characteristics of HIMAC clinical irradiation system for heavy-ion radiation therapy. Int J Radiat Oncol Biol Phys. 1999;44:201–10.
22. Krämer M, Jäkel O, Haberer T, et al. Treatment planning for heavy-ion radiotherapy: physical beam model and dose optimization. Phys Med Biol. 2000;45: 3299–317.
23. Loeffler JS, Durante M. Charged particle therapy – optimization, challenges and future directions. Nat Rev Clin Oncol. 2013;10(7):411–24.
24. Mairani A, Brons S, Cerutti F, et al. The FLUKA Monte Carlo code coupled with the local effect model for biological calculations in carbon ion therapy. Phys Med Biol. 2010;55:4273–89.
25. Furukawa T, Inaniwa T, Sato S, et al. Performance of the NIRS fast scanning system for heavy-ion radiotherapy. Med Phys. 2010;37(11):5672–82.
26. Parodi K, Mairani A, Brons S. Monte Carlo simulations to support start-up and treatment planning of scanned proton and carbon ion therapy at a synchrotron-based facility. Phys Med Biol. 2012;57(12): 3759–84.
27. Raju MR. Heavy particle radiotherapy. New York: Academic Press; 1980.
28. Sato T, Watanabe R, Sihver L, et al. Applications of the microdosimetric function implemented in the macroscopic particle transport simulation code PHITS. Int J Radiat Biol. 2012;88(1–2):143–50.
29. Schardt D, et al. Heavy-ion tumor therapy: physical and radiobiological benefits. Rev Mod Physics. 2010;83:382–425.
30. Scholz M, Kraft G. Calculation of heavy ion inactivation probabilities based on track structure, x-ray sensitivity and target size. Radiat Prot Dosim. 1994;52:29–33.
31. Scholz M, Kraft G. Track structure and the calculation of biological effects of heavy charged particles. Adv Space Res. 1996;18:5–14.
32. Schulz-Ertner D, Nikoghosyan A, Didinger B, et al. Therapy strategies for locally advanced adenoid cystic carcinomas using modern radiation therapy techniques. Cancer. 2005;104:338–44.
33. Sørensen BS, Overgaard J, Bassler N. In vitro RBE-LET dependence for multiple particle types. Acta Oncol. 2011;50(6):757–62.
34. Uhl M, Mattke M, Welzel T, et al. Highly effective treatment of skull base chordoma with carbon ion irradiation using a raster scan technique in 155 patients: first long-term results. Cancer. 2014;120(21): 3410–7.
35. Uhl M, Mattke M, Welzel T, et al. High control rate in patients with chondrosarcoma of the skull base after carbon ion therapy: first report of long-term results. Cancer. 2014;120(10):1579–85.
36. Weber U, Kraft G. Comparison of carbon ions versus protons. Cancer J. 2009;15:325–32.
37. Highland VL. Some practical remarks on multiple scattering. Nuclear Instruments and Methods 1975;129:497–499. Erratum in Nuclear Instruments and Methods 1979;161:171.

10 Robustness Quantification and Worst-Case Robust Optimization in Intensity-Modulated Proton Therapy

Wei Liu

10.1 Introduction

Currently, most proton treatment centers employ passive-scattering proton therapy (PSPT), in which broad beams are shaped laterally using custom apertures and distally using compensators. However, the majority of centers recently built or under construction are using or will use scanning beams capable of delivering intensity-modulated proton therapy (IMPT), which utilizes magnetic scanning of a "pencil" proton beam to cover target volumes. IMPT is a powerful tool to design and efficiently deliver highly conformal and homogeneous dose distributions to the target, while at the same time sparing the adjacent organs at risk (OARs) to a greater degree compared to either intensity-modulated X-ray therapy (IMRT) or PSPT [1, 2]. This is mainly facilitated by the flexibility to set nonuniform intensities of "beamlets" with a sequence of energies of multiple beams incident from different directions. A beamlet is a narrow scanning beam of protons that exits the nozzle and is incident on the patient or phantom surface; all the beamlets from a given angle make up the beam from that angle.

W. Liu
Department of Radiation Oncology,
Mayo Clinic in Arizona, 5777 E Mayo Blvd.,
Phoenix, AZ 85054, USA
e-mail: Liu.wei@mayo.edu

In IMPT, the energies and intensities of thousands of individual narrow "beamlets" are optimized using sophisticated computer algorithms and mathematically specified criteria (an "objective function") to achieve an optimal compromise between an adequate tumoricidal dose to the target and the sparing of critical normal structures [3]. A common strategy in IMRT and IMPT optimization involves computing the contribution of each of thousands of beamlets to each dose voxel in volumes of interest (target and critical structures) using appropriate pencil-beam algorithms prior to optimization. The contributions to voxels from all the beamlets per unit intensity within the range of influence have been called an "influence matrix (IM)" [4]. The dose to each voxel is then calculated by adding up the contributions from all beamlets weighted with optimized intensities.

Various strategies have been proposed for designing IMPT plans [3]. The two most prominent ones are (1) the single-field uniform dose method and (2) 3D intensity modulation. In the former, intensities of beamlets of each beam are optimized individually without considering other beams, with the objective of producing, per beam, uniform dose distribution within the target volume and minimum dose outside the target volume. We call this method "single field optimized" IMPT, or SFO-IMPT (SFO is often referred to as single-field uniform dose (SFUD) optimization). In 3D intensity modulation, intensities of all beams are optimized simultaneously to balance

A.K. Rath, N. Sahoo (eds.), *Particle Radiotherapy: Emerging Technology for Treatment of Cancer*,
DOI 10.1007/978-81-322-2622-2_10

the dose and dose-volume objectives of normal tissues and the target volumes. We call this method "multi-field optimized" IMPT, or MFO-IMPT, and it is the proton spot-scanning equivalent of IMRT. For obvious reasons, it has the greatest flexibility to produce optimum dose distribution patterns, especially for complex anatomic geometries. The work reported in this book chapter is focused on the MFO-IMPT. For brevity, we will use the term IMPT to refer to MFO-IMPT in the remainder of the document unless otherwise necessary for clarity.

Although IMPT has the aforementioned advantages over IMRT and PSPT, the effectiveness of IMPT may be greatly diminished by range and patient setup uncertainties [5–11]. Range uncertainties arise from multiple sources, such as computed tomography (CT) number uncertainties, tumor shrinkage, patient weight gain or loss, and conversion from CT numbers to stopping powers. Appreciable degradation of the delivered dose distributions may also occur from setup uncertainties due to the misalignment of incident beams and the patient anatomy and due to the realignment of internal heterogeneities among themselves and with respect to the target volume. These uncertainties may cause the delivered IMPT dose distribution to be significantly different from what is seen on the treatment plan, may be of questionable reliability, and may lead to unforeseen outcomes.

For MFO-IMPT, the intensities of spots placed in the target volume and the corresponding dose distributions per beam are, in general, highly inhomogeneous. In many situations, beamlets from a given beam direction may not even reach the distal edge of the target. Inhomogeneous dose distributions within the target for individual beams are compensated for by dose deposited by beamlets from other directions. Therefore, the uncertainties in range may lead to either overshooting, i.e., beamlets producing hot spots in the target volume, or undershooting, i.e., beamlets producing cold spots. This makes IMPT even more sensitive to range uncertainties [5].

In conventional photon radiotherapy (3D conformal or IMRT), setup uncertainties are accounted for by adding margins to the clinical target volume (CTV) to form a planning target volume (PTV). The PTV margin is chosen in such a way that the CTV will remain covered with the prescribed isodose surface with high probability (e.g., 95 %) in the presence of uncertainties. This is a good assumption for photons since, as pointed out by Meleike et al. [12], the photon dose distribution is minimally perturbed by uncertainties. In other words, a photon dose distribution is relatively robust in the face of uncertainties. Meleike et al. (2006) have used the term "static dose cloud" to describe a photon dose distribution.

For proton therapy, dose distributions are affected significantly by various factors mentioned above [1, 2, 13, 14]. The perturbation occurs not only distally and proximally to the target volume but also within the target and, as a result, strongly affects the robustness of the proton dose distribution. Presence of complex heterogeneities in the path of protons may further exacerbate the perturbation of dose distributions. The traditional concept of PTV is not applicable to proton therapy. Proton dose distributions are hardly affected by rigid body shifts along the beam direction, but they are affected by lateral shifts and by anatomic variations. For PSPT, an effective method to reduce the impact of uncertainties, especially for relatively homogeneous anatomies (e.g., prostate), is the use of appropriate beam-specific distal and proximal margins (coupled with smearing of range compensators). The lateral margins used are the same as those for defining the PTV in photon therapy. It is commonly assumed that the same practice is appropriate for SFO-IMPT, although there is no equivalent of smearing in SFO (it is possibly that increasing spot size could play the role of smearing). However, because of the arbitrarily irregular beamlet intensity distributions within the target volumes for MFO-IMPT, the practice of assigning beam-specific distal and proximal margins is not meaningful.

In the absence of a suitable method to account for uncertainties, the current, though unsatisfactory, practice of MFO-IMPT has been to expand

the CTV into traditional PTV [15]. In the context of this approximation, it is assumed that anatomic changes and tumor motion have a negligible impact on the dose distribution in space [9]. The resulting dose distributions may be significantly deficient in robustness, i.e., the dose distribution actually delivered may be quite different from what is planned [5]. This lack of robustness leads to a lack of confidence in the dose distributions seen on the MFO-IMPT plans even though nominally they are often the best that can be achieved with proton therapy.

Concern about robustness has been an impediment in the broader clinical use of MFO-IMPT. Therefore, it is critical to minimize the effects of these variations on a proton treatment plan. To do so as a first step, one must quantify the plan's sensitivity to variations through a process, which is called robustness quantification [16]. A proton beam therapy plan is said to be robust, if even in the face of variations, a clinically acceptable outcome for the patient can be guaranteed. Once we develop a quantitative measure of plan robustness, we will be able to mitigate effects of variations through robust optimization [17]. Robust optimization will enable more precise and predictable delivery of proton plans, which will in turn assure the highest clinical benefit from this modern radiotherapy modality. This is becoming increasingly important since almost all emerging proton treatment centers rely on pencil beam scanning technology, allowing for IMPT.

10.2 Robustness Quantification

We will at first discuss the "robustness quantification" in this section. In order to fairly evaluate plan qualities of two different plans, the effect of uncertainties on dose distributions must be addressed. The nominal dose distributions (i.e., without considering any uncertainties) from the conventionally optimized IMPT plans do not reflect the dose distributions actually realized under uncertainties. To a considerably lesser degree, the same may be true for the robustly optimized plan (Fig. 10.1). This point has been articulated for almost three decades [16] but not instituted in routine practice due to high computational costs. For comparing photon plans among themselves, this is not a significant issue, especially if competing plans all have appropriate PTV margins. However, because the concept of conventionally defined PTV is not sufficient for the evaluation of target dose distribution for protons due to beam-specific range uncertainty, a different method of plan evaluation is necessary for comparing one proton plan with another or for comparing a proton plan with a photon plan. In theory, one can look at all possible uncertainty situations. However, it would require prohibitively large computation times and data processing efforts to evaluate plans under all realizable perturbed doses from the uncertainties. Therefore a simplification strategy needs to be adopted.

Generally, the inter-fractional patient setup uncertainties are considered to be random and are incorporated by shifting the isocenter of the patient in the anteroposterior (A-P), superior–inferior (S-I), and lateral (R-L) directions by the same margin as is used for defining the PTV, yielding six dose distributions and the corresponding "influence matrices." Range uncertainties for a single patient are systematic and propagate through the whole course of the treatment but are random for a patient population. They are incorporated by scaling the stopping powers by −3.5 and 3.5 % to generate two additional dose distributions and influence matrices corresponding to maximum and minimum proton ranges, respectively. Therefore in total there are 9 doses per voxel (the nominal dose plus 8 perturbed doses). Dose distributions are recalculated by a dose engine (either a commercial system like Eclipse™ or an in-house-developed dose engine) for each of the eight scenarios. The recalculation of the dose distributions is tedious and time consuming, especially for the situations of range uncertainties since a correspondingly modified stopping power table has to be employed.

The above method is adopted in most operational proton centers for practical reasons. However, in order to account for the impact of the combined uncertainties, some groups proposed

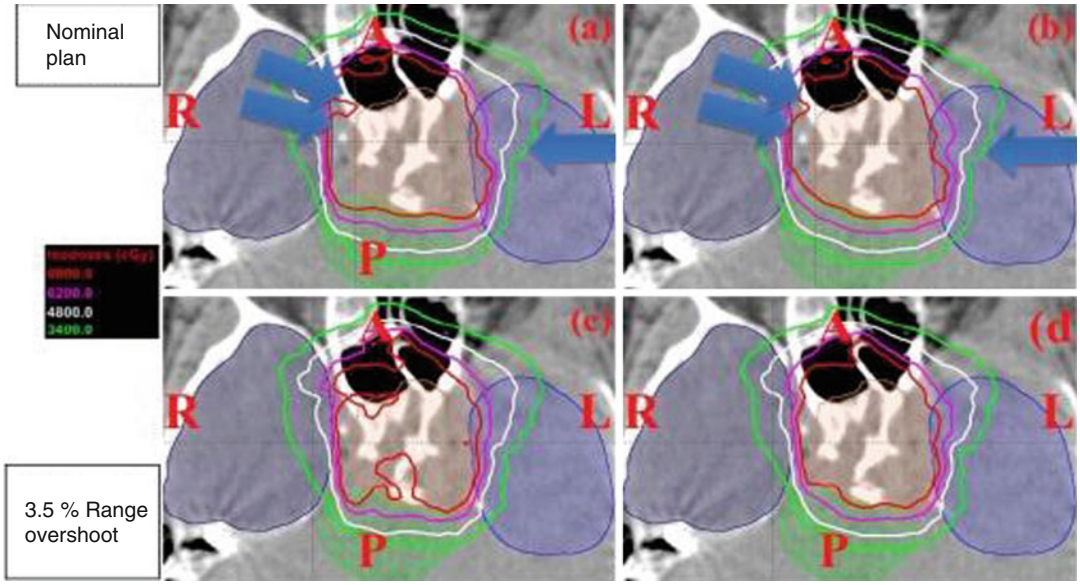

Fig. 10.1 Dose distributions in the transverse plane for a typical base-of-skull patient: The depicted distributions illustrate that the CTV-based robustly optimized plan (panels **b**, **d**) is insensitive to uncertainties relative to the PTV-based conventionally optimized plan (panels **a**, **c**). The prescription isodose lines (*red lines*) are heavily perturbed even within CTV (*indicated by the red arrow*). CTV, *orange segment*; brainstem, *green segment*; right temporal lobe, *cyan*; left temporal lobe, *blue*. The better normal tissue protection could also be seen by comparing the nominal dose distribution from the conventional optimization (panel **a**) and the one from the robust optimization (panel **b**)

to use 21 doses per each voxel, i.e., for each of nominal, minimum, and maximum proton range, the isocenter of the patient is at the nominal position and rigidly shifted in the A-P, S-I, and R-L directions respectively, yielding 21 dose distributions (7 per proton range) [18, 19].

Based on the recalculated dose distributions as described above, so far three robustness quantification methods have been published:

1. Worst-case analysis [20, 21]: We can extract the highest and the lowest dose values in each voxel from the original and the perturbed dose distributions, forming a hot dose distribution with the highest values and a cold dose distribution with the lowest values. The dose distributions derived in this way provides an estimate of the robustness of the delivered dose to spatial and range uncertainties [22]. Please note that the resultant dose distributions are unrealistic (please see the Sect. 10.4). The original DVH of each structure from the nominal dose distribution is overlaid by a shaded area that was bounded by the DVHs from the cold and the hot dose distributions obtained from the robustness analysis. The width of the DVH bands corresponds to the plan robustness for the structure indicated (Fig. 10.2).
2. Bands of DVHs [23, 24]: To evaluate or compare IMPT plans, a robustness quantification technique is used that displayed the envelope of all dose-volume histograms (DVHs) in band graphs of all the dose distributions associated with the corresponding range or setup uncertainties. For convenience, the DVHs derived by choosing the nominal dose of a voxel are also displayed in the robust quantification. The width of the DVH bands is also used to indicate the plan robustness for the structure (Fig. 10.3).
3. Robustness quantification using root-mean-square-deviation-dose-volume histograms

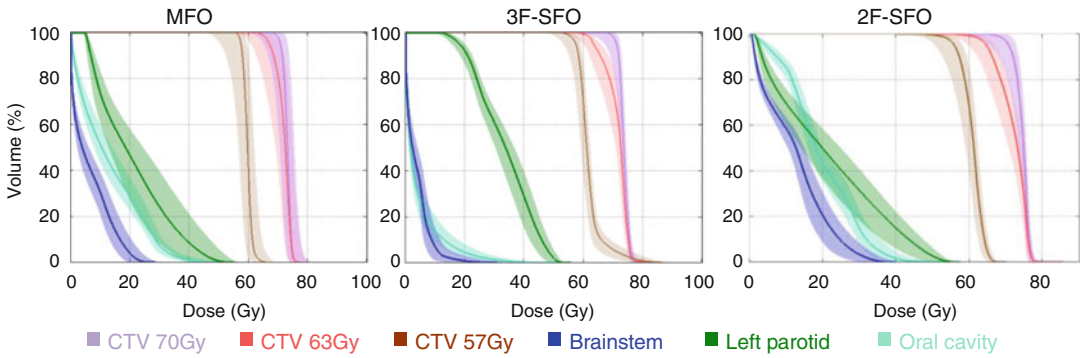

Fig. 10.2 Worst-case robustness quantification of the 3 F-MFO, 3 F-SFO, and 2 F-SFO (F is used for fields) plans for a head and neck patient: The *solid lines* are DVHs for the nominal doses, and the *shaded areas* (the bands) are bounded by the DVHs for the cold and hot doses obtained from the robustness analysis (This figure is from Fig. 2 of Quan et al. [21])

(RVHs) [18, 19, 25] (analogous to the error-bar volume histograms [EVHs] proposed by Albertini et al. [26]): The root-mean-square dose deviation (RMSD) of voxels is calculated as the square root of the sum square of the differences between the dose calculated under the uncertainty scenarios and the nominal scenario and the mean dose of those 9 (or 21) doses. This was then used to construct the RVH, which represents the relative volume on one side (vertical axis) and the dose deviation on the other (horizontal axis) (Fig. 10.4). This RVH plot captures the overall effect of uncertainties on the dose to a volume of interest that is analogous to the dose-volume histogram (DVH) used for assessing the nominal plan. We further simplified the RVH to compare the robustness of two plans by calculating the area under the RVH curve (AUC), which gives a single numerical measure of the plan's robustness for a given volume of interest and can be easily incorporated into the paired statistical tests for comparison: the smaller the AUC, the more robust the plan is for the structure between competing plans. Compared to the other methods, the RVH gives more quantitative information of the robustness of the plan. For example, the point in Fig. 10.4 as indicated by the arrow shows that 40 % of CTV from the robustly optimized plan (red solid curve) has the root-mean-square dose of at least 2.5 Gy[RBE].

Park et al. proposed a statistical method [27] by performing a more comprehensive simulation to account for the dose under uncertainties, in which the dose was recalculated 600 times per given plan under the influence of random and systematic setup errors and proton range errors. On the basis of simulation, the probability of dose variations was determined and the expected values and standard deviations of DVHs were calculated. The uncertainties in dose were spatially visualized as a probability map of failure to target coverage or overdose of critical structures.

These robust quantification tools can be applied in the clinic to help physicians and physicists judge whether IMPT plans are acceptable. We should emphasize that the advantages of the worst-case methods described here do not require a detailed model for the considered uncertainties [8, 20] and do not need to consider a large number of uncertainty scenarios.

10.3 Worst-Case Robust Optimization

In this section, we will discuss the robust optimization (especially the so-called worst-case robust optimization) and its application in IMPT planning. During the last several years, there is significant progress in this area due to efforts worldwide.

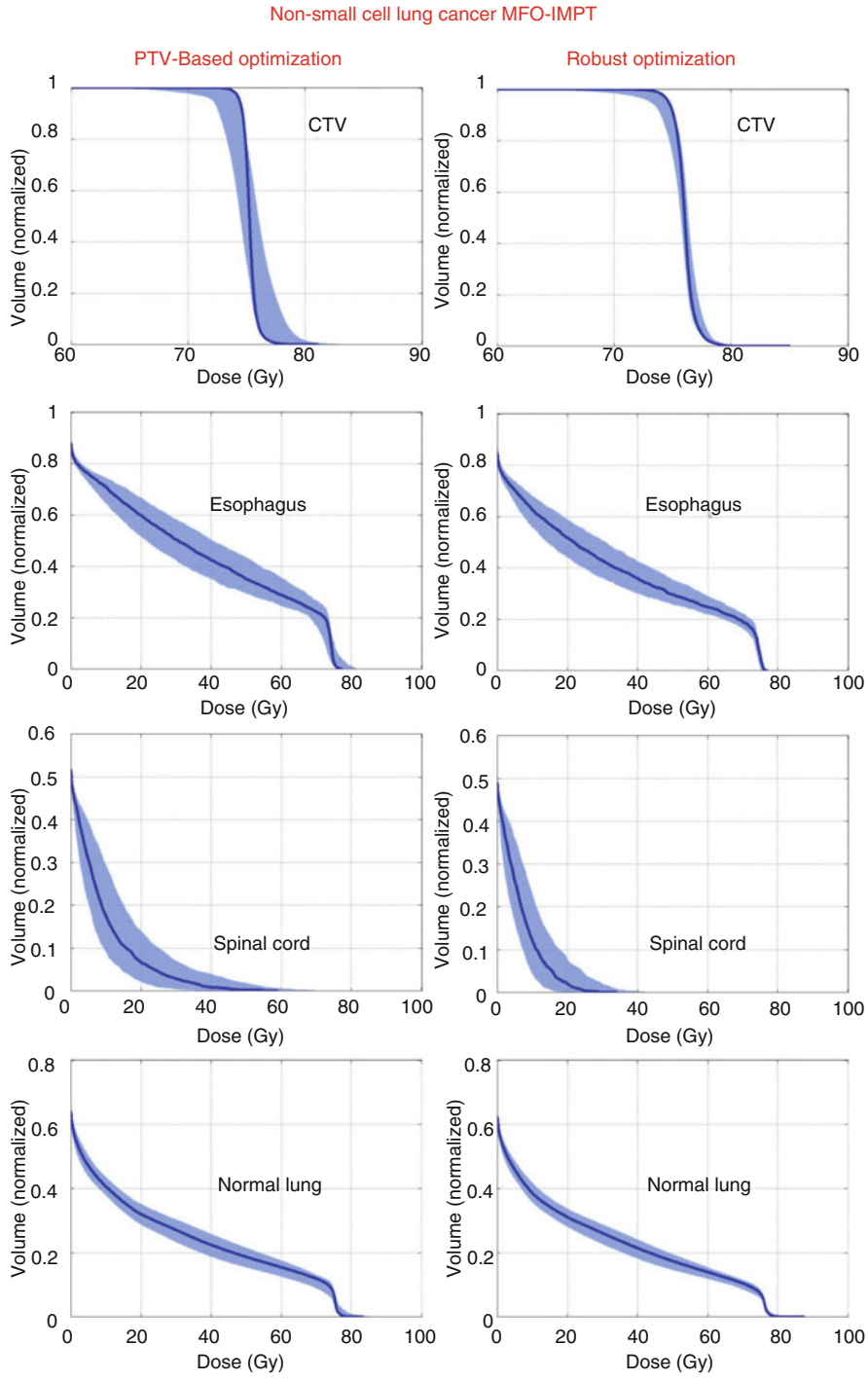

Fig. 10.3 Robustness quantification using bands of DVH: Color wash represents the DVH bands for dose distributions covering all setup and proton range uncertainties for CTV and various organs for the robustly optimized plan (*right column*) and the PTV-based plan (*left*) for the non small cell lung cancer (NSCLC) case. The *solid lines* are the DVHs for the nominal dose distribution (i.e., without consideration of uncertainties). The narrowness of CTV band for the robustly optimized plan indicates improved robustness. At the same time, the sparing for the esophagus, spinal cord, and normal lung is perceptibly improved (This figure is copied from Fig. 1 of Liu et al. [23])

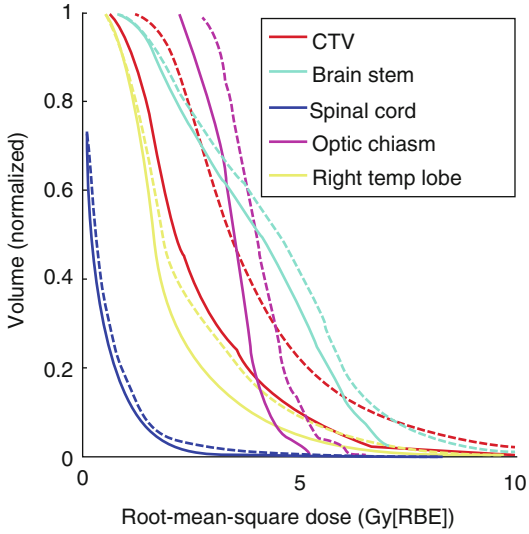

Fig. 10.4 RVH curves derived from the robust plan (*solid lines*) and the PTV-based plan (*dashed lines*) for a head and neck cancer patient: Each curve was normalized by the total volume of the corresponding organ. RVH AUCs for the robustly optimized plan were smaller than those for the PTV-based plan, indicating that AUCs can be useful for relative comparisons of the plans in terms of robustness (This figure is copied from Fig. 2 of Liu et al. [19])

A few robust optimization techniques have been reported to be effective at compensating for setup and range uncertainties in IMPT planning [8, 9, 23, 28–31]. For example, Unkelbach et al. [9] showed feasibility of probabilistic robust optimization that requires large samples of perturbed dose distributions. Chen et al. [28] included the plan robustness in the multiple criterial optimizations (MCO) by navigation in the Pareto surface to find the compromise between the plan quality and plan robustness. Fredriksson et al. [29] suggested a minimax optimization method that significantly reduces the number of required dose samples by considering extreme yet realistic dose distributions. Pflugfelder et al. [8] showed that similar optimization results can be achieved by considering the theoretically worst-case dose distribution that is derived by assigning each voxel with the lowest (for target volume) or highest (for organs at risk) dose from only 8 sampled dose distributions calculated under extreme situations. The resulting treatment plans showed reduced sensitivity to uncertainties.

During the last several years, we have developed our own worst-case robust optimization methods [23, 30]. The methods we used to design and compare robustly and conventionally optimized plans differ from those used by many other investigators [8–11]. A modification of the objective function to penalize hot spots within the target, which could potentially occur due to range uncertainties, leads to improved target dose homogeneity. The objective function value for a given iteration is computed using the "worst-case dose distribution" [20]. The worst-case dose distribution was represented by the minimum of the 9 (or 21) doses in each voxel in the CTV and the maximum of the 9 (or 21) doses in each voxel outside the CTV. This is analogous to using the PTV dose distribution for photons, which implicitly represents the worst-case dose distribution for the CTV. Our robust optimization approach inherits the simplicity of worst-case robust optimization and does not require a detailed model for uncertainties.

It is important to note that in our worst-case robust optimization the optimization target is chosen to be CTV, rather than PTV. No geometrical margin is used; rather, uncertainties are considered and accounted for in the optimization algorithm. Although robust optimization does not directly aim to minimize the dose delivered to normal tissues in the nominal scenario (without any uncertainties considered), direct targeting the CTV instead of the larger PTV improves plan quality compared to conventional PTV-based optimization [18, 23, 30, 32].

IMPT optimization, in particular robust IMPT optimization, is highly CPU time and memory intensive. The memory requirement to compute influence matrices is substantial even in non-robust IMPT treatment planning. This is due to the following reasons: (1) Spatially dense beamlets may be needed to achieve desired dose distribution in highly inhomogeneous patient anatomies. (2) A fine dose grid in the dose calculation is needed to accurately reflect the steep dose gradient near the rapid fall-off region of the proton dose distribution [33]. (3) The number of energy layers used in the treatment beams often

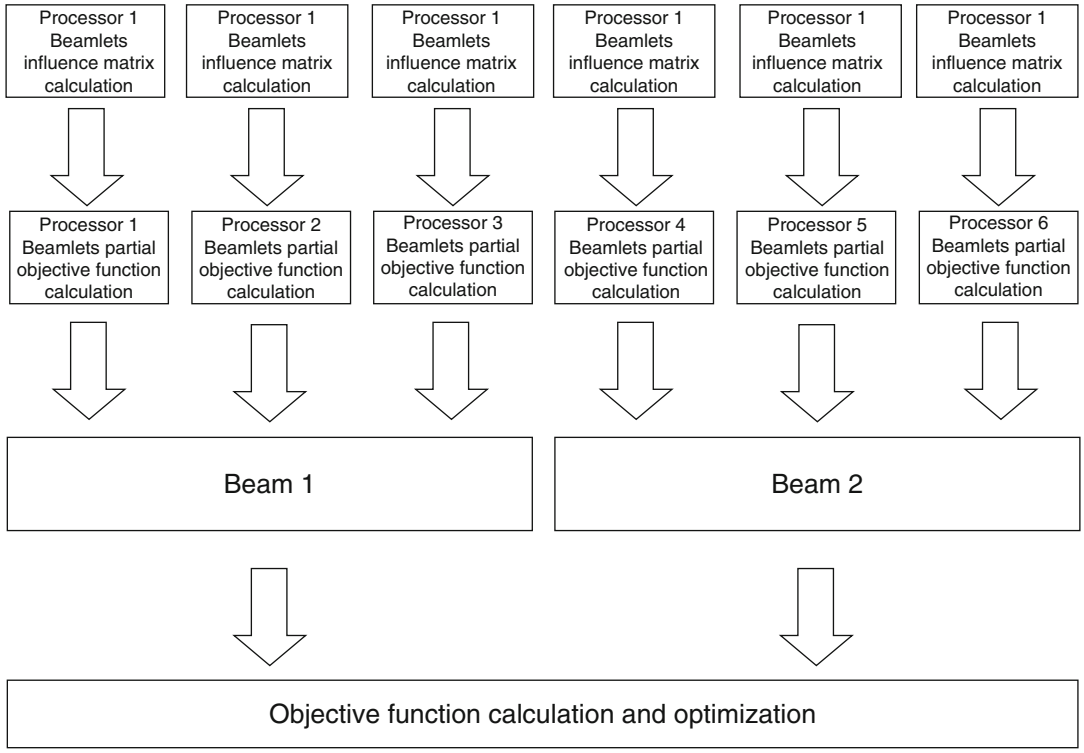

Fig. 10.5 Diagram of implementation of our parallelized large-scale worst-case robust optimizer. The optimizer is parallelized on the beamlet domain and uses the L-BFGS algorithm

reaches 50 in a reasonably complex IMPT plan to form a wide enough spread-out Bragg peak (SOBP) to cover the target from the proximal edge to the distal edge. (4) The incident protons due to scattering along the beamlet path may spread over a large region. (5) Secondary particles from nuclear interactions in the medium have a much wider angular distribution than the primary protons [34]. The latter two issues cause the lateral dose distribution of a proton beamlet to be markedly different from a Gaussian distribution. While deviations from Gaussian distributions due to these factors are seemingly negligible, the sum of the contributions from all the distant beamlets can be up to 15 % of the total dose and must be accounted for to ensure the accuracy and validity of the optimized dose distributions [35, 36]. Better accuracy of the lateral dose distribution of one proton beamlet is, however, achieved at the expense of larger memory usage than with simple Gaussian distributions (about 30 times larger). Therefore the amount of data to be computed during IMPT treatment planning increases by one to two orders of magnitude, requiring substantial memory and computation time [4].

What is more, robust optimization for IMPT is even more challenging in computation time and memory usage since many more influence matrices are needed to include the impact of setup and range uncertainties in the optimization. Beam angle optimization and 4D robust and RBE-weighted optimization for IMPT are even more challenging in terms of computation time and memory usage since even more influence matrices need to be included in order to model the impact of uncertainties in the optimization, and on-the-fly RBE calculation is extremely time consuming. The resultant influence matrices, which are stored in the memory in the form of single precision floating numbers for efficient

optimization implementation, easily consume more than 500 GB memory.

Due to the rapid development of parallelized computation via message passing interface (MPI) and CPU-clustered supercomputers, ultrafast and memory-limit-free implementation of robust optimization is now feasible. To achieve acceptable optimization times and meet memory requirements, we parallelized our robust optimization in the beamlet domain using memory-distributed parallelization on a large multiprocessor system (Fig. 10.5). All beamlet computations are dynamically allocated and distributed to the processors almost uniformly. Every processor handles the dose calculation of each dose voxel in volumes of interest for a group of beamlets belonging to a given beam. A compressed sparse matrix format is used to conserve memory for every processor. Our efficient method essentially has no memory limit and can easily be expanded to explore more demanding problems in the future. The optimization was performed using the limited-memory Broyden–Fletcher–Goldfarb–Shanno (L-BFGS) method [37] included in the optimization software OPT++ [38].

We are in the process of implementing robust IMPT optimization clinically at Mayo Clinic. Our approach has been used the University of Texas MD Anderson Cancer Center (MDACC) Proton Treatment Center at Houston (PTC-H) to generate robust IMPT plans to treat complex lung cancers. Fig. 10.6 shows the clinical work flow for robust optimization at MDACC. Steps in yellow are done in Eclipse™ (Varian Medical Systems, Palo Alto, California), except the steps in *white*. First a plan will be generated in Eclipse™. The generated plan related files, namely, CT files, RT structure files, and the associated dose-volume constraints will be exported to the in-house-developed robust optimization software. During robust optimization (i.e., the step in *white*), the fluence map will be modified by the robust optimizer to generate a robust optimal plan. The robust plan is reimported to Eclipse™ for the final dose calculation. DICOM files are used for communication between various pieces of software.

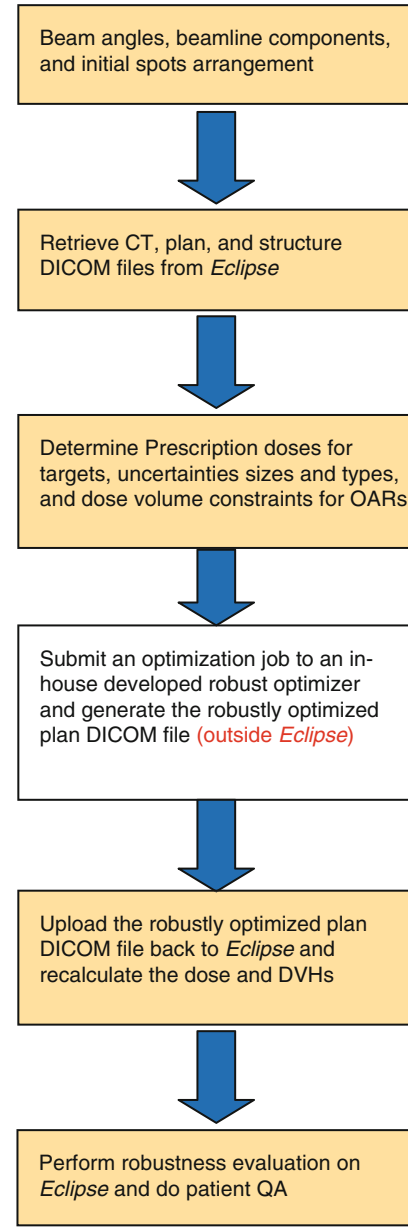

Fig. 10.6 Work flow chart of applying our worst-case robust optimization in MD Anderson Cancer Center Proton Treatment Center in Houston: Every step in *yellow color* is done in a commercial treatment planning system, Eclipse™ with DICOM as the interface. The step in *white color* is the robust optimization step done in an in-house-developed worst-case robust optimizer. Patient data are de-identified

We have successfully applied our robust optimization to several disease sites (H&N, the base of the skull, the lung, and the prostate) for popu-

lations of patients [18, 25, 32] in IMPT planning studies [23, 24, 32]. To date approximately 100 patients have been studied using our system with satisfactory results. We have demonstrated that robustly optimized dose distributions are significantly less sensitive to setup and range uncertainties than the conventionally optimized PTV-based dose distributions. An important finding of our work is that robust optimization may also result in improved quality of plans in terms of greater sparing of normal tissues and more homogeneous target dose distributions [18, 19, 23, 25, 30, 32], which is consistent with the results by other groups [29, 39].

10.3.1 How to Account for Respiratory Motion

IMPT for targets in thorax is further complicated by intra-fractional respiratory motion. Intra-fractional organ motion may also cause significant changes in patient geometry [13] and, consequently, in planned dose distributions. The interplay effect of dynamic delivery and tumor motion has been reported to degrade the quality of the resulting dose distribution, particularly in IMPT [40–47]. Furthermore, it has been shown that the pattern of breathing motion seen at the time of simulation may change during treatment [48], which has been reported to seriously perturb the resulting dose distribution in IMRT [49]. Fortunately, the availability of respiration-correlated 4D CT has yielded a better understanding of the amplitudes and characteristics of anatomy motion due to breathing [50, 51]. In order to account for respiratory motion, an internal gross target volume (IGTV) is generally formed to encompass the extent of gross target volume (GTV) motion in all phases using four-dimensional computed tomography (4D CT). The IGTV is then expanded to form internal target volume (ITV) (ICRU 1999) [52] by an additional margin (e.g., 8 mm) to account for subclinical microscopic disease. Techniques such as breath hold, gating, and tumor tracking can be used to mitigate the effects of large amplitude respiratory motion. The methods of breath holding, gating, and tumor tracking can be unreliable, difficult for patients to tolerate, and technologically demanding and may prolong the treatment time, while the ITV method may deliver more dose than is necessary to the healthy tissue surrounding the tumor [52]. In addition, the change in tissue density due to respiratory motion was generally accounted for by the use of averaged 4D CT and integrated density override of the GTV (over all phases). Kang et al. [13] demonstrated that this method was effective in preserving target coverage under the influence of respiratory motion for PSPT, while its effectiveness in IMPT is still under investigation.

We did the worst-case robust optimization in a population of lung cancer patients [25]. We found that although our worst-case robust optimization method did not directly account for respiratory motion in the optimization algorithm, it was still superior to the conventional PTV-based optimization. We speculated that the effects of respiratory motion might possibly be translated into setup and range uncertainties, which could be possibly mitigated by our method [25]. The non-serious interplay effect from our worst-case robust optimization might be due to the fact that the spot spacing is similar to the tumor motion magnitude [47] since the patients included in the study are all from an institution protocol with the tumor motion less than one specified threshold (5 mm). Our method would be an acceptable solution to mitigate the influence of residual respiratory motion combined with setup/range uncertainties in IMPT to treat lung cancer with deep breath hold or beam gating. Appropriate repainting technique [44] might appear necessary to further minimize or eliminate the consequences of interplay effects if the spot sizes are smaller. Therefore, this planning approach could have a large, immediate clinical impact as several centers either currently treat or plan to treat lung patients using breath hold or beam gating. However, motion reduced the effectiveness of our methodology

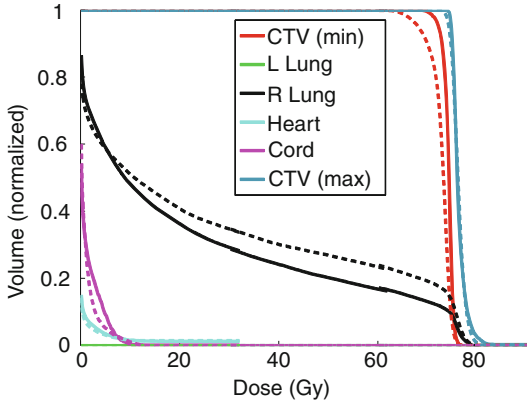

Fig. 10.7 Preliminary results of 4D robust optimization in IMPT to treat a lung cancer patient: (*Left*) Nominal 4D dose distribution; (*right*) worst-case 4D dose distribution. *Solid lines* are from the PTV-based conventional optimization, while *dash lines* are from the 4D robust optimization. In the *right panel*, the *red line* is from the lowest (cold) dose distribution of CTV, while the *blue line* is from the largest (hot) dose distribution of CTV (please refer to the worst-case robustness quantification in Sect. 10.2). The gap between them is much reduced from the 4D robust optimization. 4D robust optimization can render IMPT plans less sensitive to uncertainties and achieve better sparing of normal tissues than conventional plans optimized on the basis of margins

[25]. Thus, 4D robust optimization for IMPT might be one of the possible eventual solutions for treating lung cancer because it could potentially reduce the influence of motion uncertainty (i.e., irregular organ motion) as well. Some preliminary results are shown in Fig. 10.7. We refer the readers to Sect. 10.5.

10.4 Discussion

Due to the characteristics of proton dose depositions (e.g., sharp distal fall-off and lateral scattering) proton dose distributions are more sensitive to various forms of uncertainties than photon dose distributions. The conventional PTV concept to provide robust target coverage is not adequate for proton therapy, especially IMPT [53]. Therefore, the development of suitable methods to improve robustness (i.e., robust optimization) is vital to exploit the full potential of this important modality.

10.4.1 Worst-Case Dose Distribution

The worst-case dose distribution concept proposed by Lomax et al. [7] is considered to be nonphysical [8]. In addition to the proton range errors, it accounts for setup errors along the three major axes, without considering any nonrigid patient movements, movements in directions other than the major axes, or changes in patient anatomy. Some critics of this method points out that such simplifications may underestimate the spatial uncertainties of the proton beams. On the other hand, the worst-case dose distributions generated from this method consisted of the worst dose in each voxel out of all 8 (or 20) perturbed doses and the nominal doses. As pointed out by some critics of this method [21], this may overestimate the uncertainty. For example, the worst-case dose may include contributions from spatial perturbations along both positive and negative directions along an axis. A more thorough analysis of the plan robustness could be performed by the statistical method [27] at a much higher computational cost. However, we believe that the worst-case approach is more practical and has been shown to provide a reasonable estimate of the worst-case scenario dose distributions under uncertainties [54].

Another important point to be noted is that PTV is also unphysical and is the "worst-case" of CTV since the CTV could not appear in the left and in the right part of PTV simultaneously. We have used the PTV as the planning target and used the dose distribution of PTV to evaluate the CTV coverage in photon therapy for decades. Thus we believe that it should be a proper practice to use the worst-case dose distribution of CTV in the treatment planning and in the plan evaluation for proton therapy.

10.4.2 Understanding of Robust Optimization Results

Robust optimization incorporates setup and range uncertainties. It also takes into account differential effects due to tissue inhomogeneities within

the target and in the proximal beam path. Robust optimization is a global method and is able to account for over and underdosing globally, i.e., not only at the boundaries but also within structures. Margin-based conventional optimization is a local method and can only mitigate the impact of uncertainties at the boundaries. It is worth emphasizing again that the impact of uncertainties in IMPT is not only at the boundaries of but also in the middle of the structures. Therefore a local method like the margin-based conventional optimization is not effective in mitigating the influence of uncertainties in IMPT. On the other hand, we find that our worst-case robust optimization leads to significantly more robust dose distributions for both targets and OARs than do PTV-based optimization methods while maintaining and possibly even improving the sparing of healthy tissues.

The above conclusions at first glance appear to be counterintuitive. In general, the improvement in robustness is thought to be at the expense of normal tissue sparing [8–10, 55]. We believe this has been the result of comparing results of CTV-based robust optimization with CTV-based conventional optimization, i.e., without the incorporation of uncertainties in their CTV-based conventional optimization via a PTV margin. Because robustly optimized treatment planning strategies allows us to deliver the prescribed dose directly to the CTV rather than the PTV, it can potentially reduce doses to normal tissues compared to the PTV-based treatment planning strategy. In other words, robust optimization is more efficient in terms of sparing doses to normal tissues while providing better plan robustness than the PTV-based optimization technique. One might argue that the improved sparing of OARs from robust optimization may be due to its algorithms' implicit consideration of setup uncertainty for *both* OARs and targets, while PTV-based optimization considers only setup uncertainties and adds margins only to the target volume. We created IMPT plans using PTV-based optimization and in the presence of planning risk volumes (PRVs) (i.e., "PTV + PRV-based optimization") and compared to results obtained with robust optimization. We found that the above conclusion was still valid even under this comparison [32].

Two possible mechanisms were reported to improve plan robustness by robust optimization: (1) a localized single-field uniform dose distribution (LSFUD) mechanism [30], which usually happens within the targets to render per beam dose distribution more homogeneous (Fig. 10.8 and the difference between two dash green lines of Fig. 10.9). This is not the desired mechanism at the boundaries; otherwise normal tissue protection will be sacrificed to maintain the same target coverage (black dash lines of Fig. 10.9) and (2) perturbed dose distribution, which follows the change in anatomical geometry (Fig. 10.10). This mechanism usually takes place at the edge of targets and intends to ensure the target coverage despite the presence of the uncertainties. This mechanism does not need to sacrifice the normal tissue protection. The sensitivity of IMPT to uncertainties gives optimizers additional freedom compared to photon therapy. The optimizer can take advantage of this additional freedom and find a desired beamlet weight solution from the large degenerate solution space so that the dose distribution is automatically adjusted for the changes in anatomical geometry and is minimally perturbed by uncertainties (Fig. 10.10) [23, 30]. Thus, robust optimization results in patient-specific, optimizer-determined reduced margins for the CTV compared with a predefined fixed margin used in the PTV approach (Fig. 10.10) [23, 30]. More details are presented in two of our publications [23, 30].

10.4.3 Additional Advantages of Robust Optimization

In addition, there are also some advantages of robust optimization in the context of beam delivery over the PTV-based optimization. First of all, fewer spots might be needed from robust optimization since either some spots in the PTV margin volume are assigned zero weight or their weights are reduced. Additionally the robust optimization

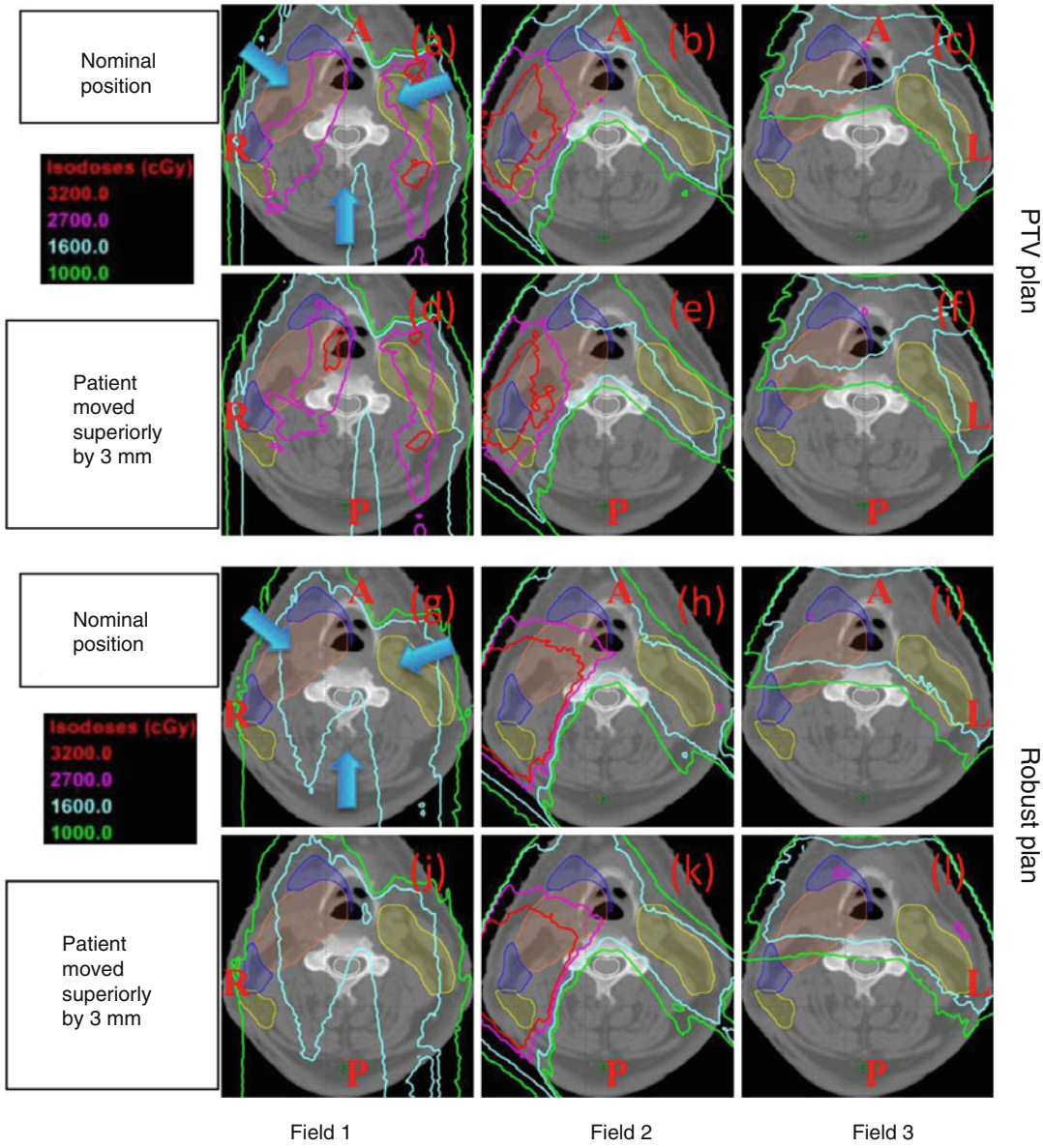

Fig. 10.8 Dose distributions per field in the transverse plane for a representative head and neck patient illustrate the relative insensitivity of the robustly optimized plan (*bottom two rows*) to set up uncertainties compared with the conventional PTV-based optimized plan (*top two rows*). Panels (**a**–**c**) and (**g**–**i**) show dose distributions in nominal position, whereas the panels (**d**–**f**) and (**j**–**l**) show corresponding data with 3 mm superior shift. Color scheme is CTV1, *orange*; CTV2, *blue*; and CTV3, *yellow*. *Blue arrows* in some of the panels indicate beam directions. The shift perturbs the dose distribution in the PTV-based plan significantly (e.g., 32 and 27 Gy (RBE) isodose lines). Robust optimization considerably reduces high dose gradients within each of the three fields (This figure is copied from Fig. 4 of Liu et al. [18])

can potentially improve the patient specific quality and assurance (QA) outcome. Currently, at MDACC, both depth dose and 2D planar dose are measured and verified against treatment planning system-calculated dose. These measurements are highly sensitive to dose gradient. Because robust

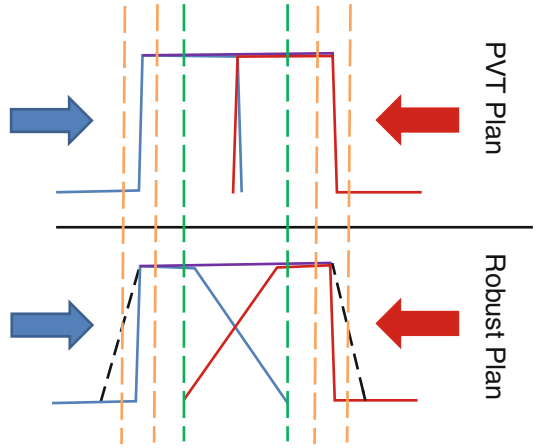

Fig. 10.9 Illustration shows the difference of the per field lateral dose profile across a target between the two mechanisms to make an IMPT plan more robust via robust optimization, (*top*) PTV-based conventional plan; (*bottom*) robust plan. In this illustration, two proton beams are irradiating laterally, one from the left (*blue arrow*) and the other from the right (*red arrow*). Those two beams meet and match within the target to form a homogeneous dose distribution in the target (*solid purple lines*). In the PTV plan, there are sharp per-field dose gradients in the middle of the target (between *two dashed green lines*), while these dose gradients become much shallower from the robust plan. This difference makes the plan more robust to the uncertainties (so-called the localized single-field uniform dose distribution). However, this mechanism only works well in the middle of the target. At the edge of the target (between *dashed yellow lines*), this mechanism would have to sacrifice the protection of the normal tissue if the same target coverage is maintained (*dashed black lines*). This is not desired in clinics. In this situation, a new mechanism (the so-called perturbed dose distribution to follow the changes of anatomy automatically) needs to be adopted (Please see Fig. 7 and details in Liu et al. [30])

optimization tends to penalize large dose gradients within a single treatment field, it can improve the accuracy of the QA measurement.

10.5 Conclusion and Future Directions

In conclusion, based on the findings so far, we believe that implementing robust optimization into IMPT planning for use in clinical practice will significantly improve the plan quality and robustness of IMPT for treating cancer patients. This effort is currently underway. There is still considerable work to be done for further improvement and assessment of robust optimization and robustness evaluation methods. Validity of alternative approaches needs to be evaluated. Nonrigid variations in anatomy and intra-fractional motion need to be accounted for. Robust adaptive re-planning needs to be developed to account for the inter-fractional anatomy changes. It would also be instructive to use tumor control probability, normal tissue complication probability, and equivalent uniform dose models to evaluate the potential clinical benefits of robust optimization.

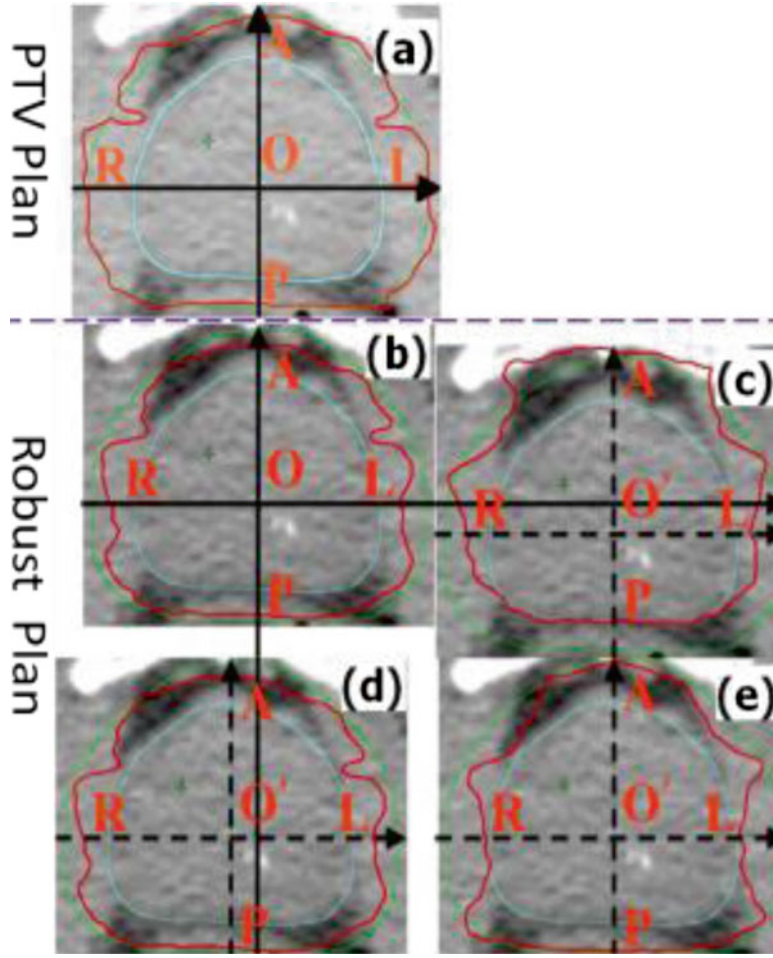

Fig. 10.10 Panel (**a**) is the nominal dose distribution for the PTV-based prostate plan. The remaining panels are the dose distributions for the robustly optimized plan: (**b**) nominal, (**c**) with patient shifted posteriorly by 5 mm, (**d**) shifted to the right by 5 mm, and (e) with beam range decreased by 3.5 %. Red is the prescription isodose contour lines (76 Gy), *green line* is the PTV, and *blue line* is the CTV. Letters O and O' indicate original and shifted positions of the isocenter. Comparison of panel (**a**) with other panels illustrates that the prescription isodose surface encloses a larger volume for the PTV-based optimization vs. robust optimization. At the same time, the CTV remains covered with the prescription dose in the face of uncertainties in the robust plan. This figure is copied from Fig. 4 of Liu et al. [23]

Acknowledgments The authors would like to thank Dr. Martin Bues for many instructive discussions. This research was supported by the National Cancer Institute through grants P01CA021239, K25CA168984, and the Fraternal Order of Eagles Cancer Research Fund, Career Development Award Program, and The Lawrence W. and Marilyn W. Matteson Fund for Cancer Research.

References

1. Register SP, Zhang X, Mohan R, Chang JY. Proton stereotactic body radiation therapy for clinically challenging cases of centrally and superiorly located stage I non-small-cell lung cancer. Int J Radiat Oncol Biol Phys. 2011;80:1015–22.
2. Zhang XD, Li YP, Pan XN, Li XQ, Mohan R, Komaki R, Cox JD, Chang JY. Intensity-modulated proton therapy reduces the dose to normal tissue compared with intensity-modulated radiation therapy or passive scattering proton therapy and enables individualized radical radiotherapy for extensive stage IIIB non-small-cell lung cancer: a virtual clinical study. Int J Radiat Oncol Biol Phys. 2010;77:357–66.
3. Lomax A. Intensity modulation methods for proton radiotherapy. Phys Med Biol. 1999;44:185.
4. Li YP, Zhang XD, Mohan R. An efficient dose calculation strategy for intensity modulated proton therapy. Phys Med Biol. 2011;56:N71–84.
5. Lomax AJ. Intensity modulated proton therapy and its sensitivity to treatment uncertainties 1: the potential effects of calculational uncertainties. Phys Med Biol. 2008;53:1027–42.

6. Lomax AJ. Intensity modulated proton therapy and its sensitivity to treatment uncertainties 2: the potential effects of inter-fraction and inter-field motions. Phys Med Biol. 2008;53:1043–56.
7. Lomax AJ, Boehringer T, Coray A, Egger E, Goitein G, Grossmann M, Juelke P, Lin S, Pedroni E, Rohrer B, Roser W, Rossi B, Siegenthaler B, Stadelmann O, Stauble H, Vetter C, Wisser L. Intensity modulated proton therapy: a clinical example. Med Phys. 2001;28:317–24.
8. Pflugfelder D, Wilkens JJ, Oelfke U. Worst case optimization: a method to account for uncertainties in the optimization of intensity modulated proton therapy. Phys Med Biol. 2008;53:1689–700.
9. Unkelbach J, Bortfeld T, Martin BC, Soukup M. Reducing the sensitivity of IMPT treatment plans to setup errors and range uncertainties via probabilistic treatment planning. Med Phys. 2009;36:149–63.
10. Unkelbach J, Chan TCY, Bortfeld T. Accounting for range uncertainties in the optimization of intensity modulated proton therapy. Phys Med Biol. 2007;52:2755–73.
11. Unkelbach J, Soukup M, Alber M, Bortfeld T. Setup and dose calculation errors in IMPT and their interrelation. World Congr Med Phys Biomed Eng. 2009;25:900–3.
12. Maleike D, Unkelbach J, Oelfke U. Simulation and visualization of dose uncertainties due to interfractional organ motion. Phys Med Biol. 2006;51:2237–52.
13. Kang YX, Zhang XD, Chang JY, Wang H, Wei X, Liao ZX, Komaki R, Cox JD, Balter PA, Liu H, Zhu XR, Mohan R, Dong L. 4D proton treatment planning strategy for mobile lung tumors. Int J Radiat Oncol Biol Phys. 2007;67:906–14.
14. Jiang SB, Pope C, Al Jarrah KM, Kung JH, Bortfeld T. An experimental investigation on intra-fractional organ motion effects in lung IMRT treatments. Phys Med Biol. 2003;48:1773–84.
15. Meyer J, Bluett J, Amos R, Levy L, Choi S, Nguyen QN, Zhu XR, Gillin M, Lee A. Spot scanning proton beam therapy for prostate cancer: treatment planning technique and analysis of consequences of rotational and translational alignment errors. Int J Radiat Oncol Biol Phys. 2010;78:428–34.
16. Goitein M. Calculation of the uncertainty in the dose delivered during radiation-therapy. Med Phys. 1985;12:608–12.
17. Schwarz M. Treatment planning in proton therapy. Eur Phys J Plus. 2011;126:67–76.
18. Liu W, Frank SJ, Li X, Li Y, Park P, Dong L, Zhu XR, Mohan R. Effectiveness of robust optimization in intensity-modulated proton therapy planning for head and neck cancers. Med Phys. 2013;40:051711–8.
19. Liu W, Mohan R, Park P, Liu Z, Li H, Li X, Li Y, Wu R, Sahoo N, Dong L, Zhu XR, Grosshans DR. Dosimetric benefits of robust treatment planning for intensity modulated proton therapy for base-of-skull cancers. Pract Rad Oncol. 2014;4:384–91.
20. Lomax AJ, Pedroni E, Rutz H, Goitein G. The clinical potential of intensity modulated proton therapy. Z Med Phys. 2004;14:147–52.
21. Quan M, Liu W, Wu R, Li Y, Frank SJ, Zhang X, Zhu XR, Mohan R. Preliminary evaluation of multi-field and single-field optimization for the treatment planning of spot-scanning proton therapy of head and neck cancer. Med Phys. 2013;40:081709.
22. Li Y, Liu W, Li X, Quan EM, Zhang X. Toward a thorough evaluation of IMPT plan sensitivity to uncertainties: revisit the worst-case analysis with an exhaustively sampling approach. Med Phys. 2011;38:3853.
23. Liu W, Zhang X, Li Y, Mohan R. Robust optimization in intensity-modulated proton therapy. Med Phys. 2012;39:1079–91.
24. Trofimov A, Kang J, Unkelbach J, Adams JA, Zhang X, Bortfeld T, Liebsch NJ, DeLaney TF. Evaluation of dosimetric gain and uncertainties in proton therapy delivery with scanned pencil beam in treatment of base-of-skull and spinal Tumors. Int J Radiat Oncol Biol Phys. 2010;78:S133–4.
25. Liu W, Liao Z, Schild SE, Liu Z, Li H, Li Y, Park PC, Li X, Stoker J, Shen J, Keole S, Anand A, Fatyga M, Dong L, Sahoo N, Vora S, Wong W, Zhu XR, Bues M, Mohan R. Impact of respiratory motion on worst-case scenario optimized intensity-modulated proton therapy for lung cancers. Pract Rad Oncol. 2015;5(2):e77–86.
26. Albertini F, Hug EB, Lomax AJ. Is it necessary to plan with safety margins for actively scanned proton therapy? Phys Med Biol. 2011;56:4399–413.
27. Park P, Cheung J, Zhu X, Lee A, Sahoo N, Liu W, Mohan R, Tucker S, Li H, Court L, Dong L. Statistical assessment of proton treatment plans under setup and range uncertainties. Int J Radiat Oncol Biol Phys. 2013;86(5):1007–13.
28. Chen W, Unkelbach J, Trofimov A, Madden T, Kooy H, Bortfeld T, Craft D. Including robustness in multicriteria optimization for intensity-modulated proton therapy. Phys Med Biol. 2012;57:591–608.
29. Fredriksson A, Forsgren A, Hardemark B. Minimax optimization for handling range and setup uncertainties in proton therapy. Med Phys. 2011;38:1672–84.
30. Liu W, Li Y, Li X, Cao W, Zhang X. Influence of robust optimization in intensity-modulated proton therapy with different dose delivery techniques. Med Phys. 2012;39:3089–4001.
31. Stuschke M, Kaiser A, Pottgen C, Lubcke W, Farr J. Potentials of robust intensity modulated scanning proton plans for locally advanced lung cancer in comparison to intensity modulated photon plans. Radiother Oncol J Eur Soc Ther Radiol Oncol. 2012;104:45–51.
32. Liu W, Frank SJ, Li X, Li Y, Zhu RX, Mohan R. PTV-based IMPT optimization incorporating planning risk volumes vs robust optimization. Med Phys. 2013;40:021709–8.
33. Li HSS, Romeijn HE, Dempsey JF. A Fourier analysis on the maximum acceptable grid size for discrete proton beam dose calculation. Med Phys. 2006;33:3508–18.
34. Gottschalk B. Passive beam spreading in proton radiation therapy. 2004.

35. Pedroni E, Scheib S, Bohringer T, Coray A, Grossmann M, Lin S, Lomax A. Experimental characterization and physical modelling of the dose distribution of scanned proton pencil beams. Phys Med Biol. 2005;50:541–61.
36. Sawakuchi GO, Zhu XR, Poenisch F, Suzuki K, Ciangaru G, Titt U, Anand A, Mohan R, Gillin MT, Sahoo N. Experimental characterization of the low-dose envelope of spot scanning proton beams. Phys Med Biol. 2010;55:3467–78.
37. Nocedal J. Updating quasi-Newton matrices with limited storage. Math Comp. 1980;35:773–82.
38. Meza JC, Oliva RA, Hough PD, Williams PJ. OPT++: an object-oriented toolkit for nonlinear optimization. Acm Trans Math Softw. 2007;33:12.
39. Fredriksson A. A characterization of robust radiation therapy treatment planning methods-from expected value to worst case optimization. Med Phys. 2012;39:5169–81.
40. Kraus KM, Heath E, Oelfke U. Dosimetric consequences of tumor motion due to respiration for a scanned proton beam. Phys Med Biol. 2011;56:6563–81.
41. Phillips MH, Pedroni E, Blattmann H, Boehringer T, Coray A, Scheib S. Effects of respiratory motion on dose uniformity with a charged-particle scanning method. Phys Med Biol. 1992;37:223–34.
42. Lambert J, Suchowerska N, McKenzie DR, Jackson M. Intrafractional motion during proton beam scanning. Phys Med Biol. 2005;50:4853–62.
43. Grozinger SO, Bert C, Haberer T, Kraft G, Rietzel E. Motion compensation with a scanned ion beam: a technical feasibility study. Radiat Oncol. 2008;3:34.
44. Seco J, Robertson D, Trofimov A, Paganetti H. Breathing interplay effects during proton beam scanning: simulation and statistical analysis. Phys Med Biol. 2009;54:N283–94.
45. Grozinger SO, Rietzel E, Li Q, Bert C, Haberer T, Kraft G. Simulations to design an online motion compensation system for scanned particle beams. Phys Med Biol. 2006;51:3517–31.
46. Dowdell S, Grassberger C, Sharp GC, Paganetti H. Interplay effects in proton scanning for lung: a 4D Monte Carlo study assessing the impact of tumor and beam delivery parameters. Phys Med Biol. 2013;58:4137–56.
47. Grassberger C, Dowdell S, Lomax A, Sharp G, Shackleford J, Choi N, Willers H, Paganetti H. Motion interplay as a function of patient parameters and spot size in spot scanning proton therapy for lung cancer. Int J Radiat Oncol Biol Phys. 2013;86:380–6.
48. Chan TCY, Bortfeld T, Tsitsiklis JN. A robust approach to IMRT optimization. Phys Med Biol. 2006;51:2567–83.
49. Sheng K, Cai J, Brookeman J, Molloy J, Christopher J, Read P. A computer simulated phantom study of tomotherapy dose optimization based on probability density functions (PDF) and potential errors caused by low reproducibility of PDF. Med Phys. 2006;33:3321–6.
50. Pan T, Lee TY, Rietzel E, Chen GTY. 4D-CT imaging of a volume influenced by respiratory motion on multi-slice CT. Med Phys. 2004;31:333–40.
51. Vedam SS, Keall PJ, Kini VR, Mostafavi H, Shukla HP, Mohan R. Acquiring a four-dimensional computed tomography dataset using an external respiratory signal. Phys Med Biol. 2003;48:45–62.
52. Bortfeld T, Chan TCY, Trofimov A, Tsitsiklis JN. Robust management of motion uncertainty in intensity-modulated radiation therapy. Oper Res. 2008;56:1461–73.
53. Engelsman M, Kooy HM. Target volume dose considerations in proton beam treatment planning for lung tumors. Med Phys. 2005;32:3549–57.
54. Casiraghi M, Albertini F, Lomax AJ. Advantages and limitations of the 'worst case scenario' approach in IMPT treatment planning. Phys Med Biol. 2013;58:1323.
55. Trofimov A, Unkelbach J, DeLaney TF, Bortfeld T. Visualization of a variety of possible dosimetric outcomes in radiation therapy using dose-volume histogram bands. Pract Rad Oncol. 2012;2:164–71.

Modeling of Biological Effect of Charged Particles for C-Ion RT

11

Naruhiro Matsufuji

11.1 Progress of Biological Models

11.1.1 Target Theory

Absorbed dose is considered to be the most fundamental physical quantity in describing biological effects of ionizing radiations. These biological effects are then expressed as a function of dose for quantitative analysis.

As a model to reproduce the radiobiological effects such as cell survival curve, the so-called target theory was developed in early days. This model assumes that radio sensitivity is distributed uniformly over entire cell nucleus. In addition, a target is assumed in the cell nucleus as an area much smaller than the cell nucleus but essential for survival of the cell. When damage by incident radiation exceeds the maximum tolerable limit, the cell is regarded to be inactivated. Radiosensitivity is associated to the number of targets in the cell nucleus. For example, radioresistant cell can be regarded as including more targets, and the resistance arises because all the targets should receive more than tolerable damages.

N. Matsufuji, PhD
Research Center for Charged Particle Therapy,
Medical Physics Research Program, National Institute of Radiological Sciences,
Chiba, Japan
e-mail: matufuji@nirs.go.jp

The interaction between incident radiation and cell nucleus can be regarded rather a rare event. If so, in order to model the target concept, Poisson distribution is considered to be applicable to describe its statistical characteristics. By the Poisson distribution with average expected number of hits h, the probability of cell survival is given as the probability that all the m targets in the cell nucleus receive less than maximum tolerable number of hits, n as given below.

$$F_{n,m} = 1 - \left(1 - F_{n,1}\right)^m \tag{11.1}$$

$$F_{n,1} = e^{-h} \sum_{n-1}^{r=0} \frac{h^r}{r!} \tag{11.2}$$

There are various possible combinations between n and m. The simplest form is "one-hit one-target model," namely, the entire cell nucleus is regarded as a single target, and if one hit is given by the radiation, the cell is going to die. When the number of hits is proportional to the irradiation dose D, the survival rate S is given by as below.

$$S(D) = F_{1,1} = \exp(-kD) \tag{11.3}$$

This "one-hit one-target model" is considered applicable for the response of viruses or chemical substances.

Or alternatively, if only one hit is tolerable for all the targets for inactivation, it is called the

A.K. Rath, N. Sahoo (eds.), *Particle Radiotherapy: Emerging Technology for Treatment of Cancer*,
DOI 10.1007/978-81-322-2622-2_11

"one-hit multi-target model," and the corresponding survival curve is:

$$S(D) = F_{1,m} = 1 - \left(1 - F_{1,1}\right)^m = 1 - \left\{1 - \exp\left(-kD\right)\right\}^m \tag{11.4}$$

Some more derivative models such as "multi-hit one-target model," i.e., a model when only one target exists in a cell nucleus, but a few hits are required to inactivate it, or a combination of "one-hit one-target model" and "one-hit multi-target model" as the "two-component model" are also proposed. The latter survival curve is rather complex:

$$S(D) = F_{1,1} \times F_{1,m} = e^{-h(D)} \times \left\{1 - \left(1 - F_{1,1}\right)^m\right\} = e^{-\mathrm{AD}} \times \left\{1 - \left(1 - e^{-\mathrm{BD}}\right)^m\right\} \tag{11.5}$$

The first component is called as the "ion kill" as less repairable mode, and the second one is as "gamma kill" as partially repairable mode.

These various target models are, however, not frequently used in the field of modern radiotherapy. The reason would be attributed to the rather complex equation in practical viewpoint and also difficult interpretation of the number of targets dependent on cell lines in mechanistic viewpoint.

11.1.2 Linear-Quadratic Model

Among possible radiation effect on cell nucleus, it was found that a DNA double-strand break (DSB) could be the most severe damage to be strongly related to the fate of the cell. Other types to be of DNA damages such as single-strand break or chemical change are considered leading to neither chromosomal aberration nor cell death at all.

The homologous nature of DSB evokes another model based on microscopic energy distributions. Probability of DSB originating from single radiation trajectory is linearly proportional to the fluence of the radiation, i.e., absorbed dose. Alternatively, even though single radiation breaks one strand of DNA but does not the other, the additional second radiation can break the remaining strand and leading to inactivation. The probability of this composite event obeys to the square of the fluence, i.e., to square of the absorbed dose. As both pathways lead to DSBs and cell inactivation, the overall radiation effect on a cell population can be expressed as the survival probability

$$S(D) = \exp\left[-\left(\alpha D + \beta D^2\right)\right] \tag{11.6}$$

with two coefficients α and β for linear and quadratic term, respectively. According to this model, the survival curves indicate shouldered line as a function of dose. This model is called as "linear-quadratic (LQ) model" or sometimes "αβ model."

Mainly due to its simplicity but adequate reproducibility of biological response in the therapeutic dose range compared with the other classical model, LQ model is still *de-facto* standard model used for analysis of experimental data or therapeutic estimation.

11.1.3 Model for Therapeutic Application

A biological model should be capable of predicting the biological response of the radiation with some extent of simplicity and robustness to be applicable in routine radiotherapy. True mechanistic approaches can be considered to build a model, which are able to represent the relevant fundamental processes, starting with the details of physical interactions followed by the formation of damages such as DSBs and possible biological response such as repair or apoptosis. At this moment, just a few pathways have been understood quantitatively; therefore, the steps should be very much simplified with vast number of parameters. The solution is strongly affected by small variations of the parameters. In the sense, at least at present, it is still not yet realized to simulate the complete network with a precision sufficient for clinical use. In other words, any model based on first principle has not yet been realized nor utilized, i.e., current models

used in radiotherapy must involve adequate assumption, simplification, or approximation therein.

As a crucial issue specific to ion beam radiotherapy, the absorbed dose alone is not sufficient to handle the biological effectiveness. RBE, relative biological effectiveness of the ion beam comparing to X-ray, increases toward the end of its range. This change in RBE enhances the peak-plateau ratio of the Bragg curve in the biological viewpoint, therefore considered advantageous for sparing surrounding normal tissues around while delivering sufficient dose to deep-seated tumor. At the same time, this change in RBE requires biological models to be used in ion beam therapy to handle the change quantitatively; otherwise, it will result in poor tumor control and/or severe normal tissue complication.

11.2 NIRS C-Ion RT Model (Version 1)

11.2.1 Concept of NIRS Model

The first NIRS model developed by Kanai et al. [6] is a kind of straightforward pragmatic extension of the LQ model to handle the RBE issue for carbon-ion radiotherapy.

In the approach, two biological subjects were taken into consideration: biological dose distribution within a spread-out Bragg peak (SOBP) for designing the depth-dose distribution and clinical RBE for determining the dose to be prescribed. Biological dose was introduced to unite absorbed dose with biological effectiveness which can be examined by experiment. Absorbed dose is designed so that the biological dose becomes flat within an SOBP. Here, as mentioned previously, RBE is dependent on the irradiation depth of the carbon-ion beam. More precisely, RBE is known to depend on various factors such as biological materials, endpoints, radiation quality, absorbed dose, and so on. NIRS selected a human salivary gland tumor (HSG) cell line because the initial patients to receive carbon-ion radiotherapy were forecasted as those with salivary gland tumors, which are known to respond well to fast-neutron therapy in the past. The 10 % surviving fraction of the HSG cells was then chosen as the endpoint to measure RBE of carbon ions for single fractional dose.

Then, in order to make use of the experience of fast-neutron therapy in the past to determine clinical RBE of carbon-ion therapy, a "neutron-equivalent point" of carbon-ion beam was exploited. The clinical RBE of neutrons is reported to be 3.0 for 18 fractions in 6 weeks. On the other hand, biological RBE values of neutrons are experimentally obtainable and can be compared with RBE values of carbon ions for HSG-cultured cells after irradiation with 290 MeV/u carbon-ion beams with a 6-cm SOBP (Fig. 11.1). RBE of carbon ions relative to 200 kVp X-rays increased with an increase of dose-averaged LET of carbon ions, and was 2.05 at 85 keV/μm. This RBE was identical to neutron's RBE for the same endpoint.

Another biological endpoint, mouse skin reaction after fractionated irradiation with 290 MeV/u carbon-ion beams with a 6-cm SOBP was also studied. On the endpoint of skin reaction score of 2.5, dry desquamation, RBE of 3.1 which was identical to fast neutrons, was pointed at an LET of 75 keV/μm. This value of RBE is close to that used in the fast neutron therapy. As two LET values thus obtained in vitro and in vivo were close to each other, namely, 75 and 85 keV/μm, the point where the dose-averaged LET is 80 keV/μm of 290 MeV/u carbon-ion beams with a 6-cm SOBP was determined as the "neutron-equivalent point." This point corresponds to 8-mm upstream of the falloff of the SOBP. At this very point, clinical RBE of the carbon-ion beam is assumed to be 3.0. As the biological dose distribution is designed to be flat within the SOBP, once RBE was clipped at one position, clinical dose distribution is also flat within the SOBP.

11.2.2 Design of Clinical Dose Distribution

In order to design the SOBP, the coefficients (α and β) in the LQ model of the survival curve for HSG cells were experimentally derived and

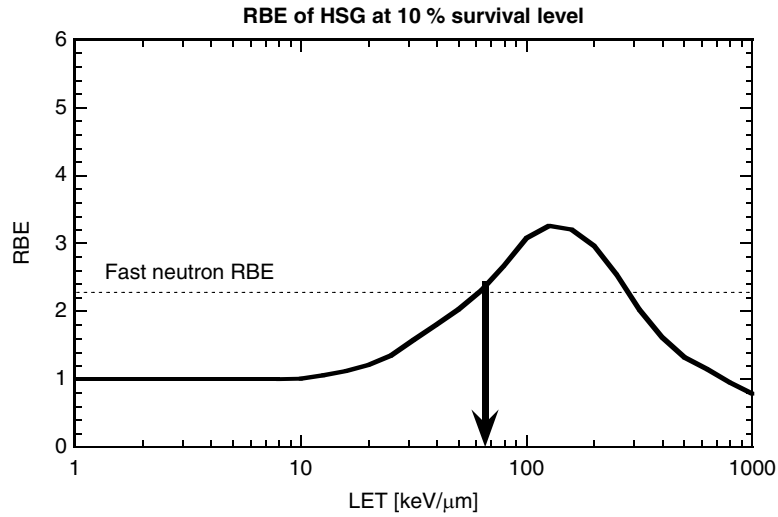

Fig. 11.1 Comparison of RBE of HSG cells at 10 % survival level for carbon ions as a function of LET with that for fast neutrons (redrawn from [6])

tabulated as a function of the energy the carbon-ion beam. Then, the absorbed dose distribution was designed to achieve a uniform survival probability (10 %) for the HSG cells over the entire SOBP region. The contribution of different energy is treated by taking the dose-averaged coefficients (α_{mix} and β_{mix}) in case of mixed-radiation field, as given below:

$$\alpha_{\mathrm{mix}} = \sum f_i \times \alpha_i \tag{11.7}$$

$$\sqrt{\beta_{\mathrm{mix}}} = \sum f_i \times \sqrt{\beta_i} \tag{11.8}$$

The biological responses for the SOBP beam designed by this approach was validated for various biological samples, such as HSG cells, MG 63 human osteosarcoma cells, V79 Chinese hamster cells, and crypt cells of mouse jejunum and confirmed to be uniform throughout the SOBP region. In this framework, it is regarded that the clinical dose distributions calculated with the model primarily reflect the response of acute reactions.

The relationship between biological and absorbed dose distributions, estimated from the responses of the HSG cells, was assumed to hold even in the clinical situation. Then the clinical dose distribution was deduced by multiplying the entire biological SOBP with a constant factor, this factor being the ratio between the clinical and biological RBE value at the point where the dose-averaged LET was 80 keV/μm. The scheme described above is summarized below:

1. The dose level of the flattop of the biological dose distributions, which corresponds to the prescribed clinical dose to the target, is first given by a radiation oncologist.
2. The physical dose at the neutron-equivalent position is determined using the RBE value of 3.0.
3. The physical dose distribution of the SOBP beam is then normalized at the neutron-equivalent position.
4. The physical dose at the center of the SOBP is obtained and the RBE values at the center of the SOBPs are then obtained by dividing the biological dose by the physical dose.

Figure 11.2 shows schematically the method of determining the RBE at the center of the SOBP for clinical situations. In case a clinical dose of 2.7 Gy (RBE) would be prescribed to the tumor, the corresponding absorbed dose at the 8-mm upstream position is 2.7 Gy (RBE)/3.0 (RBE) = 0.9 Gy. At the middle of SOBP, absorbed dose and clinical RBE are 1.13 Gy and 2.7/1.13 = 2.4, respectively.

Strictly, this approach is valid only for a single field irradiation delivered on 1 day. However, it is assumed that each single field distribution could be added in the case of multi-port irradiation in

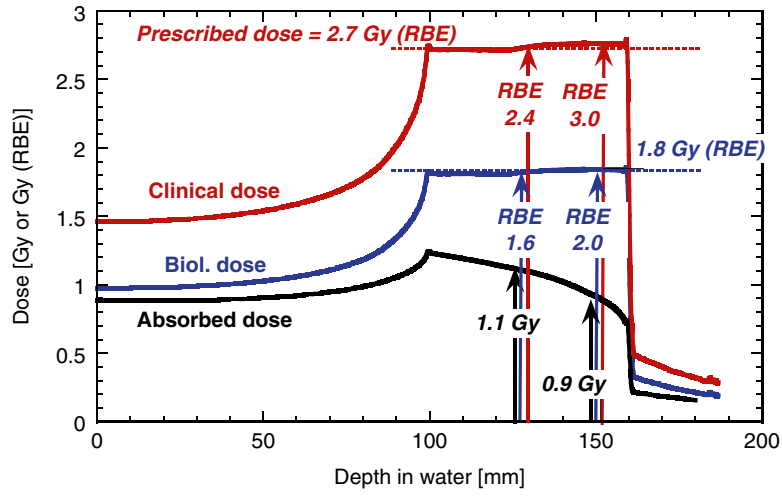

Fig. 11.2 Depth-dose distribution of NIRS model for 290 MeV/u of carbon beam of 60-mm SOBP width (redrawn from [6])

1 day. This scheme was used at NIRS broad-beam irradiations with universal depth-dose distributions to all patients, independent of tumor type or dose level. The tumor-specific radiosensitivity was examined with this fixed distribution through dose escalation and hypofractionation clinical trials.

11.2.3 Verification of the NIRS Model

In order to examine the appropriateness of the first NIRS model, the expected clinical RBE was compared with clinical outcome [12]. Miyamoto et al. [13] analyzed the clinical results of non-small cell lung cancer (NSCLC) treated by HIMAC beams. They depicted a very conspicuous dose dependency of the local control rate. A dose escalation study was performed with a treatment schedule of 18 fractions in 6 weeks. Dose dependency of tumor control probability (TCP) with the photon beam was fitted by the following formula:

$$\mathrm{TCP} = \sum_i \frac{1}{\sqrt{2\pi}\sigma}\left[-\frac{(\alpha_i-\alpha)^2}{2\sigma^2}\right]\exp\left\{-N\exp\left[-n\left(\alpha_i d+\beta d^2\right)+\frac{0.693\left(T-T_\mathrm{k}\right)}{T_\mathrm{p}}\right]\right\} \tag{11.9}$$

α and β are coefficients of the LQ model of the cell survival curve. In the analysis, α and β values of HSG cells were used. σ is a standard deviation of the coefficient α, which reflects patient-to-patient variation of radiosensitivity. N is the number of clonogens in tumor (fixed value of 10^9 was used). n and d are total fraction number and the fractionated dose, respectively. T (42 days), T_k (0 day), and T_p (7 days) are overall time for treatment, kickoff time, and average doubling time of tumor cells, respectively. The result is shown in Fig. 11.3. The analysis was carried out for the 18 fractionation cases in order to determine the tumor-specific radiosensitivity parameter α and its variation σ.

The result revealed that the α is 0.76 and σ is 0.11.

The same analysis was carried out to determine the TCP using carbon-ion radiotherapy. Here, the width of SOBP and dose-averaged LET in the SOBP region was both fixed at 60 mm and 50 keV/μm, respectively, for simplicity. The result is also shown in Fig. 11.3. It is clear from the figure that the TCP curve of the carbon beam is much steeper than that of the photon beam. The value of σ in Eq. (11.9) was 0.18 for the photon beam, while that for the carbon beam was reduced to 0.11. The result implies that carbon beam provides equally excellent local tumor control regardless of the individual radiosensitivity.

Taking into account the difference between the TCP slopes shown in Fig. 11.3 when TCP is

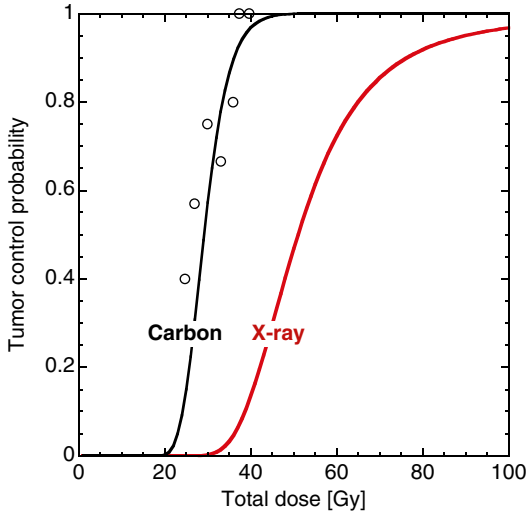

Fig. 11.3 Tumor control probability of non-small cell lung cancer by carbon ion beams and X-rays delivered by 18 fractions (redrawn from [7])

regarded as an endpoint, the RBE value is found to be dependent on the TCP level. Furthermore, the clinical RBE value corresponded to that at 80 % TCP. This agreement of the designed clinical RBE at higher TCP level is considered to be justified from the therapeutic point of view.

11.3 GSI C-Ion RT Model (LEM)

11.3.1 Concept of LEM

While the abovementioned NIRS model is a rather pragmatic approach, GSI took different approaches in estimating RBE. In GSI, a biophysical model called as local effect model (LEM) was developed by Scholz and Kraft [15] to predict the response to charged particle radiation from the known response of the biological object to photon radiation. The primal idea of the LEM is depicted as Fig. 11.4.

The intrinsic radiation sensitivity of a biological system can be characterized with the response to X-ray, and microscopic energy distribution formed by incident radiation that modifies the photon response in a rather mechanistic manner, but still simple and applicable for routine therapy.

LEM looks alike to the microdosimetric approach such as theory of dual radiation action (TDRA) or microdosimetric kinetic model (MKM) to be explained in the next section. The apparent difference is LEM is applied to much smaller, nm scale volumes compared to the μm of microdosimetry. In addition, statistical fluctuation is regarded essential in the energy deposition to the tiny volume in the microdosimetry; LEM is based on statistically averaged, expected energy distribution.

11.3.2 Biological Calculation with LEM

The energy deposition pattern of charged particles (track structure) is determined essentially by the secondary electrons (δ-electrons). The shape of the track structure is often characterized statistically by two parameters, R_c and R_p. R_c is a radius of the so-called core region near the ion track. The ion causes dense ionization there, and equilibrium in terms of energy deposition is assumable inside R_c. The size of R_c is regarded to be a function of the velocity of the ion.

A part of secondary electrons produced in the core carry out their energy beyond the core boundary, R_c, to the point defined by their maximum energy. The region is called as penumbra. Energy density rapidly decreases as a function of inverse square of the distance from track center. The maximum radius of the penumbra region, R_p, is expressed as a function of the kinetic energy of the ion. In LEM, radial energy density is expressed as follows:

$$D(r) = D_{\text{center}} = \text{const.}, \quad 0 \le r \le R_c \tag{11.10}$$

$$D(r) = D_{\text{center}} \cdot 1/r^2, \quad R_c < r \le R_p \tag{11.11}$$

$$D(r) = 0, \quad r > R_p \tag{11.12}$$

The integral of the $D(r)$ is normalized to LET.

The major part of the biological response is currently reproduced by the LQ model; however, one modification is introduced in order to account for the estrangement from the linear plus quadratic response at high dose region. It is said that

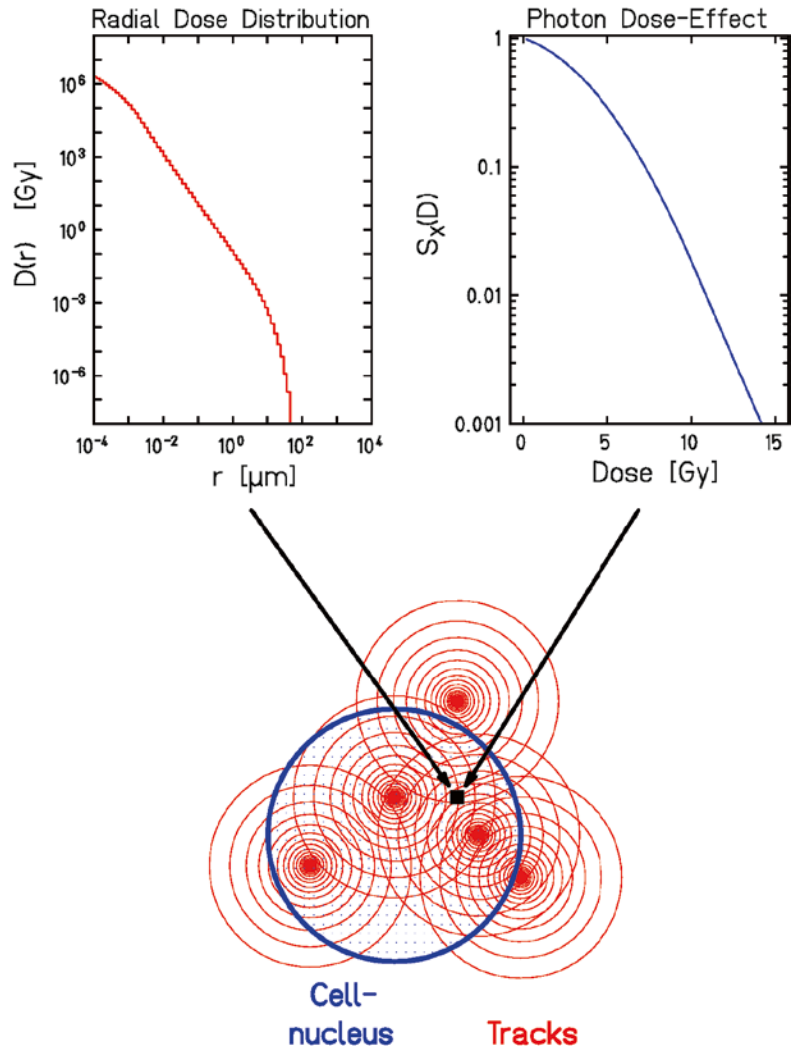

Fig. 11.4 Basic concept of the local effect model (reprinted from [14])

the response curve again takes a linear form beyond a threshold dose D_t. Number of lesions produced by dose D, $N(D)$, is expressed as

$$N(D) = \alpha D + \beta D^2,\ 0 < D \le D_t \tag{11.13}$$

$$N(D) = \alpha D_t + \beta D_t^2 + (\alpha + 2\beta D_t)(D - D_t),\ D > D_t \tag{11.14}$$

It is assumed that this macroscopic biological dose response relationship is also true for any minute microscopic local region. Then, the number of lesions produced in a cell nucleus can be derived as a summation of local lesions, as follows:

$$\bar{N}_{\text{lethal}} = \int dN = \int_{x=0}^{X} \int_{y=0}^{Y} \frac{N(D_{(x,y)})}{A_{\text{nucl}}} dxdy = \sum_x \sum_y N(D_{(x,y)}) \frac{dxdy}{A_{\text{nucl}}} \tag{11.15}$$

Here, A_{nucl} and $D_{(x,y)}$ correspond to an area of cell nucleus and local dose deposition to a voxel (x,y).

Finally, survival probability S_{total} is written as:

$$S_{\text{total}} = \prod_{x,y} S_{(x,y)} = \prod_{x,y} \exp(-N_{(D_{(x,y)})}) = \exp(-\sum N_{(D_{(x,y)})}) \tag{11.16}$$

This LEM calculation is performed for every particle incident including fragments generated by their nuclear reaction model and repeated to reduce statistical fluctuation. The process sometimes requires vast CPU time. In their treatment planning system TRiP, some approximations are introduced for the sake of reducing the computational time [11].

11.3.3 Clinical Application of LEM

The predictions of the LEM concerning the cell line specificity of RBE(LET) dependence for carbon-ion irradiation are in agreement with experimental data [16]. The significantly higher RBE for V79 cells as compared to CHO and XRS cells seen in the experimental data [16] is well reproduced by the LEM model. Furthermore, the measured [16] near-unity RBE for the repair-deficient cell line XRS is also correctly reproduced by the model.

The LEM is based on the knowledge of the photon dose response curve. However, representative photon survival curves are sometimes not available for the clinical target under consideration, and even if available, the correlation between cell survival and the clinically relevant tissue response remains unclear, at least on a quantitative level. On the other hand, at least α/β ratio of various tissues and tumors are available through vast X-ray radiotherapy.

Then, for clinical application, LEM calculation is performed using a photon survival curve, having the same α/β ratio as the tissue endpoint under consideration, and then assuming that both the survival curve and the tissue endpoint will show the same RBE at a given dose level, because the RBE value is more or less similar if α/β ratio is close. LEM has thus been implemented in the biological optimization module of the treatment planning system, TRiP, for the carbon-ion radiotherapy trial at GSI and successive carbon-ion radiotherapy at HIT (Heidelberg Ion Beam Therapy Center).

This original LEM has been used in the treatment planning for carbon-ion radiotherapy; on the other hand, LEM has been updated for research purpose. In the update, the original nm scale track structure is blurred in the sub μm region in order to take into account the diffusion of radicals [1] or biological structure [2]. The update improves the reproducibility by LEM mainly for low LET radiation such as protons.

11.4 NIRS C-Ion RT Model (Version 2, MKM)

11.4.1 Concept of MKM

For a given ion species and cell type, LET or dose-averaged LET was chosen as a predictor for the RBE in the NIRS first model. However, when comparing different ion species, LET is not flawless in a strict sense to uniquely describe the RBE. This can be attributed to the fact that LET is a simplified one-dimensional representation of the expected particle track, which neither takes into account the three-dimensional distribution of energy deposition around the particle trajectory nor its fluctuation. Since for a given LET value, the corresponding energy is lower for a light particle as compared to a heavier particle, the track radius is smaller for the lighter particle because of the lower energy transferred to the secondary electrons. As a consequence, the average energy density is higher in the track of the light particle, finally leading to the higher effectiveness. This problem was pragmatically treated in the first model by tabulating α and β parameters in the LQ model as functions of ion species and energy. In reality, this works fairly well in most conditions; however, it is inevitable to introduce a kind of assumption or interpolation at some conditions that are outside the table. Eventually, it could not only introduce a possible error in the estimation of therapeutic effectiveness of carbon ions but also it becomes difficult to make a prospective, reliable, or mechanistic estimation of the RBE the beam. In order to account for that, NIRS updated the model based on the microdosimetry.

11.4.2 Calculation with MKM

Microdosimetric characterization of the radiation field focuses on a detailed description of the stochastic energy deposition distributions. Experimental microdosimetry is based on measurements or calculation of energy deposition

events typically in spherical volumes of simulated micrometer dimensions. MKM has been developed by Hawkins [4] as a model to predict biological effectiveness of radiations based on the microscopic spatial energy distribution. MKM realizes prospective estimation of biological effectiveness of various ion species based on their physical properties. This is expected to provide more precise estimation of the biological effectiveness of the therapeutic carbon beam; therefore, MKM has been introduced as the updated biophysical model implemented in the new treatment planning system for scanning irradiation at NIRS.

MKM extended the original concept of the microdosimetric theory of dual radiation Action (TDRA) [10], which gives estimation of biological effect based on the energy deposited in a site in the order of micrometer. In TDRA, the number of lesion L is proportional to the square of the specific energy z given in the site, while MKM [4] incorporates additional component in lesion formation which is linearly proportional to the specific energy as

$$L = Az + Bz^2 \tag{11.17}$$

The units for z are the same as for the LET, namely, keV/μm. Similar to the LET, the dose-weighted average value of z, z_{1D} is expected to be representative for the biological effectiveness:

$$-\ln\ S = N\bar{L} = N\left(A\bar{z} + B\bar{z}^2\right) = (\alpha_0 + \beta \cdot z_{1D}) + \beta D^2 \tag{11.18}$$

where α_0 denotes the initial slope of the survival curve in the limit LET→0 and β is assumed to be independent on radiation quality. Since z_{1D} rises with LET, Eq. (11.18) would lead to a steady increase of RBE with LET. However, RBE is known to decrease with LET after reaching a maximum at approximately 100 keV/μm. Therefore, saturation correction on specific energy was introduced [8].

$$z_{1D}^{*} = \frac{l}{m} y_0^2 \cdot \frac{\int \left[1 - \exp\left(-y^2/y_0^2\right)\right] f(y)\,dy}{\int y f(y)\,dy} \tag{11.19}$$

By replacing z_{1D} in Eq. (11.18) with z_{1D}^{*}, the modified MKM is shown to allow a good representation of the experimental data.

This saturation-corrected modified MKM is found [8] to be useful in estimating the biological effectiveness of various ion species. The modified MKM has been installed in the treatment planning both for scanning [5] and broad-beam carbon ion irradiation.

Figure 11.5 shows the cell survival distribution of HSG cells for the beam of C-290 MeV/u with 60 mm SOBP. As shown in the figure, modified MKM can predict the HSG cell response in excellent precision.

Figure 11.6 shows the comparison of depth-biological dose profile for the beam in Fig. 11.5 with the first model (labeled as Kanai 1999 in the figure) and MKM. Both models agreed with each other in general. This proves that the original approach is pragmatically adequate enough for the therapeutic purpose. Slight difference found at the distal part of the SOBP can be attributed to the improved estimation of the modified MKM on the biological effect of the beam where the fragment particles are relatively abundant.

11.5 Translation between NIRS and GSI Models

The scheme of determining clinical RBE is different at NIRS and GSI in every level starting from model to endpoint regarded relevant to therapeutic purpose. As a matter of course, both clinical doses are expressed with the same unit "Gy (RBE)" (or conventionally "GyE"); the corresponding absorbed dose can be different. The model-basis comparison by Kase et al. [9] revealed that both models require same three basic constituents, i.e., target geometry, photon survival curve, and track structure; however, practical implementation is different especially in calculating the biological effects of the extremely high local dose in the center of the ion track.

For the TPS basis comparison, an actual treatment planning for chordoma patient at GSI was translated into NIRS model. 3.3 Gy (RBE_{GSI}) was being planned to deliver in a parallel opposing field. The corresponding physical dose and dose-averaged LET

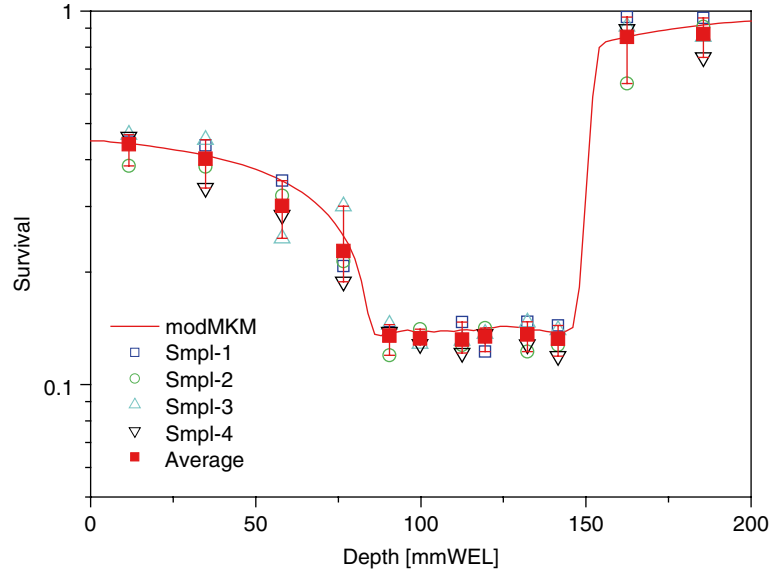

Fig. 11.5 Comparison of measured cell survival distribution of HSG cells for the beam of C-290 MeV/n with 60-mm SOBP with the results of modified MKM calculation (reprinted from [5])

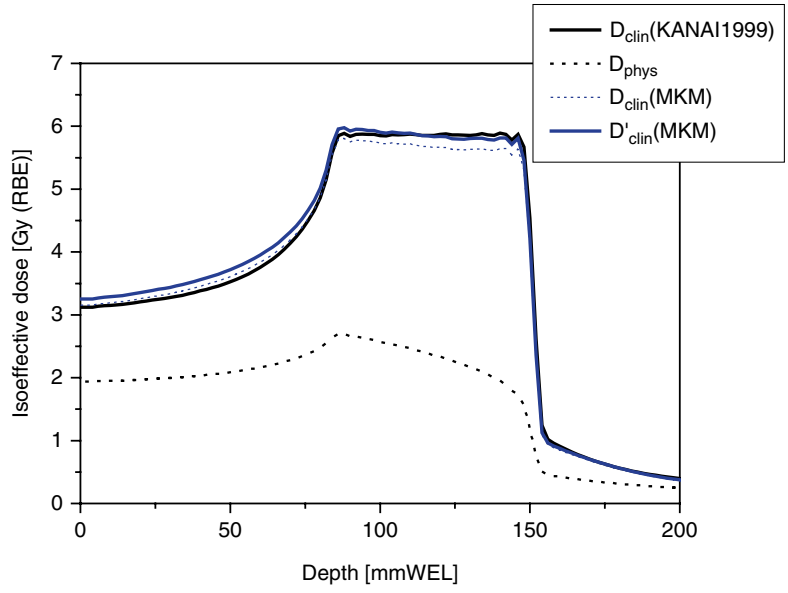

Fig. 11.6 Depth-biological dose profile corresponding to Fig. 11.5 together with the original NIRS model (Referred as Kanai 1999 in the figure). D_{clin}(MKM) in the figure corresponds to the isoeffective dose distribution given by MKM while the D'_{clin}(MKM) distribution is normalized to D_{clin}(Kanai 1999) at the middle of the SOBP

distribution calculated in TRiP was used as an input data to NIRS model. Together with these information and tabulated HSG cell survival response, biological dose in NIRS model was calculated for each voxel. Then the biological dose distribution was normalized to 3.0 at the point where dose-averaged LET=80 keV/μm to obtain Gy (RBE_{NIRS}) distribution. Figure 11.7 demonstrates the comparison of clinical dose distribution by GSI and NIRS approach. It was found that the indicated clinical RBE dose differs about 20 %, though the corresponding physical distribution at the target region is same.

Figure 11.8 shows treatment-planning basis comparison between NIRS model and GSI model [3]. The absorbed dose corresponds to 4 Gy (RBE) prescription in NIRS model and is almost

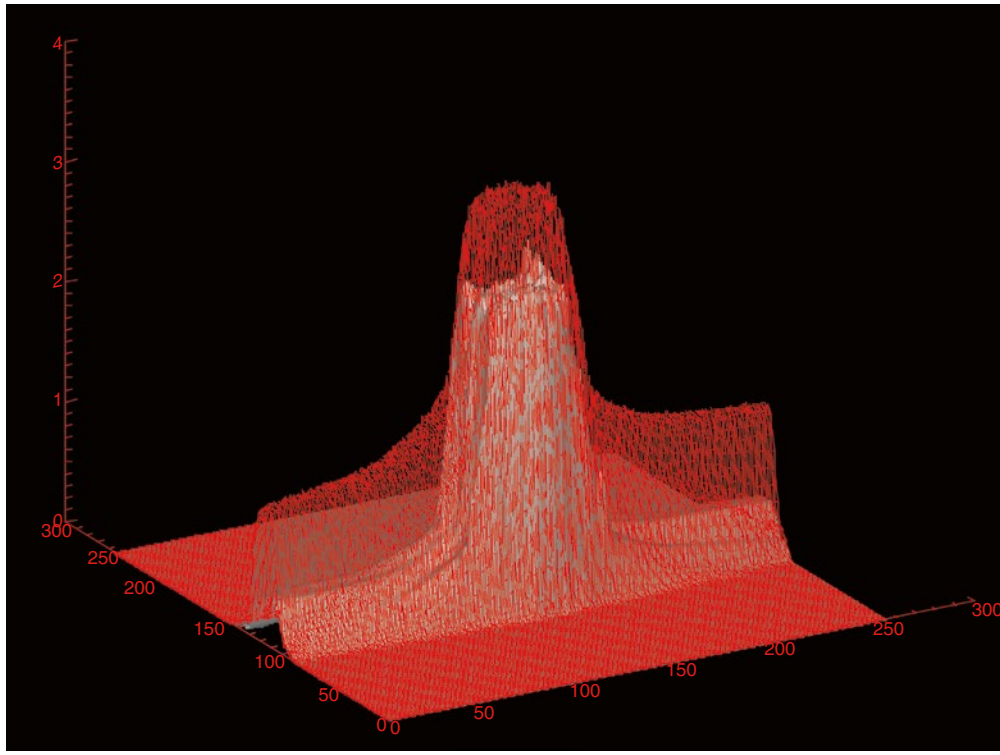

Fig. 11.7 An example of practical clinical dose distribution between GSI (*red*) and NIRS (*gray*): 3.3 Gy (RBE) in GSI model was delivered to chordoma by a parallel opposing field

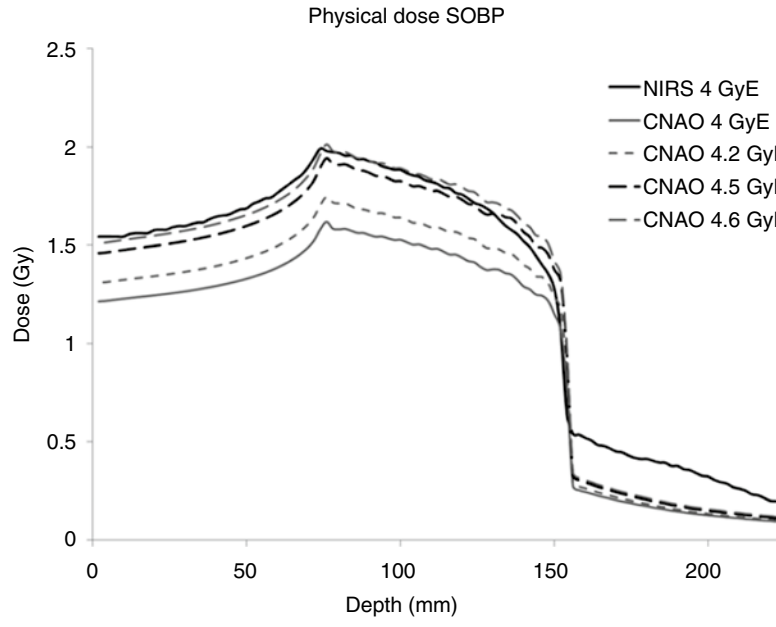

Fig. 11.8 Comparison of depth-dose profiles for the 8-cm cube and single-port case with Italian National Center for Hadron Therapy (CNAO). (LEM) and NIRS models (reprinted from [3])

equivalent when prescribing 4.5 Gy (RBE) in GSI model.

These two indications suggest that at this dose level, clinical RBE calculated by GSI LEM model is 10–20 % higher than that from NIRS model. It should be noted here that the difference is not universal but strongly dependent on dose level and could be even reversed for larger doses. Therefore, strong care should be taken when translating one dose distribution to other.

References

1. Elsässer T, Scholz M. Cluster Effects within the Local Effect Model. Radiat Res. 2007;167:319–29.
2. Friedrich T, et al. Calculation of the biological effects of ion beams based on the microscopic spatial damage distribution pattern. Int J Radiat Biol. 2012;88:103–7.
3. Fossati P, et al. Dose prescription in carbon ion radiotherapy: a planning study to compare NIRS and LEM approaches with a clinically-oriented strategy. Phys Med Biol. 2012;57:7543–54.
4. Hawkins RB. A statistical theory of cell killing by radiation of varying linear energy transfer. Radiat Res. 1994;140:366–74.
5. Inaniwa T, et al. Treatment planning for a scanned carbon beam with a modified microdosimetric kinetic model. Phys Med Biol. 2010;55(2010):6721–37.
6. Kanai T, et al. Biophysical characteristics of HIMAC clinical irradiation system for heavy-ion radiation therapy. Int J Radiat Oncol Biol Phys. 1999;44:201–10.
7. Kanai T, et al. Examination of GyE system for HIMAC carbon therapy. Int J Radiat Oncol Biol Phys. 2006;64:650–6.
8. Kase Y, et al. Microdosimetric measurements and estimation of human cell survival for heavy-ion beams. Radiat Res. 2006;166:629–38.
9. Kase Y, et al. Biophysical calculation of cell survival probabilities using amorphous track structure models for heavy-ion irradiation. Phys Med Biol. 2008;53:37–59.
10. Kellerer M, Rossi HH. A generalized formation of dual radiation action. Radiat Res. 1978;75:471–88.
11. Krämer M, Scholz M. Treatment planning for heavy-ion radiotherapy: calculation and optimization of biologically effective dose. Phys Med Biol. 2000;45:3319–30.
12. Matsufuji N, et al. 2007 Specification of carbon ion dose at the National Institute of Radiological Sciences (NIRS). J Radiat Res. 2007;48:81–6.
13. Miyamoto T, et al. Carbon ion radiotherapy for stage I non-small cell lung cancer. Radiother Oncol. 2003;66:127–40.
14. Scholz M, Elsässer T. Biophysical models in ion beam radiotherapy. Adv Space Res. 2007;40:1381–91.
15. Scholz M, Kraft G. Track structure and the calculation of biological effects of heavy charged particles. Adv Space Res. 1996;18:5–14.
16. Weyrather W, et al. RBE for carbon track-segment irradiation in cell lines of differing repair capacity. Int J of Radiation Biol. 1999;75:1357–64.

SFUD, IMPT, and Plan Robustness

12

Antony Lomax

12.1 Introduction

Pencil beam scanning (PBS) [28, 60] is rapidly becoming the modality of choice for proton therapy. With this technique, the Bragg peaks of individually weighted proton pencil beams are scanned, or "painted," over the target volume, through a combination of energy variations and two-dimensional magnetic deflections of the individual beams. In comparison to the more traditional passive scattering approach [34, 35], PBS can be fully automated in its delivery and is workflow efficient and, above all, extremely flexible. For this reason, most new proton facilities have at least one treatment room dedicated to PBS, with more and more new facilities opting for PBS only.

One of the main advantages of PBS, indeed arguably the main driving force behind its current adoption, is its inherent ability to deliver highly conformal dose distributions at all dose levels. In order to achieve this, Bragg peak (BP) positions and fluences (weights) need to be defined such as to cover the target volume or at least to be delivered with a pattern which allows for the prescribed dose distribution to be delivered to the target from one or more field directions. Once such a pattern has been determined, the optimal fluence for each BP then needs to be determined, such that the calculated distribution matches as closely as possible the prescribed dose requested for the target and any critical structures. This process is the main role of the treatment planning system (TPS) and is therefore an inherent, and indispensable, part of the delivery process. Indeed, it can be argued that the quality of delivered dose distribution, while certainly dependent on the characteristics of the scanned beam delivered by the treatment machine, can only be assured by the use of a quality TPS system that can best exploit the capabilities and flexibility of the treatment machine. Thus, the processes and procedures of planning PBS proton treatments are important to understand if one wishes to exploit the technique to its full potential.

However, the quality of a treatment or treatment plan is not just based on the quality of the final dose distribution produced by the TPS. It is also extremely important to remember a fundamental fact of all TPS-based radiotherapy, that the dose distribution resulting from the planning process is just an *approximation* of the doses actually delivered to the patient. Inevitably, many assumptions have to be made when calculating three-dimensional (3D) distributions of delivered dose in an organism as complex as a human being. Firstly, assumptions have to be made about the actual quality of the radiation itself. Secondly, assumptions have to be made about the physics of interactions of the radiation being used and how

A. Lomax, PhD
Centre for Proton Therapy, Paul Scherrer Institute, Villigen, Switzerland
e-mail: tony.lomax@psi.ch

A.K. Rath, N. Sahoo (eds.), *Particle Radiotherapy: Emerging Technology for Treatment of Cancer*,
DOI 10.1007/978-81-322-2622-2_12

these will be affected by the non-homogenous tissues, organs, and anatomy found in patients. Lastly, assumptions have to be made about the patient themselves. Although in many cases, these assumptions can be extremely good, this is not always the case, and it is therefore important to understand the limitations of the planning and dose calculation processes and particularly to understand in which circumstances these assumptions may become invalid. Given that many of the uncertainties that can affect a treatment plan are inevitable, the potential effects of such uncertainties should ideally be modeled at the planning stage, and the treatment designed such as to minimize their effects. This type of process is what is nowadays called "robust planning."

In this chapter, we will discuss treatment planning aspects of PBS proton therapy from the point of view of treatment design and optimization aspects and in particular will describe two modes of PBS planning and their variants. In addition, the important issue of plan robustness, or the sensitivity of the designed treatments to delivery uncertainties, will be discussed, concentrating on two main, patient-related uncertainties, namely, in vivo proton range and organ motion.

12.2 SFUD and IMPT

Treatment planning is a multifaceted process, consisting of imaging, the delineation of tumor and normal structures, and the selection of treatment fields which best cover the tumor while avoiding neighboring critical structures and organs. As part of the field definition, the geometry of the selected fields will also be defined and, in many cases, an optimization of the fluence or fluences of the field will be performed. In parallel to this, a 3D dose distribution in a model of the patient (usually one or more volumetric CT imaging studies of the patient) will be calculated, on which the optimization process will be based and which will be ultimately used to assess the quality of the plan. Here we will restrict ourselves to discussing the field design and optimization part of this process, as these are the most important aspects for understanding what constitutes a PBS treatment "field" or "plan" and which aspects of this can later affect the robustness of the plan to delivery uncertainties.

12.2.1 Selection, Initial Weighting, and Optimization of Pencil Beams

Figure 12.1 shows the different stages of the field design for a single PBS field as calculated by our in-house treatment planning system, PSI plan. Figure 12.1a shows a single slice of the originating patient "model," in this case, a single slice of a three-dimensional CT data set of the patient. As will be seen later, CT data is obligatory for treatment planning for PBS proton therapy. In the case shown here, this CT-based patient model is based on 98 transaxial CT slices with a separation of 2 mm and an in-plane pixel dimension of 0.98 mm. Superimposed on the CT data are various contours, as drawn by the treating clinician, to clearly define the tumor (yellow contours) and various normal and critical structures (red contours). The remaining images in this figure show the various stages of the field design for a single PBS treatment field incident from the right-hand side of the picture.

Figure 12.1b shows an initial estimation of the possible positions of all Bragg peaks (red crosses) that can be delivered from this field direction. These are determined by three main parameters. The maximum field size for the scanned beams (scan range), which determines the maximum extent of the delivered BP's orthogonal to the field direction (top and bottom in the figure), the selected separation of pencil beams in the scanning directions (in this case 4 mm), and the energy of each "layer" of Bragg peaks along the beam direction. Note that as only one slice through the patient is shown here, the second scanning direction will be in and out of the plane of this image, and thus we would have a similar pattern of BP positions in the CT slices above and below that shown (cranial and caudal directions in the patient).

The depth of BPs along the field direction is determined by the energy of each layer of BPs, with those of higher energy being deeper in the patient in relation to the incident field direction

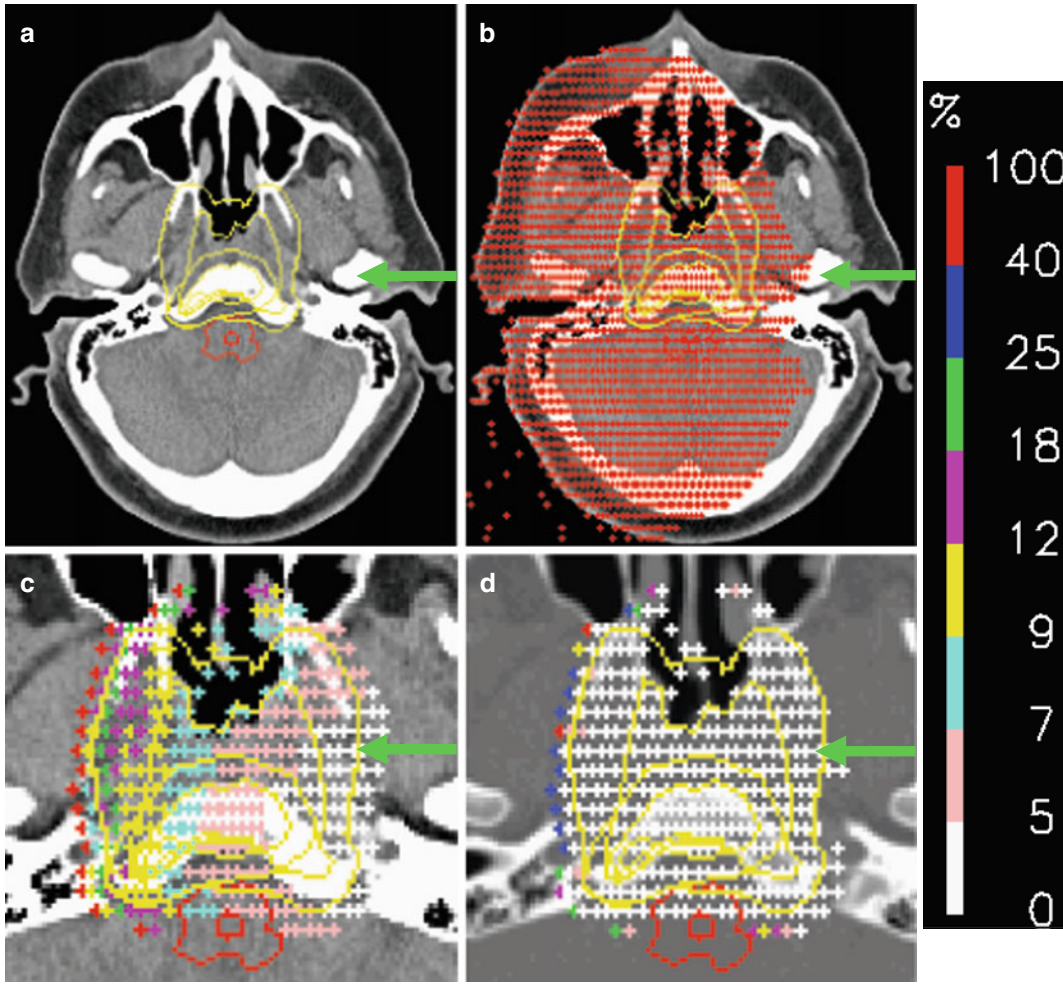

Fig. 12.1 Stages of the planning process for PBS: (**a**) Planning CT, (**b**) All deliverable BPs, (**c**) Selected and pre-weighted BPs, (**d**) Optimized BPs

than those of lower energy. Their separation is thus determined by a discretization of the deliverable energies by the treatment machine. In the case shown here, this is determined by the available "tunes" of the PSI gantry 2, where each tune corresponds to a beam line setting through the gantry appropriate for a particular energy of protons. For our machine, these have been selected to provide energy steps equivalent to 2.5 mm shifts of the Bragg peak range in water. However, as the Bragg peak width increases as a function of increasing depth (due to a statistical broadening of the energy spectrum known as range straggling), this 2.5 mm separation is unnecessary for deeper energies. In our current implementation therefore, for ranges in water above 13 cm, only every second Bragg peak is considered by the TPS, thus resulting in a water equivalent separation of BPs of 5 mm in depth. Below 13 cm, every available proton energy is considered, thus resulting in a water equivalent separation of 2.5 mm. Note that this approach is specific to the planning system at our institute, and other energy/range separations are of course possible. For instance, many commercial systems use constant energy, rather than range, steps of 3–5 MeV, which results in a naturally smoother separation of Bragg peaks as a function of depth.

The observant reader will however have noticed something about the separation of BPs along the

beam direction in the patient geometry shown in Fig. 12.1b. That is, the BPs are not regularly spaced, despite the fact that, in water, their ranges would be spaced at 5 or 2.5 mm intervals. This is of course due to the density heterogeneities in the patient. As can be seen in the underlying CT data, there are large density variations within the patient, ranging from the bones of the skull and skull base, through the gray and less dense soft tissues of the brain to the air cavities in the inner ears and nasal cavities. Thus, although the BPs are regularly spaced in depth if applied *in water*, this cannot be the case in the patient, with the protons clearly penetrating deeper into the patient where the densities are low (e.g., the air cavities) or less far where they are high (e.g., in the bones). Therefore, the actual separations in the patient will be much smaller in bone than in air, where due to minimal energy loss, the BPs shoot through to the other side. Only in the brain and other soft tissues therefore are the BP separations in the patient close to those for water.

Figure 12.1b shows *all possible* BPs that could be delivered from the defined field direction with the parameters of the machine as they have been defined. However, it is hopefully clear that this distribution of BPs is less than optimal, or at least not necessary, for conforming the dose to the target volume (yellow contour). For instance, it is obvious that any BPs delivered outside the target are unlikely to contribute any useful dose to the target and will only add to the doses delivered to the surrounding normal tissues. As such, an obvious next step is to select just those BPs that contribute dose to the target volume, the result of which is shown in Fig. 12.1c. These consist of all BPs within the target contour and also those up to 5 mm outside of the contour. Although these additional "external" BPs may not be absolutely necessary, when using BP grids with a regular spacing in all directions, as is the case here, BPs with distances from the target surface up to the inter-pencil beam spacing distance are required in order to ensure full target coverage.

In Fig. 12.1c, each of the selected BPs have also now been assigned a fluence (weight), as indicated with the differing colors of the crosses. In this case, this is a pre-weighting process before the final optimization process described next. In the pre-weighting strategy shown here, BP weights vary only along the beam direction and have been weighted such that the effective dose delivered by each line of BPs is similar to that of a spread-out Bragg peak (SOBP) as used for modulating depth doses in passive scattering [34]. Thus, the fluences vary identically along each line of BPs along the field direction, with the highest weights assigned to the most distal BP and then decreasing toward the proximal part of the target. Note that this decrease in weight to form a flat SOBP is very rapid, and therefore the BP weights in Fig. 12.1c have been displayed using an exponentially scaled color scale (shown on the right).

Figure 12.2a shows the dose distribution for this slice resulting from calculating the dose contribution from each pencil beam positioned and weighted as shown in Fig. 12.1c (plus all the other pencil beams of the field in planes parallel to that displayed). Unfortunately, although we have conformation of the dose to the target, dose homogeneity is not very good, particularly at the edge of the volume. This is invariably the case for irregular-shaped targets in inhomogenous surroundings, where there is essentially a loss of proton "equilibrium" at the edge of the target, leading to underdosage in these areas. For this reason, an optimization step is required which, based on the dose differences local to each pencil beam, increases or decreases its fluence. As is common with optimization in radiotherapy planning applications, this step is based on a gradient-based, iterative procedure which will not be described in detail here, but the details of which can be found in [3, 4, 40].

The result of the optimization step (after 60 iterations) is shown in Figs. 12.1d and 12.2b. Figure 12.1d shows the resultant BP fluences after the optimization step, while Fig. 12.2b shows the resultant dose distribution. By comparing the two dose distributions in Fig. 12.2, the result of the optimization step is clear. The resulting dose across the target volume is now much more homogenous, and the 95 % isodose contour (the blue area in the figure) almost exactly follows the target contour, indicating the level of conformation achievable with even a single field for PBS proton therapy.

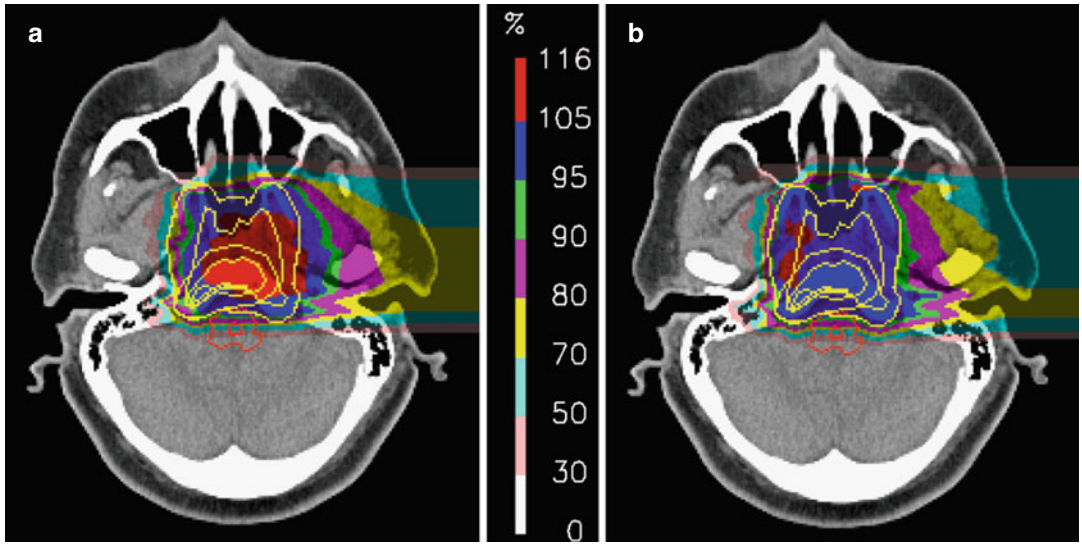

Fig. 12.2 Unoptimized (**a**) and optimized (**b**) dose distributions for the same case and slice as in Fig. 12.1

Before moving on, it is worth saying a few words about the pre-weighting step described above. In principle, given a perfect optimization engine, this step should be unnecessary, with the optimizer anyway finding the optimal solution without needing to pre-weight the pencil beams. However, as will be discussed in more detail below, there are in fact many different solutions to the optimization problem for PBS proton therapy (see, e.g., [39]) which result in remarkably similar dose distributions. The pre-weighting step described above essentially "pushes" the solution in a particular direction (one that is the closest to the SOBP starting condition) and also makes the job of the optimizer somewhat easier and quicker. This issue won't be discussed any more here, but the interested reader is referred to the work by Albertini et al. [3, 4]) for a study into the importance of pre-weighting for PBS treatment plans.

12.2.2 Combining Fields: Single-Field, Uniform Dose (SFUD), and Intensity-Modulated Proton Therapy (IMPT)

In the previous section, we described the process of constructing and optimizing a single field of a PBS treatment. In this and the next section, we will expand on this and look into different ways of combining PBS fields into clinically relevant treatment plans.

The process described above results in a more or less homogenous dose across the target volume, as seen in Fig. 12.2b. As such, if there are no other requirements or constraints for the treatment, such a single field could, in principle, be enough. Indeed, in some treatments, this may well be the case, as for example, in the irradiation of the whole cranial-spinal axis for the treatment of medulloblastoma [77]. However, in general, and as in conventional therapy with photons, typical PBS treatments consist of multiple fields, incident from different directions.

There are two main approaches to combining fields for PBS proton therapy, which have been defined as single-field uniform dose (SFUD) and intensity-modulated proton therapy (IMPT) [40–43].

SFUD is perhaps the simplest, and consists of the simple, linear addition of multiple fields constructed exactly as described in the previous section. That is, pencil beam fluences are optimized for each field independently and with the sole goal of constructing a dose distribution across the target that is as homogeneous as possible. An example SFUD plan is shown in Fig. 12.3, with the dose distribution for the full plan shown in the

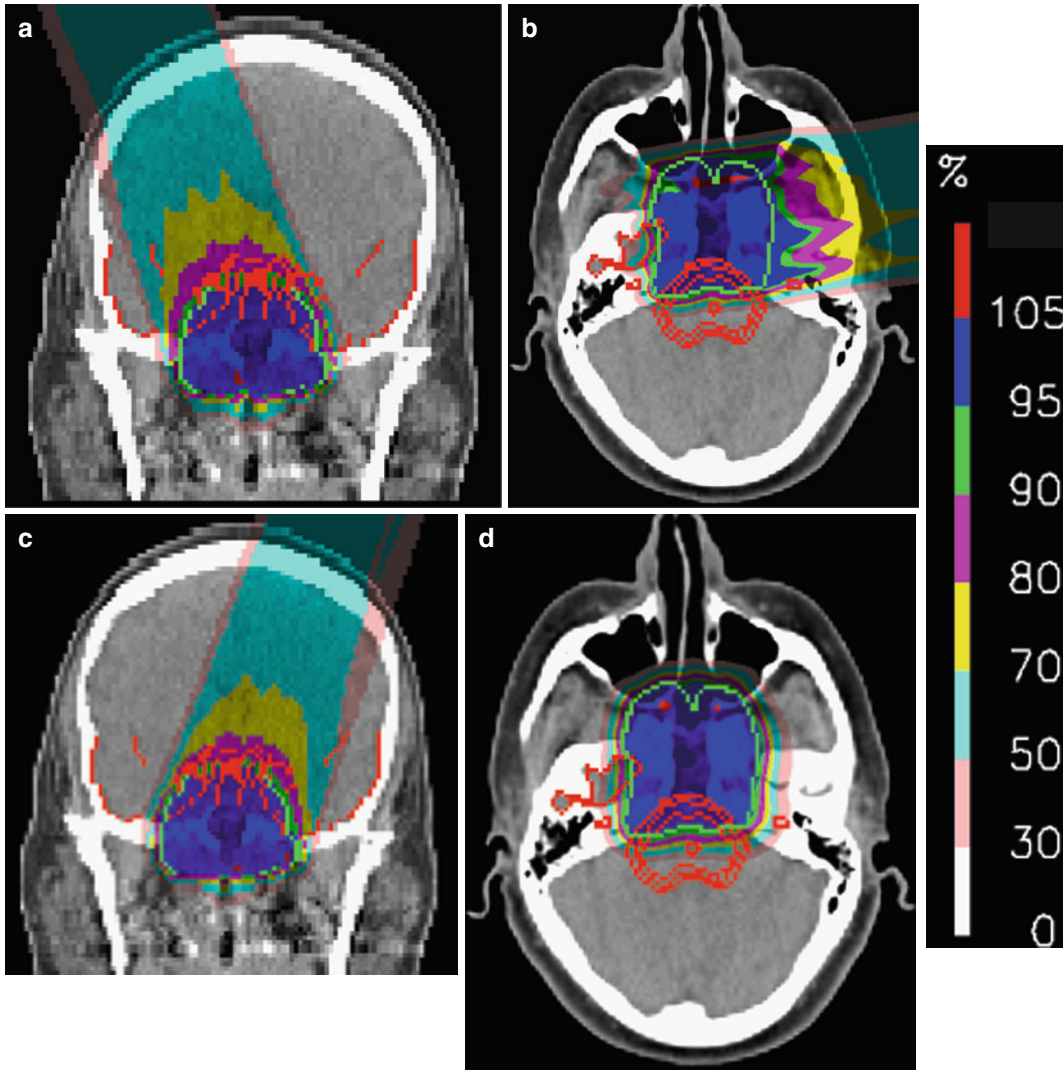

Fig. 12.3 Example fields (**a**–**c**) and full plan (**d**) for a SFUD treatment to a skull base chordoma

center, together with the dose distributions for the individual fields. Note, however, when combining such fields together, different field weights can be assigned in order to adjust the contribution of each field to the target volume. Typically, such differential weighting of fields is done in order to either reduce the weight of fields which have a worse in-field dose homogeneity or in order to reduce the weight of fields which are passing through, or stopping against, critical structures. Indeed, in the SFUD plan shown in Fig. 12.3, the weight of the lateral field has been somewhat reduced such that it only delivers a quarter of the total dose to the target, as it is partially stopping against the brain stem. Such a field arrangement and field weighting have been standard practice in our clinic for the first series planning of skull base chordomas for many years [6] and were initially adopted in order to make the planned dose to the brain stem somewhat more robust to potential range uncertainties (see below). Typically, about 60 % of all delivered plans in our clinic are SFUD, with this mode of PBS delivery being selected wherever possible.

A variant of the SFUD approach is now also becoming more popular, which has been called

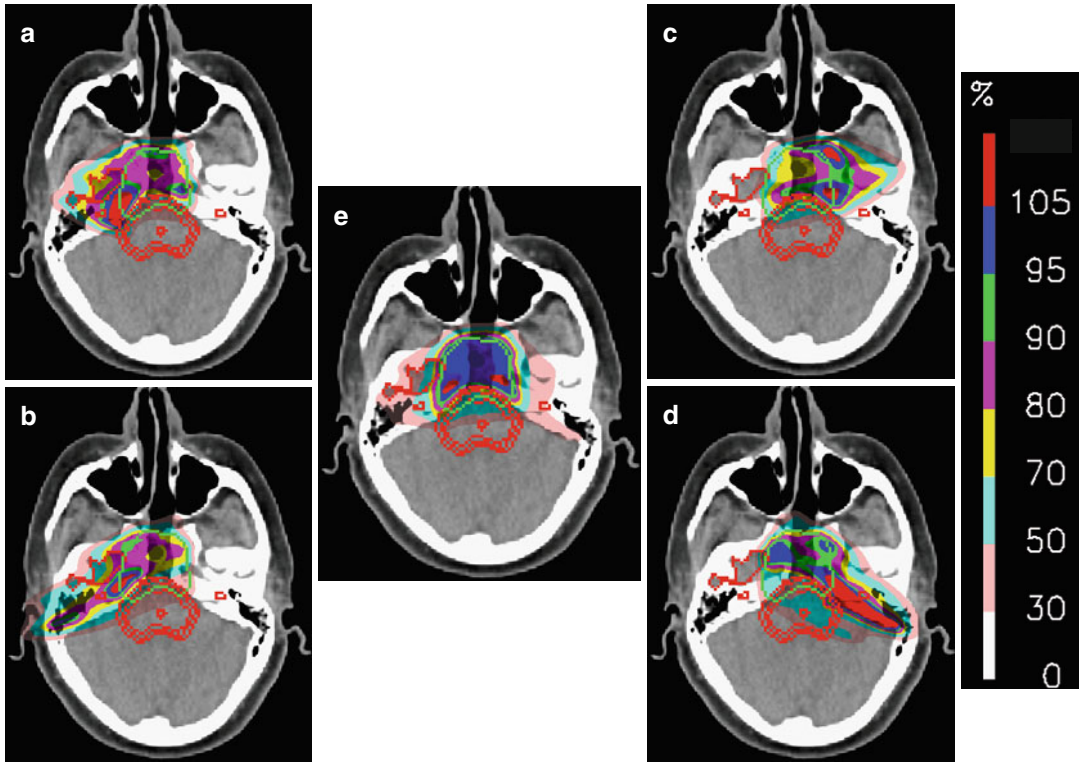

Fig. 12.4 Example fields (**a**–**d**) and full plan (**e**) for an IMPT treatment to the same case as Fig. 12.3: Note the four fields all have small table kicks of 20–30° in the cranial direction

single-field optimization or SFO. This is similar to SFUD in that the pencil beam fluences are optimized for each field individually, but the SFO approach also allows for constraints to be applied to neighboring critical structures during the optimization of each individual field. Although not applicable in all cases, it is an interesting and somewhat more flexible extension of the SFUD approach.

The second main method of combining plans is somewhat more complex but has the advantage of maximally exploiting the full flexibility of PBS. This is what is now universally called intensity-modulated proton therapy, or IMPT [40].

In contrast to the SFUD approach, IMPT *simultaneously* optimizes the fluences of all pencil beams from all fields contributing to the plan. As such, there is no guarantee that the individual fields will be homogenous across the target, as is the case for the SFUD approach. Indeed for most applications of IMPT, this will certainly not be the case. However, the optimization of all pencil beams from all fields in the same process allows for much more flexibility in constructing the total dose distribution. For instance, if for one field, the pencil beam weights need to be reduced in order to reduce the dose to a critical structure, the resulting "hole" of dose in the target can be compensated by pencil beams from other fields. Thus, although the individual fields may become very inhomogenous, the final dose across the target from all fields can still be homogenous. This is the power of IMPT. Indeed, this planning and delivery approach has been so-called as it is the proton equivalent of IMRT with photons, in which the fluences of the individual photon fields can also be highly inhomogenous (highly modulated) in order to be able to selectively avoid overdosing critical structures.

Figure 12.4 shows a four-field IMPT plan to the same patient as for the plan in Fig. 12.3. However, in addition to attempting to deliver a homogenous dose as possible to the target

volume, constraints have also been defined for the brain stem and optical structures, to which the delivered doses are clearly reduced in the full plan (Fig. 12.4e). Also shown in the figure are the dose distributions for the individual fields making up this plan, and it is immediately evident that the forms of the individual fields are very different from those of the SFUD plan shown in Fig. 12.3. Each field is now highly inhomogenous, and for the fields which are passing directly through the brainstem, the reduction in the fluences of the pencil beams is clear.

In summary, IMPT provides the automation and flexibility of IMRT with photons, allowing for both maximizing target coverage while also selectively sparing neighboring critical structures as required.

Before moving on, an important note should be made. As has been pointed out by Stephen Dowdell (private communication), the idea of separating SFUD and IMPT is, in some ways, a false classification. Indeed, SFUD can really be seen as a special case of IMPT, but which is performed in such a way that the in-field modulation is minimized, and IMPT planning, when performed with no additional constraints on critical structures and with the correct pre-weighting strategy, can approach the SFUD solution. As more and more challenging constraints are added to the problem though, more and more modulation of the fields will be required. Thus, there is actually a "spectrum" of solutions, from SFUD through to highly modulated IMPT plans which progress as a function of in-field modulation. Nevertheless, we have always found it useful in our clinic to separate out SFUD and IMPT planning, and most commercial treatment planning manufacturers now support both modes.

12.2.3 Plan Degeneracy and Multi Criteria Optimization

Optimization is a key element in the construction of fields and plans for PBS proton therapy, as outlined in the previous sections. However, "optimization" is really the wrong name for this process, as there is typically not one "optimal" result of this process, at least not if the planning goals are relatively simple (i.e., dose homogeneity across the target volume only). This has already been eluded to when discussing the pre-weighting step above. In fact, for simple planning goals, there will be very many solutions of pencil beam positions and weights that give very similar final dose distributions (see, e.g. [39]). In optimization terminology, this characteristic is known as "degeneracy" and is an important concept in any form of optimized treatment planning and delivery.

In one of the first papers on IMPT [40], the degeneracy of the IMPT planning problem was already evident. In that paper, four "flavors" of IMPT were proposed, namely, 2D, 2.5D, 3D, and distal edge tracking (DET). Briefly put, 2D IMPT assumed that the delivered pencil beams had a fixed and identical SOBP depth-dose distribution, and thus only 2D modulation of the fluences is possible (relative fluence weighting along the depth-dose distribution being fixed in order to deliver a constant SOBP), whereas 2.5D IMPT expanded this concept and assumed that although each modulated pencil beam has an SOBP depth-dose characteristic, the extent of the SOBP is defined on a pencil beam by pencil beam basis such that it is customized to the thickness of the target at every pencil beam position. 3D IMPT is defined as the completely free optimization and modulation of all pencil beams for all fields, without restricting the effective depth-dose characteristics to be that of a SOBP, while DET is a special case of 3D IMPT, where only pencil beams with Bragg peaks stopping on the distal edge of the target volume are considered (i.e., all Bragg peaks internal to the target volume are ignored). Although differences between these approaches in the normal tissue doses were observed when applied to an example case, to all intents and purposes, the final dose distributions were very similar. Thus, for target coverage alone, the four approaches can be considered to be "degenerate."

Degeneracy can be both an advantage and disadvantage. On the negative side, with no other constraints, restrictions, and defined goals, there is little control of which solution the optimizer will reach. Hence our approach of pre-weighting the

Bragg peaks before starting with the optimization process provides a good initial guess for the optimizer to move in the desired direction. As a gradient-based optimization approach is used [40], a solution will generally be found that is the closest to the starting conditions, and by pre-weighting with SOBP type weightings, this ensures that the resulting distribution of weights is uniformly distributed over the target. However, as discussed by Albertini et al. [3, 4], other pre-weighting scenarios can be used, for example, "inverse wedges" or even forcing the solution toward DET by simply setting the weights of all internal Bragg peaks to zero in the pre-weighting step.

On the positive side, however, degeneracy indicates that there is scope for posing more challenging problems to a PBS optimizer, or that, of the many similar "optimal" solutions possible, one or other may have some more desirable characteristics than others, and characteristics that may not necessarily be known a priori at the start of the planning process. This has led to the concept of Multiple Criteria Optimization (MCO), which is gaining much ground for both IMRT and IMPT optimization [12, 15–17].

Simply put, the MCO approach is a "smart" way of generating a set of plans which cover the spectrum of "optimal" solutions. Optimal may seem an odd term here, as we are deliberately talking about a *set* of plans rather than one. But when there are multiple, often conflicting criteria for a plan (e.g., achieving target coverage while also wishing to spare doses to one or more neighboring critical structures), there are indeed a "spectrum" of optimal solutions, which may vary as a function of how they 'balance' the conflicting requests (i.e., from maximizing target coverage and minimizing normal tissue sparing to minimizing target coverage in order to maximize the sparing of critical structures or even balancing target coverage against plan robustness [15]). Thus, the art of MCO is to find this spectrum of "optimal" plans (there are unfortunately many more suboptimal plans which don't do either very well!) and be able to present them to the user in such a way that they can then browse through the possible solutions to pick the best. It seems to this author that such approaches are very likely the future for treatment planning for PBS proton therapy, although much development still needs to be done.

12.3 The Problem of Range Uncertainty

As discussed above, the main role of treatment planning for PBS proton therapy is to determine the best arrangement of fields, pencil beams, and weights for treating the tumor. However, the quality of such an arrangement can only be judged by assessing the resultant, 3D dose distribution produced by the TPS. Indeed, the fact that the treatment to be delivered can be estimated a priori and with a resolution of a few millimeters by computer simulation is one of the great strengths of radiotherapy, matched by few other therapeutic techniques apart from perhaps computer and robot assisted surgery. Nevertheless, it must always be remembered that such calculated dose distributions are just that – estimates. As such, in reality, the actual delivered dose distributions may vary from this calculated distribution to a greater or lesser amount. The sensitivity of a particular treatment plan to potential variations is referred to as "plan robustness." In the second part of this chapter, we will concentrate on this important aspect, as it is generally expected that proton treatments are likely to be less robust than photon plans, and thus plan robustness, and its analysis, is an important issue for PBS proton treatments.

12.3.1 Sources of Delivery Uncertainties

There are many reasons why the delivered treatment will not be identical to the calculated dose distribution. The most obvious is the limitation of dose calculation engines by which the 3D dose distribution is calculated (and on which the optimization is based) or misalignments of the patient in relation to the beam on treatment days in relation to that assumed by the treatment planning system [5, 22, 42, 43, 63, 78, 79]. The effect of such errors will not be considered here however.

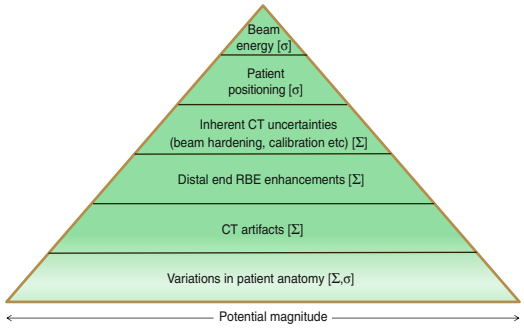

Fig. 12.5 Sources of range uncertainties. Σ systematic, σ random

Instead we will concentrate on what the author believes are the most important possible causes of differences between the calculated and delivered doses – range uncertainty and motion (discussed in the next section).

The main advantage of protons is their very well-defined range due to the Bragg peak, which provides (at least for pristine Bragg peaks) a sharp dose fall-off at the distal end. However, to best utilize this characteristic, the exact placement of such Bragg peaks in the patient needs to be known. And here lies a fundamental problem – the exact range of protons in the patient is subject to many uncertainties. This is due to many potential reasons, shown schematically in Fig. 12.5. In this figure, the sources of range uncertainties are ranked based on their estimated magnitude of effect, starting with the smallest at the top and the largest at the bottom. Thus, the clinical relevance of, e.g., CT artifacts can be more substantial than range uncertainties caused by increases in RBE in the Bragg peak. It must be pointed out however that this ranking is very subjective and other authors may rank these somewhat differently. Nevertheless, the figure gives an overview of the potential sources of range uncertainties in the patient and indicates that these are many. It also indicates whether the uncertainty is likely to be random in nature (i.e., will vary day to day over the course of fractionated treatments) or whether they are systematic (i.e., will be the *same* everyday). Systematic errors are, by their nature, the most worrying as, in contrast to random errors, they will not "wash out" with fractionation. As such, in the rest of this discussion, we will concentrate on the effects of systematic range uncertainties.

12.3.2 CT Calibration

Most modern radiotherapy is based on CT. Similarly, the use of CT is essential for proton therapy as this is currently the only modality that provides the necessary information on tissue density to allow for accurate dose and range calculations in the patient geometry. Indeed, although the first patients were treated with protons already in the 1950s, its more widespread use had to wait until the invention of x-ray CT in the 1970s for this very reason. However, CT data actually provides a 3D map of x-ray attenuation relative to water, which first needs to be converted into proton stopping powers before it can be used for dose and range calculations in proton therapy.

There are a number of ways of doing this [29, 52, 83], but the most common is to use the stoichiometric method first proposed by Schneider et al. [74]. In brief, after a parameterization of the CT scanner through the use of tissue substitutes of known composition, a Hounsfield Unit (HU) to stopping power (SP) curve is then constructed for biological tissues based on their physical characteristics such as physical density and chemical composition. However, as typically only one CT is used for planning, and only one such calibration curve, any inaccuracies in the CT data or uncertainties in this calibration will propagate through the whole treatment (i.e., will propagate as classic systematic errors).

Although this approach is quite sophisticated and based on solid theoretical concepts, it can never be a perfectly exact process. For a start, the transformation from HU to SP is non-unique. That is, materials with the same HU can have quite different SP values and vice versa. For this reason, for clinical applications, a biologically specific curve is used. However, non-biological materials in the CT (such as the table top or fixation devices) will not necessarily lie on the same curve and, unless manually corrected, will lead to systematic range uncertainties. As an example, if

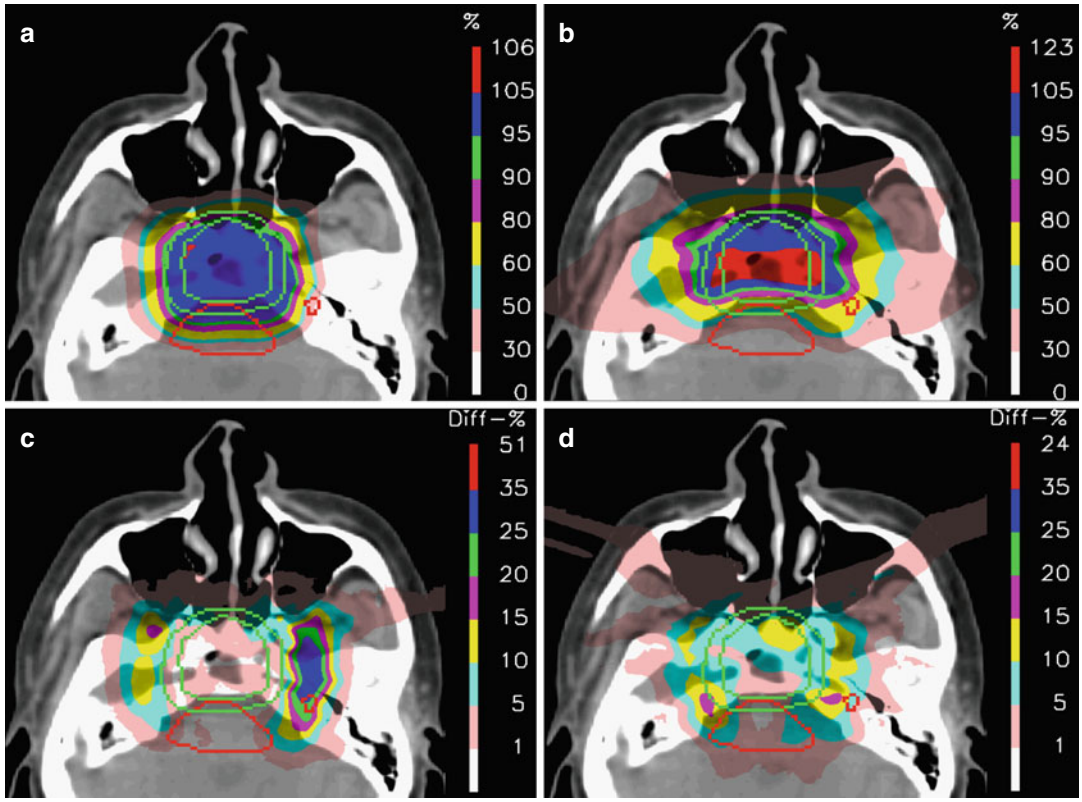

Fig. 12.6 The potential effect of range uncertainties on SFUD and IMPT plans: (**a**, **b**) Nominal SFUD and IMPT plans, (**c**, **d**) "Error-bar" distributions for ±3 % range errors, where the colors now represent the width of possible doses at each point under these error conditions (max dose – min dose)

we assume that the SP of a plastic table top of thickness 2 cm is overestimated by the calibration curve by just 5 % (i.e., the actual SP of the table lies just 5 % *below* the calibration curve), then this can already lead to a systematic range error of 1 mm. For this reason, non-biological materials in the CT are often outlined, and the HU or SP values within these structures manually changed in order to correct for these effects.

This is certainly not the end of the story however. Even for biological samples, any calibration process can never be perfectly accurate. After implementation of the stoichiometric approach at our institute, for instance, the accuracy of this approach was tested by Schaffner and Pedroni [72] on biological samples. These measurements showed that the uncertainty in the resultant calibration curve was about 1.5 % for soft tissues and 2 % in bone. Given that these measurements were performed under relatively ideal conditions (e.g., using simple phantom geometries), these uncertainties are in line with the generally accepted value usually assumed for treatment planning purposes, which is 3 to 3.5 % [5, 41, 49, 58]. Although such an accuracy is quite good, it should always be kept in mind that these nevertheless translate into absolute range errors of up to 3 mm for centrally placed cranial tumors and 6 mm for central pelvic tumors (i.e., prostate if being treated from the lateral aspect).

The effect of 3 % range uncertainties in a clinical setting is shown in Fig. 12.6 for SFUD and IMPT plans for a typical skull base chordoma. The top two figures show the dose distributions for the two plans, whereas the bottom two show so-called "error-bar" distributions [5] in which the color wash shows the potential magnitude of dose variations resulting from ±3 % range errors.

For example, all areas displayed yellow in the bottom images correspond to voxels where the *difference* in dose resulting from +3 and −3 % range errors are between 10 and 15 % of the prescription dose (so about ±5–7.5 % about the nominal dose). This comparison shows that, although in the slices shown the largest error bars are for the SFUD plan, these are only in areas outside of the PTV margin and in areas of high-dose gradients, whereas for the IMPT plan, uncertainties of up to ±5–10 % can be seen within the CTV. Thus, for target coverage, the SFUD plan can be considered to be more robust than the IMPT plan.

This example nicely shows the potential effects of the inevitable uncertainties in the CT calibration process for proton therapy and the quite different distributions of error magnitudes observed for the same case as a function of field arrangement and planning technique.

12.3.3 Range Extension Due to RBE

Relative biological effectiveness (RBE) is an important concept in particle therapy. It is a way of expressing the fact that the biological *effectiveness* of a given dose (deposited energy) can be different for different types of radiations. In comparison to photons, for example, the RBE for proton therapy is generally assumed to 1.1 globally (see, e.g., [57]). However, there is plenty of in vitro (cell-based) evidence that the RBE can also increase quite rapidly as a function of, in particular, decreasing proton energy [57]. As all protons in the Bragg peak have low energy, it is therefore expected that the RBE in this region could be considerably higher than 1.1, particularly in the distal fall-off region, where the average energy of the protons is the lowest. Such an increase can result in substantially higher biologically equivalent doses in the Bragg peak itself but also to a systematic "shift" of the distal fall-off to higher ranges. Thus, RBE uncertainty can also be considered a source of range uncertainty, with shifts in range of up to 3 mm being predicted in some conditions [14]. Such results have not been reproduced in in vivo studies, however, or necessarily for non-tumor cell lines [57], and therefore the clinical relevance of this is presently unclear [59]. Nevertheless, it is well worth keeping this potential effect in mind when planning proton treatments and is one of the reasons that most proton practitioners are extremely reluctant to "stop" single fields directly against critical structures.

12.3.4 CT Artifacts

After that short diversion into biology, let's now return to CT data and an important issue which, thankfully, is not present in every patient.

There are a number of reasons why patients may have metal implants close to the treatment area. An obvious example (which is not too uncommon) is tooth fillings out of either amalgam or (much worse) gold. However, many patients may also present for proton therapy after substantial surgery in which bony structures (such as one or more vertebrae) need to be supported by titanium implants or where whole joints have been replaced with titanium prostheses (e.g., hip replacement surgery). Why can such implants effect proton range calculations? For two reasons: first, the implants themselves are not biological, and therefore won't lie on the typical HU-SP calibration curve. Indeed, the density of these implants are so high that they will saturate CT scanners and will generally give a similar HU value whether titanium (SP ~3.1) or gold (SP ~10.0). So there is a problem with accurately calculating the correct energy loss in such structures, as it is impossible from the CT data sets to correctly predict their density or SP. In practice, this can be dealt with by identifying any metal structures and manually setting the SP for these to their true (usually measured) value. Second, the high density of these structures causes major problems for CT reconstruction algorithms, with complex or very dense structures creating large reconstruction artifacts.

An example of such artifacts is shown in Fig. 12.7a. This is a CT slice at the level of the upper thorax from a patient who has had previous surgery to remove a portion of the vertebrae, which was then subsequently supported by titanium rods fixed to the neighboring vertebrae

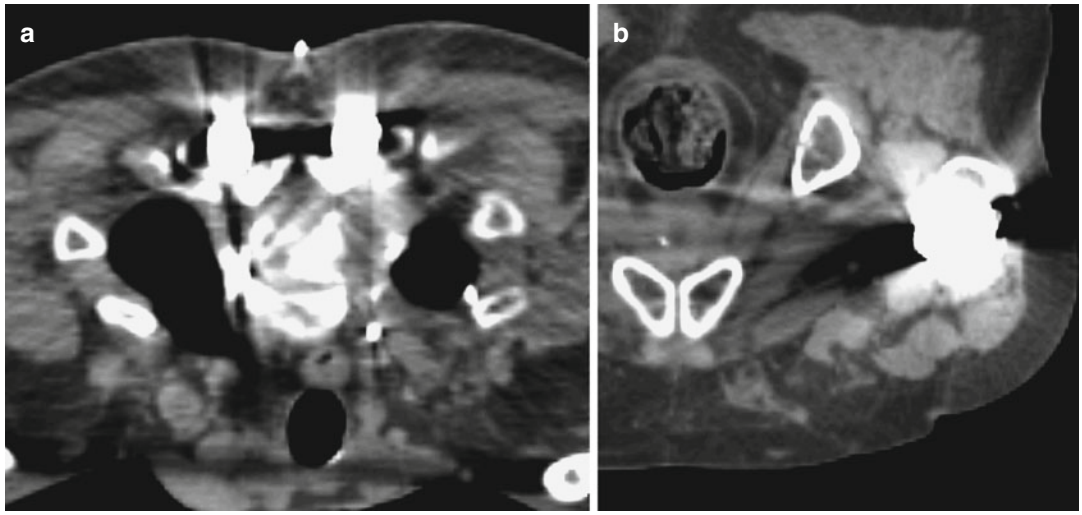

Fig. 12.7 (**a**) An example CT slice at the level of the thorax for a patient with stabilizing metal (titanium) implants and (**b**) in the pelvis for a patient with a hip prosthesis

through the use of titanium screws. Clear and coarse artifacts can be seen around the vertebrae area, with large areas of apparently very low HU values between the metal rods. These are not areas of low-density tissue, however, but rather reconstruction artifacts due to the metal. In fact, in these areas, there is actually a mixture of bone and soft tissue. Clearly, the calculation of proton range in these areas will always be wrong, simply because the CT data itself is already wrong.

Due to the complexity of such artifacts, it is impossible to put a single value on the magnitude of the effect. However, Fig. 12.8 gives an idea of how such artifacts alone can affect proton range [1, 53].

Figure 12.8a shows the dose distribution for a single SFUD field planned to a prostate carcinoma in which the field is passing directly through a titanium hip prosthesis, the CT slice of which is shown in Fig. 12.7b. The dose distribution has been planned on this KVCT data set in which the calibration curve has been modified such that the highest HU value is assigned to the stopping power of surgical grade titanium. As can be seen, although the prosthesis causes some dose irregularities in the distal fall-off of the field, the overall coverage and dose conformation is acceptable. In Fig. 12.8b, however, the same field has been recalculated on a MVCT data set of the same patient (this patient was actually treated using tomotherapy and has only been used here for simulation purposes). MVCT in this context has the advantage that reconstruction artifacts due to high-density implants are almost completely absent and is therefore a convenient imaging modality to use as a "ground truth" representation of the true anatomy of the patient. The difference in the dose distributions is obvious. When recalculated using artifact-free imaging, there is a clear undershoot of the field of 2–3 cm directly behind the metal implant in comparison to the dose planned on KVCT.

To look at this in more detail, Fig. 12.8c shows SP profiles calculated from the two CT data sets along the field direction and through the middle of the prosthesis and tumor volume. From this, it is clear that modeling of proton energy loss in the prosthesis itself will be more or less identical for both the KV and MVCT, but that on either side of the prosthesis, SP values calculated from the KVCT are severely underestimated in comparison to those from MVCT. If we assume that SPs calculated from MVCT in these areas are closer to the "ground truth" SP for the patient (a reasonable assumption given that the MVCT values throughout the profile are similar through all soft tissues, including those immediately adjacent to the implant), then we can conclude that the severe

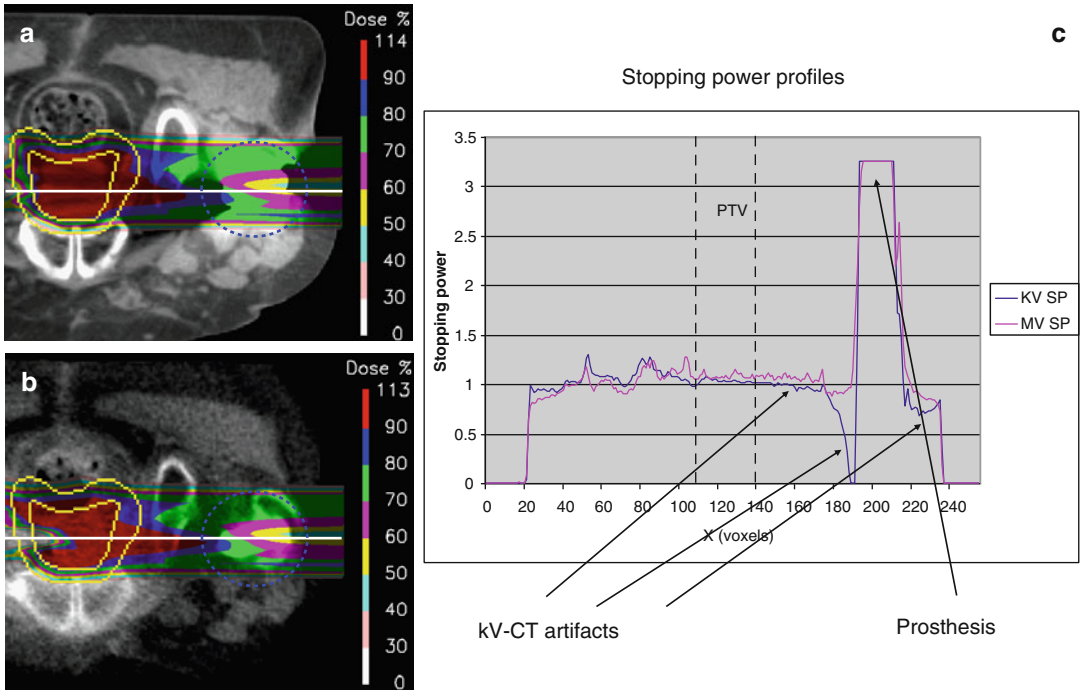

Fig. 12.8 Range and dose perturbations due to metal induced CT reconstruction artefacts: (**a**) Dose planned and calculated on KVCT, (**b**) Dose recalculated on a MVCT of the same patient, (**c**) Profiles through the KVCT (*blue*) and MVCT (*pink*)

undershoot resulting from calculation on KVCT is only due to reconstruction artifacts alone.

Although the example in Fig. 12.8 may be somewhat extreme, it nevertheless illustrates the potential effect of image artifacts from metal implants on proton range calculations and also shows that these can amount to centimeters of range error in the worst case.

So does this mean that proton therapy shouldn't be performed on patients with metal implants when based on KVCT imaging alone? Well, it certainly means that one must be cautious when treating such patients and wherever possible take precautions to reduce the effects of such artifacts. At our facility, for instance, we try to reduce the effect of such artifacts by delineating those artifacts that are deemed to be overlying soft tissue structures as accurately as possible and then manually setting the HU values of all voxels within these structures to an average value for soft tissue. The plan is then calculated on this modified CT. Although such an approach can never be totally accurate, a recent experimental study based on a realistic anthropomorphic phantom, and using the above-defined procedure, showed substantial improvement in the agreement of measured and calculated distributions when compared to planning directly on the uncorrected CT [18].

12.3.5 Patient Anatomy Variations

The last systematic source of range uncertainty we are going to discuss is that originating from the patient themselves.

Over the course of fractionated therapy, the patient will come for treatment every day over many weeks, and there can be inevitable changes of patient anatomy over this time scale. These can be due to weight changes (most often weight loss but also weight gain in some cases; see, e.g., [2]), radiation-induced changes such as inflammation or reduction of swelling, and changes in the filling of internal cavities such as the bowel and nasal cavities. In addition, depending on the

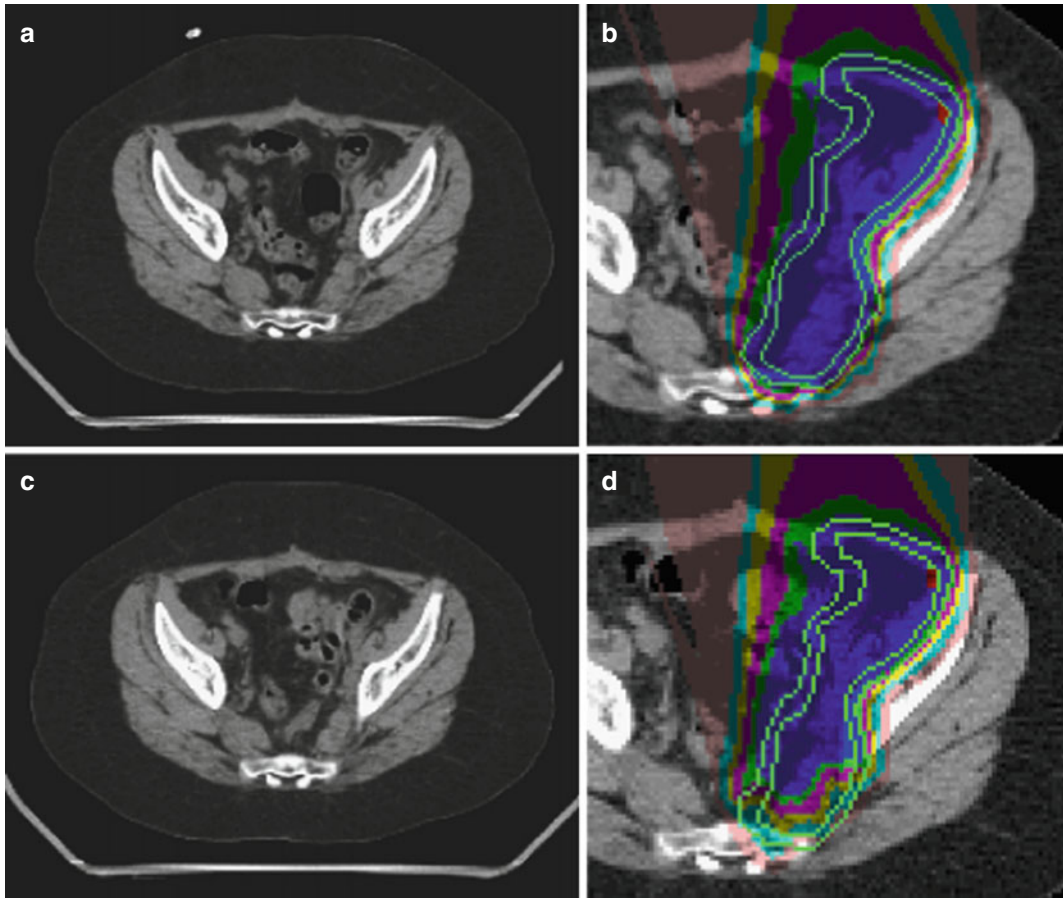

Fig. 12.9 Range and dose perturbations due to changes in intestine filling: (**a**) Planning CT, (**b**) Nominal dose distribution calculated on CT in (**a**), (**c**) Repeated CT on first fraction, (**d**) Dose distribution recalculated on repeated CT

tumor type being irradiated, there can be significant changes in the tumor volume. Although such changes are not necessarily a problem for all cases (for instance, for treatments in the high cranium, such changes will have minimal effect) for almost all other treatment sites, there is the potential of substantial anatomical changes through the course of treatment, which potentially can lead to range changes of many centimeters.

In order to illustrate the potential magnitude of such effects, we will discuss two examples from our own experience of treating over 700 patients using PBS proton therapy. The first shows the effects of varying intestine filling, while the second illustrates potential range effects as a result of postoperative changes in the brain.

Figure 12.9 shows a slice through the original planning CT for patient being treated for a tumor in the pelvis, while Fig. 12.9b shows the target volume and planned dose distribution for this case. In this example, the tumor has been irradiated using SFUD with just two fields with a small angular separation. As would be expected from the discussions above, this approach provides sufficient dose homogeneity across the target volume, with exceptional conformity of the dose to the target at all dose levels. Indeed, this is a very nice example of what can be achieved (at least in the computer!) with PBS proton therapy. However, the target volume in this case also contains a number of intestinal loops (best seen in Fig. 12.9a) through which the beams inevitably must pass as they are a part of the CTV/PTV, and

as can be seen, there are some clear air pockets within these. Due to this, it was decided to make a repeat CT on the first treatment day in order to check the status of the intestine filling. The equivalent slice in this repeat CT is shown in Fig. 12.9c where clear changes and variations in the intestinal filling can be seen.

Based on this new CT, the dose was recalculated and is shown in Fig. 12.9d. The result is rather dramatic. There is clear and consistent undershoot of the target volume of a number of centimeters, with a large portion of the PTV and CTV being significantly underdosed. Based on this, the plan was recalculated with the air pockets in the originating planning CT outlined, and the HU values inside these structures set to that of water (c.f. correction of CT artifacts as described above). By this approach, it can be ensured that under all conditions of bowel filling, the distal end of the field will always be deep enough to cover the PTV (filling the air cavities is the worse case from the point of view of maximum range, as if these areas are actually gas filled on any day, the proton range will always be extended rather than pulled back).

The second example is rather different and is shown in Fig. 12.10. Figure 12.10a shows a sagittal cut through the planning CT of a skull base chordoma patient. A clear air cavity in the fontal part of the brain can be seen which was a result of the pretreatment surgery the patient had received to partially remove the tumor. During treatment, this cavity started to resolve, and a repeat CT was acquired about 1 month into treatment, as shown in Fig. 12.10b. Given that the original cavity was air filled and this has been replaced by a regrowth of soft tissue into the cavity, then it is clear that the range change for any fields passing through this cavity will be equivalent to the dimensions of the cavity, which in this case would again be of the order of 1–2 cm depending on the beam angle used. In fact, this case was in reality treated using a different set of fields (see Fig. 12.10c) which avoided going through this cavity as these changes were expected. Nevertheless, this is a good example of how patient anatomy change could drastically affect a treatment plan if care is not taken with the selection of angles for treatment.

In both examples shown here, measures were taken to minimize the effect of such internal changes. However, depending on where these may occur, such measures may not be enough or even be possible. Thus, regular monitoring of internal anatomy, and subsequent re-planning to adapt to any anatomical changes which may significantly affect the plan quality, will certainly be necessary in the future to best utilize proton therapy for such cases. The ability to perform this more efficiently is one of the main reasons why we have installed a diagnostic CT in the treatment room of our new treatment gantry (Gantry 2) and why most proton therapy manufacturers are now providing either a similar solution, or built in 3D imaging devices such as CBCT, onto proton gantries.

12.3.6 In Range Verifications

Before we move away from the subject of range uncertainties, a few words should be said about the possibility of monitoring range on a regular basis. This has already been mentioned above from the point of view of regular 3D imaging of patients, but there are also many other methods of verifying proton range in vivo being developed or proposed. The oldest of these is proton radiography [33, 62, 73] where higher energy protons are "shot-through" the patient, and their residual range measured on exit. By comparing to simulated proton radiographs calculated from the (calibrated to SP) CT data set of the patient, direct comparisons of integrated SP from calculation and measurement can be performed. Indeed, it has also be shown that much information about range and patient positioning can be inferred from just a few "range probes" (individual high-energy proton pencil beams) applied through selected parts of the patient [50, 69].

More, but perhaps less direct, information about proton range can also be achieved by other techniques and techniques that are dependent on various characteristics of charged particle interactions with matter. These include the measurement of positron activation [37, 38, 54–56, 80] or prompt photon emissions [46, 48, 65] as a result of interactions of protons with atomic nuclei or even the detection of acoustic signals resulting from the

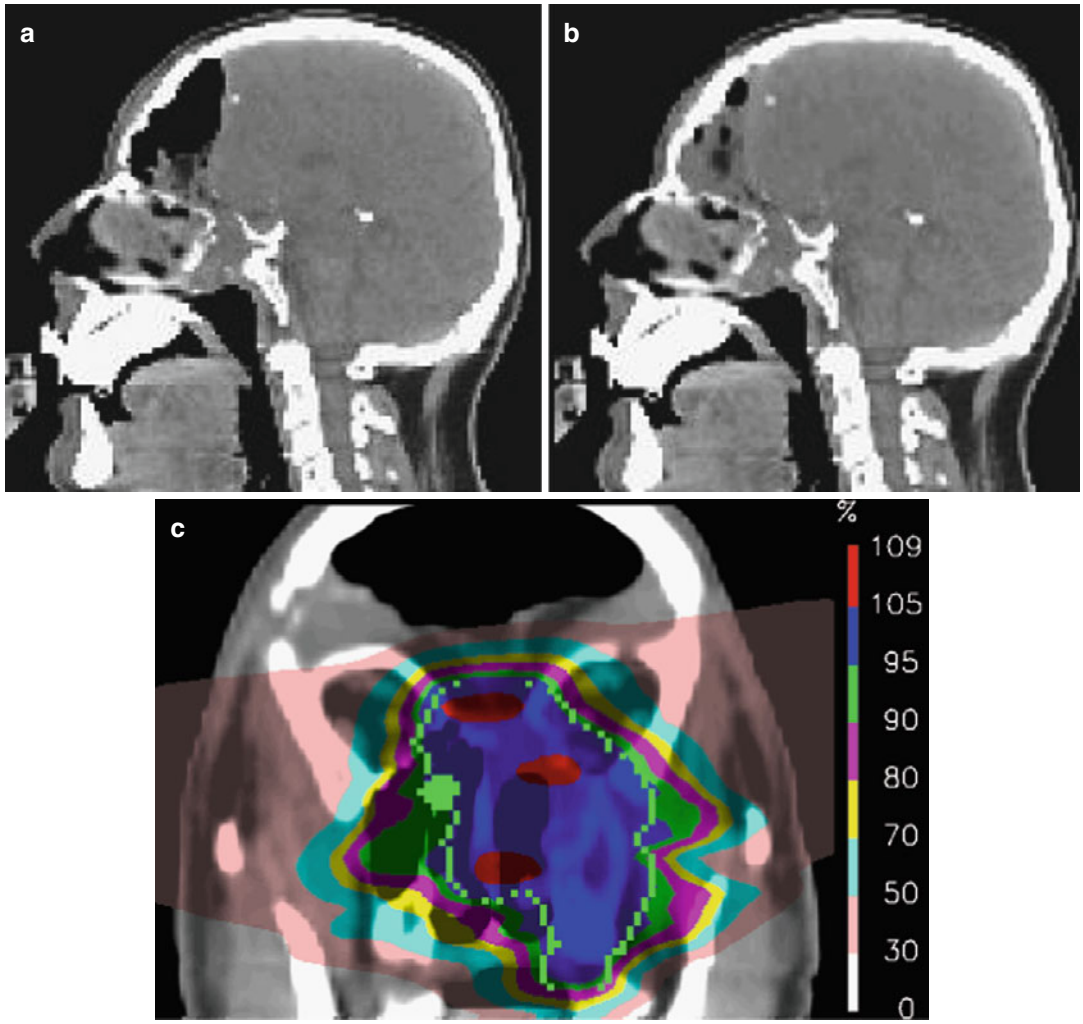

Fig. 12.10 Postoperative anatomical changes in the brain: (**a**) Planning CT, (**b**) Repeat CT 2 weeks into treatment, (**c**) Actual plan delivered to avoid the air cavity (frontal view)

"shock waves" produced by pulsed, high-intensity proton beams [7]. For a more detailed discussion on the relative merits of such in vivo range verification for protons, the reader is referred to the review article by Knopf and Lomax [32].

12.4 The Problem of Motion

We now move away from range uncertainty and on to another major problem for PBS proton therapy, namely, organ motion, or to be more precise, intra-fraction organ motion.

Below the level of the neck, there are many intra-fraction motions which can potentially affect PBS proton therapy. These include heart motion, peristalsis, and breathing. Of these, breathing is the one that has been identified as a major limiting factor for PBS and which will be concentrated on here.

There is a broad magnitude of internal motions resulting from breathing, depending on the anatomical site and patient, which can range from a few millimeters to over two centimeters (see, e.g., [36]), and such motions are a problem for all forms of radiotherapy. At the very least, much

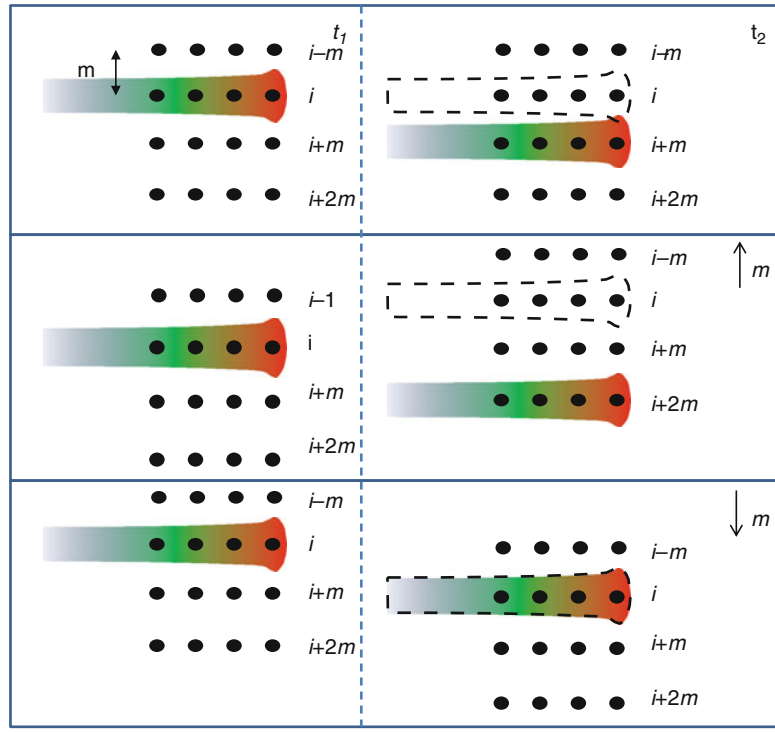

Fig. 12.11 A schematic representation of the interplay effect

larger volumes of normal tissue need to be irradiated in order to ensure that the tumor is irradiated at all times due to the need to define an internal target volume (ITV) [26], which is an additional expansion of the planned target volume designed to ensure tumor coverage under all motion positions. Thus, the larger the motion amplitude, the larger is the ITV margin. However in addition to this, for PBS proton therapy, there is another important effect that must be considered and which will be discussed in the next section.

12.4.1 The Interplay Effect

PBS proton therapy is an inherently dynamic form of delivery, with the individual proton pencil beams being delivered sequentially [60] or continuously [71, 84]. Whichever method is used, there is an inevitable time dependence on the application of each pencil beam or line, and this time dependence can have a strong influence on the delivered dose distribution in the presence of motion. Briefly put, pencil beam scanning and motion are two, time-dependent dynamic systems which can potentially interfere with one another.

This is schematically shown in Fig. 12.11. At the top of this figure are two "frames" of the application of two pencil beams to a "patient." At the left is shown the application of pencil beam 1 at time t_1 and on the right pencil beam 2 at time t_2. As long as the patient is static, then the relative spacing between the pencil beams will be as planned, in this case the distance m between the pencil beams (typically of the order of 5 mm; see above). In the middle and lower rows however are two scenarios for the application of the two pencil beams when in time Δt ($\Delta t = t_2 - t_1$) the grid has also moved distance m upward (middle) or downward (bottom). As can be seen, in the middle scenario (for a motion of the "patient" opposite to the motion of the pencil beam), then the effective separation of the two pencil beams in the patient will be of the order of $2m$, whereas for the bottom scenario (patient motion in same direction as motion of the pencil beam) the effective separation will be 0, i.e., the two pencil beams will be applied at exactly the same position in the patient, despite being delivered at two different positions in relation to the isocenter of the

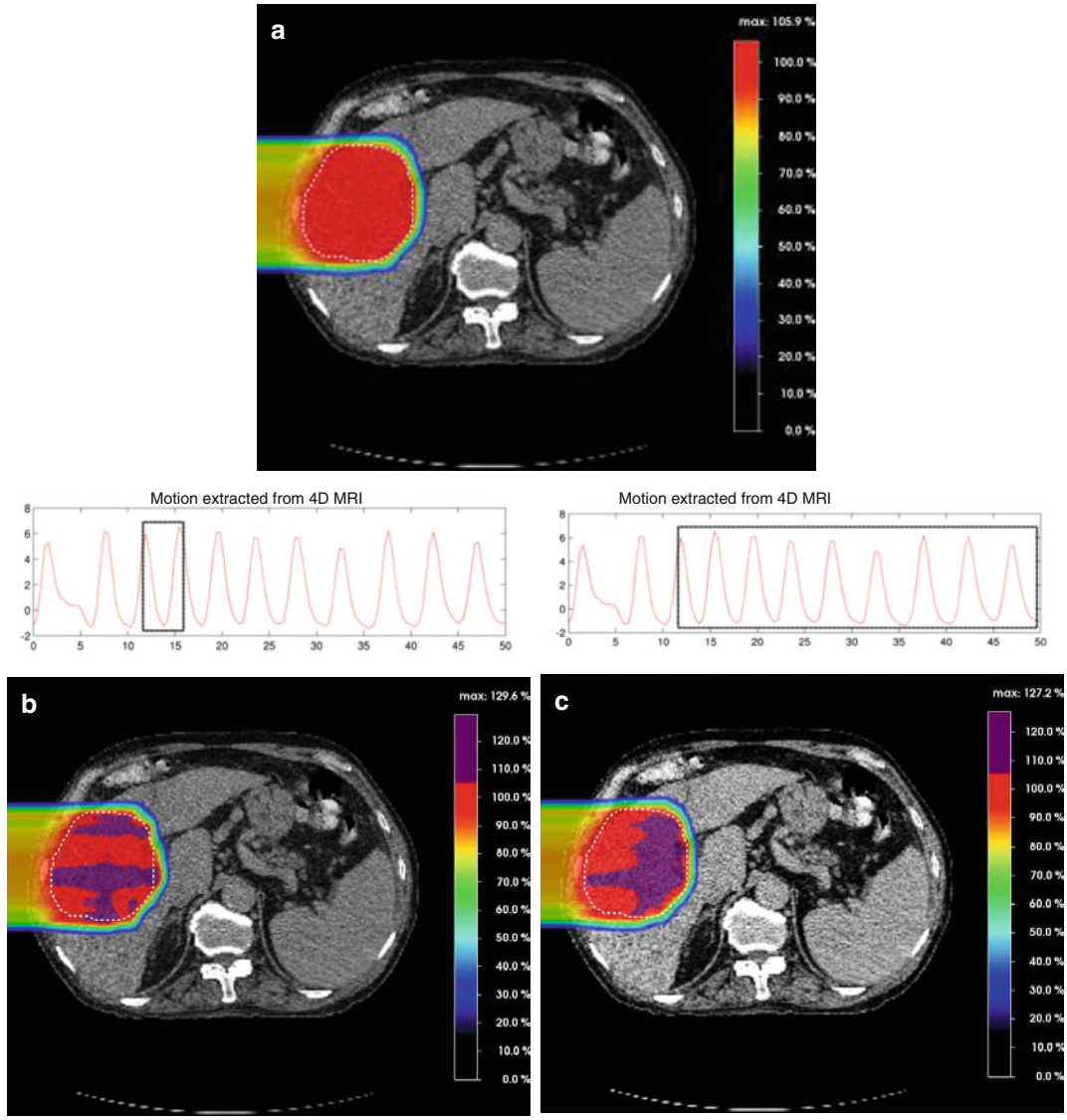

Fig. 12.12 A clinical simulation of the interplay effect for a single SFUD field to a liver tumor and for different motions: (**a**) The static dose distribution, (**b**) 4D distribution for a single breathing cycle and (**c**) 4D dose distribution based on multiple breathing cycles

machine. Thus, in the middle scenario, there will be a "cold spot" between the two pencil beams, whereas in the bottom scenario, a hot-spot will occur due to the exact superposition of two pencil beams at the same position. Such a dynamic effect of these two time-dependent systems is what is called the "interplay" effect.

The potential problem of the interplay effect was first identified by Phillips and Pedroni in their seminal paper of 1992 [64] where it was shown that, for even small motions (of the order of 2.5 mm), hot and cold-spots of up to 20 % of the prescription dose could result when the effect was simulated for a simple square target. The magnitude of these effects in more clinical cases has more recently been studied by a number of authors by both simulation [8, 30, 67, 75] and experiment [20, 70, 85].

As an example, see Fig. 12.12. In Fig. 12.12a, a single-field PBS plan has been calculated for a liver tumor, assuming static conditions. In Fig. 12.12b however, the dose for the same case

has been recalculated taking into account an example motion pattern extracted from 4D-MRI (for details of the 4D calculation used for this, see [13]). There is a clear degradation of dose homogeneity in the 4D dose calculation, consistent with the effects predicted by Phillips and Pedroni [64]. However, this is not the only problem, as indicated in Fig. 12.12c.

Here a 4D dose calculation has been performed in the same way, but this time taking into account *multiple* breathing cycles which vary somewhat from cycle to cycle (see breathing cycle plot associated with this calculation). The resulting dose distribution is somewhat different. So although we can in principle predict the effects of motion, in reality, this may be close to impossible without an exact representation of how the patient is breathing throughout the delivery and how the treatment is synchronized with the breathing (i.e., even for perfectly regular breathing, the delivered distribution will be dependent also on the phase of motion in relation to the delivery).

Clearly then, interplay is a potentially major problem for PBS proton therapy, and a problem for which it is extremely difficult to fully predict exactly what is (or will be) delivered in reality. It is for these reasons that at our institute, we have been extremely cautious with the treatment of mobile tumors with PBS proton therapy.

So, is the interplay effect an unsurmountable problem for PBS? In the next section, we will show that it is not, by looking at different motion mitigation methods that are currently being studied and clinically applied.

12.4.2 Motion Mitigation

12.4.2.1 Gating

Conceptually at least, the simplest motion mitigation technique is simply to stop motion. In reality of course, this is not so easy. Although apnea (stopping internal breathing completely by treating patients under anesthesia and bypassing breathing to an external device) is being employed at one institute [68], this is not widely favored due to the perceived risks of regular, deep anesthesia as part of a fractionated radiotherapy regime. Alternatively, motion can be reduced through the use of a variety of methods. For instance, abdominal compression has been used for the treatment of liver patients at the HIT facility [66], whereas assisted or voluntary breath-hold has been widely used in photon therapy [23, 25, 81].

However, perhaps the most common motion reduction technique in particle therapy is gating (see e.g., [24, 44, 47]). With this approach, the breathing of the patient is monitored using external or internal markers, with the therapeutic beam being switched off and on (i.e., gated) based on this monitored signal. Such a breathing signal can be acquired using a variety of methods, including spirometry, pressure belts attached to the chest wall or abdomen of the patient or optical systems following single or multiple points or surface imaging (see e.g. [19, 51]). Based on these signals, the ratio of gate 'open' (i.e., beam on) to 'closed' is called the duty factor, and determines both the residual motion within the gate and the total time for delivery. To minimize residual motion, the lower the duty factor the better, but this then leads to longer treatment times. Thus in practice, a balance needs to be found between motion mitigation and treatment time. Delivery is therefore typically gated to the exhale phase of breathing which is usually somewhat flatter than the inhale phase, allowing for larger duty factors.

As an example of the potential clinical effectiveness of gating, Fig. 12.13 shows a simulation for a liver tumor. This has been performed using the 4D dose calculation developed at our institute for PBS proton therapy [13, 86], which is based on motions extracted from 4D-MRI studies of volunteers [76]. Figure 12.13a shows the nominal dose distribution for a single-field (SFUD) plan to the liver tumor, while Fig. 12.13b shows the breathing patterns used for the simulations. Also shown in this figure are the gating amplitude thresholds used for the different simulations. For motion displacements above these thresholds, the beam is assumed to be switched off. Finally, in Fig. 12.13c, cumulative dose-volume histograms for the CTV are shown for the different scenarios (no motion, motion and no gating, and motion mitigation using each of the amplitude thresholds).

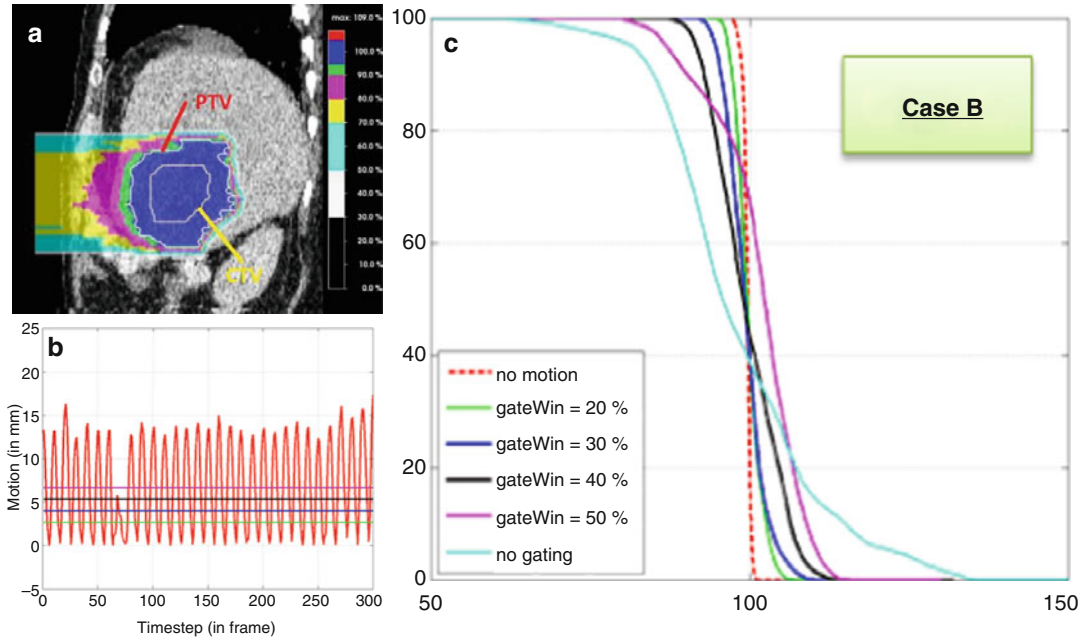

Fig. 12.13 A simulation of gating based on motions extracted from 4DMRI: (**a**) Nominal plan to a liver tumor, (**b**) Breathing patterns and gating amplitude thresholds, (**c**) DVHs to the CTV for the nominal case and different gating thresholds

Figure 12.13b clearly demonstrates one of the problems of patient motion mentioned above – that breathing is often not at all regular – but also how gating can potentially reduce motion amplitudes within the gate to below 5 mm if amplitude thresholds of less than 40 % were to be used. The effects of the residual motions on the resultant dose are then shown in the comparative dose-volume histograms shown in Fig. 12.13c. Without any motion mitigation, the effects are significant (compare the light blue DVH to the broken red DVH of the static case), with a substantially compromised dose homogeneity across the CTV due to the interplay effect. However, the mitigating effect of gating can also be observed, with the DVHs becoming steeper and steeper as the amplitude threshold is reduced from 50 % (red DVH) down to 20 % (green). Although none of the gated DVHs are quite as steep as for the static case, using a 30 % threshold or less (at least for this case) recovers dose homogeneity to the CTV to clinically acceptable levels.

12.4.2.2 Rescanning

We now move on to a motion mitigation technique that is specific to pencil beam scanning, namely, rescanning. In comparison to gating, this is a somewhat different approach, in that it doesn't try to reduce motion, but rather attempts to "wash out" interplay effects by the repeated application of the same scanning pattern. The idea behind this approach is the following. As the exact position and form of hot- and cold-spots resulting from the interplay effect are dependent on the synchronization of the delivery to the phase of breathing, then by applying the scanning pattern of each field many times and assuming that the start of each sub-scan is not at the same breathing phase each time, these dose heterogeneities should appear in different positions for each sub-scan and over the whole treatment will then be "washed out."

This approach has been intensively studied at our institute by both simulations and experiment [8, 30, 70, 85], as well as by a number of other groups [20, 67, 75]. An example of the effectiveness of this approach is shown in Fig. 12.14.

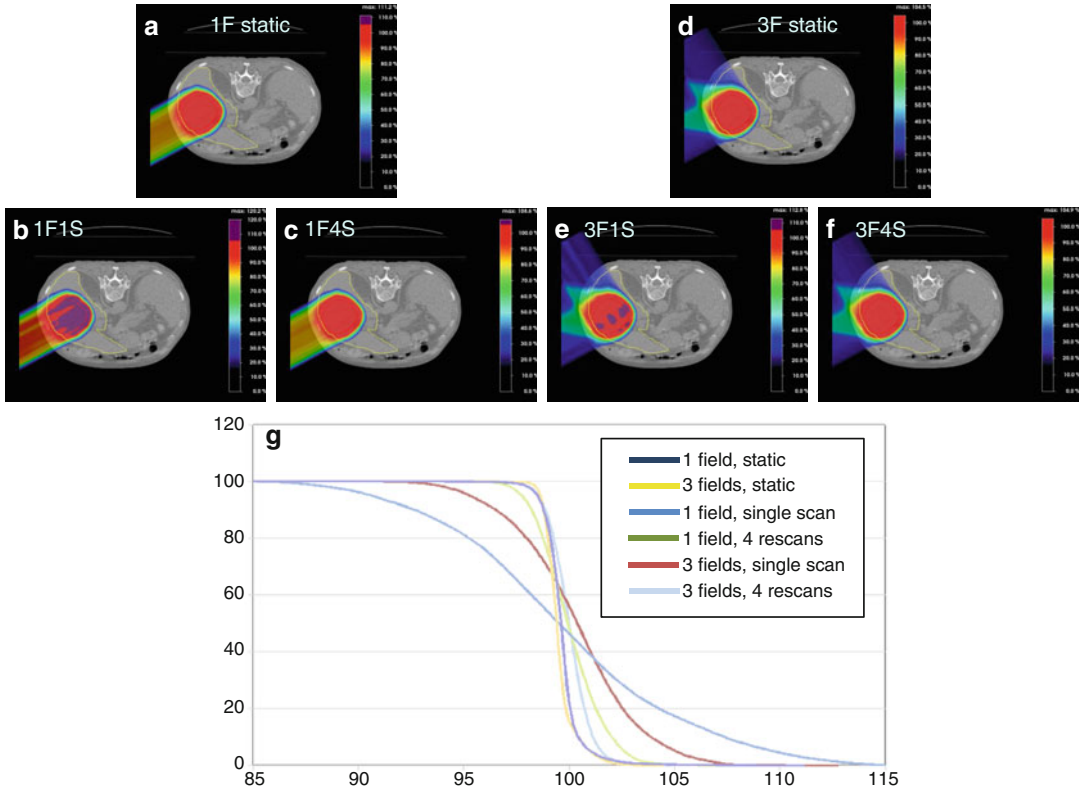

Fig. 12.14 Interplay effects and rescanning for single and multiple field, SFUD plans to a liver tumor: (**a**–**c**) Single-field plan, (**d**–**f**) Three-field plan, (**g**) Corresponding DVHs

As with gating, our example case is a liver tumor, to which both single- and three-field SFUD plans have been calculated (Fig. 12.14a–f) and for which 4D dose calculations based on 4D-MRI motions have been performed. For both plans, three dose distributions are shown corresponding to the static case (Figs. 12.14a, d), under conditions of motion (12.14b, e) and under conditions of motion but with four times rescanning of each field (12.14c, f). Already with these dose distributions, one sees the benefit of rescanning and the use of multiple SFUD fields. The distributions in Fig. 12.14c, e show much improved dose homogeneity when compared to the corresponding motion only cases, and this is confirmed in the DVHs for all plans shown in Fig. 12.14g, with the DVHs for the three-field plan being significantly steeper under conditions of motion than for the single-field plan. However, the most homogenous result, and that has the closest DVHs to the DVHs for the static plans, is for the three-field plan for which four times rescanning has been applied to each field. Thus, the combination of multiple SFUD fields, each with a rather moderate amount of rescanning, would appear to be sufficient for the case shown in order to recover dose homogeneity in the presence of motion. This maybe not a surprise because, as has been pointed out by Knopf et al. [30], the use of multiple SFUD fields is also a type of rescanning, so the rescan "factor" for the three-field plan with each field rescanned four times is equivalent to rescanning a single field 12 times. Note however that this multiple field effect does not necessarily help for IMPT plans, due to the much more inhomogeneous character of the individual fields for IMPT (see Fig. 12.4 above).

Although a conceptually simple approach, there are many details that have to be considered for rescanning in practice: first is the form of

rescanning used. From the dose (MU) scaling point of view, there are two variants, scaled and iso-layered, while there are also (at least) two variants on the sequencing of the rescanning within an individual field, layered and volumetric [70, 85]. So there are at least four variants to rescanning, with additional variants based on deliberately synchronizing the start of each sub-scan at different phases based on the breathing signal [20] and random time delays between scans [75]. For detailed descriptions of all these variants, the reader is referred to the relevant literature, plus the excellent review on motion and motion mitigation for particle therapy by Bert and Durante [11]. In addition, for lung tumors, it has been shown that rescanning and gating alone cannot fully recover dose coverage and homogeneity due to the significant range changes that occur due to motion in the lung area. For this reason, it has been proposed that range adaptive PTVs may need to be used that effectively extend the distal end of the PTV in order to ensure that the CTV is covered under all range modulated motion states (see, e.g., [31]).

Finally, it should not be thought that rescanning and gating are mutually exclusive – quite the opposite is true. Indeed, there are good reasons to combine gating and rescanning, with gating being used to reduce the overall motion amplitude, while modest levels of rescanning can then be used to correct for the remaining residual motion. This combined approach could be particularly useful for patients with large breathing amplitudes but is probably less useful for motions below about 5 mm, where rescanning will work sufficiently well on its own.

12.4.2.3 Tracking

The last motion mitigation technique to be discussed is what many consider to be the "holy grail" of mitigation techniques, the concept of following ("tracking") the tumor as it moves. This has been investigated in detail for heavy ion therapy by Bert and co-workers [9, 10, 21, 45] but, to the author's knowledge, has not yet been applied clinically anywhere. Although the concept has been shown to work experimentally in relatively simple setups, the real problem with tracking is actually knowing where the tumor (and range varying normal tissues) is in real time, as well as being able to react with the steering elements of the treatment machine (particularly energy) quickly enough to follow the motions. For the first problem, algorithms have been developed that can predict 3D motion within the liver based on population and patient-specific models and fluoroscopic x-ray 2D imaging (see, e.g., [87]), but these still need to be verified clinically. For the second problem, faster scanning systems are being developed (GSI papers), including faster energy changes [61], but it may also be possible to deal with potential range changes through a combination of tracking and range adapted PTV margins. In addition, retracking (the combination of tracking and rescanning) has been proposed by van de Water et al. [82] in order to reduce the effect of residual positioning errors due to inaccuracies on the tracking procedure. However, much work still needs to be performed in this direction to show that tracking is a clinically feasible, and accurate, approach.

12.5 Summary

Pencil beam scanning (PBS) is without doubt the future of proton therapy. Based on recent statistics [27], the worldwide number of treatment rooms equipped with PBS will overtake those with passive scattering sometime in the near future. This trend will certainly continue.

In this chapter we have outlined the fundamental approaches to treatment planning of PBS and have tried to accentuate the flexibility, automation, and efficiency of this process. Indeed, with PBS, protons now have a delivery technique, and associated planning processes, to be truly comparable with the technologies that have been common place in conventional photon therapy for the last 10–15 years (i.e., IMRT). It is such features of PBS that are making it the modality of choice of all new and planned proton facilities.

However, we have also highlighted two important issues about planning and delivering PBS proton therapy – range uncertainty and motion. Both can be considered to be limiting factors for the technique. On the other hand, the inherent

flexibility and degeneracy associated with PBS also provide many methods by which these can be countered. Indeed, from the point of view of motion, the possibility to quickly scan and modulate proton energy of individual, narrow proton beams could mean that PBS becomes the proton modality of choice for treating mobile tumors. Whatever the case, the potential of PBS proton therapy is only just beginning to be exploited, and much interesting and exciting technological and clinical work lies ahead.

References

1. Albertini F, Bolsi A, Ares C, Broggi S, Cattaneo G M and Lomax T. Advantage of using a MVCT for proton planning. Proceeding of the 44th PTCOG conference. Zurich: PSI; 2006.
2. Albertini F, Bolsi A, Lomax AJ, Rutz HP, Timmerman B, Goitein G. Sensitivity of intensity modulated proton therapy plans to changes in patient weight. Radiother Oncol. 2008;86:187–94.
3. Albertini F, Gaignat S, Bosshardt M, Lomax AJ. Planning and optimizing treatment plans for actively scanned proton therapy. In: Censor Y, Jiang M, Wang G, editors. Biomedical mathematics: promising directions in imaging, therapy planning and inverse problems. Madison: Medical Physics Publishing; 2010. p. 1–18.
4. Albertini F, Hug EB, Lomax AJ. The influence of the optimization starting conditions on the robustness of intensity-modulated proton therapy plans. Phys Med Biol. 2010;55:2863–78.
5. Albertini F, Hug EB, Lomax AJ. Is it necessary to plan with safety margins for actively scanned proton therapy? Phys Med Biol. 2011;56:4399–413.
6. Ares C, Hug EB, Lomax AJ, Bolsi A, Timmermann B, Rutz HP, Schuller JC, Pedroni E, Goitein G. Effectiveness and safety of spot scanning proton radiation therapy for chordomas and chondrosarcomas of the skull base: first long-term report. Int J Radiat Oncol Biol Phys. 2009;75:1111–8.
7. Avery S. Simulation study of proton beam characterization through acoustic measurements. PTCOG 44 Shanghai; 2014.
8. Bernatowicz K, Lomax AJ, Knopf A. Comparative study of layered and volumetric rescanning for different scanning speeds of proton beam therapy in liver patients. Phys Med Biol. 2013;58:7905–20.
9. Bert C, et al. Target motion tracking with a scanned particle beam. Med Phys. 2007;34:4768–71.
10. Bert C, et al. Dosimetric precision of an ion beam tracking system. Radiat Oncol. 2010;5:61.
11. Bert C, Durante M. Motion in radiotherapy: particle therapy. Phys Med Biol. 2011;56:R113–44.
12. Bokrantz R. Multicriteria optimization for volumetric-modulated arc therapy by decomposition into a fluence-based relaxation and a segment weight-based restriction. Med Phys. 2012;39:6712–25.
13. Boye D, Lomax AJ, Knopf A. Mapping motion from 4D-MRI to 3D-CT for use in 4D dose calculations: a technical feasibility study. Med Phys. 2013;40:0617021:11.
14. Carabe A, Moteabbed M, Depauw N, Schuemann J, Paganetti H. Range uncertainty in proton therapy due to variable biological effectiveness. Phys Med Biol. 2012;57:1159–72.
15. Chen W, Unkelbach J, Trofimov A, Madden T, Kooy H, Bortfeld T, Craft DL. Including robustness in multi-criteria optimization for intensity-modulated proton therapy. Phys Med Biol. 2012;57:591–608.
16. Chen H, Craft DL, Gierga DP. Multicriteria optimization informed VMAT planning. Med Dosim. 2014; 39:64–73.
17. Craft DL, Hong TS, Shih HA, Bortfeld TR. Improved planning time and plan quality through multicriteria optimization for intensity-modulated radiotherapy. Int J Radiat Oncol Biol Phys. 2012;82:83–90.
18. Dietlicher I, Casiraghi M, Ares C, Bolsi A, Weber DC, Lomax AJ, Albertini F. The effect of surgical titanium rods on proton therapy delivered for cervical bone tumors: experimental validation using an anthropomorphic phantom. Phys Med Biol. 2014;59(23):7181–94.
19. Evans PM. Anatomical imaging for radiotherapy. Phys Med Biol. 2008;53:R151–91.
20. Furukawa T, et al. Design study of a raster scanning system for moving target irradiation in heavy-ion radiotherapy. Med Phys. 2007;34:1085–97.
21. Groezinger SO, et al. Simulations to design an online motion compensation system for scanned particle beams. Phys Med Biol. 2006;51:3517–31.
22. Goitein M. Calculation of uncertainty in the dose delivered in radiation therapy. Med Phys. 1985;12:608–12.
23. Hanley J, et al. Deep inspiration breath-hold technique for lung tumors: the potential value of target immobilization and reduced lung density in dose escalation. Int J Radiat Oncol. 1999;45:603–11.
24. Hashimoto T, et al. Repeated proton beam therapy for hepatocellular carcinoma. Int J Radiat Oncol Biol Phys. 2006;65:196–202.
25. Hof H, et al. Stereotactic single-dose radiotherapy of stage I non-small-cell lung cancer (NSCLC). Int J Radiat Oncol. 2003;56:335–41.
26. ICRU Report 62. Prescribing, recording, and reporting photon beam therapy (Supplement to ICRU Report 50). Bethesda: ICRU; 1999.
27. Jermann M. Particle Therapy Worldwide-2013 Survey by PTCOG. PTCOG 53, Shanghai; 2014.
28. Kanai T, Kanai K, Kumamoto Y, Ogawa H, Yamada T, Matsuzawa H. Spot scanning system for radiotherapy. Med Phys. 1980;7:365–9.
29. Kanematsu N, Inaniwa T, Koba Y. Relationship between electron density and effective densities of body tissues for stopping, scattering and nuclear interactions of proton and ion beams. Med Phys. 2012; 39:1016–20.

30. Knopf AC, Hong TS, Lomax AJ. Scanned proton radiotherapy for mobile targets – the effectiveness of re-scanning in the context of different treatment planning approaches and for different motion characteristics. Phys Med Biol. 2011;56:7257–71.
31. Knopf A, Boye D, Lomax AJ, Mori S. Adequate margin definition for scanned particle therapy in the incidence of intra-fractional motion. Phys Med Biol. 2013;58:6079–94.
32. Knopf A, Lomax AJ. In-vivo range verification: a review. Phys Med Biol. 2013;58:R131–60.
33. Koehler AM. Proton radiography. Science. 1968; 160:303–4.
34. Koehler AM, Schneider RJ, Sisterson JM. Range modulators for protons and heavy ions. Med Phys. 1975;131:437–40.
35. Koehler AM, Schneider RJ, Sisterson JM. Flattening of proton dose distributions for large fields. Nucl Instrum Methods. 1977;4:297–301.
36. Korreman SS. Motion in radiotherapy: photon therapy. Phys Med Biol. 2012;57:R161–91.
37. Litzenberg DW, Bajema JF, Becchetti FD, et al. Online monitoring and PET imaging of proton radiotherapy beams. IEEE Trans Nucl Sci. 1993;40:954–6.
38. Litzenberg DW, Roberts DA, Lee MY. Online monitoring of radiotherapy beams: experimental results with proton beams. Med Phys. 1999;26:992–1006.
39. Lomax AJ, Pedroni E, Schaffner B, Scheib S, Schneider U, Tourovsky A. 3D treatment planning for conformal proton therapy by spot scanning. In: Proceedings of 19th L H Gray conference. London: BIR Publishing; 1996. p. 67–71.
40. Lomax AJ. Intensity modulated methods for proton therapy. Phys Med Biol. 1999;44:185–205.
41. Lomax AJ. Intensity modulated proton therapy. In: Delaney T, Kooy H, editors. Proton and charged particle radiotherapy. Boston: Lippincott, Williams and Wilkins; 2008.
42. Lomax AJ. Intensity modulated proton therapy and its sensitivity to treatment uncertainties 1: the potential effects of calculational uncertainties. Phys Med Biol. 2008;53:1027–42.
43. Lomax AJ. Intensity modulated proton therapy and its sensitivity to treatment uncertainties 2: the potential effects of inter-fraction and inter-field motions. Phys Med Biol. 2008;53:1043–56.
44. Lu HM, et al. A respiratory-gated treatment system for proton therapy. Med Phys. 2007;34:3273–8.
45. Luechtenborg R, Saito N, Chaudhri N, Durante M, Rietzel E, Bert C. On-line compensation of dose changes introduced by tumor motion during scanned particle therapy. In: Doessel O, Schlegel W, editors. World congress on medical physics. 1st ed. Heidelberg: Springer; 2009. p. 449–52.
46. Min CH, Kim CH, Youn MY, et al. Prompt gamma measurements for locating the dose fall-off region in the proton therapy. Appl Phys Lett. 2006;89:183517.
47. Minohara S, et al. Respiratory gated irradiation system for heavy-ion radiotherapy Int. J Radiat Oncol. 2000;47:1097–103.
48. Moteabbed M, España S, Paganetti H. Monte Carlo patient study on the comparison of prompt gamma and PET imaging for range verification in proton therapy. Phys Med Biol. 2011;56:1063–82.
49. Moyers MF, Miller DW, Bush DA, Slater JD. Methodologies and tools for proton beam design for lung tumors. Int J Radiat Oncol Biol Phys. 2001; 49:1429–38.
50. Mumot M, Algranati C, Hartmann M, Schippers JM, Hug EB, Lomax AJ. Proton range verification using a range probe: definition of concept and initial analysis. Phys Med Biol. 2010;55:4771–82.
51. Murphy MJ. Tracking moving organs in real time. Semin Radiat Oncol. 2004;14:91–100.
52. Mustafa A, Jackson DF. The relation between x-ray CT numbers and charged particle stopping powers and its significance for radiotherapy treatment planning. Phys Med Biol. 1983;2:169–76.
53. Newhauser WD, Giebeler A, Langen KM, Mirkovic D, Mohan R. Can megavoltage computed tomography reduce proton range uncertainties in treatment plans for patients with large metal implants? Phys Med Biol. 2008;53:2327–44.
54. Oelfke U, Lam GK, Atkins MS. Proton dose monitoring with PET: quantitative studies in Lucite. Phys Med Biol. 1996;41:177–96.
55. Paans AM, Schippers JM. Proton therapy in combination with PET as monitor: a feasibility study. IEEE Trans Nucl Sci. 1993;40:1041–4.
56. Parodi K, Enghardt W. Potential application of PET in quality assurance of proton therapy. Phys Med Biol. 2000;45:N151–6.
57. Paganetti H, Niemierko A, Ancukiewicz M, Gerweck LE, Loeffler JS, Goitein M, Suit HD. Relative biological effectiveness (RBE) values for proton beam therapy. Int J Radiat Oncol Biol Phys. 2002;53:407–21.
58. Paganetti H. Range uncertainties in proton therapy and the role of Monte Carlo simulations. Phys Med Biol. 2012;57:99–117.
59. Paganetti H, van Luijk P. Biological considerations when comparing proton therapy with photon therapy. Semin Radiat Oncol. 2013;23:77–87.
60. Pedroni E, Bacher E, Blattmann H, et al. The 200 MeV proton therapy project at PSI: conceptual design and practical realization. Med Phys. 1995;22:37–53.
61. Pedroni E, Bearpark R, Böhringer T, Coray A, Duppich J, Forss S, George D, Grossmann M, Goitein G, Hilbes C. The PSI Gantry 2: a second generation proton scanning gantry. Z Med Phys. 2004;14:25–34.
62. Penfold SN, Rosenfeld AB, Schulte RW, et al. A more accurate reconstruction system matrix for quantitative proton computed tomography. Med Phys. 2009;36:4511–48.
63. Pflugfelder D, Wilkens JJ, Oelfke U. Worst case optimization: a method to account for uncertainties in the optimization of intensity modulated proton therapy. Phys Med Biol. 2008;53:1689–700.
64. Phillips M, Pedroni E, Blattman H, Böhringer T, Coray A, Scheib S. Effects of respiratory motion on dose uniformity with a charged particle scanning method. Phys Med Biol. 1992;37:223–34.

65. Polf JC, Peterson S, Ciangaru G, et al. Prompt gamma-ray emission from biological tissues during proton irradiation: a preliminary study. Phys Med Biol. 2009;54:731–43.
66. Richter D, et al. Mitigation of residual motion effects in scanned ion beam therapy. Radiother Oncol. 2010;96:S72.
67. Rietzel E, Bert C. Respiratory motion management in particle therapy. Med Phys. 2010;37:449–60.
68. RPTC 2011 Erfahrungsbericht zweiter Monat klinischer Betrieb RPTC. 2009. http://www.rptc.de/de/infobereich/aktuelle-meldungen/erfahrungsberichte/news-detail/article/erfahrungsbericht-zweiter-monatklinischer-betrieb-rptc-mai-09.html.
69. Romero JL, Osborne JH, Brady FP, et al. Patient positioning for proton therapy using a proton range telescope. Nucl Instrum Methods Phys Res A. 1994;356:558–65.
70. Schätti A, Zakova M, Meer D, Lomax AJ. Experimental verification of motion mitigation of discrete proton spot scanning by re-scanning. Phys Med Biol. 2013;8:8555–72.
71. Schätti A, Meer D, Lomax AJ. First experimental results of motion mitigation by continuous line scanning of protons. Phys Med Biol. 2014;59(19):5707–23.
72. Schaffner B, Pedroni E. The precision of proton range calculations in proton radiotherapy treatment planning: experimental verification of the relation between CT-HU and proton stopping power. Phys Med Biol. 1998;43:1579–92.
73. Schneider U, Pedroni E. Proton radiography as a tool for quality control. Med Phys. 1995;22:353–63.
74. Schneider U, Pedroni E, Lomax AJ. On the calibration of CT-Hounsfield units for radiotherapy treatment planning. Phys Med Biol. 1996;41:111–24.
75. Seco J, et al. Breathing interplay effects during proton beam scanning: simulation and statistical analysis. Phys Med Biol. 2009;54:N283–94.
76. von Siebenthal M, Cattin P, Lomax AJ, Boesiger P, Székely G. 4D MRI imaging of respiratory organ motion and its variability. Phys Med Biol. 2007;52:1547–64.
77. Timmermann B, Lomax AJ, Nobile L, Grotzer MA, Weiss M, Kortmann RD, Bolsi A, Goitein G. Novel technique of craniospinal axis proton therapy with the spot-scanning system: avoidance of patching multiple fields and optimized ventral dose distribution. Strahlenther Onkol. 2007;183:685–8.
78. Unkelbach J, Bortfeld T, Martin BC, Soukup M. Reducing the sensitivity of IMPT treatment plans to setup errors and range uncertainties via probabilistic treatment planning. Med Phys. 2009;36:149–63.
79. Urie M, Goitein M, Doppke K, Kutcher G, LoSasso T, Mohan R, et al. The role of uncertainty analysis in treatment planning. Int Radiat Oncol Biol Phys. 1991;47:1121–35.
80. Vynckier S, Derreumaux S, Richard F, et al. Is it possible to verify directly a proton-treatment plan using positron emission tomography? Radiother Oncol. 1993;26:275–7.
81. Wong JW, et al. The use of active breathing control (ABC) to reduce margin for breathing motion. Int J Radiat Oncol Biol Phys. 1999;44:911–9.
82. van de Water S, Kreuger R, Zenklusen S, Hug EB, Lomax AJ. Tumour tracking with scanned proton beams: assessing the accuracy and practicalities. Phys Med Biol. 2009;54:6549–63.
83. Yang N, Virshup G, Clayton J, Zhu XR, Mohan R, Dong L. Theoretical variance analysis of single- and dual-energy computed tomography methods for calculating proton stopping power ratios of biological tissues. Phys Med Biol. 2010;55:1343–62.
84. Zenklusen SM, Pedroni E, Meer D, Bula C, Safai S. Preliminary investigations for the option to use fast uniform scanning with compensators on a gantry designed for IMPT. Med Phys. 2011;39:5208–16.
85. Zenklusen SM, Pedroni E, Meer D. A study on repainting strategies for treating moderately moving targets with proton pencil beam scanning at the new Gantry 2 at PSI. Phys Med Biol. 2010;55:5103–21.
86. Zhang Y, Knopf A, Tanner C, Lomax AJ. Online image guided tumour tracking with scanned proton beams: a comprehensive simulation study. Phys Med Biol. 2014;59(24):7793–817.
87. Zhang Y, Knopf A, Tanner C, Boye D, Lomax AJ. Deformable motion reconstruction for scanned proton beam therapy using on-line x-ray imaging. Phys Med Biol. 2013;58:8621–45.